Adsorption of Single-Wall Carbon nanotubes at Liquid/Liquid Interface

A thesis Submitted to the University of Manchester for the degree of

Doctor of Philosophy

In the Faculty of Science and Engineering

2017

Aminu Rabiu Koko

School of Chemistry

Table of Contents

List of Tables

List of Figures

The University of Manchester

Aminu Rabiu Koko

Doctor of philosophy

Adsorption of Single-wall Carbon nanotubes at Liquid/Liquid Interface

2017

Abstract

In this thesis, the adsorption of single-wall carbon nanotubes (SWCNTs) at the liquid/liquid interface, and the subsequent electrochemical investigation of the electrical properties of the adsorbed nanotubes have been studied.

Prior to the adsorption of the nanotube, the stability of dispersion of SWCNTs in non-aqueous solvents was assessed by determining the onset of aggregation of the SWCNTs when organic electrolyte was introduced. It was found that electrostatic repulsion between the SWCNTs contributes significantly to the stability of the SWCNTs in non-aqueous solvents. Similar result was also found when the aggregation kinetics of molybdenum disulphide (MoS_2) dispersion in non-aqueous media was studied using the same organic electrolyte.

The formation of nanomaterial-polymer composites by deliberate electrochemical oxidation of pyrrole and the sonochemical polymerisation of the organic solvent was also studied. Electrolyte addition was shown to be a promising way to separate the 2D material from the sonopolymer.

Declaration

I, Aminu Koko Rabiu, declare that no portion of the work referred to in this thesis has been submitted in support of an application for another degree or qualification of this or any other university or other institute of learning.

Copyright

Acknowledgment

First and foremost, I would like to give my special thanks to my supervisor, Prof. Robert Dryfe for his continuous support, patience and guidance throughout my PhD research period. I would also like to thank Kebbi State University of Science and technology, Aliero (KSUSTA) in collaboration with Tertiary Education Trust Fund (TETFund) Nigeria for funding of my studentship. Thanks also to the staff at the NEXUS facility, Newcastle University for carrying out all my XPS measurements.

Special thanks go to Dr Peter Toth and Dr Andrew Rodgers for their support and guidance and to all members of the electrochemistry group who helped in my project directly or indirectly.

My acknowledgment would not be complete without thanking my family members and friends for their support and understanding.

Publications

Aminu K. Rabiu, Peter S. Toth, Andrew J. N Rodgers and Robert A. W. Dryfe, Electrochemical investigation of adsorption of single wall carbon nanotubes at liquid/liquid interface, *Chemistry open*, 6, 57-63 (2017).

Peter S. Toth, Matěj Velický, Mark A. Bissett, Thomas J. A. Slater, Nicky Savjani, Aminu K. Rabiu, Alexander M. Rakowski, Sarah J. Haigh, Paul O'Brien, and Robert A. W. Dryfe, Asymmetric MoS_2-Graphene sandwiches: preparation, functionalization and application, *Adv. Mater.*, 28, 8256-8264 (2016).

P. S. Toth, A. N. J. Rodgers, A. K. Rabiu, D. Ebanez, J. X Yang, A. Colina and R. A. W. Dryfe. Interfacial doping of carbon nanotubes at polarisable organic/water: a liquid/liquid pseudo capacitor, *J. Mater. Chem. A*, 4, 7365-7371(2016)

P. S. Toth, A. K. Rabiu and R. A. Dryfe, Control preparation of carbon nanotube-conducting polymer composites at polarisable organic/water interface, *Electrochem. Commun.*, 60, 153-157 (2015).

P.S. Toth, A.N.J. Rodgers, A.K. Rabiu and R.A.W. Dryfe, "Electrochemical activity and metal deposition using few-layer graphene and carbon nanotubes assembled at the liquid–liquid interface", *Electrochem. Commun.*, 50, 6-10 (2015)

P.S. Toth, S.J. Haigh, A.K. Rabiu, A.N.J. Rodgers, A. Rakowski and R.A.W. Dryfe, Preparation of low dimensional carbon material-based metal nanocomposites using a polarisable organic/water interface, *J. Mater., Res.*, 30, 2679-2687 (2015).

Abbreviations

AD	Arc discharge
AFM	Atomic force microscopy
Ag/AgCl	Silver/silver reference electrode
BTPPA	Bis(triphenylphosphoranylidene)ammonium
BTPPACl	Bis(triphenylphosphoranylidene)ammonium chloride
BWF	Breit–Wigner–Fano
CCC	Critical coagulation concentration
CE	Counter Electrode
CNT	Carbon nanotube
CV	Cyclic voltammetry
CVD	Chemical vapour deposition
DB18C6	Dibenzo-18-crown-6
DCB	1,2-Dichlorobenzene
DCE	1,2-Dichloroethane
DLVO	Derjaguin, Landau, Verwey and Overbeek
DMF	Dimethylformamide
DMSO	Dimethyl sulphoxide
DOS	Density of states
EDL	Electrical double layer
ITIES	Interface between two immiscible electrolyte solutions
NMP	N-Mehtyl-2-pyrrolidone
PTFE	Polytetrafluoroethylene
PVDF	Polyvinylidene fluoride
PF_6^-	hexafluorophosphate

Py	Pyrrole
PPy	Polyppyrrple
RBM	Radial breathing mode
RE	Reference electrode
SEM	Scanning electron microscopy
SWCNT	Single-wall carbon nanotube
TBA	Tetrabutylammonium
$TFPB^-$	Tetrakis[3,5-bis-(trifluoromethyl)phenyl]-borate
TMA^+	Tetramethylammonium ion
TPB	Tetraphenylborate
TPBCl	Tetrakis(4-chlorophenyl)borate
$TPFB^-$	Tetrakis(pentafluorophenyl)borate ion
TPA	Tetraphenylarsonium
TPrA	Tetrapropylammonium
UV-Vis	Ultraviolet –Visible
vHs	van Hove singularities
VdWs	van der Waals
WE	Working electrode
XPS	X-Ray photoelectron spectroscopy

Chapter 1

Introduction

1.1 Carbon Nanotubes

Carbon nanotubes (CNTs) have been extensively studied since their discovery in 1991 by Iijima[1] due to their remarkable physical and structural properties. They are composed of a single or few-layer thick graphene sheet seemingly rolled-up into seamless cylindrical tubes (Figure 1.1). The ends of the tubes may be open or closed by a hemi-fullerene.[2] Graphene is a single sheet of graphite, one atom thick, consisting entirely of sp^2 hybridized carbon atoms arranged in a hexagonal honeycomb lattice.[3]

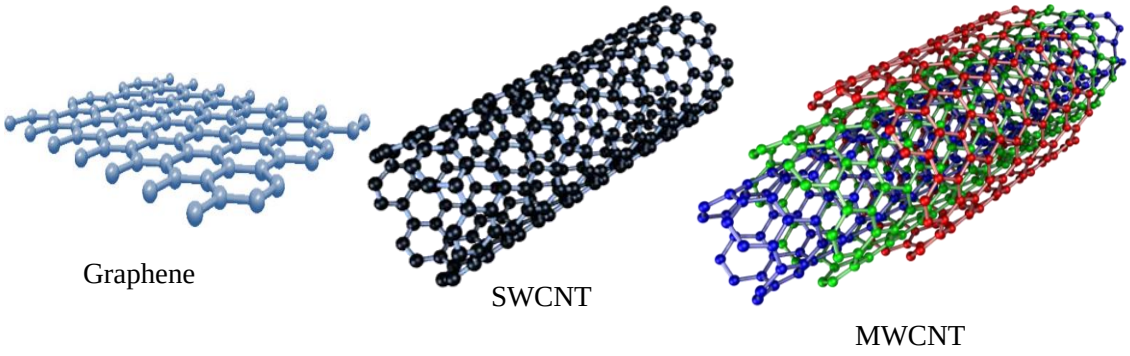

Figure 1. 1. Schematic representation of a graphene sheet, SWCNT and a MWCNT.

As indicated in Figure 1.1, the two main types of CNTs are single-wall carbon nanotubes (SWNTs) and Multiwall carbon nanotubes (MWCNTs). SWNTs consist of a single cylindrical layer of graphene sheet, whilst MWCNTs are composed of more than one layer of graphene rolled into concentric cylinders, with a

spacing of 0.34 nm between the individual cylinders.[2] The diameters of the nanotubes are typically 0.8 – 2 nm for SWCNTs and 5 – 20 nm for the MWCNTs, whilst their lengths range from about 100 nm to several centimetres.[2] Thus, CNTs possess large length to diameter ratio (aspect ratio, 10^2 – 10^7), and are commonly regarded as quasi-one-dimensional (1D) nanostructures.[4, 5]

CNTs hold great potential for numerous applications, including fillers in nanocomposite materials,[1] nanoelectronics,[6] field effect transistors,[7] electrochemical and sensor devices[5, 8] and as catalyst support.[9, 10] These applications are suggested based on the unique material properties exhibited by the nanotubes. For example, CNTs possess excellent mechanical properties, with a reported Young's modulus of ~1 TPa and a tensile strength that is between 10–100 times higher than that of steel.[1, 11] A thermal conductivity of 3500 W m^{-1} K^{-1} has been measured at room temperature for a SWCNT;[12] this value is impressively higher than that of diamond (2000 W m^{-1} K^{-1}).[2] In metallic SWCNTs and MWCNTs, the electronic transport takes place ballistically (*i.e.*, electrons transport through the nanotube without scattering) for distances in the range of microns, enabling the nanotubes to carry a large amount of current without dissipating heat.[5, 13] CNTs have been shown to tolerate current densities in excess of 10^9 A cm^{-2},[14] which is *ca.* three orders of magnitude greater than copper.[11, 13] In the case of semiconducting SWCNT, ballistic electron transport is also possible, but occurs only over nanotube lengths in the range of a few hundreds of nanometres.[11, 15] Moreover, CNTs exhibit a large surface area, up to 1500 m^2 g^{-1} and good chemical stability.[11]

1.1.2 Structure of a SWCNT

As mentioned previously, a SWCNT can be visualized as a single layer of graphene sheet rolled into a cylindrical tube. Depending on the direction about which the graphene sheet is rolled, various kinds of SWCNTs are produced (Figure 1.2). The structure, diameter and physical properties of each SWCNT are stated by a chiral vector, $\mathbf{C}_h$**,** which is defined by the relation

$$\mathbf{C}_h = n\mathbf{a}_1 + m\mathbf{a}_2 \tag{1.1}$$

where the integers n and m are called chiral indices and denotes the number of unit vectors ($\mathbf{a}_1$ and $\mathbf{a}_2$) in the hexagonal honeycomb lattice.[5, 16, 17] The diameter d_t and the chiral angle, θ, (angle between $\mathbf{C}_h$ and $\mathbf{a}_1$ direction) can be expressed in terms of the integers, n and m as[17, 18]

$$d_t = C_h/\pi = \frac{a}{\pi}\sqrt{n^2 + nm + m^2} \tag{1.2}$$

$$\theta = \tan^{-1}\left[\sqrt{3}m/(2n + m)\right] \tag{1.3}$$

where a is the lattice constant of the hexagonal honeycomb lattice, which is given as $a = \sqrt{3} \times a_{cc}$ (a_{cc} is the C-C bond length, which is ~ 0.142 nm in graphite), and C_h is the length of the chiral vector, $\mathbf{C}_h$.

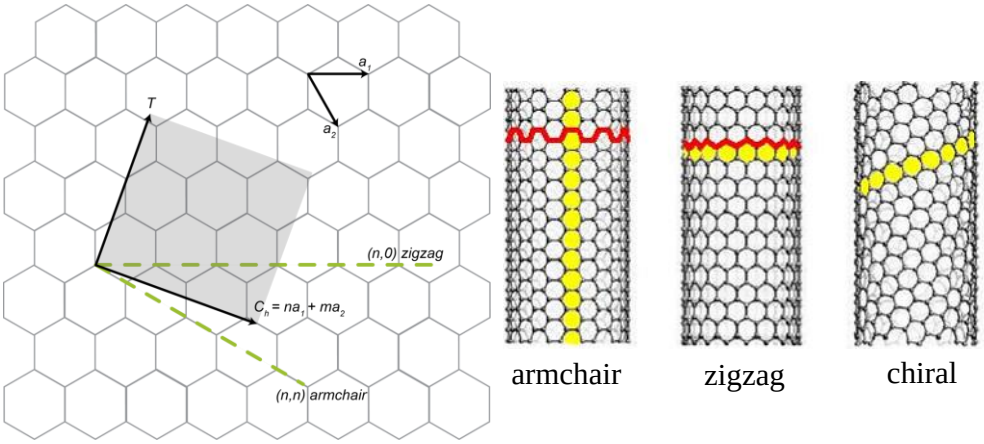

Figure 1. 2. Schematic illustration of the rolling up of a graphene sheet to form a variety of SWCNTs.

Based on the values of the n and m indices, SWCNTs can be grouped into three categories: zigzag, armchair and chiral nanotubes (Figure 1.2). A SWCNT is termed zigzag if its value of $m = 0$, armchair if its value of $m = n$, and chiral for all other values of m.[19] Alternatively, the chiral angle can also be used to define the different types of SWCNTs: zigzag nanotubes correspond to $\theta = 0$, armchair nanotubes correspond to $\theta = 30^{o}$ and the nanotubes are chiral for values $0 < \theta < 30^{o}$.[17]

Depending on the chirality of the tubes, they can be either metallic or semiconducting nanotubes. They are metallic if they are armchair or zigzag with $n - m = 3k$, where k is an integer that is not equal to zero.[20] Otherwise, the SWCNT are semiconducting with a band gap that is inversely proportional to their diameters.[5] Based on this, it has been predicted that, in a given sample of SWNTs in which the nanotube's chirality is not controlled, two-thirds of the nanotubes will be semiconducting and one-third will be metallic.[21]

1.1.2 Methods of SWCNT Synthesis

There are currently three main methods, namely, arc discharge (AD), laser ablation and chemical vapour deposition (CVD), that can be used to synthesise SWCNTs. These methods can allow high-quality and bulk quantities of SWCNTs to be produced.[22] The AD technique, initially applied for the synthesis of fullerenes, was the earliest method to be utilised to grow SWCNTs.[23, 24] In this method, a potential difference is applied across two graphite electrodes contained in a reaction chamber filled with an inert gas, such as helium or argon. As the electrodes are brought into close proximity, an arc is produced which results in the vaporisation of the graphite anode to form CNTs.[19, 25] The nanotubes produced in this way are usually MWCNTs. To form SWCNTs, a metal catalyst (*e.g.*, cobalt, iron, nickel-yttrium mixture, *etc*.) has to be incorporated into the arc-discharge system.[19, 26] A yield of 70 – 90% SWCNTs has been obtained with the nickel-yttrium catalyst using this technique.[26] The main advantage of AD method is that SWCNTs with a high degree of structural perfection can be produced by careful control of process parameters since high temperatures (> 2000 K) are used in the synthesis.[19, 27] However, a major drawback of this technique is that the SWCNTs are formed alongside other carbonaceous impurities (usually, fullerenes, amorphous carbon and graphitic polyhedrons) and metal catalysts, thereby necessitating post-synthesis purification.[28]

The laser ablation method, initiated by the Smalley's group,[29] was the next method to be applied for the synthesis of SWCNTs. In this technique, a high power laser is used to vaporise a graphite/metal (e.g., Ni-Co) composite target contained in a chamber heated to 1200 °C. The chamber is filled with a flowing inert gas, which during synthesis sweeps the produced nanotubes to a water-cooled copper collector

placed outside the reaction chamber. The laser ablation method has been used to obtained high quality SWCNTs with a yield comparable to that of AD method.[30] The main disadvantage of this technique, however, is that it is relatively more expensive than the AD method, as it requires high purity graphite rods, high laser powers and produces lower amounts of SWCNTs per day.[20]

The CVD technique is generally considered as the most promising method for industrial synthesis of SWCNTs because it can be easily scaled-up and, also, allows more control over the morphology and structure of the formed nanotubes.[22] In this technique, the carbon source is a hydrocarbon gas (acetylene or methane), which is made to flow along with an inert gas into a tube furnace reactor inside which a metal catalyst (usually, iron, nickel or cobalt nanoparticles) is deposited on a solid substrate. The furnace is typically held at temperatures between 500 °C and 1000 °C. The catalytic thermal decomposition of the hydrocarbon gas is followed by nucleation and growth of the SWCNTs. The yield of SWCNT is very high as compared to the other methods. One of the main advantages of this method is that it allows the growth of nanotubes directly on conventional, as well as patterned, solid substrates. There are several variants of CVD process that can be used to synthesise SWCNTs. One such method is the high pressure carbon monoxide (HipCO) method, in which carbon monoxide is used as the carbon feedstock and iron pentacabonyl, $Fe(CO)_5$, is employed as the catalyst precursor.[19, 22, 28]

1.1.3 Dispersion of SWCNTs in Liquid Phase

Owing to strong tube-tube attractive Van der Waals interaction and the hydrophobic graphene surface, as-produced SWCNTs tend to aggregate into bundles or ropes and are not easily dispersed in either water or organic solvents. Presently,

there are three main approaches that can be used to disperse SWCNTs in the liquid phase. The first approach involves coating or wrapping the SWCNTs with a dispersant material, typically a surfactant,[31, 32] a polymer[33] or a biomolecule[34] to aid their solubilisation in a given solvent. Mechanical agitation (ultra-sonication or high shear mixing) is usually applied to help in de-bundling and dispersing the nanotubes.[32] The coated or wrapped nanotubes are stabilised in the surrounding solvent medium by steric hindrance or electrostatic repulsion, arising from the adsorption of surfactant molecules onto the SWCNTs.[32, 35] One of the main advantages of this strategy is that water is frequently used as the dispersing medium, which is particularly important for a myriad of applications in which water must be used. Additionally, it also allows high weight fractions of SWCNTs to be suspended; up to 20 mg mL^{-1} of SWCNTs has been successfully dispersed with the aid of a surfactant.[31] However, the introduction of a third component into the system, which may be difficult to remove, is undesirable in many applications and most fundamental investigations.

The second approach that has been used to disperse SWCNTs in liquid phase is chemical functionalisation of the SWCNT sidewalls or ends caps prior to their dissolution. This approach has been used to increase the dispersibilty of SWCNTs in both water[36] and various organic solvents.[37] Several functionalisation strategies, including halogenation, oxidation, thiolation, amidation, esterification, radical addition, cycloaddition and electrochemical reduction have been employed and varying levels of enhancement in dispersibility has been achieved.[38] However, this approach results in the modification of the intrinsic properties of the SWCNTs and must be avoided in the case of investigations aimed at studying the pristine properties of the SWCNTs.[38, 39]

In order to avoid perturbation of the nanotube's intrinsic properties or the introduction of a third component into the system, the direct dispersion of pristine SWCNTs into non-aqueous solvents has been widely used. As in the case of aqueous dispersion preparation, ultrasonication is used to de-bundle and disperse the nanotubes in the non-aqueous solvents. To date, a large number of common solvents have been tested and varying degrees of exfoliation and dispersion quality demonstrated.[40, 41, 42] Amongst the successful solvents, cyclohexyl-pyrrolidone (CHP), *N*-methyl-2-pyrroldone (NMP) and *N*, *N*-dimethylformamide (DMF) are commonly regarded as the best for dispersing pristine SWCNTs.[35, 42, 43] Other solvents, which have been shown to successfully exfoliate and disperse SWCNTs include, 1,2-dichloroethane (DCE)[44-46] and 1,2-dichlorobenzene (DCB).[40, 47] These latter solvents are particularly relevant to the work described in this thesis.

There have been numerous studies aimed at understanding what distinguishes a "good" solvent for dispersing SWCNT from a "bad" one.[35, 42, 48-50] The majority of these studies have been based on solubility parameters, including the Hildebrand solubility parameter, Hansen solubility parameters and solvent surface energy. Initially, the Hildebrand solubility parameter was applied to study the dispersibility of SWCNTs in a range of solvents.[40, 42, 48, 49] The Hildebrand or total solubility parameter (δ_{T}), defined as the square root of the cohesive energy density (Equation 1.4), is a numerical value that indicate the total attractive intermolecular forces that must be overcome when dispersing solute molecules in a given solvent.[51] Solvents whose Hildebrand parameter matches that of the solute are regarded as "good" solvents. In the case of SWCNTs, it was found that the Hildebrand parameter is not specific enough to predict good nanotubes solvents as only a fraction of the solvents with the appropriate δ_T values were found to disperse SWCNTs.[42, 49, 50]

$$\delta_T = c^{1/2} = \left(\frac{\Delta H - RT}{V_m}\right)^{\frac{1}{2}} \quad (1.4)$$

where c = cohesive energy density, ΔH = enthalpy of vaporisation, R = gas constant, T = temperature and V_m = molar volume. This led to the consideration of the Hansen solubility parameters, which arise on the basis that the cohesive energy density of a material (*i.e.*, Hildebrand solubility parameter) is the sum of three different intermolecular interactions, namely, dispersive (δ_D), polar (δ_P) and hydrogen bonding (δ_H) interactions ($\delta_T = \delta_D + \delta_P + \delta_H$).[52] Therefore, by taking into account the different interactions, a clearer picture of the contribution of each component to the total interactions can be obtained. By using the set of thee Hansen parameters, Bergin *et al.*[42] found that SWCNTs were dispersed in solvents with δ_D in the range 17–18 $MPa^{1/2}$, δ_P in the range $5 < \delta_P < 14$ $MPa^{1/2}$ and δ_H in the range $3 < \delta_P < 11$ $MPa^{1/2}$. Similar results were also demonstrated by other researchers.[49, 50] However, while the Hansen solubility parameters could be useful in predicting nanotube solvents, it was also observed that many solvents having the correct Hansen parameters were not effective at dispersing SWCNTs.[42]

Since SWCNTs exhibit a well-defined surface, it was suggested[42, 53] that the surface energies rather than the cohesive energies should best describe the nanotube-solvent interactions. Indeed, it was demonstrated experimentally that solvents with surface energies close to that of SWCNTs (*ca.* 70 mJ m^{-2}) were successful at dispersing SWCNTs.[42, 53] However, many solvents with surface energies close to 70 mJ m^{-2} were also found to be ineffective at dispersing SWCNTs.[42] In addition solvents with very similar surface energies were observed to demonstrate different nanotube dispersibility. Therefore, while both the Hansen solubility parameters and

the solvent surface energy can be used as a guide to predict SWCNTs solvents, further work is needed to fully understand SWCNT dispersibility in non-aqueous solvents.

1.2 Molybdenum disulphide

The recent isolation of two-dimensional (2D) graphene and the demonstration of its exotic properties,[54, 55] have led to an upsurge of renewed interest in other 2D layered materials, particularly the transition metal dichalcogenides (TMDs).[56, 57] Layered TMDs are a family of materials with the general formula MX_2, where M is a transition metal element (*e.g.*, Nb, Ta, W, Mo) and X is a chalcogen atom (*e.g.*, S, Se, Te).[56, 58] Historically, this family of materials have been studied and used in various applications including lithium ion batteries, dry solid lubricants and catalysis.[59, 60] The exfoliated forms of the layered TMDs exhibit a diverse range of interesting mechanical, optical, thermal and electronic properties, due to surface and quantum confinement effects.[61] These properties are different from, but complementary to, those of graphene.[56, 62] While graphene is a zero-band gap semiconductor, single-layers of TMDs show sizeable bandgaps, which is important for a range of applications, such as electronics and optoelectronics.[56, 62] Among the different members of the TMDs family, molybdenum disulphide (MoS_2) has received the most attention due to its unique optical, catalytic and electronic properties.[57, 63, 64] For instance, MoS_2 in its three-dimensional (3D) bulk form possesses an indirect band gap of 1.2 eV, but changes to a direct band gap of 1.8 eV upon exfoliation down to a monolayer,[62] and exhibits strong photoluminescence.[65] The field-effect transistor fabricated from monolayer MoS_2 has been shown to demonstrate carrier mobility of about 200 $cm^2 V^{-1} s^{-1}$ and a current on/off ratio of 1×10^8.[66] Additionally,

single-/few-layer MoS_2 has demonstrated promise as a catalysis for hydrogen evolution reaction (HER) and energy storage devices.[67]

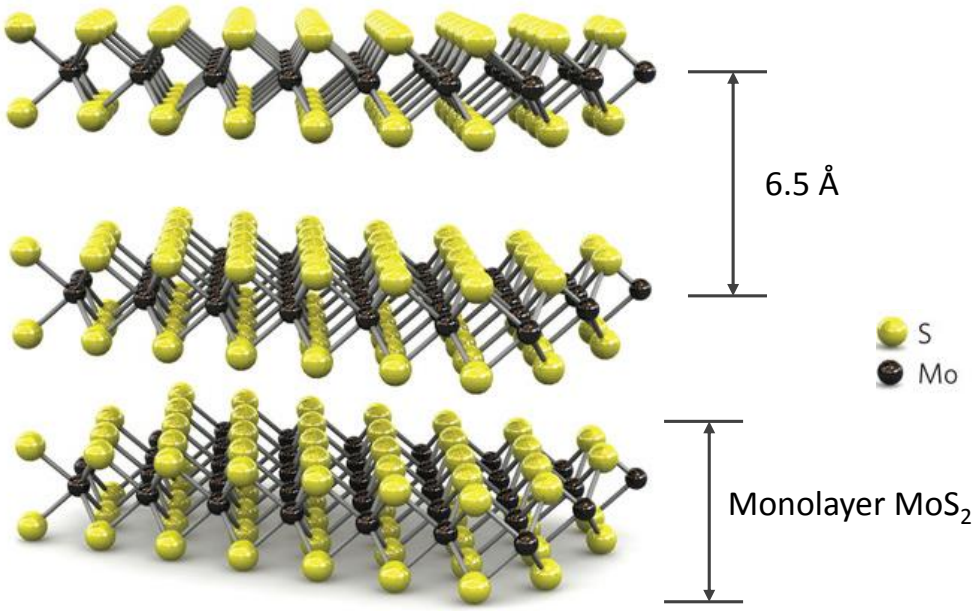

Figure 1. 3. Crystal structure of layered MoS_2. Adapted with permission from ref.[66] Copyright 2011 Macmillan Publishers Ltd.

A single-layer or monolayer MoS_2 consists of a hexagonal layer of molybdenum atoms sandwiched between two layers of sulphur atoms, in the form S-Mo-S (Figure 1.3).[63] The thickness of the three atoms (S-Mo-S) layer is reported to be in the range 0.6–0.7 nm.[63, 68] Bulk MoS_2 crystals are constructed from these S-Mo-S layers, while individual monolayers are attached to each other *via* van der Waals interaction forces, just as in the case of graphite.[56, 63] Because of the weak van der Waals interaction energies between the single layers, MoS_2 crystals can readily be exfoliated down to single- or few-layers 2D structures. Depending on the coordination of the Mo atoms, monolayer-MoS_2 can occur in either the trigonal prismatic (2H-MoS_2) phase or in an octahedral (1T-MoS_2) phase (Figure 1.4).[64, 68]

The two crystal phases exhibit different electronic properties and stabilities; 2H-MoS_2 is semiconducting and thermodynamically stable while 1T-MoS_2 is metallic and metastable.[61, 67, 68] The 1T-MoS_2 is believed to exhibit superior electrocatalytic activity towards hydrogen evolution reaction than the 2H-MoS_2, with charge transfer kinetics cited as one of the key factors responsible for the enhancement.[69-71] Interconversion between the two different phases has been demonstrated; 2H-MoS_2 can be converted *via* intercalation with alkali metals (*e.g.*, Li or K) to 1T-MoS_2,[72, 73] and since the latter is thermodynamically less stable, it converts slowly during storage at room temperature back to the 2H-MoS_2 phase.[74] 2H-MoS_2 has also been obtained by annealing freshly prepared 1T-MoS_2 at 300 °C.[73]

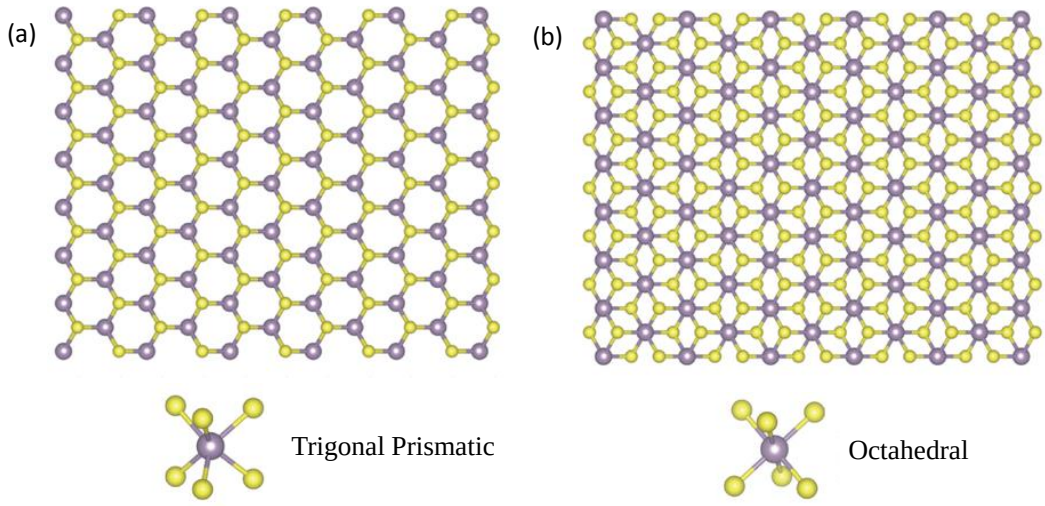

Figure 1. 4. (a) trigonal prismatic and (b) octahedral structures of monolayer MoS_2. The purple and yellow spheres represent molybdenum and sulphur atoms, respectively. Adapted with permission from ref.[68] Copyright 2013 Macmillan Publishers Ltd.

1.2.1 Liquid-Phase Exfoliation of MoS_2

Several methods have been employed to date to prepare single- or few-layer MoS_2. The first method that was used to isolate high quality single-layer MoS_2 is micromechanical cleavage.[75] This method involves using adhesive tape to detach

atomically thin flakes from the bulk MoS_2 crystals. The detached single- or few-layer crystals can easily be transferred to a substrate (often, Si/SiO_2 because it allows the prepared nanosheets to be optically detected).[56, 63, 66] Although this method produces the highest quality single-MoS_2 nanosheets, it suffers from lack of scalability and control over the size and thickness of the MoS_2 layers.[56, 63] As such, the application of this method is limited, largely, to fundamental characterisations as well individual device fabrication.[65, 68, 76] For fundamental and practical applications requiring large quantities of exfoliated MoS_2 nanosheets, liquid phase-exfoliation methods are commonly utilised. These methods are not only capable of producing large quantities of single- and few-layer MoS_2, but also, allow for solution-based processing of the resultant dispersion, such as deposition on solid substrates, formation of thin or free-standing films and nanocomposite materials, which can be prepared by simple mixing of the suspension with other nanomaterials.[77-80] There are many approaches that have been used to obtain MoS_2 nanosheets in the liquid-phase. These include chemical or electrochemical lithium-intercalation, followed by exfoliation in water or ethanol, and exfoliation by direct ultrasonication in appropriate organic solvents, aqueous-surfactant solutions or polymer solutions.[77, 81, 82]

1.2.1.1 Chemical and Electrochemical Lithium-Intercalation Methods

Although the chemical lithium-intercalation and exfoliation of bulk MoS_2 into single-layers was first reported in 1986,[83] dedicated effort on isolation and deposition of high quality monolayer MoS_2 sheets was only reinitiated recently after the discovery of graphene.[68, 73, 84] In a typical procedure, the bulk MoS_2 powder is soaked in a solution containing organic-based lithium intercalant, such as *n*-butyllithium (*n*-BuLi) or lithium borohydride ($LiBH_4$) for 1–3 days to allow lithium

to intercalate between the sheets of the MoS_2. When the intercalated MoS_2 is exposed to water, the lithium reacts vigorously with the water evolving hydrogen gas, which separates the MoS_2 layers, forming a colloidal suspension.[83-86] The MoS_2 nanosheets are stabilised electrostatically by a surface charge (presence of OH^- groups).[83, 85] Ultrasonication is typically employed to aid in the exfoliation of the nanosheets.[83-86] Although a high yield of monolayers can be obtained using this method, it has some drawbacks, which includes extreme environmental sensitivity, long lithiation time (1- 3 days) and cleaved reaction temperature (*e.g.* 100 °C).[73, 84]

In order to overcome some of the drawbacks of the chemical exfoliation method, Zeng *et al.*[87] proposed an alternative approach that uses electrochemical control to drive the lithium intercalation process. Lithium insertion into the MoS_2 inter-sheets occurs during galvanic discharge of the electrochemical cell, which comprised of bulk MoS_2-containing cathode and a lithium foil anode (serves as lithium ion source). As before, the lithium-intercalated species are exfoliated in water or ethanol *via* ultrasonication. The use of electrochemical control to intercalate lithium into the MoS_2 nanosheets has made the process faster, requiring only few hours (*e.g.*, 6 h) as compared to days for the case of chemical lithium-intercalation route. Moreover, the amount of lithium inserted can be monitored and accurately controlled, which is advantageous as sufficient lithium-intercalation can be achieved, and the decomposition of the lithium-intercalated species into metal nanoparticles and LiS_2, due to over-lithiation, can also be avoided.

Generally, the lithium-intercalation approach produces nanosheets which differ with respect to their structure and electronic properties from those of the bulk starting material.[73, 88] Specifically, the molybdenum atom coordination changes from

trigonal prismatic (2H), associated with the pristine MoS_2, to octahedral (1T), while the electronic structure changes from semiconducting to metallic.[73] As mentioned previously, annealing at 300 °C can lead to the conversion of the metallic 1T-MoS_2 to the semiconducting 2H-MoS_2, though 100% conversion is not usually achieved.[73]

1.2.1.2 Direct Exfoliation of MoS_2 in Liquids

An effective alternative route to using lithium-intercalation is the direct exfoliation of MoS_2 in suitable organic solvents, surfactants or polymer solutions. First described by the Coleman group,[77, 89] this represents a simple, scalable and inexpensive strategy that can be used to prepare pristine (2H) 2D MoS_2 nanosheets in solution. This approach is similar to that described in section 1.1.3 for the case of SWCNT dispersion preparation. Typically, the bulk MoS_2 is submerged in an appropriate liquid medium and sonication is used to provide energy sufficient enough to overcome the van der Waals interlayer attraction, resulting in the exfoliation of the MoS_2 nanosheets in solution. When water is used as the dispersion medium, a third phase component (*e.g.*, a surfactant) must be incorporated as a stabiliser.[81, 90] In this case, the nanosheets are stabilised against re-stacking either by steric or electrostatic repulsive interaction arising from the adsorption of the surfactant molecule on the nanosheets.[81, 90] Alternatively, the deliberate addition of a stabilising agent can be avoided by exfoliating the nanosheets in specific organic solvents.[77, 78] A wide range of organic solvents have been used to exfoliate and disperse MoS_2 nanosheets, with NMP and CHP appearing to be the most successful.[89] It is important to note that these solvents were also among the best solvents for dispersing SWCNTs. Direct solvent exfoliation produces mostly few-layer MoS_2 nanosheets, with small lateral size (50–1000 nm).[77] As with SWCNTs, attempts to describe the stabilisation

mechanism in terms of solvent solubility parameters have been reported and it was suggested that MoS_2 were dispersed in solvents that had surface energies close to that of nanosheets (~70 mJ m^{-2}, estimated by the authors from the exfoliation work and inverse gas chromatography measurements).[89] In addition the Hansen solubility parameters were also suggested to be useful in describing MoS_2 dispersibility.[89] However, not all solvents exhibiting the correct surface energy or Hansen solubility parameters were efficient in dispersing MoS_2, suggesting that as with SWCNTs further work is needed to fully understand MoS_2 dispersibility in non-aqueous solvents.

1.3 Particle Adsorption at Liquid/Liquid Interface

The adsorption of colloidal particles at liquid/liquid interfaces was first described by Ramsden[91] and Pickering[92] more than 100 years ago. Pickering[92] demonstrated that different micrometre size solid particles can adsorb at the interface between two immiscible liquids and generate a resistant film, which inhibits droplet coalescence, thereby stabilising emulsion droplets. Although using particles as emulsion stabilisers may have several advantages over surfactant stabilisation (*e.g.*, better emulsion stability), little attention was paid to the former approach until recently, with the renewed interest attributed to the present activity in nanoscale technology for fabrication of functional nanomaterials.[93, 94] There is also considerable interest in solids adsorbed at liquid/liquid interfaces for applications in catalysis and sensing.[95] The benefits of using liquid/liquid interfaces for the self-assembly of nanostructures is that the interface is defect-free and dynamic, allowing errors generated during the assembly to be corrected easily.[96] Several groups have successfully demonstrated the self-assembly of various kinds of nanoscale objects

including metal nanoparticles,[97, 98] two-dimensional (2D) nanomaterials (*e.g.*, graphene[99, 100] and MoS_2[101]) and CNTs[102-106] at the liquid/liquid interface. Depending on whether the liquid/liquid interface is curved (*i.e.,* involving emulsion droplets) or flat, the resultant particle assembly can form rings,[106] microporous capsules[107] or 2D nanoparticle films, localised between the bulk liquid phases[97].

Generally, the adsorption of colloidal particles from either the organic or aqueous phase to the water/oil interface is considered to be driven by a decrease in the free energy of the interface.[95, 96, 108] When a single spherical particle with radius, *r*, is adsorbed at the water/oil interface, the decrease in the interfacial energy from an initial value, E_0 (before adsorption) to a final one E_1 (after adsorption) is given by[109]

$$\Delta E = E_0 - E_1 = -\frac{\pi r^2}{\gamma_{o/w}}\left[\gamma_{o/w} - \left(\gamma_{p/w} - \gamma_{p/o}\right)\right]^2 \qquad (1.5)$$

where ΔE is the desorption energy (*i.e.*, the energy input required to desorb the particle), $\gamma_{o/w}$, $\gamma_{p/w}$ and $\gamma_{p/o}$ are the interfacial tensions arising from the oil/water, particle/water and particle/oil interfaces, respectively.

Equation 1.5 shows that for a given liquid/liquid system (keeping $\gamma_{o/w}$, $\gamma_{p/w}$ and $\gamma_{p/o}$ constant), the reduction in interfacial energy increases with increasing particle size, r^2. This means that larger particles will form more stable assemblies at the liquid/liquid interface than smaller ones. For micron-size particles, the energy required to desorb a particle is typically much larger than the thermal energy, k_bT, (on the order of 10^7 k_bT)[96]. As a result of this, micron-sized particles are generally held irreversibly at the liquid/liquid interface. On the other hand, nanometre sized particles exhibit desorption energy that is comparable to the thermal energy. This

leads to a dynamic adsorption of these nanoparticles to the interface, with particles being reversibly adsorbed and desorbed.[109, 110]

Besides particle size, the interfacial tensions $\gamma_{o/w}$, $\gamma_{p/w}$ and $\gamma_{p/o}$ (i.e., wettability of a particle surface) also controls the strength with which a particle is adsorbed at liquid/liquid interface (Equation 1.5). Practically, the measurement of $\gamma_{p/w}$ and $\gamma_{p/o}$ is not straightforward, and often the three-phase contact angle (θ) between the solid and the two immiscible liquid phases is used as a measure of particle wettability. The three-phase contact angle is related to the interfacial tensions of the three phases by Young's equation (Equation 1.6)[111]

$$\cos\theta = \frac{\gamma_{p/o} - \gamma_{p/w}}{\gamma_{w/o}} \tag{1.6}$$

By convention, θ is measured through aqueous phase. As shown in Figure 1.5, when $\theta < 90°$ the particle is hydrophilic and a larger portion of the particle is located in the bulk of the water phase. If $\theta > 90°$ the particle is hydrophobic and a larger portion of the particle is located in the bulk of the oil phase. When θ is around 90°, the particle prefers to sit at the interface between the two bulk liquid phases.[111, 112]

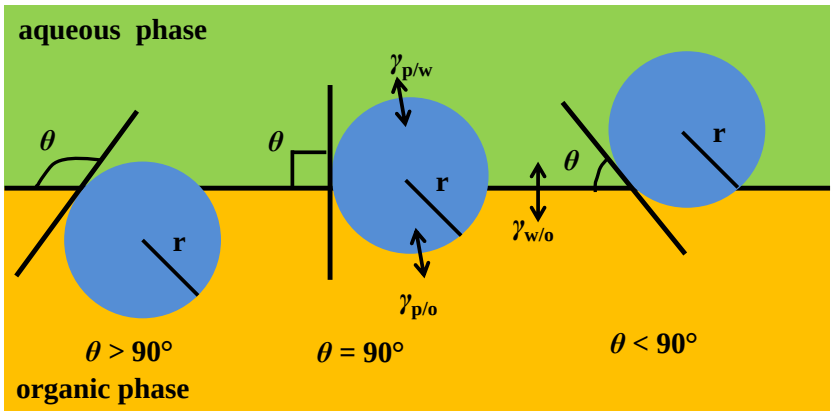

Figure 1. 5. Schematic illustration of the various positions of a spherical particle at liquid/liquid interface as a function of its contact angle.

Using the three-phase contact angle, the desorption energy of a spherical particle can be more easily calculated by employing the following Equation (1.7):[93]

$$\Delta E = \pi r^2 \gamma_{o/w} (1 \pm \cos\theta)^2 \qquad (1.7)$$

The sign inside the bracket of Equation 1.7 is positive for particle removal from the liquid/liquid interface into the organic phase and negative for removal into the aqueous phase.

It is important to note that Equations (1.5) and (1.7) are only applicable to spherical particles. For rod-like or cylindrical particles, such as SWCNTs, the expressions must be modified to account for the particle's geometry. Wang *et al.*,[113] have recently derived an expression for the change in interfacial energy (ΔE) due to the adsorption of a SWCNT at the liquid/liquid interface (Equation 1.8), where L and R are the length and radius of the SWCNT, respectively.

$$\Delta E = -2RL\gamma_{ow}(\pi\theta/180° \cos\theta - \sin\theta) \qquad (1.8)$$

In the above equation, SWCNT are assumed to adsorb with their long axis parallel to the liquid/liquid interface (Figure 1.6) because of their large aspect ratio.[105, 114, 115] On the basis of Equation 1.8, bundles and full-length nanotubes should be more effective at stabilising liquid/liquid interfaces than individual or short-length nanotubes. Using Equation 1.8, Wang *et al.*[113] estimated ΔE to be about 200 k_bT for an individual SWCNT and 4500 k_bT for a bundle of the same length comprising 7–10 individual tubes (the length and diameter of the nanotubes were however not specified). It has also been observed experimentally that short-length nanotubes produced by acid cut procedure exhibit reduced emulsion stabilisation capabilities compared to longer nanotubes.[116] Further discussion on CNT adsorption at liquid/liquid interfaces is presented in chapter 4.

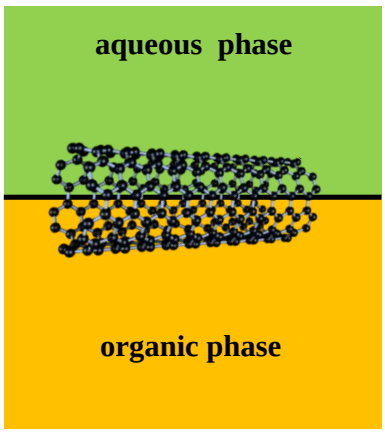

Figure 1. 6. Schematic representation of a SWCNT oriented parallel to the liquid/liquid interface.

1.4 Liquid/Liquid Electrochemistry

Liquid/liquid electrochemistry is concerned with the study of electrochemical processes occurring at the interface between two immiscible electrolyte solutions (ITIES). Typically, one of these solutions is an aqueous electrolyte and the other is a polar organic solvent containing an electrolyte. The organic solvent should be of moderately high relative permittivity (ε_r), typically in the range 10–35,[117, 118] so as to allow the dissociation of the dissolved electrolyte. Several organic solvents have been used in ITIES studies, with the most common ones being nitrobenzene (NB, ε_r = 34.8),[119] and DCE (ε_r = 10.36)[120]. Hydrophobic room temperature ionic liquids (RTIL) have also been used in place of organic electrolyte.[121, 122] The presence of electrolytes makes the respective phases conductive and allows external control of the electrical potential difference across the interface. Under proper set-up, the ITIES acts in a similar way to the metal/electrolyte interface. The difference between the two is that, in the case of the metal/electrolyte interface, current is observed due to redox reactions taking place on the surface of the electrode, whilst interfacial transper of charged species (either ions or electrons) governs the observed current flow for the case of ITIES.[123-125] Due to this similarity in behaviour of the two interfaces, many of the established electrochemical methods, such as chronoamperometry, cyclic voltammetry and impedance spectroscopy can be utilised in ITIES studies.[119, 120, 124-127]

The history of studies on the ITIES dates back to the end of nineteenth and the beginning of twentieth centuries, but major progress in the field started only in the 1970s after it was demonstrated that the ITIES could be polarised electrochemically.[123, 128-132] The introduction of a four-electrode potentiostat, with positive feedback loop to allow the elimination of ohmic drop, by Samec and co-

workers[130, 133] during this period was a major development that advanced electrochemical measurements at the ITIES.

There are two main factors that make electrochemical studies at the ITIES of great interest. Firstly, the ITIES can serve as a simple model of biological membranes for investigating many important biological processes, such as ion transfer.[134] Secondly, charge transfer reactions across liquid/liquid interfaces have a wide range of applications in chemistry, including solvent extraction,[135] electrocatalysis[136, 137] and phase transfer catalysis,[138] amperometric sensors[139] and electroanalysis[140]. Recently, the functionalisation or modification of liquid/liquid interfaces with metal or semiconducting nanoparticles, carbon nanostructures (including graphene and CNTs) has attracted significant attention for a range of applications, particularly, optics, catalysis and sensing.[100, 141-143] The study of the ITIES has focused mainly on ion-transfer, electron-transfer and assisted ion-transfer reactions.[144, 145]

1.4.1 Galvani Potential Difference and Nernst Equation for ITIES

The thermodynamic equilibrium condition for partitioning of an ion *i* between the aqueous (w) and organic (o) phase solutions is expressed by equating the electrochemical potential ($\tilde{\mu}_i^{\alpha}$, α = w or o) of the ion in both phases[127, 146]

$$\tilde{\mu}_i^{o} = \tilde{\mu}_i^{w} \tag{1.9}$$

where $\tilde{\mu}_i^{\alpha}$ is given by Equation (1.10) as

$$\tilde{\mu}_i^{\alpha} = \mu_i^{\alpha} + z_i F\phi \tag{1.10}$$

In the above Equation, ϕ is the inner (Galvani) potential of the phase α, and μ_i^{α} is the chemical potential of the ion i in that phase, z_i is the charge number of the ion

and *F* is the Faraday constant. The $z_i F\phi$ term represents the electrostatic contribution to the electrochemical potential.[146] From Equations (1.9) and (1.10), the Galvani potential difference between the two phases ($\Delta_o^w\phi = \phi^w - \phi^o$) can be expressed as[117, 127, 146]

$$\Delta_o^w\phi = \frac{1}{z_i F}(\mu_i{}^o - \mu_i{}^w) \tag{1.11}$$

Equation (1.11) can leads to Equation (1.12) by taking into account the concentration dependence of chemical potential of the ion[146]

$$\Delta_o^w\phi = \frac{1}{z_i F}(\mu_i{}^{o,^\circ} - \mu_i{}^{w,^\circ}) + \frac{RT}{z_i F}\ln\frac{a_i{}^o}{a_i{}^w} \tag{1.12}$$

where $\mu_i{}^{\alpha^\circ}$ is the standard chemical potential of the ion in phase *α*, *T* is the absolute temperature, *R* is the gas constant, and a_i is the activity of *i* in phase *α*. At an activity ratio of unity, the standard Galvani potential difference ($\Delta_o^w\phi_i^\circ$, also known as the standard ion transfer potential) for *i* can be expressed as[117]

$$\Delta_o^w\phi_i^\circ = \frac{1}{z_i F}(\mu_i{}^{o,^\circ} - \mu_i{}^{w,^\circ}) = \frac{1}{z_i F}\Delta G_i^{w\to o,^\circ} \tag{1.13}$$

where $\Delta G_i^{w\to o,^\circ}$ is the standard molar Gibbs energy of transfer of ion *i* from the aqueous phase to the organic phase and is given by the difference, $\mu_i{}^{o,^\circ} - \mu_i{}^{w,^\circ}$. Ions exhibiting large negative or positive values of $\Delta G_i^{w\to o,^\circ}$ are termed hydrophobic and hydrophilic ions, respectively.[122] The standard ion transfer potential is an important parameter as it measures the relative affinity of a given ion for two immiscible phases in contact.[146] From Equation (1.12 & 1.13), the Nernst equation for the ITIES can be written as[125, 127, 144, 146]

$$\Delta_o^w \phi = \Delta_o^w \phi_i^\circ + \frac{RT}{z_i F} \ln \frac{{a_i}^o}{{a_i}^w} \qquad (1.14)$$

Although Equation (1.14) is similar in form to the Nernst equation for redox reactions at the solid electrode/solution interface, it should be noted that there is no redox process involved in the former case.[125, 144] The similarity, however, suggests that the energetics at ITIES is described by the same laws as those in the redox process at solid electrodes.[146] It is also clear from this equation that the composition of the liquid phases can be altered by applying a positive or negative Galvani potential difference from an external source which causes an ion to transfer from one phase to the other.

When more than one ion is involved in the partition equilibrium, which is typically the situation in practical ITIES systems, the equilibrium Galvani potential difference is given by[117, 125]

$$\sum_i \frac{z_i c_i}{V^\alpha + V^\beta \left(\frac{\gamma_i^\alpha}{\gamma_i^\beta}\right) \exp\left[\frac{z_i F}{RT}(\Delta_o^w \phi - \Delta_o^w \phi_i^\circ)\right]} = 0 \qquad (1.15)$$

where V^α and V^β are the volume of the two immiscible phases (e.g., *w* and *o*), c_i is the concentration of the ion across both phases, γ_i^α and γ_i^β are the activity coefficients in each phase. This equation is complicated and can only be solved analytically in some limiting cases. *e.g.* the case of a monovalent salt ($A^+ B^-$) that dissociates completely in both phases.[117, 122, 125] Two of these limiting cases are relevant to the work described in this thesis and are discussed in section 1.5.2.

1.4.2 Polarisable and Non-polarisable ITIES

Generally, the interfaces between two immiscible electrolyte solutions can be classified as polarisable or non-polarisable interfaces depending on whether the interface can be polarised externally using a potentiostatic control or not. When the two immiscible solutions in contact contain a common ion such as tetrabutylammonium (TBA^+) with hydrophobic and hydrophilic counterions, the TBA^+ will achieve partition equilibrium between the two solutions, such that the interface becomes polarised at a fixed potential called the distribution potential. This distribution potential is given by Equation (1.14), which is rewritten as Equation (1.16) provided the condition,

$$\Delta_o^w\phi^\circ_{\mathrm{TBA^+}} - \Delta_o^w\phi^\circ_{\mathrm{X^-}} \gg 4\left(\frac{a^0_{\mathrm{TBAY}}}{a^0_{\mathrm{TBAX}}}\right)\left(1+\frac{a^0_{\mathrm{TBAY}}}{a^0_{\mathrm{TBAX}}}\right)$$

applies, where X and Y are aqueous and organic counterions respectively.

$$\Delta_o^w\phi = \Delta_o^w\phi^\circ_{\mathrm{TBA^+}} + \frac{RT}{F}\ln\frac{a_{\mathrm{TBA^+}}{}^o}{a_{\mathrm{TBA^+}}{}^w} \qquad (1.16)$$

Since this polarisation potential is fixed, the interface cannot be polarised by applying potential from an external source without changing the chemical compositions of the adjacent phases. Thus, the interface is said to be non-polarisable and this constitutes one limiting case of Equation (1.15).[144] This type of interface is typically used as a reference liquid/liquid interface because it is reversible for one of the organic phase ions (*e.g.*, bis(triphenylphosphoranylidene)ammonium ion, $BTPPA^+$, used in this thesis).

On the other hand, a polarisable (or more accurately, ideally polarisable) interface is one in which a hydrophilic salt, such as LiCl, is dissolved in water and a

hydrophobic salt such as tetrabutylammonium tetraphenyl borate (TBATPB), is dissolved in organic phase so that the concentration of each salt in the other phase is negligible. Under these conditions, the Galvani potential of the interface will be undefined and thus the interface will be ideally polarisable, *i.e.*, the interface can be polarised from an external potential provided $\Delta_o^w\phi^\circ_{\mathrm{Li}^+}$, $\Delta_o^w\phi^\circ_{\mathrm{TPB}^-} \gg 0$ and $\Delta_o^w\phi^\circ_{\mathrm{TBA}^+}$, $\Delta_o^w\phi^\circ_{\mathrm{Cl}^-} \ll 0$.[117, 119, 125, 144] This represents the second limiting case of Equation (1.15) that is important in this thesis.

1.4.3 The potential Window

For the case of the ideally polarisable ITIES discussed above, there is a Galvani potential range over which negligible ion re-distribution occurs (*i.e.*, within this range all ions remain essentially in their parent phases). This potential range is called the potential window and its limits are dictated by the lowest values of the standard Galvani potentials of the ions involved.[117] Figure 1.7 illustrates the principles of the potential window for a liquid/liquid system in which the aqueous phase contains lithium chloride (LiCl, a hydrophilic salt) and the organic phase (DCE) contains bis(triphenylphosporanylidene)ammonium tetrakis(4-chlorophenyl) borate (BTPPATPBCl, a hydrophobic salt).

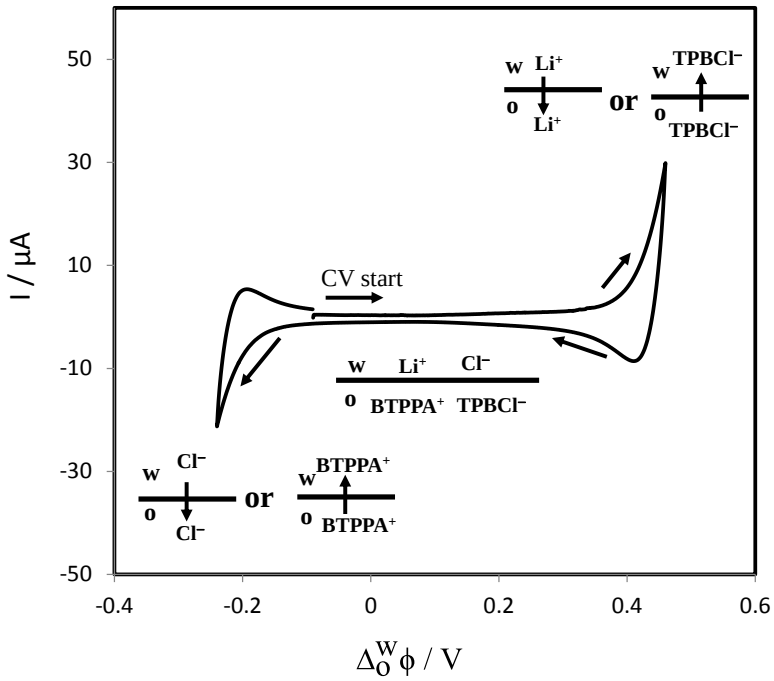

Figure 1. 7. Cyclic voltammogram of an ITIES system (10 mM $LiCl_{(aq)}$/10 mM $BTPPATPBCl_{(DCE)}$) illustrating the potential window for the supporting electrolyte (the window is limited by the transfer of aqueous phase ions, Li^+ and Cl^-). Scan rate: 50 mV s^{-1}.

By ITIES convention, the polarity of the interface is assigned to the aqueous phase, so that positive polarisation implies that the aqueous phase becomes more positive and negative polarisation means the opposite.[124, 125] If a positive or negative Galvani potential is applied from an external source, only a little current flows within the potential window due to charging of the interface. As the polarisation continues in either direction, ions limiting the potential window will begin to transfer from their original phase into the adjacent phase and a large increase in current is recorded. At high positive polarisation, either the positive ion in the aqueous phase, Li^+ in this case, or the negative ion in the organic phase, $TPBCl^-$, transfers to the opposite phase. Similarly, at high negative polarisation either the negative ion in the aqueous phase (Cl^- in the present case) or the positive ion in the organic phase ($BTPPA^+$) transfers into the opposite phase. Faradaic processes, e.g., ion transfer can

only be studied within the available potential window. Thus, it is important to have as large a potential window as possible. The size of the potential window is influenced by the choice of the organic solvent (since water is typically used as the aqueous phase) and the supporting electrolytes in each phase.[147, 148]

Due to inherent thermodynamic limitations, the Galvani potential difference $\Delta_o^w\phi$ across the ITIES cannot be measured directly. In order to estimate this potential difference, an extra-thermodynamic assumption must be employed. The assumption that is most frequently used is the Parker's[149] hypothesis which states that the cation and the anion of tetraphenylarsonium teraphenylborate ($TPAs^+$ TPB^-) have equal standard Gibbs energy of transfer between any pair of solvents (*i.e.*, $\Delta G_{\mathrm{TPA}^+}^{w\to o,^\circ} = \Delta G_{\mathrm{TPB}^-}^{w\to o,^\circ}$) considering that the two ions are of similar size. $\Delta G_{\mathrm{TPA}^+}^{w\to o,^\circ}$ and $\Delta G_{\mathrm{TPB}^-}^{w\to o,^\circ}$ can be determined from the standard Gibbs energy of transfer of the salt, TPAsTPB. On the basis of this, the standard Gibbs energy of transfer of all other ions can be evaluated by determining the standard Gibbs energy of transfer of their salt from solubility, partition or volatammetric measurement with either $TPAs^+$ or TPB^-. The standard Galvani potential difference for the ion transfer can thus be obtained by applying Equation (1.9).[122, 127, 131, 150]

1.4.4 Simple Ion Transfer across Polarised ITIES

Ion transfer across polarised liquid/liquid interfaces is probably the commonest charge transfer reaction studied at these interfaces. Apart from the transfer of the supporting electrolyte ions described previously, it is also possible to observe the transfer of ions which can partition between the two phases and are less soluble in either phase than the supporting electrolyte of that phase. The transfer of these semi-hydrophobic or semi-hydrophilic ions will take place at intermediate

Galvani potentials within the ideally polarisable potential range of the ITIES system. This will result in the observation of an electric current due to ion transfer from one phase to the other. Figure 1.8 shows a typical cyclic voltammogram demonstrating the transfer of a tetramethylammonium (TMA^+) ion (added to the aqueous phase) across the water/DCE interface. The aqueous phase contains 0.1 M LiCl and the DCE phase contains 10 mM BTPPATPBCl as supporting electrolytes. The transfer of the TMA^+ ion occurs in the middle of the potential window, displaying features similar to those observed for a diffusion limited redox reaction at a metal electrode/electrolyte interface. The forward peak current is now due to the TMA^+ crossing the interface from the aqueous phase into the DCE phase on positive polarisation and back into the aqueous phase on reverse polarisation. Ion transport across the liquid/liquid interface is typically considered to be fast and, therefore, can be described by the same equations as those for transport of redox species to and away from an electrode. The separation of the positive and negative peak potential for a reversible ion transfer is also similar to that of a redox process at solid electrode/electrolyte interface (*i.e.* $59/z_i$ mV).[120, 124, 125]

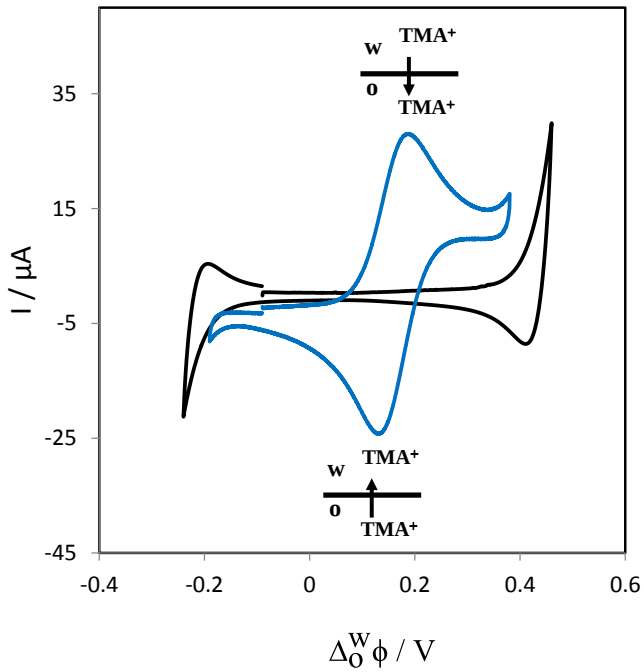

Figure 1. 8. Cyclic voltammetric response of supporting electrolytes ions (black curve, shown previously in Figure 1.5) and reversible TMA^+ (0.2 mM) transfer across 10 mM $LiCl_{(aq)}$/10 mM $BTPPATPBCl_{(DCE)}$ interface (blue curve). Scan rate: 50 mV s^{-1}. The voltammetric response of the supporting electrolyte ions is shown for comparison.

1.4.5 Facilitated Ion Transfer across Polarised ITIES

The facilitated, or assisted, transfer of ions by a ligand (or ionophore) present in the organic phase is an important class of ion transfer reactions studied at the polarised liquid/liquid interface. If an ion present in the aqueous phase can selectively combine with a hydrophobic ligand in the organic phase to form a complex, the ion's Gibbs energy of transfer can be lowered and the transfer process is said to be facilitated.[145, 151] This type of ion transfer reaction was first studied by Koryta[131] in 1979, where it was shown that the transfer of K^+ and Na^+ ions dissolved in the aqueous phase was facilitated by a natural antibiotic, valinomycin and synthetic ionophore, dibenzo-18-crown-6 (DB18C6), present in the organic phase. These ions, which would normally limit the potential window on the positive end, were observed to transfer within the polarisation range due to the complex formation

which effectively shifts their transfer potentials to less positive values. In the case of a simple complex formation with a 1:1 stoichiometry (either the ligand in the organic phase or the ion in the aqueous phase is in excess with respect to the other), the association constant of the complex, K_a, can be written as[144, 145]

$$K_a = \frac{a^o_{\mathrm{ML}}}{a^o_{\mathrm{M}} a^o_{\mathrm{L}}} \tag{1.17}$$

where a^o_{ML} stands for the activity of the complex, a^o_{M} and a^o_{L} are the activity of ion and ligand, respectively. The Galvani potential difference for the facilitated ion transfer is now given by[139]

$$\Delta^w_o \phi = \Delta^w_o \phi^{\circ}_{\mathrm{M}} + \frac{RT}{z_i F} \ln \frac{a^o_{\mathrm{ML}}}{K_a a^w_{\mathrm{M}} a^o_{\mathrm{L}}} \tag{1.18}$$

Equation 1.18 indicates that the presence of a ligand in the organic phase can shift the potential of ion transfer depending on the association constant of the complex.[122, 144] Similar to simple ion transfer, facilitated ion transfer is also considered to be fast, and therefore limited by the diffusion of either the ligand in the organic phase or the ion in the aqueous phase.[139, 152]

With regards to the mechanism of facilitated ion transfer, four possible mechanisms (Figure 1.9) have been proposed by Girault *et al*:[153] transfer by interfacial complexation (TIC), transfer by interfacial dissociation (TID), transfer followed by organic phase complexation (TOC) and aqueous complexation followed by the transfer of the complex (ACT). The precise mechanism involved depends on several factors, namely, relative concentrations of the aqueous ion and the ligand, distribution coefficient of the ligand in the respective phases and/or association constant.[139] When using the ligand, DB18C6 or valinomycin, the concentration of the aqueous ion to be transferred is in excess compared with that of the ligand in the

organic phase, which is the condition used in facilitated ion transfer studies reported in this thesis, the mechanism involved is believed to be TIC.[139, 153]

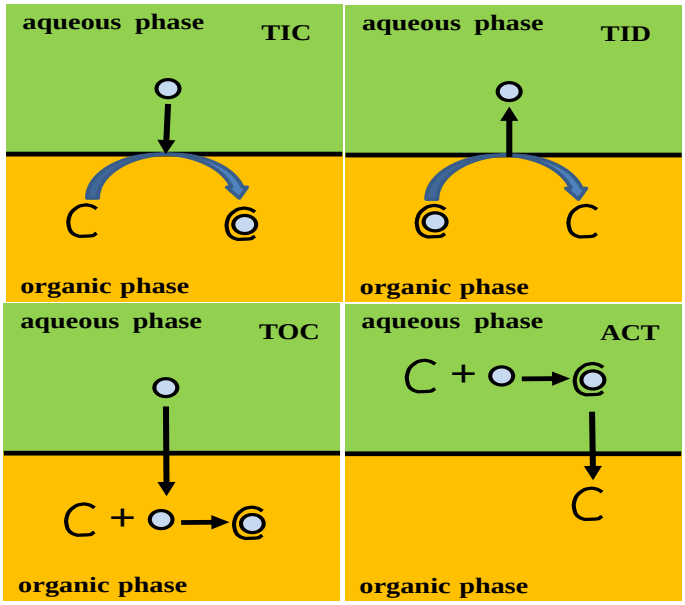

Figure 1. 9. Schematic of mechanisms of facilitated ion transfer across polarised ITIES. Adapted from ref.[153]

1.4.6 Electron Transfer across Polarised ITIES

In addition to ion (simple and facilitated) transfer reactions, heterogeneous electron transfer at the ITIES can also be observed between a hydrophilic redox couple (O_1^w/R_1^w) present in the aqueous phase and a hydrophobic redox couple (O_2^o/R_2^o) contained in the organic phase (Figure 1.10). The interfacial electron transfer can be driven in either direction *via* the application of an external potential, just as in the case of ion transfer. For the generic electron transfer reaction

$$O_1^w + R_2^o \rightleftharpoons R_1^w + O_2^o \qquad (1.19)$$

The equivalent Nernst equation can be written as Equation (1.21) starting with the equilibrium condition (Equation 1.20)

$$\tilde{\mu}_{\mathrm{O1}}{}^{w} + \tilde{\mu}_{\mathrm{R2}}{}^{o} = \tilde{\mu}_{\mathrm{R1}}{}^{o} + \tilde{\mu}_{\mathrm{O2}}{}^{w} \tag{1.20}$$

$$\Delta_o^w \phi = \Delta_o^w \phi_{\mathrm{ET}}^{\circ} + \frac{RT}{F} \ln \frac{a_{\mathrm{R1}}^o a_{\mathrm{O2}}^w}{a_{\mathrm{R2}}^o a_{\mathrm{O1}}^w} \tag{1.21}$$

where $\Delta_o^w \phi_{\mathrm{ET}}^{\circ}$ is the standard Galvani potential difference for the interfacial electron transfer or simply the standard redox potential. This is given by Equation (1.22), *i.e.*, as the difference between the standard redox potentials of the two redox species stated on the aqueous SHE (standard hydrogen electrode) scale.[136]

$$\Delta_o^w \phi_{\mathrm{ET}}^{\circ} = \left[E_{\mathrm{O2/R2}}^{\mathrm{o}}\right]_{\mathrm{SHE}}^{\mathrm{o}} - \left[E_{\mathrm{O1/R1}}^{\mathrm{w}}\right]_{\mathrm{SHE}}^{w} \tag{1.22}$$

The term, $\left[E_{\mathrm{O2/R2}}^{\mathrm{o}}\right]_{\mathrm{SHE}}^{\mathrm{o}}$, representing the standard redox potential of the organic redox couples *vs.* SHE is difficult to measure experimentally, since such a measurement would include a liquid junction potential. One approach that is commonly used to avoid this difficulty is to measure the standard redox potential of the organic redox couple on Fc^+/Fc (ferrocenium/ferrocene) scale,[136, 137] as the standard redox potential of the Fc^+/Fc couple in DCE, $\left[E_{\mathrm{Fc^+/Fc}}^{\mathrm{o}}\right]_{\mathrm{SHE}}^{\mathrm{DCE}}$, has been evaluated using thermodynamic cycle to be 0.64 V.[154]

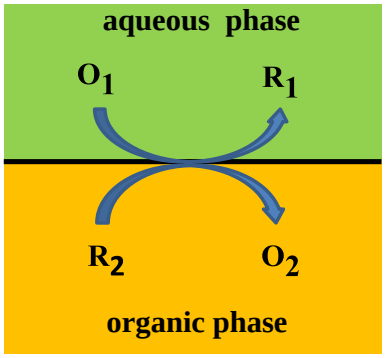

Figure 1. 10. Schematic illustration of heterogeneous electron transfer at ITIES.

1.4.7 Activity of Ionic Solutions

In the previous sections, 1.4.1–1.4.6, the Nernst equations for the ion and electron transfer at the ITIES and other formulations were expressed in terms of activities rather than concentrations. This is because in electrolyte solutions, electrostatic interactions between ions are typically non-negligible even in dilute solutions and are, in fact, believed to be the main cause of non-idealities in these solutions.[155] The activity of an ionic species, a_i, can be viewed as its effective concentration that takes part in a physical or chemical process and is related to the actual ion concentration, c_i, as given by the following relation:[156]

$$a_i = \gamma_i \frac{c_i}{c_i^{\circ}} \tag{1.23}$$

where γ_i is termed the activity coefficient and serves as the correction factor for the non-ideal behaviour; c_i° denote a standard state concentration (usually taken to be 1 mol L^{-1}). In the above equation, both a_i and γ_i terms are dimensionless.

In very dilute solutions (in which interactions between the ions can be neglected, $\gamma_i \rightarrow 1$), the concentration and activity terms can be considered to be identical (*i.e.*, $a_i = c_i$) and the solution is said to exhibit "ideal behaviour".[156] Because of the stronger Coulombic forces between ions, the concentration at which electrolyte solutions loses its ideality is generally low (in the range of micro-molar in aqueous solution).[157]

The activity coefficient, γ_i, can be determined with the help of either the Debye-Hückel limiting law or the Debye-Hückel extended law, depending on the ionic strength, *I*, of the solution. *I* (in mol L^{-1}) measures the total concentration of the ions present in a solution and can be calculated using equation 1.24:[156, 158]

$$I = \frac{1}{2}\sum_i c_i z_i^2 \tag{1.24}$$

where z_i is the charge on the ion and c_i is its concentration. When the ionic strength of the solution is $\leq 10^{-3}$ mol L^{-1}, the Debye-Hückel limiting law (equation 1.25) is used to calculate the activity coefficient. For solutions having higher ionic strength (up to 10^{-1} mol L^{-1}), the Debye-Hückel extended law (equation 1.26) becomes applicable.[156, 158]

$$\log \gamma_i = -Az^2\sqrt{I} \tag{1.25}$$

$$\log \gamma_i = -\left(Az^2\sqrt{I}\right)/\left(1 + Ba\sqrt{I}\right) \tag{1.26}$$

In the above equations, A and B are constants and depend on temperature and the relative permittivity of the solvent; a (measured in angstroms) is the radius of the hydrated ion. All other parameters have their usual meanings. For water at 25°C, the values of A and B are found to be 0.509 and 0.329, respectively.

Experimentally, the activity of a single ion cannot be measured since every solution has to be electrically neutral. What is measured instead is the mean ionic activity, $\gamma_{\pm}$, which represents the average contributions of all ions in a solution.[156]

1.5 Aim and Objectives

The main aim of the current work is to investigate the adsorption of single-walled carbon nanotubes at the interface between two immiscible liquids, probe their electrochemical properties at the interface and the formation of carbon nanotube-conducting polymer composites.

The specific objectives of the project are as follows:

1. To prepare SWCNTs dispersions in organic solvents, characterise them and study nanotubes' aggregation induced by the presence of an organic electrolyte.
2. To adsorb SWCNTs at the liquid/liquid interface by ultrasonication and investigate the effect of both organic and inorganic electrolytes on the adsorption behaviour, as well as characterise the film produced *in-situ* using optical microscopy and *ex-situ* using electron microscopy.
3. To use electrochemical techniques, based on ion transfer, to characterise the adsorption of SWCNTs at the liquid/liquid interface.
4. To prepare carbon nanotubes-conducting polymer nanocomposites *via* interfacial oxidation of the monomer in the presence of an adsorbed nanotube film.
5. To prepare MoS_2 dispersion, characterise it, and study its aggregation behaviour in the presence of an organic electrolyte.

1.7 Thesis Overview

The present thesis is divided into seven chapters. Chapter one provides an introduction to the relevant literature and theory pertaining to the work presented in this thesis. Chapter two presents the experimental details including materials, methods, equipment and some additional background to some techniques used in this work. Chapters three to six present the experimental work and discussion of results obtained. Each of these chapters begins with a brief introduction, which serves to augment the introduction presented in the current chapter, and conclusions.

Chapter three presents work on the effect of organic electrolyte on the kinetic stability of non-aqueous dispersions of single-wall carbon nanotubes (SWCNTs).

The SWCNTs dispersions were prepared in 1,2-dichloroethane (DCE) and characterised using UV-Vis absorption spectroscopy, atomic force microscopy (AFM) and Raman spectroscopy. Aggregation of the SWCNTs when electrolyte was introduced into the dispersion was studied using UV-Vis absorption spectroscopy.

Chapter four describes a study on the adsorption behaviour of SWCNTs at the non-polarised and polarised liquid/liquid interface. The effect of introducing electrolyte in either, or both, of the phases on the adsorption behaviour of the nanotubes was initially investigated. The assembled structures were characterised *in-situ* at the non-polarised and polarised liquid/liquid interface, and *ex-situ* after the nanotube layer had been transferred to a solid substrate. Electrochemical characterisation based on ion transfer across the liquid/liquid interface was used as a probe of the adsorption of SWCNTs at the interface. Simple ion transfer of tetramethylammonium (TMA^+), hexafluorophosphate (PF_6^-) and a facilitated transfer of potassium ion across the interface were studied in the absence and presence of adsorbed nanotubes in order to evaluate the electrical properties of the assembled SWCNTs. *Ex-situ* XPS measurement was used to determine the elemental composition of the interfacial SWCNTs after electrochemical measurement of ion transfer with a view to investigate adsorption of ionic species by the interfacial nanotubes from the surrounding solution.

Chapter five describes the elecropolymerisation of pyrrole at the interface between two immiscible electrolyte solutions, both in the absence and in the presence of interfacial SWCNTs leading to the formation of polypyrrole (PPy) and SWCNT/PPy composites at the interface. The morphologies of the prepared free-

standing films were characterised ex-situ after transfer to a solid substrate using atomic force microscopy, scanning electron microscopy and Raman spectroscopy.

Chapter six presents similar study to chapter three, but now involving electrostatic stabilisation of molybdenum disulphide dispersion in 1,2-dichlorobenzene (DCB). The dispersion was also characterised using UV-Vis absorption spectroscopy, AFM, zeta potential and Raman spectroscopy. The stability of the dispersion was also studied using UV-Vis absorption spectroscopy.

Finally, chapter seven gives the overall conclusions and recommendations for future work.

Chapter 2

Material and Methods

2.1 Materials

2.1.1 Chemicals

Molybdenum disulphide (MoS_2), 1,2-dichloroethane (DCE, ≥99.8%), 1,2-dichorobenzene (DCB, ≥99%), acetone (99%), ethanol (99.8%), lithium chloride (LiCl, ≥99%), tetramethyl ammonium chloride (TMACl, ≥99%), potassium tetrakis (4-chlorophenyl) borate (KTPBCl, 98%), Bis(triphenylphosphoranylidene) ammonium chloride (BTPPA, 97%), sodium hexafluorophosphate ($NaPF_6$, 99.99%), ammonium hexachloroiridate (III) ($(NH_4)_3IrCl_6$, 99.99%) and ammonium hexachloroiridate (IV) $(NH4)_2IrCl_6$, 99.99%) were purchased from Sigma Aldrich, UK and used as received. The pyrrole monomer (Py, 98%) was also obtained from Sigma Aldrich, UK, but was distilled before used. Sulfuric acid (H_2SO_4, >95%), potassium chloride (KCl, 99.8%), and hydrogen peroxide (H_2O_2, 6%) were obtained from Fisher scientific, UK. Dibenzo-18-crown-6 (DB18C6, 98+%) was a product of Lancaster Synthesis, UK. Potassium tetrakis(pentafluorophenyl)borate (KTPFB, 97%) was purchased from Alfa Aesar. Deionized water (18.2 MΩ cm resistivity) was obtained from a Milli-Q "Direct 8" purification system (Merck Millipore. USA). Bis(triphenylphosporanylidene) ammonium tetrakis(4-chlorophenyl) borate and Bis(triphenylphosporanylidene) ammonium tetrakis(pentafluorophenyl) borate were synthesized as outlined in section 2.2.2.

2.1.2 Single Wall Carbon Nanotubes

The SWCNTs used in this research work were produced by electric arc discharge (AD) and chemical vapour deposition (CVD) methods. The AD SWCNTs (purified via density gradient centrifugation, >95% carbon, <1% metal catalyst) were purchased from Sigma Aldrich and arrived in the form of small plain sheets. The diameter and length quoted by the manufacturer for this nanotube sample are 1.2–1.7 nm and 0.3–5 μm, respectively.[159] The supplied nanotubes were composed of 30% metallic and 70% semiconducting SWCNTs, based on the supplier information. The CVD SWCNTs (Elicarb TM, purity > 90%) were a gift from Thomas Swan & Co. Ltd (Consett) and were in powdered form. The average diameter of the CVD nanotubes, as published on the producer website, is 0.9–1.7 nm.[160] Both nanotubes samples were used as received.

2.1.3 Other materials

Silver wire (temper annealed, 0.37 mm diameter, 99.9%), platinum wire (temper hard, 0.5 mm diameter, 99.99%), and platinum woven mesh (0.1 mm diameter, 99.9%) were purchased from Advent Research Materials Ltd. Platinum disc electrode (2.07 mm diameter, CHI 102) was purchased from CH Instrument, Inc. Whatman cellulose filter papers (grade 42, 2.5 μm nominal retention rating) were a product of GE Health care, UK. Poly(vinylidene fluoride) membrane, PVDF (hydrophobic, 0.1 μm pore size, 13 mm diameter, 125 μm thickness) were obtained from Merck Millipore, UK. Silicon-silicon dioxide wafer (oxide thickness 290 nm) was used as a substrate for atomic force microscopy, Raman spectroscopy and Scanning electron microscopy studies.

2.1.4 Equipment

An Elmasonic P 70 H ultrasonic bath (Elma Schmidbauer, GmbH) was used for the preparation of SWCNT and MoS_2 dispersions and to induce nanotube adsorption at the liquid/liquid interface. The ultrasonic bath was connected to a recirculating cooling unit (F250, Julabo, GmbH) to maintain a low water bath temperature (< 30 °C) during sonication. UV-Vis absorption spectroscopy was performed on an Ocean Optics USB2000 spectrometer, equipped with DH-2000BAL UV-Vis-NIR light source, using either a 1 cm or 2 mm quartz cuvette. An Attention theta optical tensiometer (Biolin Scientific) was used for surface tension and contact angle measurements. A 1001 TPLT gastight syringe (Hamilton) was used to dispense sessile drops on solid substrates. Optical images of interfacial SWCNT layer/film were recorded with a Stereo Zoom microscope (SMZ168, Motic) connected to a digital live camera (GXCAM-9, GX Optical). An S230 SevenCompact™ (Mettler Toledo) conductivity meter was used to measure the conductivity of the organic electrolyte in DCB. A 2-16P centrifuge was used for the centrifugation of bulk MoS_2 and SWCNT dispersions, while a 1-14 microcentrifuge was used for centrifuging small volume samples. The two centrifuges were produced by Sigma Laborzentrifugen GmbH, Germany.

2.2 Methods

2.2.1 Preparation of SWCNT and MoS_2 Dispersions

SWCNT dispersions were prepared in both DCE and DCB, while exfoliation and dispersion of MoS_2 was carried out in DCB only. In the case of nanotubes, small amounts (between 0.6 to 2.2 mg) of the powdered material or sheets of SWCNT were placed in a 500 ml flat-bottom glass bottle and 100 mL of the organic solvent

was added. The mixture was then bath sonicated for 12 h at 37 kHz and 30% power setting. The as-prepared dispersion was further centrifuged at 15000 rpm for 1 h to remove any large aggregates and the supernatant was carefully collected. For MoS_2, 12 h bath sonication of a mixture of 1 g of MoS_2 powder and 100 mL organic solvent was employed. Large aggregates or unexfoliated materials were removed from the dispersion by centrifuging it twice, first at 6000 rpm and then at 12 000 rpm for 30 min each. The supernatant was carefully collected and stored.

2.2.2 Preparation of Organic Electrolytes

Bis(triphenylphosporanylidene) ammonium tetrakis(4-chlorophenyl) borate (BTPPATPBCl) and Bis(triphenylphosporanylidene) ammonium tetrakis(pentaflourophenyl) borate (Figure 2.1) electrolytes were prepared by metathesis of Bis(triphenylphosporanylidene) ammonium chloride (BTPPACl) and the salt of the corresponding anion (potassium tetrakis (4-chlorophenyl) borate, KTPBCl and potassium tetrakis(pentaflourophenyl) borate, KTFPB).[100, 161] Equimolar amounts of the BTPPATPBCl and KTPBCl (or KTFPB) were dissolved separately in a minimum amount of 2:1:1 acetone/ethanol/water mixture. The resulting solution of one of the salts was added to the other whilst stirring. This resulted in the formation of a white precipitate which was further stirred for a minute and then left standing for 20 min. The precipitate was filtered under vacuum through a Whatman filter paper and washed first with a mixture of acetone/ethanol/water, then with copious amounts of deionized water in order to get rid of the water soluble by-product, KCl. A boiling 1:1 mixture of acetone and ethanol was then added to the dry residue until it dissolved. The mixture was then left to recrystallize overnight. This resulted in the formation of white crystals of BTPPATPBCl or BTPPATFPB.

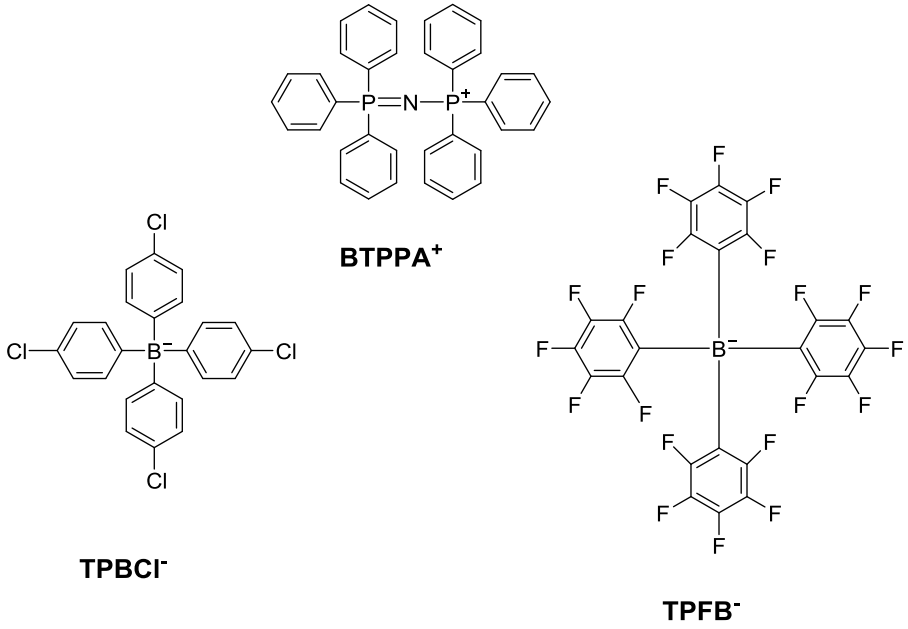

Figure 2. 1. Structures of the ions of the organic electrolytes, BTPPATPBCl and BTPPATPFB. The cation, $BTPPA^+$ is the same for both electrolytes.

2.2.3 Stability of SWCNT Dispersion in Electrolyte Solution

The stability of both the AD-SWCNT and CVD-SWCNT dispersions in the presence of BTPPATPBCl electrolyte was studied using UV-Vis absorption spectroscopy. The sedimentation method described by Giordani and co-workers[162] was adapted for this study. Single bulk dispersions of each SWCNT type was used to prepare all the samples for the dispersion stability experiment. The samples were prepared by adding 0.2 mL of appropriately diluted BTPPATPBCl solution to 1.8 mL of SWCNT dispersion (6 mg L^{-1}). The concentration of BTPPATPBCl in the dispersions ranged from 1 µM to 10 µM. The dispersions were mixed thoroughly by agitation and then allowed to stand for 48 h, after which they were centrifuged at 5000 g for 20 min in order to sediment any aggregated nanotubes. The supernatants were carefully collected and their absorption at 660 nm was recorded. The concentration of SWCNT that remained dispersed was calculated based on the extinction coefficient determined, as discussed in section 3.3.1. UV-Vis absorption

of all samples was collected using a 2 mm quartz cuvette. Pure DCE was used as the reference when measuring the absorbance of control samples, which were prepared and treated in a similar way as the other samples, but had pure DCE added to them instead of BTPPPATPBCl. For the rest of the samples (*i.e.* SWCNT dispersions containing different concentrations of the electrolyte), the appropriate BTPPATPBCl electrolyte concentration in DCE was used as reference.

2.2.4 Aggregation Kinetics of MoS_2

The aggregation behaviour of MoS_2 dispersion was similarly studied using UV-Vis absorption spectroscopy. As in the case of SWCNT stability studies, all aggregation samples were prepared from one bulk MoS_2 dispersion. The procedure used for the aggregation kinetics experiment was based on centrifuging the dispersions of MoS_2 at 8000 rpm for varying time periods (2 – 20 min) immediately after the addition of the BTPPATPBCl electrolyte solution. The samples were prepared by adding 0.2 mL of appropriately diluted BTPPATPBCl solution to 1.8 mL of a dispersion of MoS_2 (9.3 mg L^{-1}). The concentration of the BTPPATPBCl in the dispersions ranged from 2 μM to 1 mM. Control samples were prepared in the same way, except that pure DCB was added instead of BTPPATPBCl electrolyte solution. All samples, including controls, were shaken by hand before inserting them into a microcentrifuge. For each electrolyte concentration, a sample and a control were centrifuged together and absorption at 670 nm of the supernatants was recorded to determine the concentration of MoS_2 using the extinction coefficient calculated, as discussed in section 6.2.1.

2.2.5 Adsorption of SWCNT at Liquid/Liquid interface

The self-assembly of SWCNT at the liquid/liquid interface (water/DCE or water/DCB) was achieved using the following procedure. Firstly, an aliquot of the SWCNT dispersion in a given organic solvent was mixed with the organic electrolyte solution and added to a four-electrode electrochemical cell (see section 2.3 for description of a four-electrode cell). An approximately equal volume of aqueous electrolyte was then placed on top of the organic phase. The cell was bath sonicated (37 kHz and 40% power) for 10 - 15 min to induce nanotube adsorption at the interface. Before sonication, the open ends of the cell were properly sealed with Parafilm to prevent evaporation of the liquids. Because ultra-sonication leads to the formation of emulsions in both liquids, as well as at the interface, the cell was always left to stand for 12 h before any further work is carried out. This time period was sufficient for any unstable emulsions to coalesce. This procedure was also used in preliminary interfacial assembly studies of the SWCNTs. The only difference is that screw top glass vials were used, and the assembly was made with different combinations of electrolyte solutions (DCE/water, DCE/0.1 M LiCl (aq), 10 mM BTPPATPBCl (DCE)/water and 10 mM BTPPATPBCl (DCE)/0.1 M LiCl).

2.2.6 UV-Vis Absorption Spectroscopy

This was used for the qualitative characterisation of the SWCNT and MoS_2 dispersions, and for the determination of the concentration of the materials in a given dispersion. According to the Beer-Lambert law (Equation 2.1), the absorbance, *A* of the SWCNT/MoS_2 dispersion is related to its concentration, *C*, where *l* is the light path length and α is the extinction coefficient.

$$A = \alpha C l \tag{2.1}$$

In order to determine α, which will allow for the calculation of the dispersion concentration at any time, a calibration procedure was undertaken. Firstly, the absorbance of the as-prepared SWCNT or MoS_2 dispersion was obtained. Then, 15 to 30 mL of the dispersion was filtered through a 0.1 μm PDVF membrane that had been previously dried in an oven overnight at 70 $^{\circ}$C, cooled in the desiccator and weighed. After filtration, the membrane was again dried in an oven at the same conditions, cooled in the desiccator and weighed. The difference in the weight of the membrane before and after filtration gave the amount of the deposited material. The UV-Vis absorbance of the filtrates was also measured. For the SWCNTs, the absorption spectrum (Figure 2.2a) of the filtrate indicates that all the SWCNTs in the original dispersion had been removed by the membrane. Therefore, the amount of the SWCNTs in the dispersion was determined as the mass of the material deposited on the membrane. For the MoS_2 dispersion, however, it was found that about 10 – 14% mass of the material had passed through the membrane into the filtrate (Figure 2.2b). Therefore, the actual mass of the MoS_2 in the original dispersion was calculated by taking into account the loss of material. As the mass of both the SWCNT and the MoS_2 in the as-prepared dispersions are now known, the concentration of each material in the dispersion could be determined. The remaining portion of the original dispersion that had not been filtered was diluted to yield five portions of diluted dispersions of each material and their absorbance at 660 nm was recorded and a plot of absorbance versus concentration was obtained.

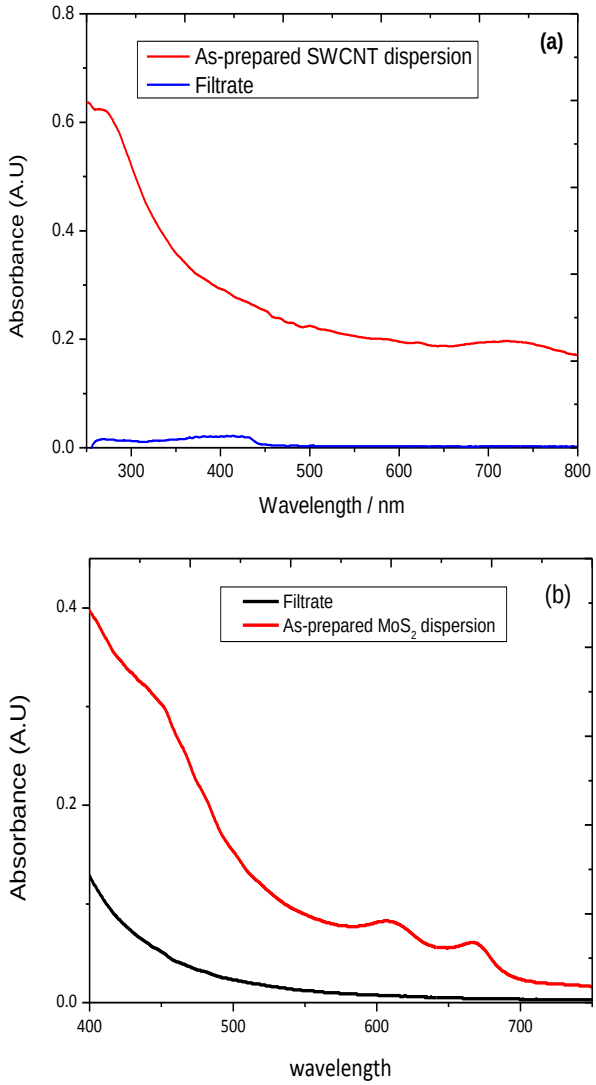

Figure 2. 2. UV-Vis absorption spectra of (a) SWCNT and (b) MoS_2 dispersions before and after filtration through a 0.1 µm PDVF membrane.

2.2.7 In-situ Optical Microscopy of Interfacial SWCNT layers

The structure of the interfacial SWCNT layers, formed between the bulk aqueous and organic phases, were visualized *in-situ* using a stereo zoom microscope with a working distance of 113 mm. To view this layer, the microscope was focused on the interface through the aqueous phase (top layer) as illustrated in Figure 2.3. Optical micrographs of the nanotube interfacial layer were captured with a digital live camera and processed using GXcapture software. Images were taken at least 12 h after sonication (*i.e.* when both aqueous and organic phases are clear of any

emulsions). Initial measurements were made with small glass vials (*ca.* 1.5 cm tall) to observe the morphology of the adsorbed nanotube layer without the influence of an applied potential. Then, with the SWCNTs assembled at water/DCE interface in a four electrode cell, videos clips of the interfacial layer was recorded as a function of the applied interfacial potential between the aqueous and organic phases.

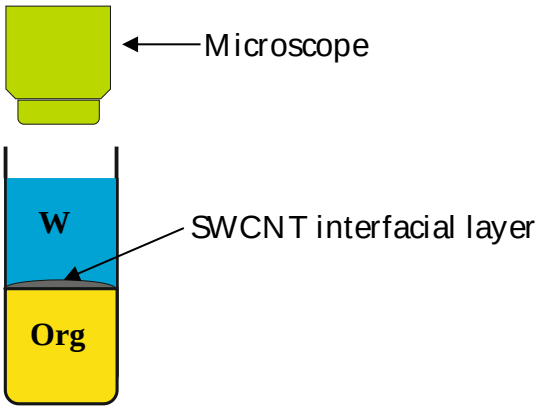

Figure 2. 3. Schematic illustration of the arrangement used for *in situ* optical microscopy of interfacial SWCNT layer.

The scale bars of the micrographs were determined by imaging a copper grid of known pore size each time a micrograph of the interfacial nanotube was taken. The TEM grid was placed on top of a water phase contained in a separate vial. The height of the water was adjusted to the level of the interfacial nanotube layer. By comparing the actual pore size of the copper grid with the measured one, the scale of the micrographs of the nanotube interfacial layers were estimated.

2.2.8 Contact Angle Measurement

The three-phase contact angle (θ) formed between the SWCNT, water and DCE was measured in order to evaluate the wettability of the nanotubes at the

water/DCE interface and the effect of introducing electrolyte in either or both of the phases. Measurements were carried out on SWCNT films prepared at the water/DCE interface by the adsorption procedure described in section 2.2.4 and deposited on the surface of clean Si/SiO_2 wafers. To transfer a film, the vial containing the biphasic system, with the SWCNT layer located at the interface, was tilted and the wafer was carefully inserted into the DCE phase below the interfacial film with the help of tweezers. The wafer was lifted gradually until the film rested on its surface. After deposition, the films were dried with N_2 and then left for 3 h in an oven heated at 70 °C to evaporate any residual solvent. The SWCNT film transfer protocol is illustrated in Figure 2.4. Fresh SWCNT film was used for each measurement and an average of three measurements were obtained for each liquid/liquid system.

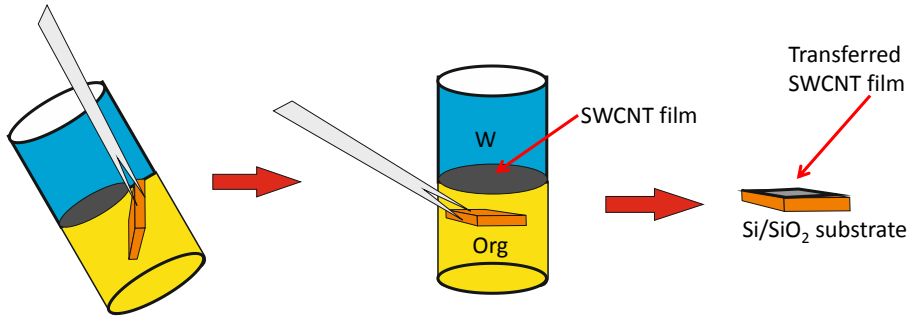

Figure 2. 4. Schematic illustration of SWCNT film transfer protocol from the water/DCE interface to a Si/SiO_2 substrate.

To take a measurement, the substrate was placed in a cubic quartz cuvette containing the less dense aqueous phase. A sessile drop of the heavier organic phase was then injected onto the surface (Figure 2.5). The droplet was allowed to stabilise (typically, less than 1 min) before images of the droplet were recorded. θ was determined by measuring the angle formed between the solid substrate and the droplet surface. This was achieved by using the OneAttension software provided

with the instrument to fit the Young-Laplace equation ($\Delta p = \gamma(\frac{1}{R_1} + \frac{1}{R_2})$, where Δp is the pressure difference across the curved liquid interface, γ is the surface tension, R_1 and R_2 are the radii of curvature) to the shape of the recorded drop.

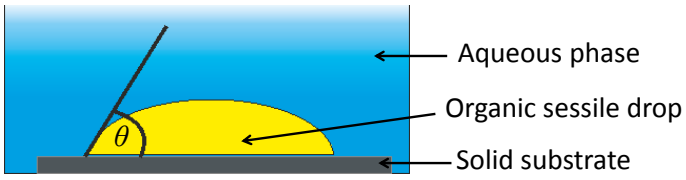

Figure 2. 5. Schematic representation of configuration used for the determination of three phase contact angle between a solid substrate (SWCNT) and two immiscible liquids.

2.2.9 Raman spectroscopy

Raman spectroscopy has been used extensively for the characterisation of a wide range of materials, including carbon nanostructures, transition metal dichalcogenides and their composites. It is based on inelastic scattering of electromagnetic radiation. In a typical Raman scattering experiment, a monochromatic laser beam (usually from a laser in the visible, near-infrared or near-ultraviolet region) is irradiated on a sample. The majority of the scattered light is of the same energy as the incident light and constitutes what is known as elastic or Rayleigh scattering. However, a tiny fraction (about 1 in 10 million) of the scattered photons is shifted in energy owing to its interaction with the vibrational energy levels of the molecules (or phonons for a solid) in a sample. This inelastically scattered light is termed Stokes or anti-Stokes Raman scattering, depending on whether energy is lost or gained by the photons. By detecting the shifted light (usually the Stokes lines because they are more intense), information about the molecular structure of the material can be obtained.[163]

In this study, Raman analysis was performed on a Renishaw inVia Raman microscope with 532 nm (2.33 eV) and 633 nm (1.96eV) laser excitations and at a power < 1 mW using 50× or 100× objective. This resulted in a theoretical laser spot size (calculated using Equation 2.2) of about 0.87 μm and 1.03 μm for the 532 nm and 633 nm laser, respectively.

$$d_s = \frac{1.22\lambda}{NA} \qquad 2.2$$

In the above Equation, d_s and *NA* represent laser spot size and numerical aperture of the objective used, respectively. The *NA* for both the 50× and 100× objectives employed in this work are the same and equals 0.75.

2.2.10 Scanning Electron Microscopy

Scanning electron microscopy (SEM) is an imaging technique that uses a focused beam of high energy electrons (typically, 1 to 30 kV)[164] to produce images of a solid sample. The electrons in the beam interact with the sample's atoms and generate various signals (*i.e.,* secondary electrons, backscattered electrons and characteristic X-rays) that can be processed to derive information regarding the sample's surface topography, crystallography and chemical composition.[165] In contrast to light microscopes, whose theoretical resolution limit is about 0.2 μm (due to the limit imposed by the wavelength of visible light, 400 – 700 nm), SEM can provide a much higher resolution (on the order of 1 – 5 nm),[165] since electrons have much smaller wavelength (40 pm – 1 nm, depending on the accelerating voltage)[164] compared to the visible light. In addition, the SEM has a larger depth of field, better surface sensitivity and longer working distance than the light microscopes. As a result, SEM has been widely used for characterisation of a wide variety of inorganic and organic materials on a micron to submicron scale.[165]

Figure 2.6 shows a simple schematic diagram of a typical SEM system. Electrons are produced and accelerated down the column by the electron gun (electron source and anode). The electrons are then finely focussed to the sample by the condenser (electromagnetic) lenses. Once the beam hits the sample various signals are produced, which can be detected by a selection of detectors. The signals of interest for imaging are the secondary (electrons emitted after absorption of primary electrons) and backscattered electrons. The electron column is usually held at high vacuum, generally between 10^{-5} – 10^{-7} torr[166] to avoid scattering of the electrons via interaction with air or any particulate matter before reaching the sample.

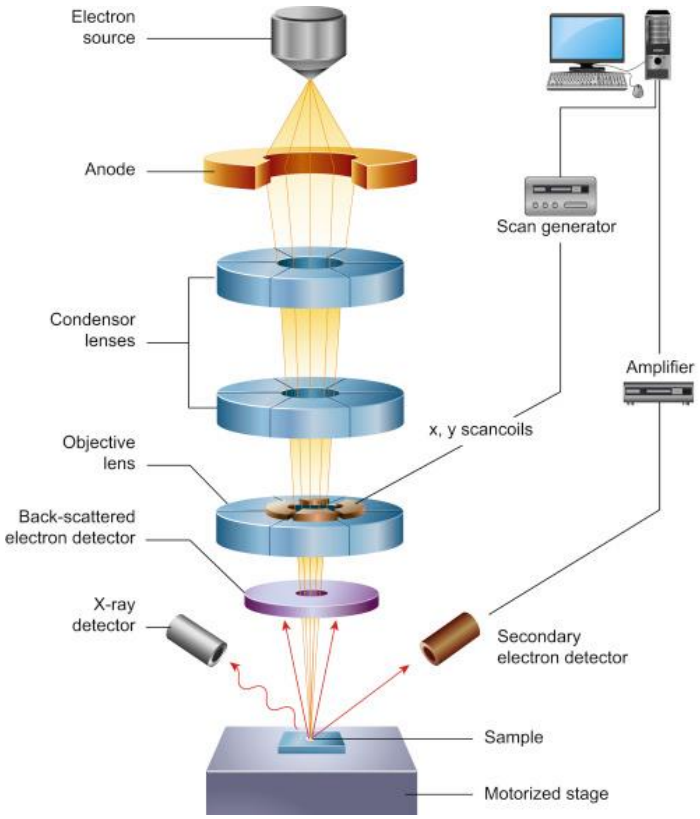

Figure 2. 6. Schematic representation of the main components of an SEM. Reproduced with permission from ref.[164] Copyright © 2016 Elsevier Ltd.

In this work, the SEM images were taken using an FEI XL30 Environmental SEM – Field Emission Gun, operated at 10 kV Emission. SEM images of SWCNT films prepared at the liquid/liquid interface were analysed using image J (version 1.48)[167] to determine the extent of surface coverage by the nanotubes.

2.2.11 Atomic Force Microscopy

Since its invention in 1986,[168] atomic force microscopy (AFM) has become a widely used surface characterisation tool. This is because the AFM is a very high-resolution measurement and imaging technique that is capable of generating surface topographic images of a material down to the atomic scale on the vertical axis and to a few nanometres on the horizontal axis. Thus, one of its main advantages over SEM

is its ability to produce a three-dimensional topography of a sample surface, which is beneficial for height analysis.[169]

The working principle of an atomic force microscope is schematically illustrated in Figure 2.7. A cantilever equipped with a sharp tip is used to scan over the surface of a sample. The cantilever, which is typically made from either silicon or silicon nitride, probes the sample surface by detecting the forces between the tip and the sample.[170] As the tip is brought near the sample, these forces cause a deflection of the cantilever which is monitored using a laser beam. By using a photodetector together with a feedback loop mechanism, a three-dimensional image of the sample surface can be generated.

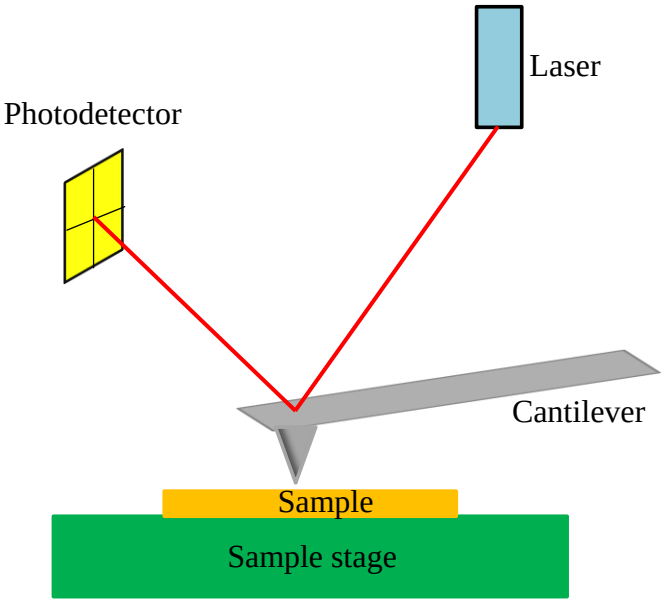

Figure 2. 7. Schematic illustrations of the working principle of an Atomic force microscope.

AFM imaging is typically performed in three basic modes – contact, non-contact and tapping modes – which are dependent on the way the tip interacts with

the sample surface. In the contact mode, the AFM tip is physically made to contact the sample during scanning. In this mode, the cantilever experiences repulsive forces, which cause the cantilever to deflect as it scans across the topographic features of the sample surface. This deflection is used as the input signal to a feedback loop which tries to maintain the cantilever at a specified deflection. The major disadvantage of this imaging mode is that either the sample or tip could be damaged during the scanning process.[169, 170]

In the non-contact mode, however, the cantilever tip does not touch the sample, but instead the cantilever is made to vibrate very close to the sample surface at a frequency near, or just above, its resonant frequency. The amplitude of this vibration is normally less than 10 nm. In this mode, the tip experiences van der Waals attractive forces, which act to decrease the resonant frequency of the cantilever.[169] Topographic images of the sample can be obtained by measuring the changes in the resonant frequency of the cantilever owing to the attractive interactions between the sample and the tip.[171] The main drawbacks of this imaging mode is that the presence of a contaminant fluid (typically, water) layer found on most surfaces under ambient conditions may lead to low-resolution images being obtained.[170, 171]

The tapping mode is the preferred AFM operation mode when imaging soft materials, films or particles that are loosely held on a surface.[169] In this mode, the cantilever is made to vibrate at or near its resonant frequency (50 – 500 kHz).[171] The amplitude of this vibration is typically in the range 20 nm to 100 nm. As the cantilever vibrates, the tip makes intermittent contact with the sample surface. The tip only slightly "taps" or touches the sample surface for a very short time period,

which means that the lateral forces exerted by the tip on the sample surface are dramatically reduced as compared to the contact mode.[169]

In this work, a Bruker Multimode 8-HR atomic force microscope operated in "PeakForce" tapping mode with a silicon tip on a silicon nitride cantilever was used to collect AFM images of all samples. The images were analysed using NanoScope Analysis software (version 1.40, Bruker instruments) and WSxM SPM software (4.0 Beta 8.1).

2.2.12 X-Ray Photoelectron Spectroscopy

X-ray photoelectron spectroscopy (XPS) is a powerful surface-sensitive spectroscopic technique that is popular for investigating the composition and electronic structure of solid surfaces. The technique is based on the principle of the photoelectric effect and utilizes monochromatic X-rays to excite the electronic states of atoms from the surface of a sample. The photoelectrons ejected from the sample atoms are filtered based on their kinetic energy by a hemispherical analyser. The intensity of the analysed photoelectrons as a function of their kinetic energy is measured by an electron detector. The kinetic energy of the photoelectrons (*KE*) is described by the following relation:[172]

$$BE = h\upsilon - KE - \phi \tag{2.3}$$

where $h\upsilon$ is the energy of the incident X-ray photons, *BE* is the binding energy of the photoelectrons and ϕ is the spectrometer work function. Because the binding energy of the electron is characteristic of the electronic structure of the element from which it was ejected, information about the sample surface composition as well as chemical environment of each element can be determined. Although X-rays can penetrate micrometres below the sample surface, ejected electrons from depths greater than 10

nm are usually not detected because they undergo energy loss events, and thus only contribute to the background noise.[172, 173]

The XPS measurements reported in this work were performed at the EPSRC NEXUS facility (Newcastle, UK) using a K-Alpha X-ray photoelectron spectrometer (Fisher scientific), which utilises a micro-focused monochromatic Al Kα source. The survey spectra were taken at 0.4 eV step size at three different locations on each sample.

2.2.13 Zeta Potential

Zeta potential (ζ), also referred to as the electrokinetic potential, is the electrostatic potential at the location of the shear or slipping plane of a colloidal particle moving under the influence of an electric field.[174] As shown in Figure 2.8, the shear/slipping plane is the boundary (actually, notional) within the diffuse part of the electrical double layer (EDL) which divides the moving particle and the dispersion medium around it. Although ζ is not the actual surface potential of the particles, it is often used to assess the surface charge on colloidal particles.[174, 175] It is also widely used as a key indicator of dispersion stability: colloidal particles with large negative or positive ζ are usually considered to be stable against aggregation due to electrostatic repulsion between the particles.[174-176] However, it is important to note that while ζ does provide indications of colloidal stability, the magnitude of the ζ alone does not guarantee stability since it does not provide any information regarding the van der Waals attractive forces.[174, 176]

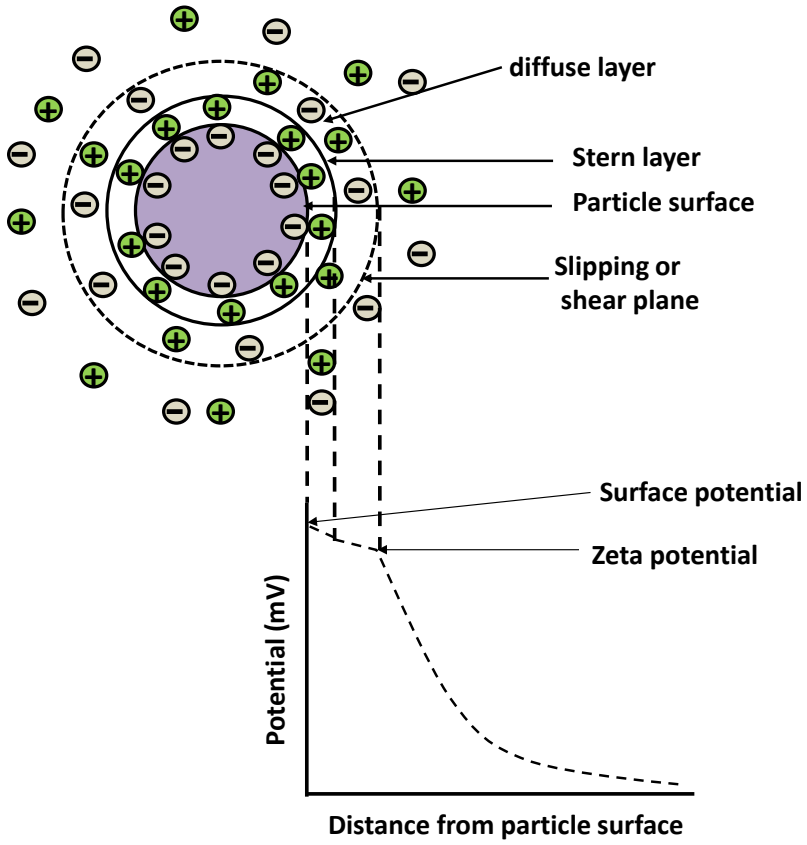

Figure 2. 8. Schematic illustration of the electrical double layer around a particle in a suspension and the location of the slipping plane, where zeta potential is measured.

Zeta potential is usually determined indirectly from the measurement of electrophoretic mobility (μ_e) of the colloidal particles. One method that is commonly used to measure μ_e is the electrophoretic light scattering, also known as laser Doppler electrophoresis. In this method, an electric field is applied, by means of two electrodes, across a dispersion contained in a sample holder. This causes the charged particles in the dispersion to migrate towards the oppositely charged electrode. The velocity (v, m s^{-1}) with which the particles move is related to μ_e by[174, 177]

$$\mu_e = \frac{v}{E} \qquad 2.4$$

where E is the electric field strength (V m^{-1}). v is measured by a light scattering technique known as laser Doppler velocimetry (LDV). The mobile particles under

the influence of the electric field scatter an incident light and the shift in frequency of the scattered light with respect to the incident light is proportional of the velocity of the moving particles. This allows the calculation of μ_e, and in turn, the ζ using Henry's Equation (2.5)[174, 177]

$$\mu_e = \frac{2\varepsilon_r \varepsilon_0 \zeta f(\kappa a)}{3\eta} \qquad 2.5$$

where ε_r and ε_0 (8.854×10^{-12} kg m V^{-2} s^{-2}) are the relative permittivity of the dispersant and permittivity of vacuum, respectively; η is the viscosity of the dispersant at the experimental temperature (kg m^{-1} s^{-1}) and $f(\kappa a)$ is the Henry's function. $f(\kappa a)$ is taken as either 1.5 (Smoluchowski approximation) or 1 (Hückel approximation) depending on the ratio of the particle size to the thickness of the EDL. When the thickness of the EDL is much smaller than the particle size (*i.e.,* due to particle size > 0.2 μm and moderate electrolyte concentration ca. 10^{-3} M), the Smoluchowski approximation applies, whereas for smaller particles in low dielectric media, the Hückel approximation is mostly used.[174, 175, 177]

In this work, ζ measurement was carried out using a Malvern Zetasizer Nano ZS (Malvern Instruments) with irradiation at 633 nm from a He-Ne laser. A Malvern universal Dip-cell, made with glass, was used to hold the MoS_2 – DCB dispersion. This cell is required when measuring ζ of particles dispersed in a non-aqueous (low dielectric constant) medium, because the two electrodes are positioned in close proximity, which allows for the generation of high field strengths at low applied voltages.[178] The Zetasizer Nano ZS uses M3-PALS (Mixed Measurement Mode – Phase Analysis Laser Scattering), which is a variant of LDV, for detection. Because PALS is extremely sensitive for detection of very small particle velocities, it is

currently considered the best technique for measurements of ζ in non-aqueous dispersions.[178] It measures changes in phase of the scattered light with respect to the incident light instead of the shift in frequency used by LDV. Typically, for non-aqueous dispersions, the default voltage (i.e., 40 V) is too high because of the close spacing of the electrodes in the sample cell. In order to find an optimum voltage for the ζ measurement, voltage "titration" was initially carried out. Several voltages (5, 10, 15 and 20 V) were applied and the data obtained was evaluated in terms of repeatability of the average ζ measured and phase plot symmetry. Examples of phase plots obtained with applied voltages of 10 V and 20 V are shown in Figure 2.9. The optimum voltage was found to be 10 V, as this gives a repeatable average ζ value and a symmetrical phase plot with low noise.

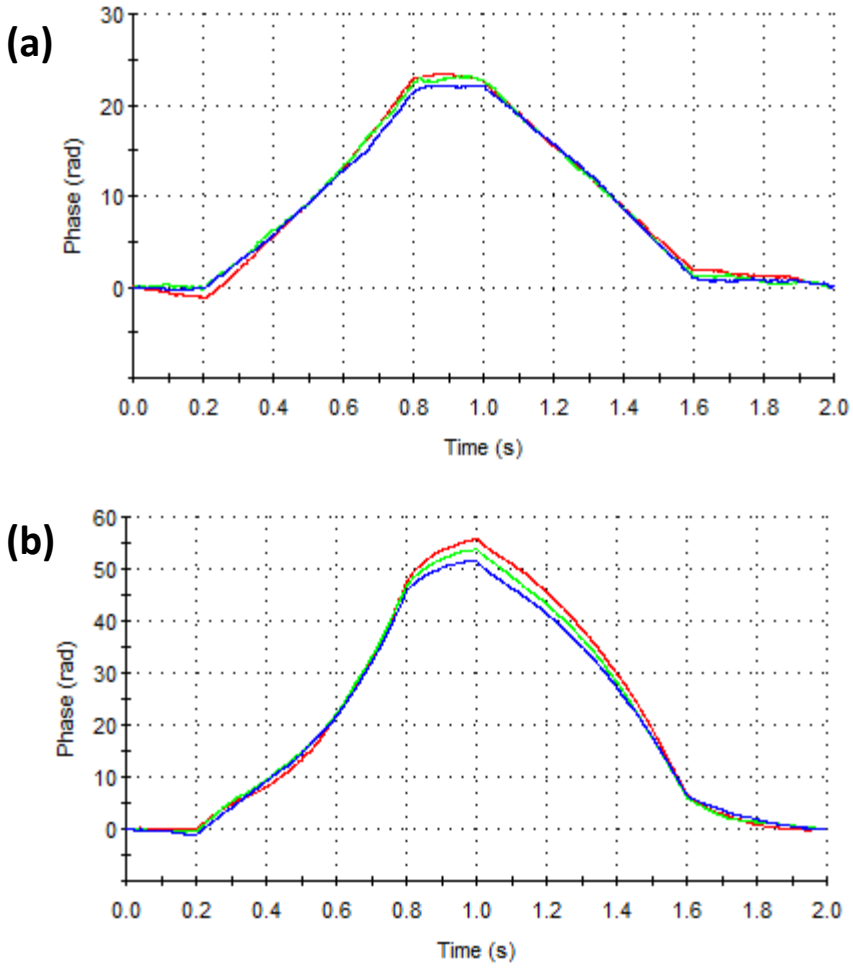

Figure 2. 9. Phase plots obtained with an applied voltage of (a) 10 V and, (b) 20 V for MoS_2 dispersion at a concentration of 9. 3 mg L^{-1}.

2.3 Electrochemical Experiments

2.3.1 Liquid/Liquid Electrochemistry

Liquid/liquid electrochemical measurements were carried out in home-made glass cells illustrated in Figure 2.10(a-b). The two immiscible liquids used to form the liquid/liquid interface, in the present work, were water and either DCE or DCB. These solvents were selected because of their common use in liquid/liquid

electrochemistry[127, 179] and as they have also been used previously in the preparation of CNTs dispersions.[41, 44] The solvents were added to the cells in such a way that the ITIES is positioned between the two Luggin capillaries. The cell was operated in four-electrode configuration (Figure 2.10c): two reference electrodes (RE_1 and RE_2) and two counter electrodes (CE_1 and CE_2), one pair for each phase. The CEs (platinum mesh), dipped into the bulk of each phase, were used to supply the electric current, whilst the REs (Ag|AgCl), positioned in the two side arms terminating with luggin capillaries near the ITIES, were used to control the potential difference between the two phases. Due to problems associated with reference electrodes dipped directly into the organic solvents,[127] the RE for the organic phase was placed in a second aqueous solution containing chloride ions and a common ion with the organic phase. This configuration resulted in the formation of a second interface, called the reference interface, in the RE_1 arm (Figure 2.10). Because the two phases are in contact and contain a common ion, which equilibrates between the phases, the potential across the interface can be considered to be constant. In the preliminary work, the two-arm cell shown in Figure 2.10a was used. In this cell design, the organic CE was inserted through the aqueous phase and across the interface into the organic solution (bottom phase). Therefore the electrode surface in contact with both the aqueous phase and interface was coated with glass to avoid any electrical contact. However, in this configuration, the CE distorts the structure of SWCNT adsorbed at the interface. To circumvent this problem, the three-arm cell shown in Figure 2.10b was used, where the CE was directly immersed into the organic phase through the provision of the additional side arm.

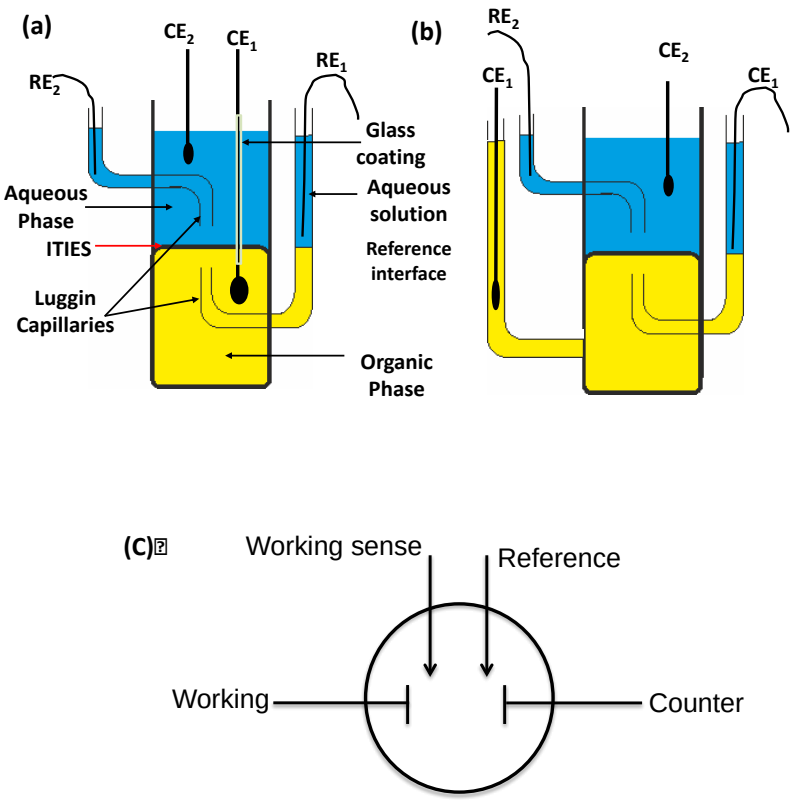

Figure 2. 10. Schematic of four-electrode cells used for ITIES investigations. (a) Two-arm cell, (b) Three-arm cell, and (c) Four-electrode configuration.

As the cells were constructed with glass, the interface between the two immiscible liquid phases was curved due to the preferential wetting of the hydrophilic glass surface by the aqueous phase. Thus, the geometric area (A) of the interface was found using Equation 2.6 for the three-arm cell and Equation 2.7 for the two arm cell.[180] Both Equations take into account the curved nature of the interfacial area.

$$A = \pi\left(h^2 + r_g^2\right) \qquad 2.6$$

$$A = \pi\left(h^2 + r_g^2\right) - \pi r_c^2 \qquad 2.7$$

where h is the height of the interface curvature, r_g is the internal radius of the glass cell and the term, πr_c^2 represent the area of the organic phase counter electrode with r_c representing its radius.

The electrochemical measurements were performed in a faraday cage, so as to shield the system from electrical noise. Cyclic voltammetry and potential step experiments were controlled with an Autolab potentiostat (PGSTAT100, Metrohm-Autolab). Positive feedback *iR* compensation was applied during all cyclic voltammetry measurements of ion transfer in order to eliminate the effect of ohmic drop within the cell. The measured potentials between the aqueous and organic phase were converted to Galvani potentials by using the standard ion transfer of TMA^+ ($\Delta_o^w\phi$) taken as +0.16 V for water/DCE[118] and +0.277 V for water/DCB[181] system.

2.3.2 Three-Electrode Configuration

The three-electrode configuration was used to study electropolymerisation of pyrrole at a metal electrode. A platinum (Pt) disc electrode, 2.07 mm diameter, was used as the working electrode. The Pt electrode was polished with Diamond suspension (Kemet International Ltd, UK) and rinsed several times with deionised water. Pt mesh and saturated calomel electrode (SCE) were used as the counter and reference electrodes, respectively. The electropolymerisation was conducted in DCB solution containing 0.1 M pyrrole monomer and 10 mM BTPPATPFB, as supporting electrolyte. Polypyrrole was deposited on the Pt electrode by cyclic voltammetry, using the Autolab potentiostat (PGSTAT100).

2.3.3 Supporting Electrolytes

The commonest choice of supporting electrolytes in liquid/liquid electrochemistry work are lithium chloride for aqueous phases and either BTPPATPBCl or BTPPATPFB for the organic phase. The reason for their popularity is that lithium chloride is highly hydrophilic, whilst BTPPATPBCl and BTPPATFPB are very hydrophobic and the combination of lithium chloride with one of the aforementioned organic electrolytes gives a large potential window for studying charge transfer reactions of interest. However, both BTPPATPBCl and BTPPATFPB organic electrolytes are not commercially available and are typically prepared by metathesis, as described previously in section 2.2.2.

2.3.4 Preparation of Silver/Silver Chloride Reference Electrodes

The silver/silver chloride (Ag/AgCl) reference electrodes were prepared by electroplating. The Ag wire was immersed in a 0.1 M solution of potassium chloride, and served as the anode. A platinum electrode, immersed in the same solution, was used as the cathode. Electrolysis was carried out at constant current of 5 mA for 600 s. This resulted in the formation of a thin film of AgCl on the Ag wire. The potential of the Ag/AgCl electrode, $E_{\mathrm{Ag/ACl}}$, is dependent on the activity (concentration) of the chloride ions in solution, as dictated by the Nernst equation;

$$\mathrm{AgCl_{(s)} + e^- \rightleftharpoons Ag_{(s)} + Cl^-_{(aq)}} \qquad 2.8$$

$$E_{\mathrm{Ag/ACl}} = E^{o}_{\mathrm{Ag/ACl}} - {}^{RT}/_{F} \ln a_{\mathrm{Cl^-}} \qquad 2.9$$

where, $E^{o}_{\mathrm{Ag/ACl}}$=+0.222 V at 25°C vs. SHE (standard hydrogen electrode), $a_{\mathrm{Cl^-}}$ represents the activity of the chloride ions in solution, R (8.314 J $\mathrm{K^{-1}mol^{-1}}$) and

F (96485 C mol^{-1}) are the molar gas constant and the faraday constant respectively. $E_{Ag/ACl}$ remains constant as long as the concentration of the chloride ions in the solution does not change.

Chapter Three

Electrostatic Stabilisation of Single Wall Carbon nanotubes Dispersed in DCE

3. Introduction

Since the discovery of CNTs, there have been numerous reports focusing on dispersion and stabilisation of nanotubes in liquid media. As previously discussed in section 1.3, because of their strong hydrophobicity, pristine SWCNTs can only be dispersed in non-aqueous solvents and require chemical or physical (*e.g.*, by adsorption of surfactant) functionalisation to disperse them in water. It is now well established that a number of common solvents such as CHP, NMP, DCE and DMF can be used to prepare stable dispersions of SWCNTs.[42-44, 53, 182-184] However, because of their size and rigidity, SWCNTs may not form a true solution.[35] As such, SWCNT dispersions can best be considered as lyophobic colloids.[185] This implies that the dispersions are thermodynamically unstable and will eventually form aggregates and coagulate out of the suspension.

Although extensive work addressing the kinetic stability of CNTs in aqueous media has been carried out,[185-187] only limited studies have investigated this behaviour in non-aqueous dispersions. In one of these studies,[188] the aggregation mechanism of pristine SWCNTs in NMP was investigated by molecular dynamics (MD) simulations. It was shown that a layer of structured NMP molecules is confined between pairs of nanotubes, which provides a steric barrier preventing the nanotubes from aggregation.[188] Similarly, Azar and Pourfath[189] also used the MD simulation approach to study the aggregation kinetics and stability mechanisms of pristine and functionalised (carboxylated or hydroxylated) carbon nanomaterials

(CNTs and graphene) in ten different solvents, including water, DMF, NMP, chloroform and DCB. They found that the functionalised carbon nanomaterials were more stable in the investigated solvents than their pristine counterpart and attributed the enhanced stability to the stronger confinement of the solvent molecules between the nanotubes or graphene sheets due to the presence of the functional groups, thus leading to higher solvent-induced repulsion.[189] While this organised solvent barrier is believed to contribute to the dispersion stability, it may not be the dominant mechanism responsible for SWCNTs dispersion stability in non-aqueous solvents, as demonstrated by recent electrolyte–induced aggregation studies by the Poler group.[190]

In a series of papers,[162, 190-192] the Poler group highlighted the contribution of the electrical double layer (EDL) repulsion, as described by the DLVO (Derjauin, Landau, Vewey and Overbeek) theory, to the stabilisation of pristine SWCNTs dispersions in non-aqueous solvents. The group investigated the dispersion stability and aggregation kinetics of SWCNTs in two different solvents, NMP and DMF, and their mixtures using three types of coagulants: simple inorganic salts, mononuclear and multinuclear metal coordination complexes. They found that the dispersion stability depended on the solvent properties, with NMP and mixtures of NMP/DMF showing greater stability over pure DMF.[190-192] Similarly, the chemical nature of the coagulant was also shown to influence the stability of the SWCNT dispersion: dispersion stability decreased in the order; simple inorganic ion > mononuclear complexes > dinuclear complexes > multinuclear complexes.[190] The difference between the inorganic and mononuclear complexes was attributed to the size of the solvated ion, as both coagulants were found to exhibit similar CCC α Z^{-2} dependence[190] predicted by the Debye-Hückel approximation for systems with low

zeta potentials.[193] However, the behaviour of the multinuclear complexes was reported to be different, as these coagulants did not obey the CCC α Z^{-2} or CCC α Z^{-6} scaling law.[190] It was suggested that the multinuclear complexes were in direct contact or even bonded to the SWCNTs.[190]

The origin of the surface charge on pristine SWCNTs that gave rise to EDL repulsion is, however, not clear. The Poler group[190] has remarked that the levels of oxygen functional groups on the surface of the nanotubes will contribute to the surface charging of the nanotube and consequently dispersion stability. Indeed, Rodgers et al.[194] found, through electrolyte-induced aggregation study of pristine graphene dispersions made from graphite of differing oxygen content, that the more oxidised graphite resulted in a more stable dispersion.[194] In this study, DCE was used to prepare the graphene dispersions and the coagulant was an organic electrolyte, bis(triphenylphosphoranylidene)ammonium tetrakis(4-chlorophenyl)borate (BTPPATPBCl).[194] It has also been suggested[195] that electron transfer occurs between the solvent and the SWCNTs, leading to the nanotubes to acquiring a charge. In some solvents, such as NMP and DMF, the suggested charge on the SWCNT is negative, while in others, such as 1, 2-dichlorobenzene and chloroform, the suggested charge is positive.[195]

The focus of the work presented in this chapter is to compare the stability of two types of pristine SWCNTs dispersed in DCE using BTPPATPBCl as the coagulant. Firstly, the nanotubes were characterised using several techniques to ascertain their quality, size and oxygen content. Then the stability of the nanotube was studied using UV-Vis absorption spectroscopy sedimentation procedure described previously in the literature.[185, 191]

3.1 SWCNT Dispersion in DCE

As the main focus of this work was to use electrochemistry to investigate the properties of SWCNTs adsorbed at the liquid/liquid interface, the choice of solvent for dispersing SWCNTs was limited to those solvents that can be used in ITIES studies – the solvent must be immiscible with water and able to dissolve electrolyte.[123, 137] DCE, being one of the commonest solvent employed in ITIES studies and having been used successfully to obtain stable CNTs dispersions,[40, 44-46, 196] was selected.

Two types of SWCNTs (produced by chemical vapour deposition, CVD, and arc discharge, AD, methods) were dispersed in DCE by sonication. The resulting suspension was centrifuged at 15000 rpm for 1 hour to remove large aggregates. The detail experimental procedure can be found in the experimental chapter (section 2.2.1). The resultant dispersion, in the case of AD-SWCNT, was observed to be stable for at least nineteen months without any significant aggregation – no macroscopic aggregates can be seen with the naked eye and the UV-Vis absorbance did not change significantly. The CVD SWCNT dispersion was only observed for a period of about two weeks, but was found to be very stable over this time period with no visible aggregates formation or change in intensity of UV-Vis absorption. Figure 3.1 shows the photographs of SWCNTs dispersions obtained immediately after sonication (Figure 3.1 A) and after centrifugation (Figure 3.1 B).

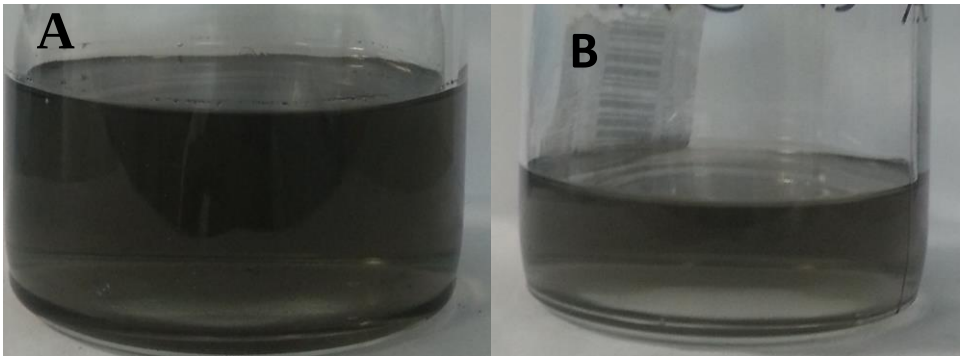

Figure 3. 1. SWCNT in DCE dispersion immediately after sonication (A) and after centrifugation (B).

3.2 Characterisation of SWCNT Dispersions

3.2.1 UV-Vis Absorbance and Extinction Coefficient Measurements

Optical absorption spectroscopy can be used to characterise the electronic properties of SWCNTs and to estimate the amount of suspended nanotubes in a given solvent. The absorption spectrum of a single species of SWCNT is characterised by a series of sharp features, which could be assigned to various inter-band transitions between the van Hove singularities (vHs) in the electronic density of states (see Figure 3.2) of the SWCNT.[197] As the energies of these transitions depend on the diameter and the chiral angle of the SWCNT, the relatively wide variations of nanotubes diameters and chiral angles, typically found in many nanotube samples, will significantly affect the resolution of these features, leading to broad and unresolved optical absorption peaks.[197, 198] Furthermore, the bundling state of most SWCNTs samples is also known to diminish the sharpness of the optical absorption signals.[199]

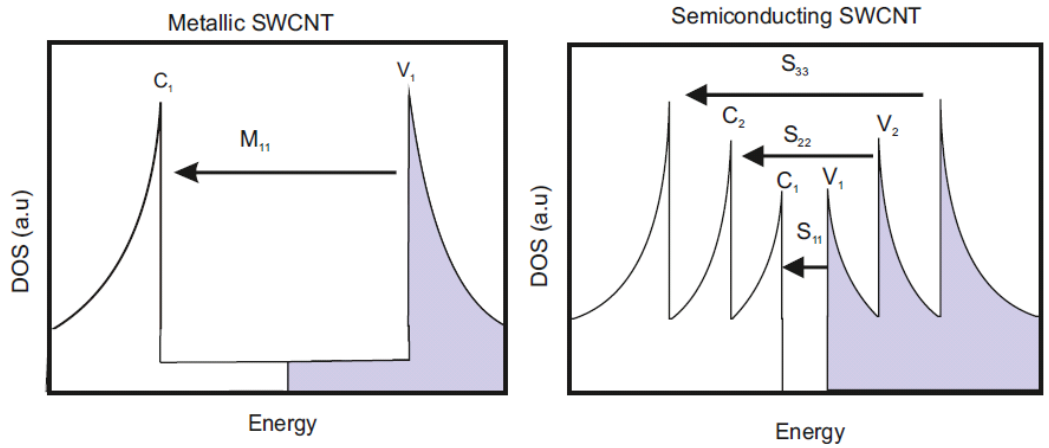

Figure 3. 2. Schematic of the electronic density of states (DOS) of metallic and semiconducting SWCNTs. The arrows show the various transitions between the van Hove singularities that are allowed.

In Figure 3.3, the UV-Vis absorption spectra of both the CVD and AD SWCNTs samples are shown. The spectrum of the CVD-SWCNTs shows less clear absorption features in the wavelength range 400 to 800 nm, which suggests that, the diameter and chiral angle distributions in this sample is very broad. This observation is in agreement with the report of Koh *et al,*[200] who observed a featureless absorption spectrum for SWCNTs prepared by CVD method. In contrast, the UV-Vis spectrum of the AD-SWCNTs exhibit characteristic peaks in the range 600–800 nm and 400– 600 nm that are assigned to the electronic transitions between the van Hove singularities for metallic M_{11} and semiconducting S_{33} nanotubes, respectively.[200, 201] The presence of these transitions suggests that the AD-SWCNTs have narrower tube dimeter and chiral angle distributions.[200] The low resolution of the peaks, however, indicates that individual tubes were not isolated; instead the nanotube dispersion contains mainly small nanotube bundles.[199] This is plausible considering that DCE is not the best solvent for solubilisation of SWCNTs.

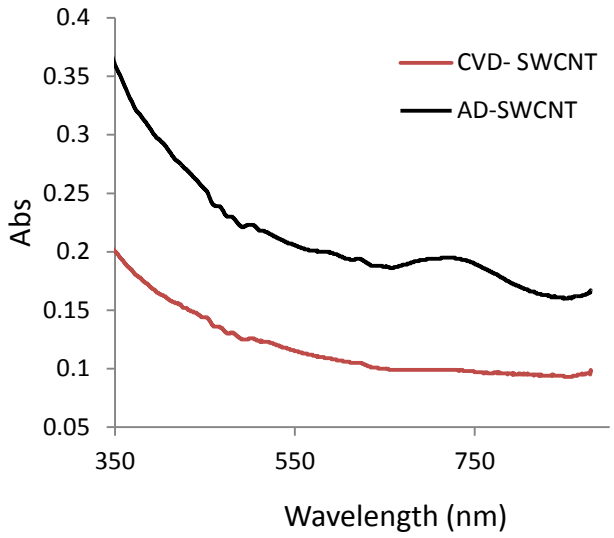

Figure 3. 3. UV-Vis absorption spectra of pristine CVD SWCNT (12 mg L^{-1}) and AD SWCNT (18 mg L^{-1}) dispersions.

As the two SWCNT samples showed different absorption features, attributed to differences in the types and distribution of nanotubes species, their extinction coefficient, α may also be different. As such, UV-Vis calibration was performed for each sample to determine α. The Beer-Lambert law ($A = \alpha C l$), states that the absorbance, *A* of a solution is directly proportional to its concentration, *C*. Therefore, by fixing the light path length, *l* and measuring the absorbance at a given wavelength for a range of concentrations, α can be determined. Figure 3.4 shows the plots of absorbance of the SWCNT dispersions at 688 nm as a function of nanotube concentration. In each case, the absorbance can be seen to increase linearly with concentration. By dividing the slope of each plot by the path length (2 mm), α was determined as 4.2×10^3 mg^{-1} mL m^{-1} and 3.9×10^3 mg^{-1} mL m^{-1} for CVD and AD SWCNTs, respectively. The similarities of the extinction coefficients may be due to the nearly identical diameters (*i.e.* 0.9 – 1.7 nm for CVD[160] and 1.2 – 1.7 nm for AD[159] SWCNTs) of the two types of SWCNTs. The slight differences can be

attributed to different levels of impurities (see AFM characterisation in section 3.3.2). Nevertheless, the calculated α values are comparable to $3.2 \times 10^3\ mg^{-1}\ mL\ m^{-1}$ obtained at 688 nm by Jeong *et al* for arc discharge SWCNTs dispersed in water,[8] but significantly different from that reported by Cheng *et al* ($1.7 \times 10^3\ mg^{-1}\ mL\ m^{-1}$ obtained at 660 nm) for HiPCO nanotubes dispersed in DCE.[40] It should be noted that the HiPCO SWCNTs exhibit smaller tubes diameters (typically, 0.8 to 1.2 nm)[202] as compared to CVD or AD SWCNTs. The smaller tube diameters are known to cause a shift in the inter-band electronic transitions of the SWCNTs to higher energies, with the M_{11} transitions, which occur in the 600 – 800 nm regions in the case of AD-SWCNT being shifted to between 400 – 650 nm wavelength regions.[201] Thus, the 688 nm wavelength used to evaluate α represents a different (S_{22}) electronic transition for the case of HiPCO SWCNTs[201] hence the large difference in α. Additionally, the purity levels and processing conditions may all contribute to the differences in the extinction coefficient.

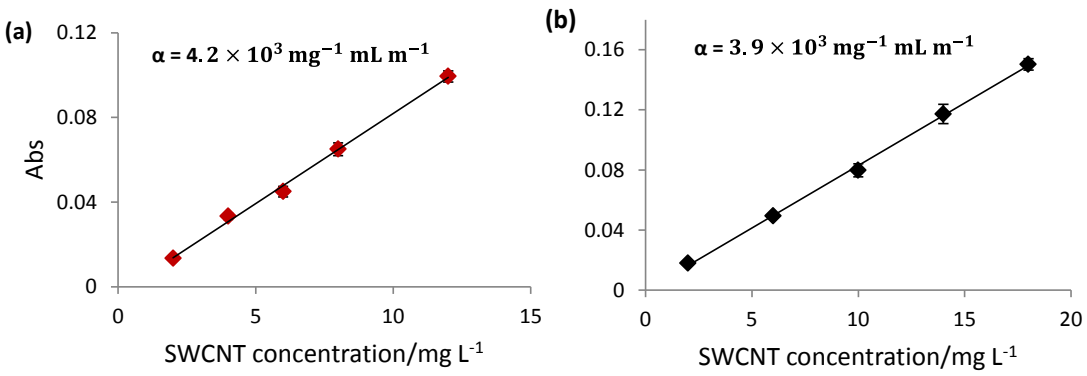

Figure 3. 4. Plots of absorbance (688 nm) vs concentration of CVD (a) and AD (b) SWCNT dispersions.

3.2.2 Atomic Force Microscopy of Dispersed SWCNTs

Atomic force microscopy (AFM) was used to evaluate the quality, length and diameter distributions of dispersed SWCNTs. Figure 3.5 shows representative AFM images for both CVD and AD SWCNTs. The AFM samples were prepared by drop casting one or two drops of dilute SWCNT dispersion (4 mg L^{-1} or 1 mg L^{-1}) on a clean Si/SiO_2 wafer. From these images, it can clearly be seen that both AD (Figure 3.5 a-d) and CVD (Figure 3.5 e-f) samples show the presence of a number of tubular structures and significant amount of impurities, in the form of white patches. The relative amount of these additional materials, which could be metal catalysts and other carbonaceous materials,[200, 203] is much higher in the CVD sample compared to AD SWCNT, suggesting that the AD SWCNT is cleaner than the CVD SWCNT. This finding is consistent with earlier reports, which have suggested that the AD route yields high purity nanomaterials.[200, 201]

Figure 3.6 shows the diameter and length distributions of the dispersed nanotubes, derived from the AFM images. The diameters were estimated from the topographic heights of the tubular structures. As can be seen from the histograms, the two types of SWCNTs show different diameter distributions and bundling state. For the case of AD SWCNT (Figure 3.6a), the histogram exhibits a diameter distribution of about 1–21 nm, with an average bundle diameter of ~6 nm, suggesting that the AD SWCNT dispersion is dominated by bundles of a few nanotubes. In contrast, the CVD SWCNTs (Figure 3.6c) show relatively narrower bundle diameter distribution, with the majority of the tubes dispersed as aggregates exhibiting a bundle diameter of ~11 nm, which is slightly higher than the mean bundle diameter of the AD SWCNT.

As with the diameters of the different nanotubes samples, the length distributions produced for each sample is also different. As shown in Figure 3.6b, the

average length of the AD SWCNT bundles is 0.7 μm. The length distribution ranged from 0.2 μm to 1.7 μm. Compared to AD SWCNTs, the length distribution of CVD nanotubes is again narrower (0.05 μm to 1.05 μ nm) and exhibit a much shorter mean length (0.255 μm). As the manufacture's quoted length distribution in the case of AD SWCNT (data not provided for the CVD sample), ranged from 0.3 μm to 5 μm, the AFM data indicated that the processed SWCNTs have shorter lengths and narrower distribution, consistent with SWCNTs dispersions prepared by sonication.[200, 204]

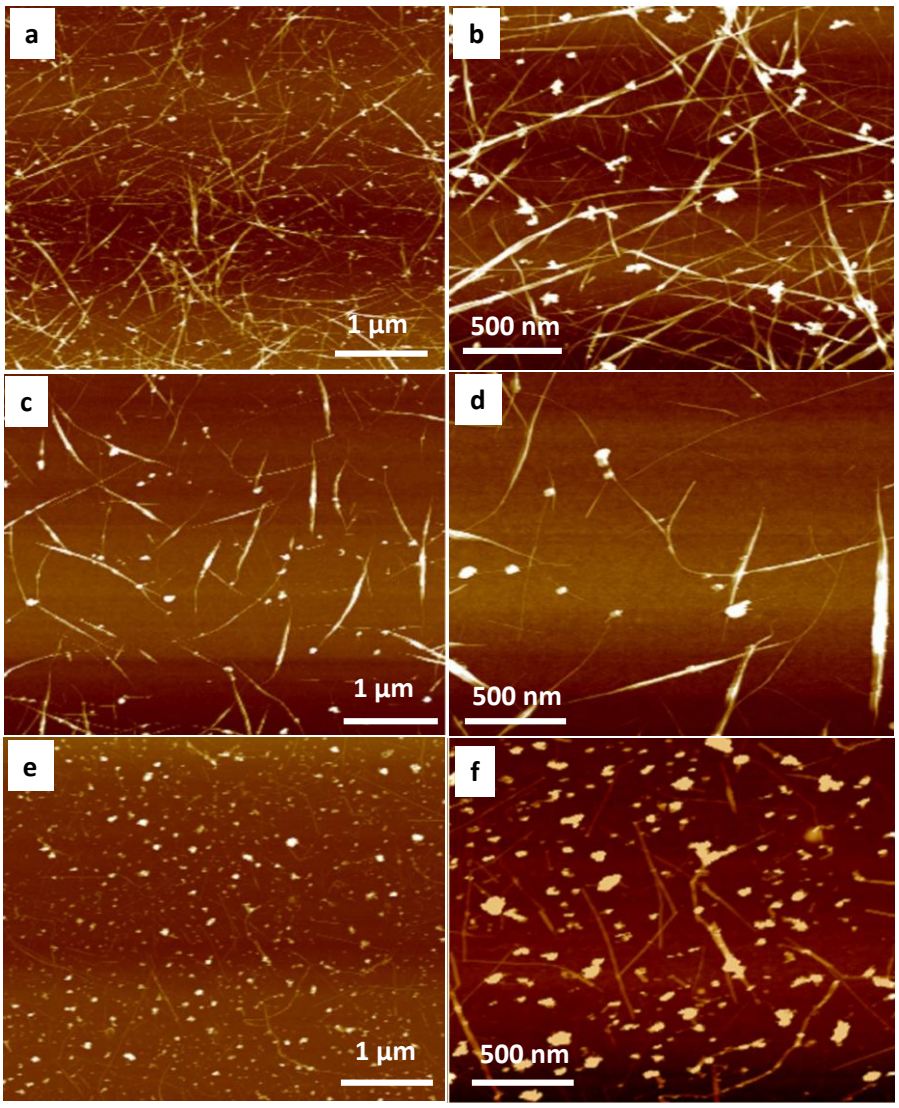

Figure 3. 5. Representative AFM images of AD (a-d) and CVD (e-f) SWCNT in DCE dispersions.

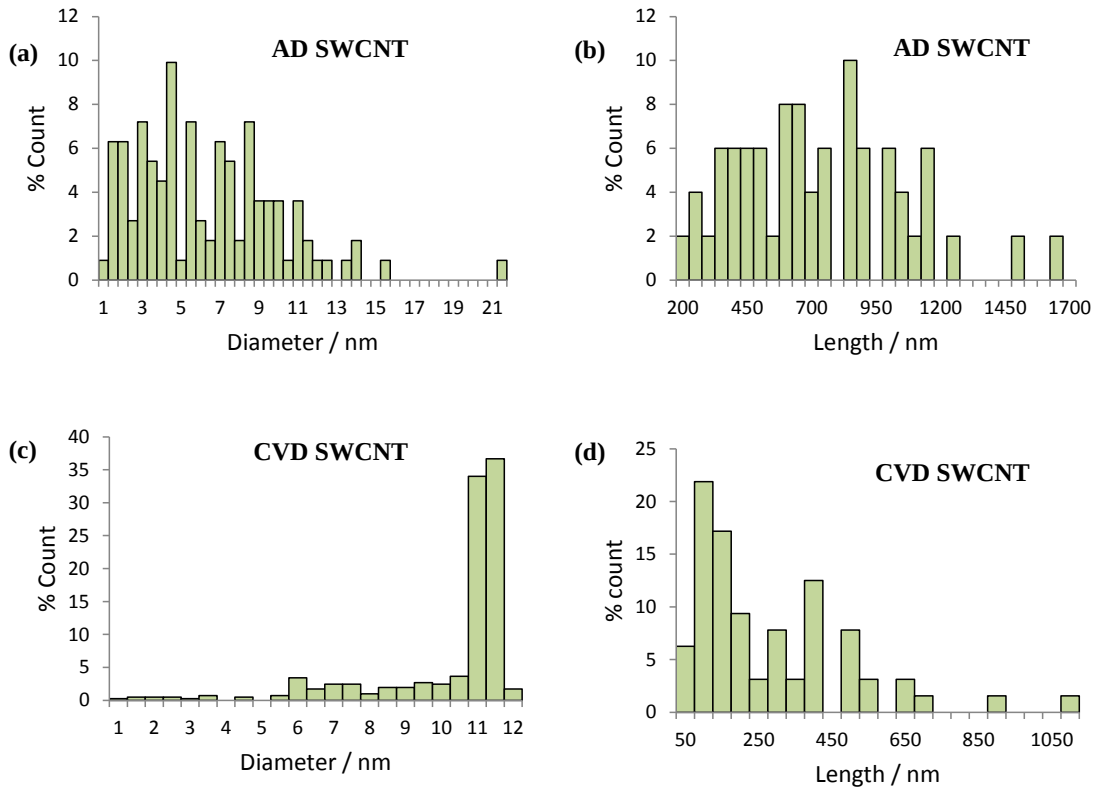

Figure 3. 6. AFM derived diameter and length distributions for AD (a-b) and CVD (c-d) SWCNT in DCE dispersions.

3.2.3 Raman Spectroscopy

Raman spectroscopy has been widely used to gain information about the structure and properties of SWCNTs.[17, 205-207] The spectra can be collected on either isolated or bundled nanotubes.[206] The characteristic features of major importance in the SWCNT Raman spectra include the radial breathing mode (RBM), the tangential mode (G-band), the D-band (disorder-induced band) and the G'-band. The RBM modes, located in the lower wavenumber region (about 120–350 cm^{-1}), are produced by the collective atomic vibration of all the carbon atoms in the radial direction. The position of the RBMs, ω_{RBM} is directly related to the tube diameter, (d_t) of the SWCNTs, as expressed by Equation 3.1[17]

$$\omega_{RBM} = A/d_t + B \tag{3.1}$$

where *A* and *B* can be taken as 217 cm^{-1} and 15 cm^{-1}, respectively.[208] The *B* parameter is included to account for the interactions between the individual nanotubes in a bundle.[205]

The G-band is a feature that is observed for all graphitic materials and is associated with the stretching of the C–C bond.[209] However, unlike the graphite or graphene, which exhibit only one single peak at about 1582 cm^{-1}, the G-band in SWCNTs is split into multiple peaks due to curvature effects.[17, 209] The two most intense peaks, G^+ (appearing around 1590 cm^{-1}) and G^- (appearing around 1560 cm^{-1}) that arise due to symmetry breaking when the graphene sheet is rolled to make a nanotube, are the dominant features commonly observed in the G-band area.[205] The lineshape of the G^- peak is dependent on the electronic properties of the nanotubes: metallic SWCNTs exhibit a Breit–Wigner–Fano (BWF) lineshape, while semiconducting SWCNTs have a Lorentzian lineshape.[205] The position of the G-band can be employed to investigate charge transfer from dopants additional to the nanotubes.[17, 208] The disorder or D band, appearing around 1350 cm^{-1} is usually associated with a decrease in symmetry of the SWCNTs due to functionalisation or presence of structural disorder.[198] The ratio of the intensity of D to G peaks (I_D/I_G) is commonly employed as measure of defect density or extent of subsequent functionalisation.[198]

The Raman spectra of the AD and CVD SWCNTs were obtained using two laser excitation wavelengths, 633 nm (1.96 eV) and 532 nm (2.33 eV). Figure 3.7 shows representative Raman spectra obtained at 633 nm for each SWCNT type. The spectra display the nanotubes' characteristic peaks, such as the G-band, the RBMs and D-band. In order to gain more information about each type of SWCNT, the three regions were further analysed, as discussed below.

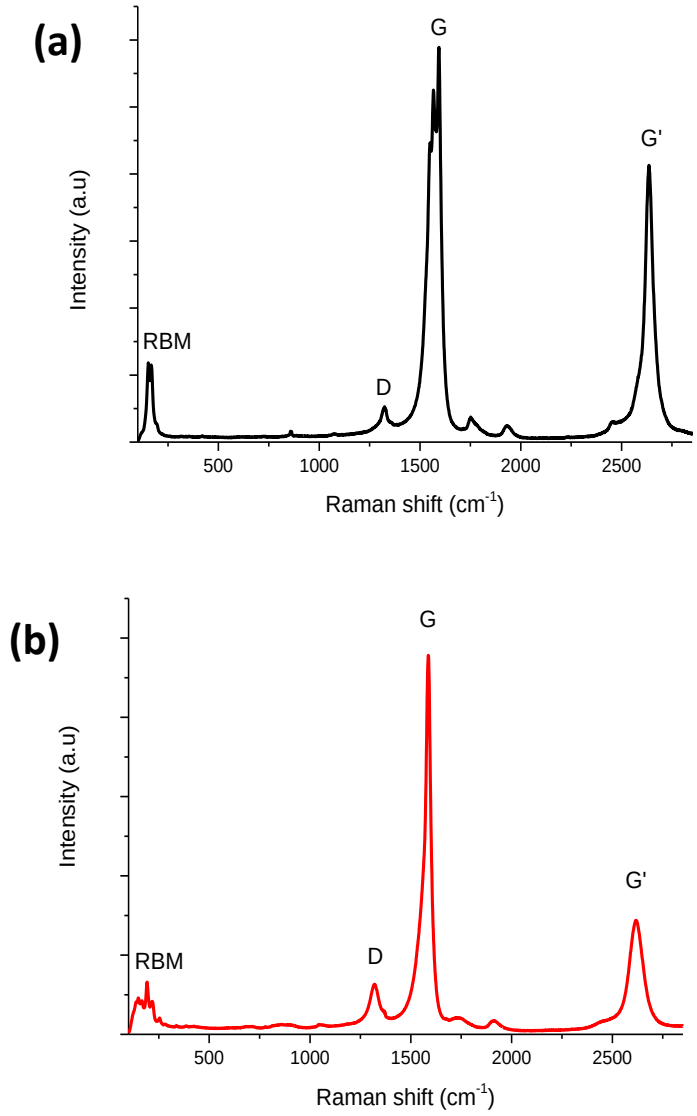

Figure 3. 7. Raman spectra of AD (a) and CVD SWCNTs (b) obtained using a 633 nm excitation wavelength (1.96 eV).

The RBM Region

In Figure 3.8 the spectra of the RBM region recorded at the two laser excitation wavelengths (633 nm and 532 nm) are shown. The spectra of the AD SWCNT (Figure 3.8a-b) show two dominant peaks at the 633 nm, and a single peak at 532 nm excitation wavelengths. The wavenumber of each peak and the corresponding tube diameter, calculated using Equation 3.1, are given in Table 3.1. For the case of CVD SWCNT (Figure 3.8c-d), the number of peaks observed at each

excitation wavelength is higher: with the 633 nm laser wavelength, seven prominent peaks were observed, whilst with the 532 nm laser wavelength, four peaks were found. The wavenumber of each peak and the corresponding peak diameter, calculated using Equation 3.1, are given in Table 3.2. Although for full characterisation of the nanotubes diameter distribution, several excitation wavelengths must be used, nonetheless, the distributions derived from the two laser wavelengths indicate that the CVD SWCNT is composed of many different types of SWCNTs that are in resonance at the 633 nm and 532 nm excitation wavelengths compared to the AD SWCNT, thus, corroborating the result obtained from the UV-Vis absorption spectroscopy. On the other hand, the Raman results may seem to contradict the AFM data discussed in section 3.2.2, however, it is important to note that the two techniques gives different information. The AFM gives information on the dispersion state of the SWCNTs (*i.e.*, whether the dispersion contains individual nanotubes or bundles, and the diameter of the isolated or bundled nanotubes) but cannot provide information regarding the diameters of individual tubes present in a bundle, while the Raman spectroscopy, through analysis of the RBM region can provide information (including diameter distribution) on the different types of nanotubes contained in a given bundle provided the tubes are in resonance with the excitation wavelength. In the present study, individual nanotubes were not isolated as evident from the AFM data (see section 3.2.2); instead the SWCNTs were dispersed as aggregates of small bundles. Therefore, the diameter distributions given by the AFM data represent the bundled diameter of the aggregates and not the actual diameters of the individual tubes making up the aggregates. On the contrary, the diameters calculated from the Raman spectra were the actual diameters of the individual nanotubes contained in the dispersed aggregates.

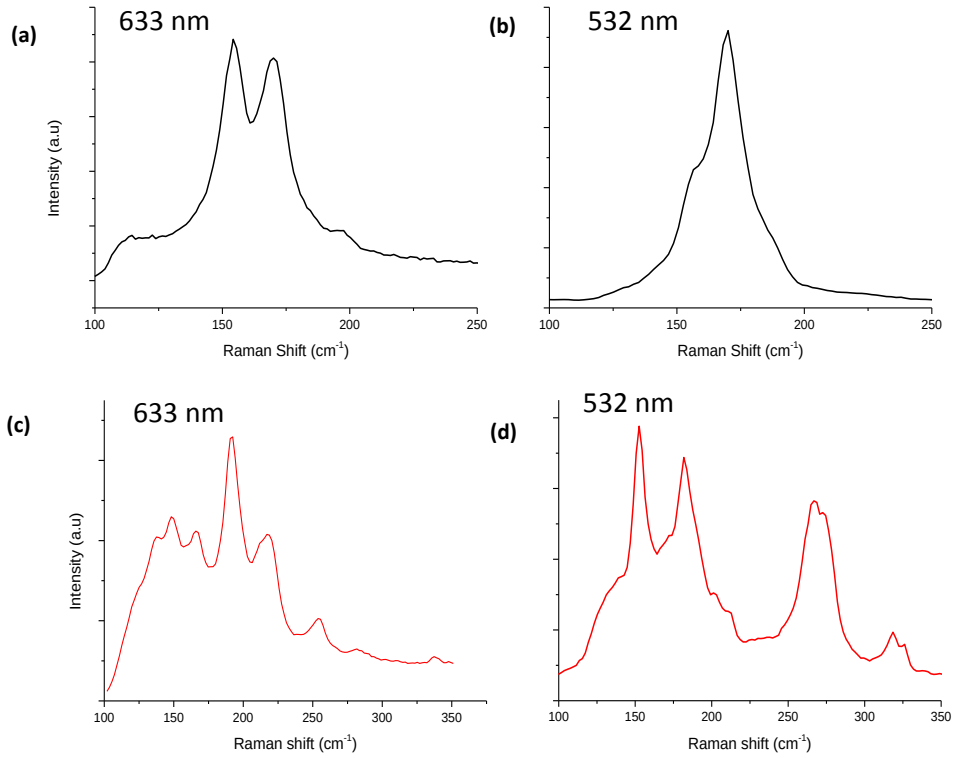

Figure 3. 8. RBM spectra of AD (a-b) and CVD SWCNTs (c-d) excited at 633 nm (1.9 eV) and 532 nm (2.33 eV).

Table 3. 1 Diameter distribution calculated from the ω_{RBM} of AD SWCNT

Laser excitation wavelength (nm)	ω_{RBM} (cm^{-1})	SWCNT diameter (nm)
633	154	1.56
	170.1	1.4
532	170.1	1.4

Table 3. 2 Diameter distribution calculated from the ω_{RBM} of CVD SWCNT

Laser excitation wavelength (nm)	ω_{RBM} (cm^{-1})	SWCNT diameter (nm)
633	148.2	1.63
	166	1.44
	190.6	1.24
	217	1.07
	255.6	0.90
	281.76	0.81
	337	0.67
532	152.6	1.58
	181.8	1.30
	266.8	0.86
	318.5	0.71

The Raman scattering in SWCNTs is typically a resonant process, in that only those tubes with the electronic transitions between the vHs that matches the excitation energy of the laser can produce a strong peak in the spectrum.[210] Therefore, it is a common practice to use the Kataura plot,[207] which correlates the allowed vHs transitions with the nanotube diameter, and the RBM frequencies to retrieve the SWCNTs' semiconducting or metallic character.[198] According to the Kataura plot (Figure 3.9), both the AD and the CVD SWCNTs contain a mixture of metallic and semiconducting SWCNTs, based on their diameters derived from the RBM. In the Kataura plot (Figure 3.9), the RBM derived diameters (table 3.1) for the AD SWCNTs are shown by the two black vertical lines, while the range of nanotube diameters for the CVD SWCNTs are indicated by the two orange lines.

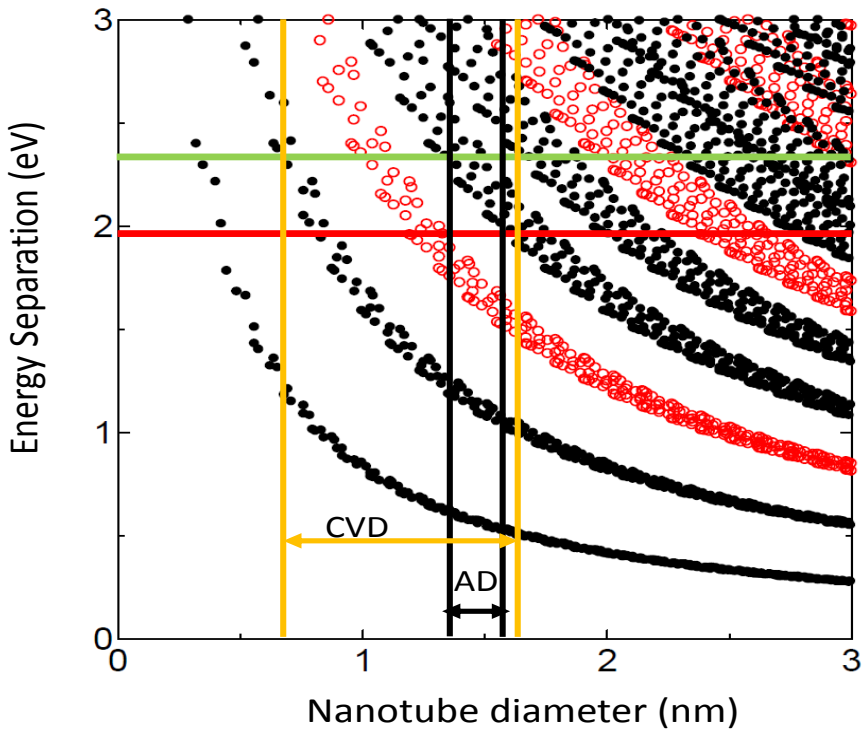

Figure 3. 9. Kataura plot showing the excitation energies of the two lasers (red and green horizontal lines) and the measured diameter range (orange vertical lines for CVD SWCNTs and black vertical lines for AD SWCNTs). The black circles represent families of semiconducting SWCNT while the red circles represent the metallic nanotubes. Adapted from ref [211].

G and D Bands

The Raman spectra of the G-band region for the two types of SWCNTs are compared in Figure 3.10. The spectra for the CVD nanotubes at the 532 nm and 633 nm laser excitation wavelength revealed the presence of a G^+ feature at 1590 cm^{-1} and a G^- feature around 1560 cm^{-1}, both of which appear to show the dominance of semiconducting SWCNTs based on their line shapes as well as the intensity ratio, I_{G+}/I_{G-}.[212] The G^- peak is diameter dependent and its wavenumber increases with increase in tube diameter, while the G^+ peak is independent of the nanotube diameter.[205] Therefore, the splitting between the G^+ and G^- depends on the diameter of tube; for large tubes, the splitting is expected to be very small.[205] This suggests

that the tubes dominating the observed response in the G-band region of the Raman spectrum of CVD nanotubes are large; hence, the closeness of the G^+ and G^- peaks.

Similarly, the G-band spectra of the AD SWCNTs also show peaks between 1540 cm^{-1} and 1591 cm^{-1}, but in this case, the features are different for the different excitation wavelengths. At 633 nm, the G^+ peak occurs as a sharp feature, which is expected regardless of whether the tube is metallic or semiconducting (both types of nanotubes exhibit a G^+ feature with a Lorentzian line shape).[17] But the appearance of the G^- peak (1540 cm^{-1}) as a broad feature is indicative of the presence of metallic tubes.[205] Furthermore, the appearance of some additional peaks in the G-band region is indicative of the presence of some semiconducting nanotubes also in resonance at the 633 nm excitation wavelength.[201, 207] The occurrence of both nanotube types is also consistent with the observation of both semiconducting and metallic tubes in the RBM area of the Raman spectrum at the 633 nm excitation wavelength. With the 532 nm, both the G^+ and G^- peaks occur as sharp features, suggesting that the tubes in resonance at the 532 nm are predominantly semiconducting.

The ratio of the intensity of the D to G band (I_D/I_G) has been used previously to monitor sonication induced damage to SWCNTs.[40] For both nanotube types, the I_D/I_G ratio was found to be low (0.13 and 0.12, respectively for CVD and AD nanotubes), indicating that no significant damage has occurred to the nanotubes.[213]

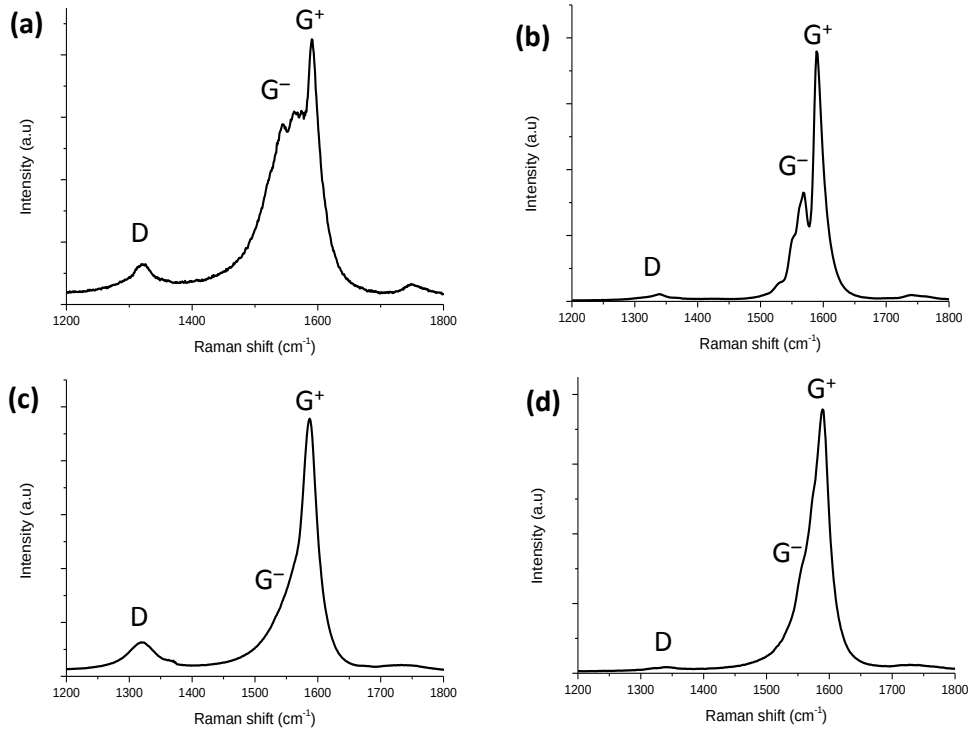

Figure 3. 10. **G and D band spectra of AD (a-b) and CVD SWCNTs (c-d) excited at 633 nm (1.9 eV) and 532 nm (2.33 eV). Spectra (a-c) were taken from nanotubes dispersed in DCE, while (b-d) were taken from as received nanotubes samples.**

3.2.4 X-ray Photoelectron Spectroscopy (XPS)

XPS was used to determine the elemental composition of the SWCNT samples. Figure 3.11 shows the XPS survey spectra of the AD and CVD SWCNTs. The only elements detected in each sample, were C (1s) and O (1s). The percentage atomic concentration of each element is shown in the inset tables of Figure 3.10. From these data, it can be seen that the surface oxygen impurity content in the CVD SWCNT is slightly lower than that of the AD SWCNT. The higher surface oxygen content of the AD sample might be expected to give the SWCNTs relatively greater surface charge, which in turn can impact on dispersion stability.[187]

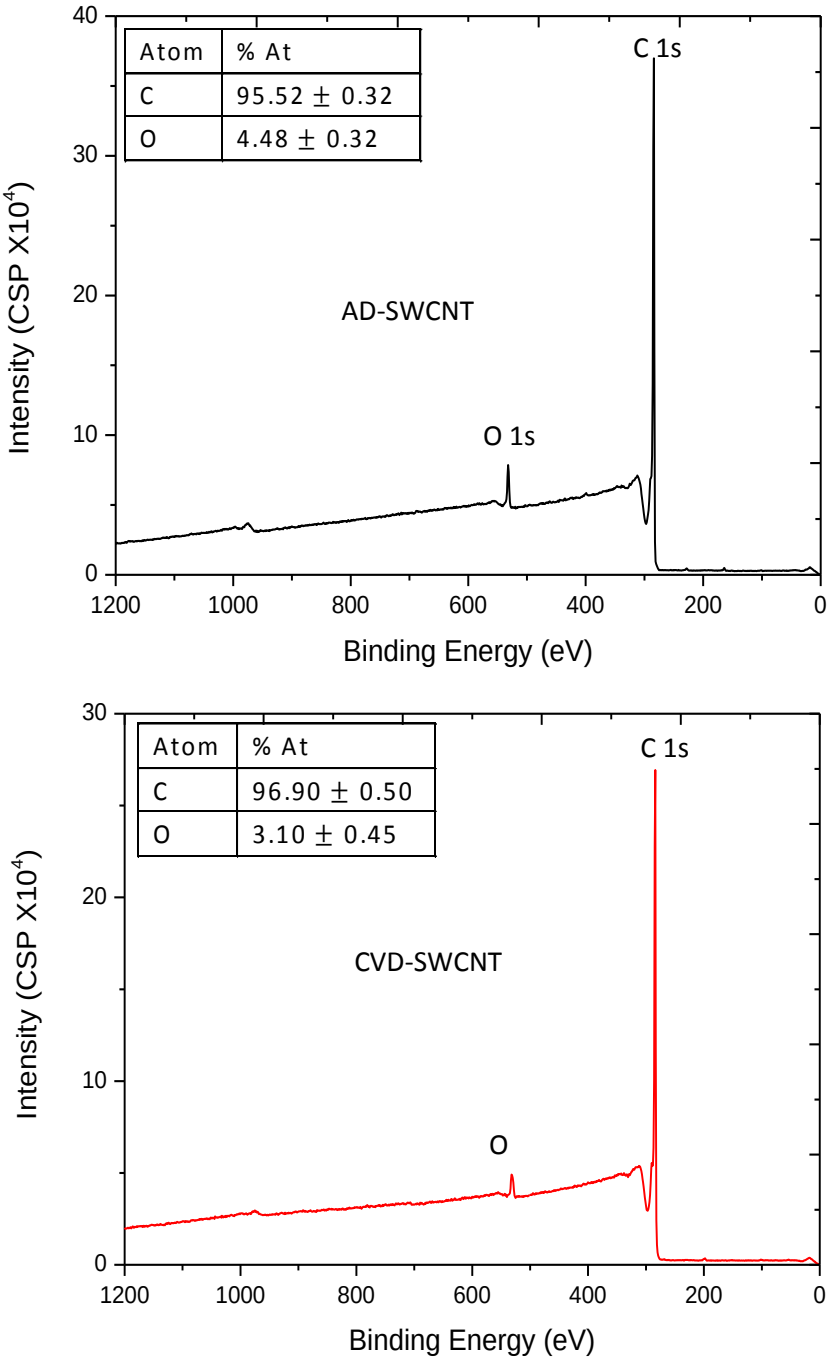

Figure 3. 11. XPS survey spectra of AD and CVD SWCNTs.

3.3 SWCNT Dispersion Stability

The stability of both CVD and AD SWCNT in DCE dispersions was investigated using the organic electrolyte, Bis(triphenylphosporanylidene) ammonium tetrakis(4-chlorophenyl) borate (BTPPATPBCl), as the coagulant. This electrolyte was selected because of its relevance to the work described in chapter four and, in general, to the

study of electrochemistry at the liquid/liquid interfaces. The electrolyte is also known to dissociate almost completely in DCE at the concentration range used in this study.[194] Figure 3.12 shows the effect (qualitatively) of adding different amounts of the organic electrolyte to a stable dispersion of CVD SWCNT dispersion (6 mg L^{-1}). The experimental result shown in Figure 3.12 was obtained 48 h after the addition of the BTPPATPBCl electrolyte solution into the stable dispersions. The electrolyte concentration ranged from 0 to 10 μM. The amount of aggregates produced can be seen to increase with increasing electrolyte concentration. When higher electrolyte concentrations (1 μM and 10 μM) were employed, the SWCNTs aggregated almost instantaneously.

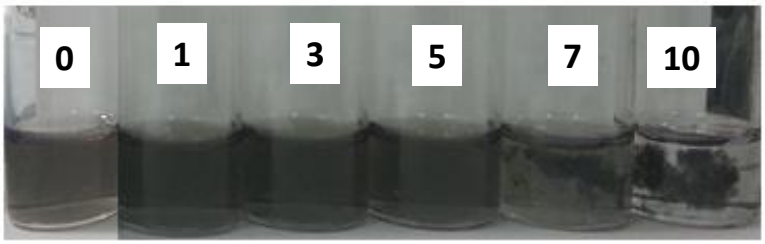

Figure 3. 12. SWCNTs in DCE dispersion 48 h after addition of different concentrations of BTPPATPBCl (0–10 μ M). SWCNTs concentration in each case is 6 mg L^{-1}.

In order to investigate the effect of the organic electrolyte more quantitatively, UV-Vis absorption spectroscopy was used to monitor the concentration of SWCNTs remaining in suspension after sedimentation for a fixed time period.[162, 185] The aggregates were separated from the nanotube suspension by centrifugation at 5000g for 20 min. Figure 3.13 shows the plot of the amount of SWCNTs remaining in the suspension after 48 h, normalised to the concentration of SWCNTs dispersion that had no added electrolyte. The result indicated that both

nanotube dispersions are stable below a threshold electrolyte concentration, but above it, the dispersed amount decreases with increasing electrolyte concentration. However, the observed electrolyte concentration, below which the dispersion is stable, is seen to be lower in the case of AD SWCNT (~1 μM), as compared to the CVD SWCNT (~3 μM), which suggests better stability in the latter case.

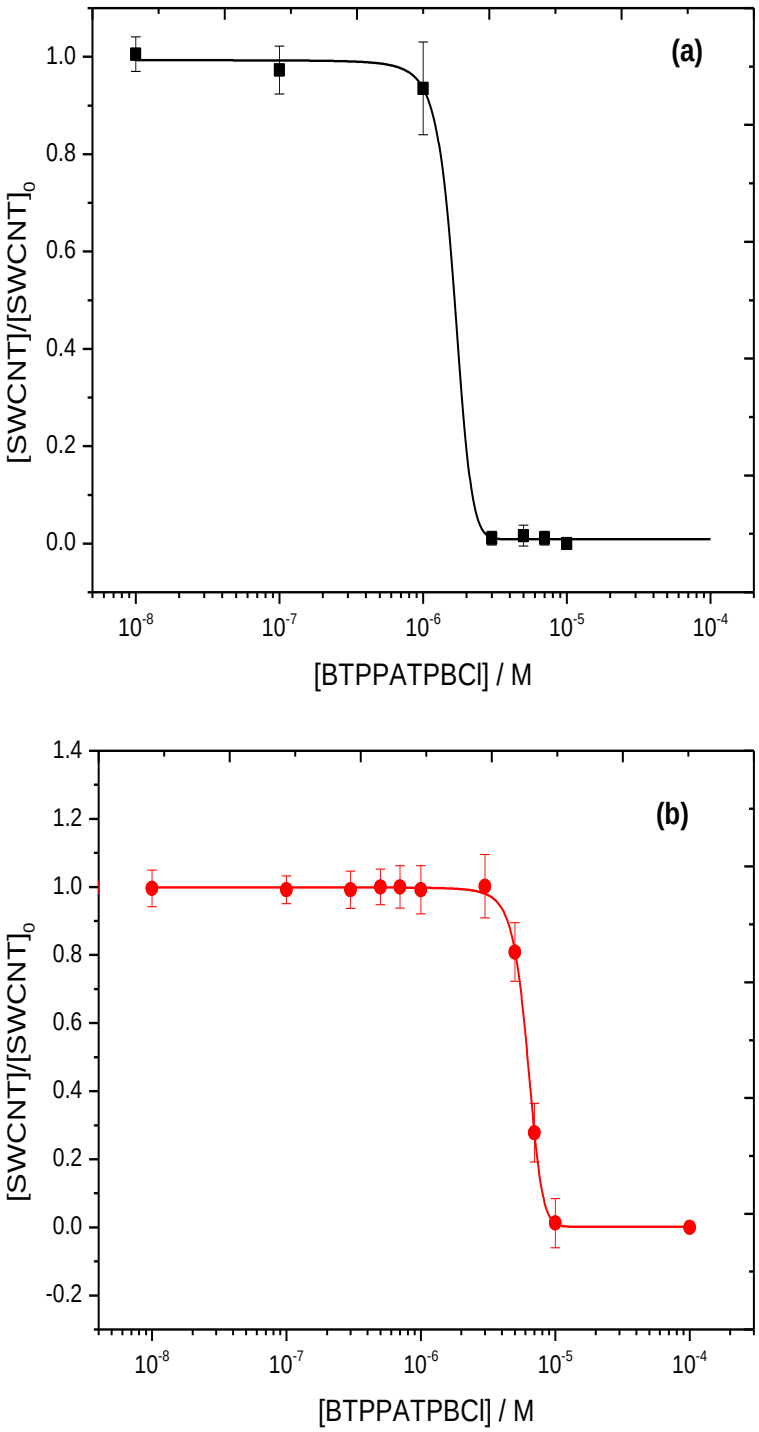

Figure 3. 13. Normalised concentration of (a) AD SWCNT (b) CVD SWCNT remaining dispersed in DCE after 48 h of sedimentation as a function of BTPPATPBCl concentration.

Ameen et al.[190] and Forney et al.[192] studied SWCNT dispersion stability in DMF and NMP using inorganic electrolytes and quantified the dispersion stability in

terms of the onset of aggregation (X_o), which they defined as the concentration of electrolyte required to induce the aggregation of 50% of the dispersed SWCNTs after a given period of time. Because X_o is obtained at lower electrolyte concentration than the critical coagulation concentration (CCC), it is suggested to be more relevant for SWCNTs dispersion processing in which electrolytes may be introduced.[192] X_o can be determined by fitting the data shown in Figure 3.13 with an empirical relationship (Equation 3.2)[190] which is a simplified version of the integrated Maxwell-Boltzmann distribution for energies greater than the electrical double layer (EDL) barrier[190];

$$\frac{[\mathrm{SWCNT}]}{[\mathrm{SWCNT}]_o} = \frac{A}{1 + \exp\left[\frac{[\mathrm{electrolyte}] - X_O}{\Delta X}\right]} \tag{3.2}$$

where A is the fraction of SWCNTs remaining in suspension, which is approximately equal to [SWCNT]/[SWCNT]$_o$ at infinite electrolyte concentration; ΔX is the width of the sigmoidal function. Table 3.3 presents the values of A and X_o obtained from the fitted data in Figure 3.3. The experimental values of [SWCNT]/[SWCNT]$_o$ at infinite dilution are also shown for comparison.

Table 3. 3 Values obtained from fitting the data shown in Figure 3.3, together with the relative values of [SWCNT]/[SWCNT]$_o$ in the absence of electrolyte.

SWCNT type	[SWCNT]/[SWCNT]$_o$	A	X_o / μM
CVD	1	0.999 ± 0.004	6.22 ± 0.04
AD	1	0.987 ± 0.008	1.65 ± 0.35

As can be seen in table 3.3, the measured dispersion stability, X_o of CVD SWCNT is more than three times higher than that of the AD SWCNT. This difference can be attributed to different levels of impurities and differences in size distribution. Nonetheless, the 6.22 ± 0.04 μM obtained in the case of the CVD SWCNT is similar to 8.27 ± 2.23 μM reported by Rodgers et al.[194] for graphene dispersions in DCE aggregated for 24 h using the same electrolyte (BTPPATPBCl). The measured values are, however, much lower than those reported by Ameen et al.[190] for SWCNT dispersion in DMF aggregated for 48 h using inorganic electrolytes with the same charge, $Z_+ = +1$ (150 ± 6 μM for Na^+ and 49.7 ± 0.5 μM for (Ru(1,10-phenanthroline-5,6-dione)(2,2′;6′,2″-terpyridine)Cl]$^+$). These differences may derive from the fact that the electrolyte used in this work was hydrophobic and more likely to make stronger contact with the hydrophobic SWCNTs and destabilise the dispersion than any of the inorganic coagulants used by the previous studies.[162, 190-192]

The observed aggregation behaviour of the SWCNT dispersions in DCE induced by the addition of electrolyte is consistent with an electrostatic stabilisation mechanism, as opposed to the "salting out" mechanism proposed by Rozhin et al.[214, 215] for SWCNTs dispersed in NMP. According to the "salting out" mechanism, the introduction of electrolyte into the dispersion increases the chemical potential of the SWCNTs, which in turn make the nanotubes more solvophobic. This increases the interaction between SWCNTs making them aggregate and coagulate out of the suspension at high enough electrolyte concentration.[214] However, while the addition of electrolyte at high concentration, similar to the one used by Rozhin and co-workers (0.15 M and 0.01 M NaI),[214] can affect the solvophobicity of the SWCNTs, the electrolyte concentrations used in the present investigation to destabilise the

dispersion were much lower. In addition, the contact angle and XPS data presented in chapter 4 sections 4.3 and 4.5.2 respectively, suggest that the BTPPATPBCl electrolyte adsorbs onto the carbon nanotubes. Furthermore, the dispersion stability data presented in Figure 3.13 clearly shows that the concentration of SWCNTs decreases sigmoidally with electrolyte concentration, which is an indication that the dominant stabilisation mechanism of the nanotubes is electrostatic.[190, 194] This is in contrast to the linear relationship between solvophobicity and electrolyte concentration suggested by the Rozhin group.[214]

3.4 Conclusions

In this chapter, the characterisation and dispersion stability of commercially obtained SWCNTs produced by the CVD and AD methods have been studied. The nanotubes were dispersed in DCE by ultra-sonication, followed by centrifugation to remove large aggregates. It was found that the AD SWCNT contains a lower amount of impurities compared to the CVD SWCNTs. Size characterisation by AFM revealed that individual SWCNTs were not isolated in both cases; instead the dispersions were composed of mainly small nanotube bundles. The bundled diameter and length distributions were found to be narrower in the case of CVD dispersion than the AD type. However, the Raman analysis of the bundled nanotubes revealed the CVD SWCNT exhibits a broader distribution of different types of SWCNTs, which were present and dispersed as bundles compared to the AD SWCNTs. This distribution is further supported by broad UV-Vis absorption spectrum resulting from various transitions between the vHs of the different nanotubes. The introduction of electrolyte into the stable dispersions resulted in the aggregation of the dispersed nanotubes, with the extent of the aggregation dependant on the electrolyte

concentration. The nanotube concentration was found to decrease sigmoidally with electrolyte concentration, which is consistent with an electrostatic stabilisation mechanism, in which the added electrolyte causes compression of the EDL around a charged stabilised colloidal particle. Although the AD SWCNT has slightly higher oxygen impurity content, it also showed lower dispersion stability compared to the CVD SWCNT. This result is in contrast with a previous report,[194] which indicated significant increase in dispersion stability of graphene with increased oxygen impurity content. The findings further suggest that the slight difference in oxygen impurity levels on SWCNT may be insignificant. An alternative explanation is that the charge transfer between the nanotube and the solvent could be the dominant charge stabilisation in the nanotubes' dispersion. Finally, the differences in size distribution and type of SWCNT are also expected to contribute to the differences seen in the dispersion stability.

Chapter 4

Electrochemical Characterisation of Single Wall Carbon Nanotubes Adsorption at Liquid/Liquid Interface

4.1 Introduction

The processing of CNTs into stable assemblies has been a topic of major importance in both fundamental investigations and practical applications of CNTs. Recently, the liquid/liquid interfaces, particularly the oil/water interface, have been exploited for the self-assembly of the CNTs (SWCNTs and MWCNTs). Work in this area is focused, mainly, on the use of CNTs as emulsion stabilisers[104, 106, 216] and as a 2D template to generate functional CNTs films[102, 217, 218] that can be transferred onto a solid substrate for various applications. In a typical liquid/liquid assembly strategy, the material (*i.e.* SWCNTs in this case) to be assembled at the interface must be suspended in one of the liquids and the suspension is contacted with a second liquid, after which the assembly can be induced by mechanical agitation[104] or by the addition of an inducing solvent, such as ethanol.[97] CNTs are commonly dispersed in water, which can be achieved either by covalent functionalisation of the CNTs through acid treatment, for example,[219] or by the use of surfactants as solubilising agent[31]. There are also a number of studies of interfacial assembly in which CNTs were dispersed in organic solvents.[104, 106] The advantage of this approach (*i.e.* dispersing CNTs in organic solvent) is that stable and relatively homogeneous dispersion can be achieved while preserving the inherent properties of the CNTs, since dispersion can be achieved without functionalisation or introduction of a solubilising agent.

The earliest work on the liquid/liquid interfacial assembly of CNTs was reported by Wang and Hobbie, in which aggregates of pristine SWCNTs initially suspended in toluene phase were segregated to the water/toluene interface by an emulsion method, with the SWCNTs stabilising water-in-oil (w/o) emulsions.[104] Following this pioneering work, several stable w/o and o/w emulsions stabilised by CNTs have been prepared, with the majority of these studies employing oxidised SWCNTs[220] or MWCNTs[216, 221]. Oxidation, by acid or oxygen plasma treatment, results in CNTs with both hydrophobic and hydrophilic groups (*e.g.* OH and COOH), which are useful for CNTs localisation at the aqueous/organic interface, as well as modulating the emulsion type (w/o or o/w).[221, 222] In addition to the use of oxidised or pristine nanotubes to stabilise w/o or o/w emulsions, the segregation of non-covalently modified CNTs with bio-macromolecules,[223] polymers and surfactants,[221, 222] at the oil/water interface has also been documented. An important property of CNTs stabilized emulsions is improved stability, as demonstrated by a previous study where CNTs stabilised emulsions were found to greatly suppress droplet coalescence due to the formation of an extended structure at the water/oil interface, caused by the strong π-π interactions between individual CNTs.[224]

In terms of assembling individual CNTs into thin films using the liquid/liquid interface as a 2D template, the Miyashita group and others have demonstrated the viability of this technique to yield ultrathin films of both MWCNTs[102, 103, 225] and SWCNTs[218, 226, 227] at the water/oil interface. The nanotubes' aspect ratio and wettability were suggested by these previous works as the key parameters influencing the nanotubes interfacial assembly.[218, 226]

While the majority of these earlier studies on nanotube interfacial assembly focused more on the assembly process, few have investigated the properties of the CNTs

layers/films *in-situ* at these interfaces. For example, Matsui and co-workers[218] investigated the optical and electrical properties of ultrathin films of SWCNTs fabricated at the bulk water/*n*-hexane interface *ex-situ*, after the film had been transferred onto a silicon substrate. The use of SWCNTs to transport enzymes from bulk aqueous phase to an aqueous/organic interface, and the subsequent characterisation of the biocatalytic activity of the resulting SWCNTs-enzyme interfacial layer was examined, with an enhancement in the rate of biotransformation observed with the interfacial layer.[227] This was interpreted in terms of the high intrinsic surface area provided by the nanotube and the absence of intraparticle diffusion limitations.[227] In their studies, Zhang et al.[226] obtained a flexible thin film of imidazolium functionalised SWCNTs (Im-SWCNTs) at a non-polarised water/chloroform interface and attempted electrochemical characterisation of the resultant interfacial layer using scanning electrochemical microscopy (SECM). With only the oxidised form of the redox species ($Ru(NH_3)_6^{3+}$) present in the aqueous phase, it was shown that at the ‘’bare’’ water/chloroform interface a negative feedback current was generated as the tip approached the interface due to the interface acting as an insulator, whilst in the presence of an Im-SWCNTs interfacial layer, a positive feedback current was generated at the tip, indicating that the Im-SWCNTs film was electroactive. However, as there was no redox species in the chloroform phase, no charge transfer reaction occurred between the two immiscible liquids.

Concerning the assembly and interfacial properties of CNTs at the ITIES, much less is known, despite the fact that ITIES has been shown to be a useful and convenient system to deposit/adsorb solids and to characterise their interfacial properties.[117, 228] The advantage of this system over the non-polarised liquid/liquid

systems is that accurate control of potential drop across the adsorbed particles layer can be achieved, thus enabling various electrochemical methods to be applied.[229] Recent works from our group have used this approach to investigate the electrochemical properties of graphitic carbon nanostructures (CNTs and few-layer graphene) adsorbed at the ITIES. It was shown that, the interface assembled SWCNTs/graphene layers served as electron mediators, aiding heterogeneous electron transfer between aqueous and organic redox couples, which remain isolated in their respective phases.[99, 230] This was utilised to functionalise interfacial SWCNTs and graphene layers with metal nanoparticles, by reducing an organic electron donor[99, 231] and conducting polymer (polypyrrole),[231] through oxidation of the pyrrole monomer dissolved in the organic phase by an aqueous oxidising agent. Similarly, the electron mediating properties of pristine liquid-phase exfoliated graphene at water/organic interface were found to result in a catalytic effect on the heterogeneous oxygen reduction reaction.[100] Additionally, the electrochemical doping of the interfacial SWCNTs studied using *in-situ* Raman spectroelectrochemistry.[230]

In this chapter, the adsorption of SWCNTs at the water/DCE interface is first described, including the effects of introducing electrolytes in either, or both, of the phases on the interfacial behaviour of the nanotubes. Next, liquid/liquid electrochemistry based on ion transfer voltammetry was applied to study the electrical properties of the adsorbed SWCNTs.

4.2 SWCNT Adsorption at Water/DCE Interface

Arc discharge (AD) SWCNTs were used in the entire work presented in this chapter. The nanotubes were dispersed in DCE by sonication, as detailed in the

experimental chapter (section 2.2.1). The resulting dispersion was stable for more than one year without any significant aggregation. The adsorption of the SWCNTs from the DCE phase to the water/DCE interface in the absence and in the presence of electrolytes was initially investigated. The electrolytes tested were LiCl and BTPPATPBCl. These electrolytes were selected because of their frequent use in liquid/liquid electrochemistry studies and were also used in the ion transfer study presented in the later sections of this chapter. Four different liquid/liquid systems containing various combinations of the electrolytes (water/DCE, 0.1 M LiCl (aq)/DCE, water/10 mM BTPPATPBCl (DCE) and 0.1 M LiCl/10 mM BTPPATPBCl (DCE)) were prepared. In addition, a control liquid/liquid (water/DCE) system was prepared. In each case, the SWCNTs were present in the DCE phase and interfacial adsorption was induced by a 15 min ultra-sonication in all samples with the exception of the control. The SWCNTs were seen to self-assemble at the water/DCE interface, forming a thin SWCNT layer between the bulk aqueous and organic phases, a few hours after sonication (Figure 4.1). However, no interfacial assembly was observed in the control sample. As can be seen, the presence of electrolytes in either or both of the phases did not appear to have any significant influence on the adsorption behaviour of the nanotubes. In each case, all the SWCNTs initially dispersed in the DCE phase were transferred to the water/DCE interface leaving clear liquids on either side of the nanotube layer. This result suggests that the surface charge on the SWCNTs is weak and is readily overcome by other interfacial forces favouring the interfacial assembly process. This is in contrast to the assembly of liquid-phase exfoliated graphene at the liquid/liquid interface, where organic electrolyte was found to be important for the interfacial assembly of the graphene flakes initially dispersed in the organic phase.[180] It was suggested that

the organic electrolyte is needed to screen the relatively strong inter-graphene flakes electrostatic repulsion that opposes the interfacial assembly.[180, 194]

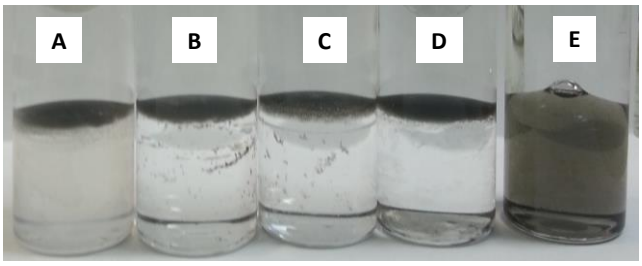

Figure 4. 1. Assembly of SWCNTs at (A) 0.1 M LiCl/DCE (B) 0.1 M LiCl (aq)/10 mM BTPPATPBCl (DCE) (C) Water/10 mM BTPPATPBCl (DCE) (D) Water/DCE interface 12 h after ultra-sonication of the biphasic systems. (E) Water/DCE prepared at the same time as samples A – D, but no sonication was carried out. The SWCNTs were initially dispersed in DCE phase and the concentration used in each case is 6 mg L^{-1}.

4.3 Interfacial Wettability of SWCNT

The interfacial adsorption behaviour of the SWCNTs was further characterised by studying their wettability at the four liquid/liquid systems containing various combinations of electrolytes. To achieve this, the static three-phase contact angle (θ) between SWCNT film, deposited on Si/SiO_2, and the two immiscible liquids was measured. θ was also measured on a bare Si/SiO_2 for comparison. Figure 4.2 shows images of sessile organic droplets on Si/SiO_2 substrate and on SWCNT films immersed in the aqueous phase. As it is a common convention to report θ with respect to the aqueous phase, the measured contact angle values with respect to the organic phase were subtracted from 180°. It can be seen that for pure water/DCE systems, θ increased from 76.5° for the bare Si/SiO_2 substrate (Figure

4.2a) to 138.5° for the SWCNT film (Figure 4.2b). This increase in θ clearly demonstrates that the SWCNTs are wetted more by the organic phase than water (*i.e*. the SWCNTs surface is hydrophobic). The addition of LiCl in the aqueous phase had little effect on the measured contact angle (Figure 4.2c). This observation is similar to a previous study[232] in which the contact angle of silicon oil droplets deposited on hydrophobic polystyrene surface was found to change only slightly in the presence of aqueous electrolytes (KCl and $CaCl_2$) (see also Borisenko *et al.*[233]). However, when BTPPATPBCl was added to the organic phase, a marked increase in the contact angle of the aqueous phase (either water or $LiCl_{(aq)}$) can be observed (Figure 4.2 d and e).

The balance of forces at the three-phase contact line, between the SWCNTs surface, organic drop and the aqueous phase, is described by the Young relation (Equation 4.1):[234, 235]

$$\gamma_{ow} cos\theta = \gamma_{so} - \gamma_{sw} \tag{4.1}$$

where γ_{so} and γ_{sw} represent the SWCNT/organic and SWCNT/water interfacial tensions respectively; θ is the three-phase contact angle and γ_{ow} is the organic/water interfacial tension. According to Equation (4.1), spreading of the organic droplet on the surface of the SWCNT film will be enhanced by a decrease in γ_{so} and γ_{ow} and by an increase in γ_{sw}. Previous work in our laboratory[180] has investigated the effect of $LiCl_{(aq)}$ and $BTPPATPBCl_{(DCE)}$ electrolytes on γ_{ow}, and the result of this study (table 4.1) indicated that γ_{ow} increases slightly in the presence of either of the electrolytes. This implies that the increase in the contact angle seen in the presence of $BTPPATPBCl_{(DCE)}$ is not due to the increase in γ_{ow}, but rather due to the alterations of the SWCNT/liquid interfacial energies, γ_{so} and γ_{sw}. This suggests that

BTPPATPBCl is adsorbed on the surface of the SWCNT through π-π interactions leading to a significant reduction in the SWCNT/DCE interfacial tension.

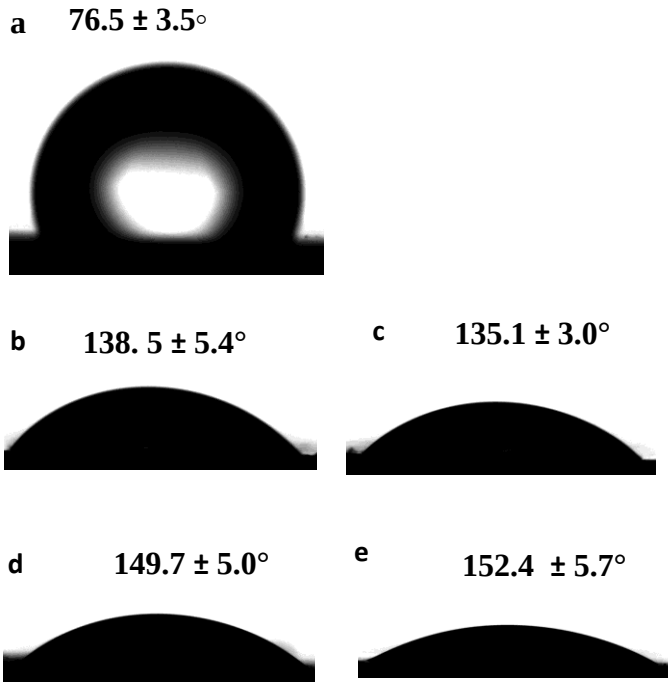

Figure 4. 2. Images showing sessile droplets of (a) DCE on Si/SiO_2 wafer covered with water (b) DCE on SWCNT film covered with water (c) DCE on SWCNT film covered with 0.1 M $LiCl_{(aq)}$ (c) 10 mM $BTPPATPBCl_{(DCE)}$ on SWCNT film covered with water (d) 10 mM $BTPPATPBCl_{(DCE)}$ SWCNT film covered with 0.1 M $LiCl_{(aq)}$. The measured contact angles were subtracted from 180° and the values shown in the figure are with respect to aqueous phase.

Using the measured contact angle and the literature values of interfacial tensions (Table 4.1), the stabilisation energy (ΔE) resulting from the localisation of an individual SWCNT at the four different liquid/liquid interfaces was calculated using the following relation (Equation 4.2):[113]

$$\Delta E = 2RL\gamma_{ow}(\pi\theta/180° \cos\theta - \sin\theta) \quad (4.2)$$

where γ_{ow} is the organic/water interfacial tension, L and R are the length and radius of the SWCNT, respectively; θ is the three-phase contact angle with respect to the aqueous phase. Because of their high aspect ratio, the rod-like SWCNTs are assumed to bind to the liquid/liquid interface with their long axis parallel to the interfacial plane.[114, 115] Table 4.2 summarises the values of ΔE calculated. It can be seen that for all the four liquid/liquid systems investigated, the stabilisation energies were of the same order of magnitude higher than the thermal energy, *i.e.* 10^4 k_bT, suggesting that in each case, the nanotubes were strongly held at the interface. Furthermore, it can also be inferred that the change in nanotubes wettability due to the presence of organic electrolyte had only little impact on the nanotubes behaviour at the interface.

Table 4. 1 values of interfacial tension for the water/DCE systems containing various combinations of electrolytes.

Liquid/Liquid system	$\gamma_{o/w}$ (mNm^{-1})
water/DCE	26.8[a]
0.1 M LiCl /DCE	27.1[a]
water /10 mM BTPPABCl	27.0[a]
0.1 M LiCl /10 mM BTPPABCl	27.0[a]

[a] values were reproduced from a previous work.[180]

Table 4. 2 Values of Δ*E* calculated for the water/DCE systems containing various combinations of electrolytes.

Liquid/Liquid system	$\Delta E\ (10^4\ k_bT)$
water/DCE	6.82
0.1 M LiCl /DCE	6.58
water /10 mM BTPPABCl	7.72
0.1 M LiCl /10 mM BTPPABCl	7.75

4.4 Microscopic Characterisation of SWCNT Interfacial Layer

4.4.1 *In-situ* Optical Microscopy

The SWCNT layers formed at the water/DCE interface were visualised *in situ* using a stereomicroscope. The microscope was focused through the top aqueous phase to the interface and images were taken with a digital camera. Figure 4.3 shows the *in-situ* microscopy images of the SWCNT interfacial layers prepared using nanotube dispersion concentrations of 3 mg L^{-1} and 6 mg L^{-1}, respectively. As can be seen, in each case the interfacial layers are composed of emulsion droplets stabilised by the nanotubes. Although the type of emulsions produced was not probed here, however, pristine SWCNTs are more likely to stabilise w/o emulsions due to their strong hydrophobicity, as demonstrated by the measured contact angle. Furthermore, their initial localisation in the DCE phase also suggests that the w/o emulsions variety would be preferentially stabilised. Nonetheless, as can be observed, the structure of the emulsion droplets produced depended on SWCNT concentration.

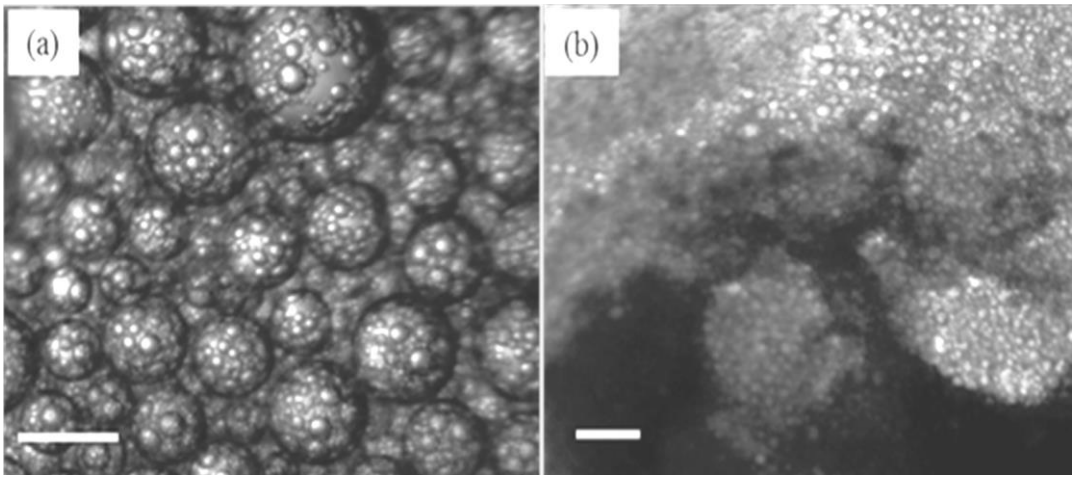

Figure 4. 3. ***In-situ*** **optical micrographs of SWCNT adsorbed at water/DCE interface prepared using SWCNTs concentrations of (a) 3 and (b) 6 mg L^{-1}. Scale bars in a and b represent 200 µm.**

At SWCNT concentration of 3 mg L^{-1}, multiple emulsion droplets were formed. The diameter of the larger globules ranges from ca. 90 – 300 µm, while that of the smaller inner droplets ranges from 20 – 50 µm. Previously in the literature, emulsions stabilised solely by CNTs were either o/w[216, 222] or w/o[104] type, with only a single report on multiple emulsions of the type o/w/o obtained using a SWCNT – silica hybrid.[236] According to this previous work, the inner o/w droplets were stabilised by the silica particles that were not fully covered by the SWCNT and multiple emulsions were only observed at very low SWCNT concentration (≤ 0.005 wt %). In the present work, the formation of multiple emulsions may likely be connected with the preparation method used. It was observed that during bath ultra-sonication of the biphasic system, complete mixing of the two liquid phases did not occur; instead emulsion droplets were seen to exist in each phase with a clear interfacial layer separating the two emulsified phases. The extent of droplets formation was always seen to be higher in the organic phase (bottom layer) than in

the aqueous phase (top layer). Figure 4.4 illustrates the stages thought to be involved in the formation of SWCNT interfacial layer.

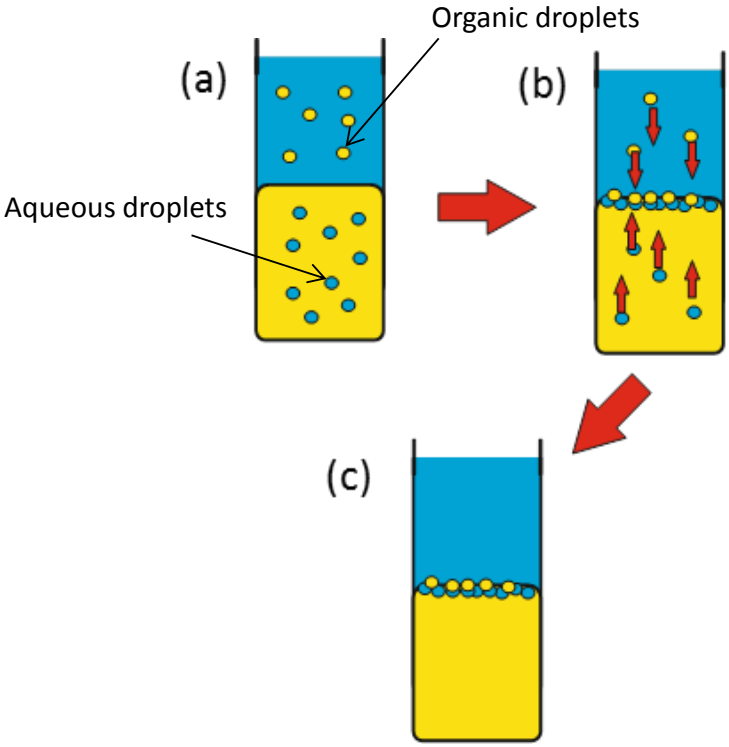

Figure 4. 4. Schematic illustration of processes involved in interfacial emulsion formation.

First, emulsion droplets are formed in each liquid phase (Figure 4.4a). Next, the less dense water droplets produced in the organic phase creamed to the planar liquid/liquid interface alongside the adsorbed nanotubes, whilst the denser DCE droplets sediment from the bulk aqueous phase down to the same liquid/liquid interface (Figure 4.4.b). The interfacial droplets might then undergo various processes such as flocculation, Ostwald ripening and coalescence to produce the final resultant SWCNT interfacial layer (Figure 4.4c). Evidence of droplets flocculation can be clearly seen in the microscopy images of the SWCNT layers (Figure 4.3).

Flocculation of emulsion droplets stabilised using CNTs is commonly attributed to the strong inter-tube van der Waals attraction.[236] When a higher SWCNT concentration (6 mg L^{-1}) was employed, the structure of the droplets produced changed to the simple emulsion type. The droplet size also decreases and the heavy particle aggregation even resulted in deposition of large excess of solid SWCNTs at the interface.

4.4.2 Scanning Electron Microscopy

In order to gain information about the morphologies and density of the adsorbed SWCNTs, SEM analysis was performed. The interfacial layers were deposited on Si/SiO_2 wafer and the solvents were evaporated. Figure 4.5 shows the SEM images of the deposited SWCNT layers prepared from different SWCNT dispersion concentrations. As can be observed, the interfacial preparation method resulted in two types of SWCNT film morphologies depending on the initial dispersion concentration: at low SWCNT concentration (1 mg L^{-1}), the SWCNTs were predominately bent into rings (Figure 4.5a) with only a few straight or partially bent tubes, whereas at higher CNTs concentrations of 6, 12 and 18 mg/L, porous interfacial films were formed, which are composed of random networks of multilayer SWCNT (Figure 4.5 b-d). The density of these multilayer films can be seen to increase with increasing nanotube concentration. The observed concentration-dependant morphologies, from rings to straight or bent tubes, is similar to the findings of Wang *et al.*[106], who reported the production of rings of SWCNTs from a water/DCB system using a Pickering emulsion method. They found that most of the SWCNT structures were rings when the amount of SWCNT-DCB dispersion (SWCNT concentration, 0.13 mg mL^{-1}) was 0.02 wt.% and straight or partially bent

when the SWCNT-DCB fraction was raised to 0.08 wt.%. The liquid/liquid interfacial energy was suggested to be responsible for bending the SWCNTs at the curved interfaces and that the ability of this energy to bend the SWCNTs depends not only on the surface tension of the probe liquids but also on the bundle size of the nanotubes (bundling was assumed to increase with nanotube concentration).[106]

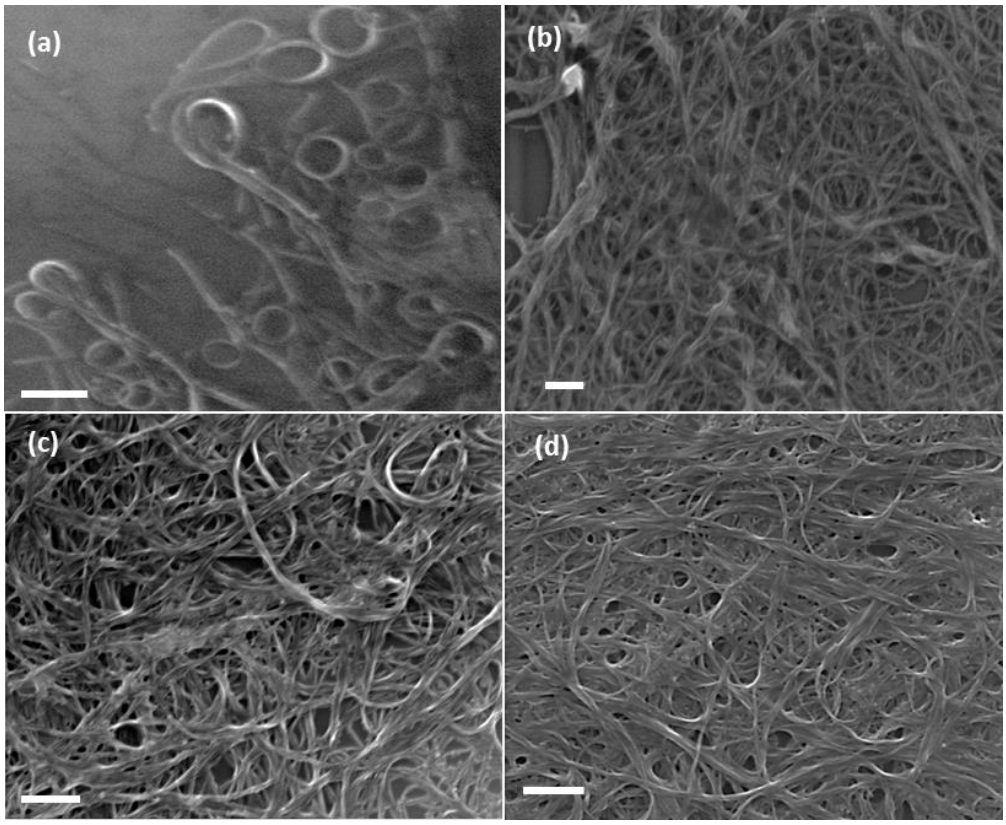

Figure 4. 5. SEM images showing the morphologies of dried SWCNTs films formed at water/DCE interface using a C_{SWCNT} of (a) 1 mg L^{-1} (B) 6 mg L^{-1} (c) 12 mg L^{-1} and (d) 18 mg L^{-1}. Scale bars in a-d represent 1µm.

4.5 Electrochemical Characterisation

The solvents used to form the liquid/liquid interface were water and DCE (or SWCNT dispersion in DCE). This solvent system gives a fairly large potential window for the study of a number of ion or electron transfer reactions.

BTPPATPBCl was used as the organic electrolyte in all the electrochemical investigations presented here, while lithium chloride was always used as the aqueous supporting electrolyte in simple ion transfer experiments. The compositions of the cells employed for the measurements are schematically outlined in Figure 4.6.

Cell 1

$$Ag_{(s)} \mid AgCl_{(s)} \mid \begin{matrix}10^{-2}\text{ M LiCl,}\\ 1\text{ mM BTPPACl}\\ \text{(aq)}\end{matrix} \parallel \begin{matrix}10^{-2}\text{ M BTPPATPBCl}\\ \text{(DCE)}\end{matrix} \mid \begin{matrix}10^{-2}\text{ M LiCl,}\\ 0.2\text{ mM Y}\\ \text{(aq)}\end{matrix} \mid AgCl_{(s)} \mid Ag_{(s)}$$

Cell 2

$$Ag_{(s)} \mid AgCl_{(s)} \mid \begin{matrix}10^{-2}\text{ M LiCl,}\\ 1\text{ mM BTPPACl}\\ \text{(aq)}\end{matrix} \parallel \begin{matrix}10^{-2}\text{ M BTPPATPBCl}\\ 0.4\text{ mM DB18C6}\\ \text{(DCE)}\end{matrix} \mid \begin{matrix}10^{-2}\text{ M KCl}\\ \text{(aq)}\end{matrix} \mid AgCl_{(s)} \mid Ag_{(s)}$$

Figure 4. 6. Schematics of the electrochemical cells used in ion transfer studies.

4.5.1 Stability of SWCNT−Stabilised Interfacial Emulsions under Potential Control

The emulsion droplets formed between the bulk aqueous and organic phases were found to be stable for up to seven days when left undisturbed. Longer time stability of the droplets was not studied in the present work. However, the effect of external polarisation of the water/DCE interface on the stability of these emulsion droplets was probed by the *in-situ* optical microscopy method described in section 4.4.1. The cell used is schematically shown in Figure 4.6 (cell 1, with Y absent). The micrographs shown in Figure 4.7 (a-f) were captured at different applied interfacial potential difference ($\Delta\phi$) during a cyclic voltammetry experiment, where $\Delta\phi$ was

swept from –0.24 V to +0.46 V. It can be seen that the SWCNTs stabilised emulsion droplets were stable against coalescence across all the potential range. The only effect observed was the movement of the interfacial film towards the right on positive polarization (Figure 4.7, a-c) and back again to its original position on reverse polarization (Figure 4.7, d-f). The arrows indicate where the film meets the glass cell wall and also highlight the change in the space between the film and the glass cell wall as the film moves during forward and reverse polarisations. At extreme positive interfacial potential difference ($\Delta\phi \geq +0.45$ V), corresponding to background ion transfer, the interfacial film rotates clockwise on positive scan and anticlockwise on reverse (negative) scan. Figure 4.7c was taken during this rotation, hence the reason it appears like it is slightly out of focus. This movement of the interfacial film may be connected with the movement of the individual SWCNTs[9] and indicates that the SWCNTs located between the two immiscible liquids are charged. However, the same movement could also be caused by Marangoni flow. That is, the movement is induced by interfacial tension gradient, indicating that local changes in interfacial tension occur on polarisation of the interface. This behaviour was similarly observed with SWCNT concentrations of 3 and 1 mg L^{-1}, as well as with repeated cycling (at least three cycles were performed in each case).

Higher SWCNT concentration was not studied due to the partial blockage of the interface by the flocculated nanotubes, which makes the interface black and difficult to resolve the interfacial structures. However, when very low concentration of SWCNT (0.1 mg L^{-1}) was used in film formation, the resulting interfacial emulsions were less stable and coalesces upon polarisation of the interface, suggesting that the SWCNT is too low to form a protective particle layer around the droplets (Figure 4.8).

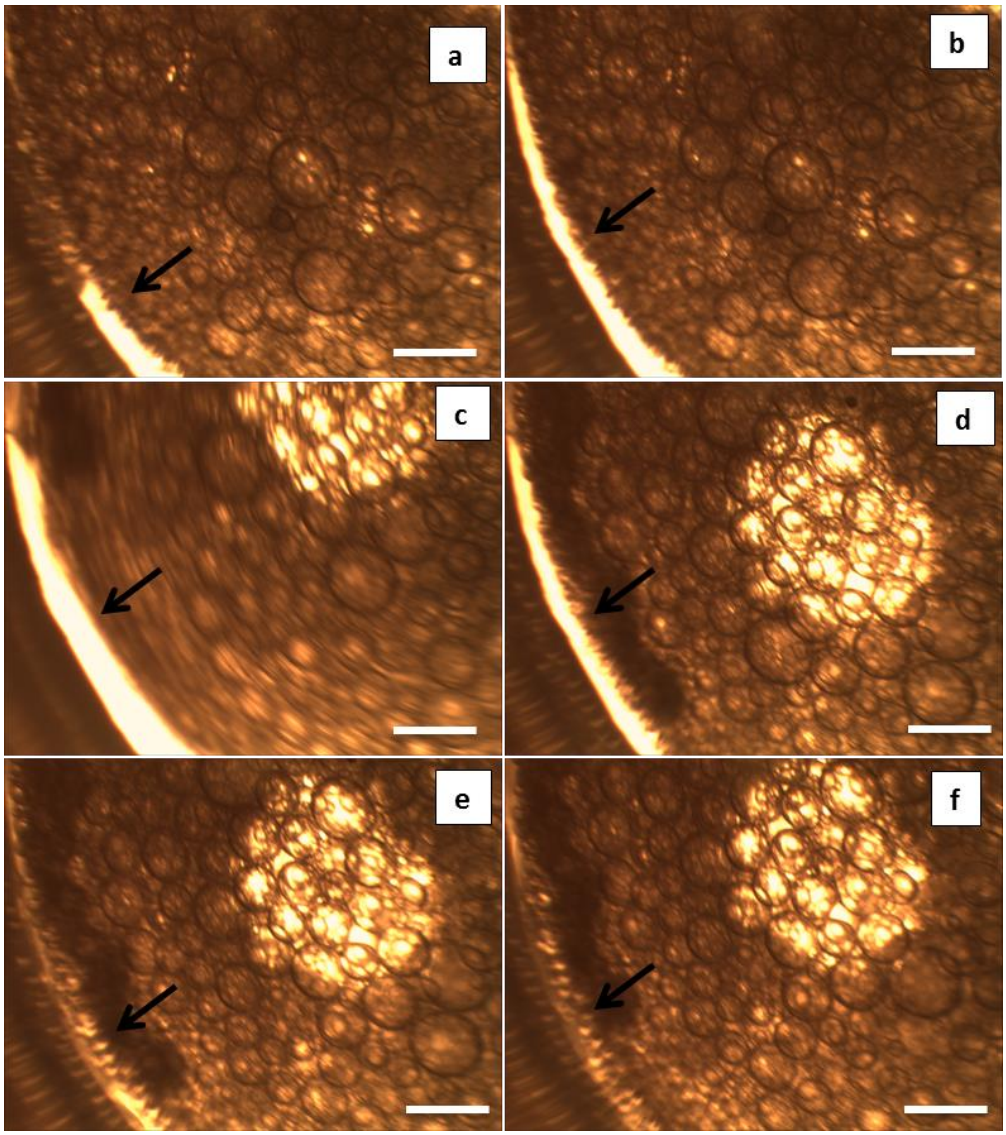

Figure 4. 7. ***In-situ*** **optical micrograph of SWCNT interfacial film taken at applied interfacial potential of (a) –0.09 V (b) +0.01 V (c) +0.46 V (d) +0.31 V (reverse scan) (e) +0.19 V (reverse scan) (f) –0.24 V (reverse scan). SWCNT concentration used in film formation was 2 mg L^{-1}. Scale bars in (a–f) represent 150 µM. The arrows highlight where the film meets the cell wall. Scan rate used was 0.05 V s^{-1}.**

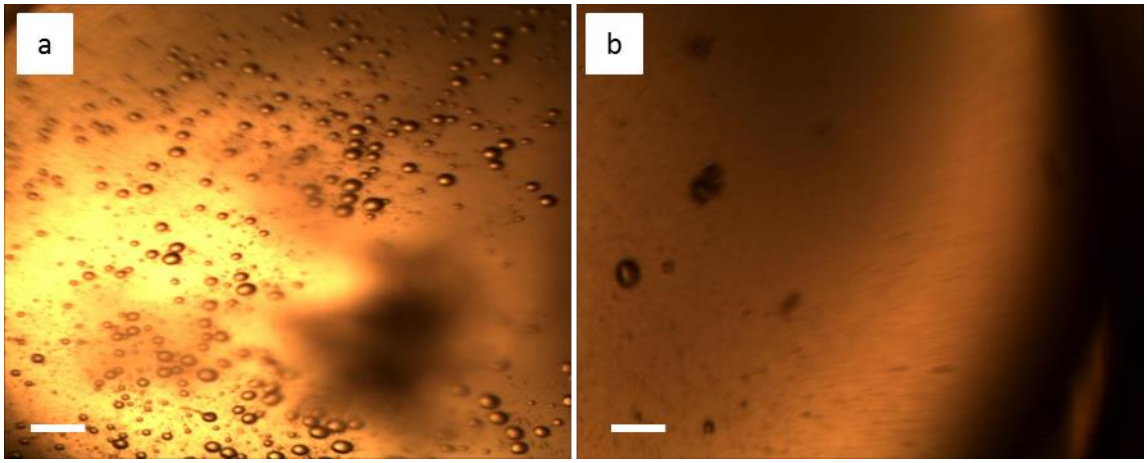

Figure 4. 8. ***In-situ*** **optical micrograph of SWCNT interfacial film taken (a) before the application of interfacial potential (b) After completing one CV at a scan rate of 0.05 V s^{-1}. SWCNT concentration used in film formation was 0.1 mg L^{-1}. Scale bars in (a–b) represent 150 µM**

4.5.2 Ion Transfer across SWCNT Interfacial Films

Ion transfer across ITIES modified with surface active compounds or solids has been widely used to investigate the properties of the adsorbed materials. Herein, we studied the ion transfer across SWCNT-modified water/DCE interface in order to characterise the electrical properties of the interfacial nanotubes. The probe ions used were TMA^+, PF_6^- and K^+. The K^+ ion transfer was facilitated by dibenzo-18-crown-6 (DB18C6) dissolved in the DCE phase. To serve as a bench mark for comparison, the transfer of each ion across the pristine interface was studied first.

Background Electrolyte Response

The cyclic voltammograms (CVs) obtained with only the background electrolytes in the absence and presence of interfacial SWCNT layers formed from two different bulk SWCNT dispersion concentrations (1 mg L^{-1} and 18 mg L^{-1}) are shown in Figure 4.9. The blank CV (*i.e.*, without adsorbed SWCNTs, black curve) exhibits clearly defined potential window, limited by the transfer of Li^+ and Cl^- ions

on the positive and negative ends, respectively. Within this ideally polarisable window, only the charging current flows. In the presence of adsorbed SWCNTs (Red and green curves), enhancement in the charging current as a function of SWCNTs bulk concentration can be seen across the entire potential window. The corresponding increase in the capacitance of the water/DCE interface was evaluated at 0.2 V and found to increase from 24 µF at the ‘’bare’’ interface to 48 µF and 73 µF, respectively at SWCNTs bulk concentrations of 1 and 18 mg L^{-1}. This increase in the capacitance can be attributed to an increase in the liquid/liquid interfacial roughness due to the presence of multiple emulsion droplets formed at the interface when the SWCNTs are adsorbed.[237, 238] Additionally, the interfacial SWCNT films affected the magnitude and shape of the background electrolyte ion transfer peaks (Li^+ and Cl^-); the current magnitudes were reduced and the transfer peaks became broader, indicating that the presence of an interfacial SWCNT film has made the ion transfer across the interface more difficult.

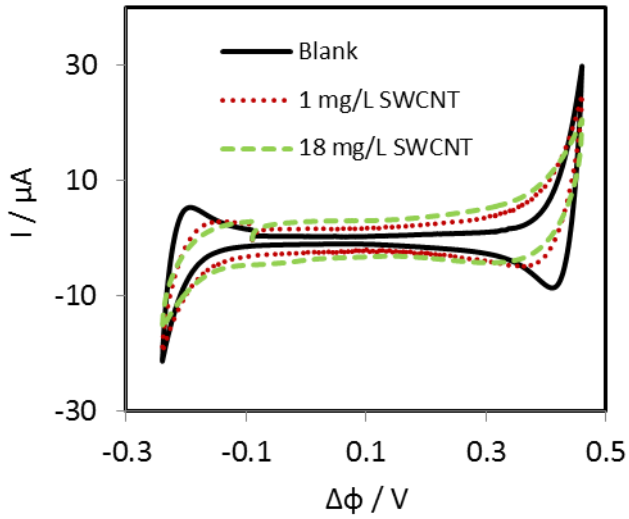

Figure 4. 9. Cyclic voltammograms of the supporting electrolytes obtained in the absence (black line) and presence of SWCNTs films prepared at different bulk CNTs concentrations (green and red lines). The scan rate used was 0.05 V s^{-1} for all the voltammograms.

TMA^+ and PF_6^- Ion Transfer

The cyclic voltammetry of TMA^+ and PF_6^- transfer across the water/DCE interface in the absence and presence of SWCNT films was next studied. Figure 4.10 shows the CV recorded at several scan rates for TMA^+ ion transfer across the unmodified water/DCE interface. The scan was began at a potential of –0.095 V and swept in the positive direction first. During this positive polarisation, which corresponds to the aqueous phase becoming more positive with respect to the organic phase, the TMA^+ ion begins to transfer from the aqueous phase into the DCE phase, with a peak transfer potential around +0.18 V. On the reverse scan (*i.e.*, the aqueous phase now becoming more negative with respective to the organic phase) the TMA^+ ion transfers back into its original phase, with a peak transfer potential around +0.12 V. Ion transfer process is usually treated as reversible,[144] in which case the ideal separation between the forward and reverse peak (ΔE_p) for an ion with a single charge (*e.g.* TMA^+) is expected to be 59 mV at room temperature and is independent

of the scan rate. In some literature, the ion transfer reaction is considered to be a quasi-reversible process.[117] The measured ΔE_p for the TMA^+ ion was found to be 61 mV at 50 mV/s scan rate, and did not change significantly with the scan rate, indicating that the transfer process was reversible (or very near reversible).

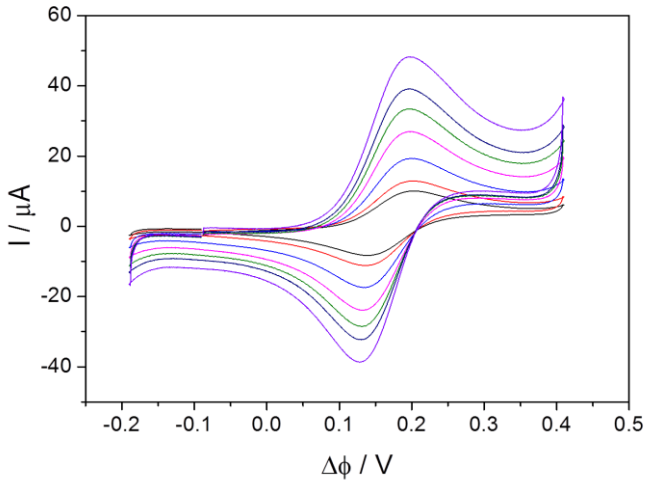

Figure 4. 10. Cyclic voltammogram obtained for TMA^+ ion transfer across unmodified water/DCE interface. Scan rates: 0.005, 0.01, 0.025, 0.05, 0.075, 0.1 and 0.15 V s^{-1}.

The plot of the forward peak currents (I_p) against the square root of the scan rates ($v^{1/2}$) is shown in Figure 4.11. The Randles-Sevčik plot indicated that I_p is linearly related to the $v^{1/2}$. From the linear plot the aqueous diffusion coefficient (D_w) of TMA^+ can be extracted using Equation 3:

$$I_p = 0.4463nFA\left(\frac{nF}{RT}\right)^{1/2} D^{1/2}v^{1/2}c \qquad (4.3)$$

Where, I_p is the peak current, n is the charge number of the ion transferred, F is the Faraday constant, A is the interface area, D is the diffusion coefficient, v is the scan rate, c is the bulk concentration of the ionic species, R and T are the gas constant and temperature, respectively. The D_w obtained for the TMA^+ transfer (1.2×10^{-5} cm^2 s^{-1}) agrees with that reported (1.2×10^{-5} cm^2 s^{-1}) in the literature[239] for the water/DCE system.

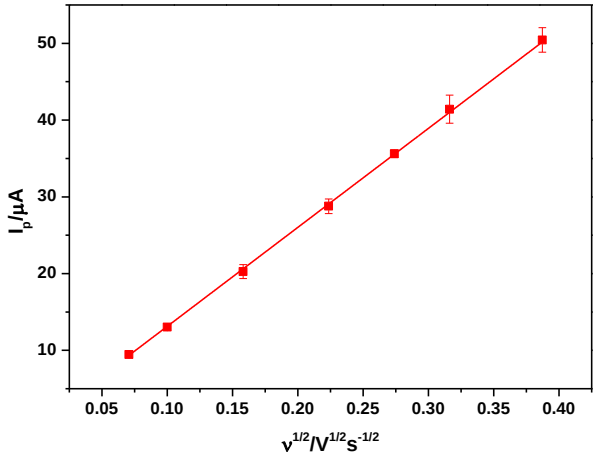

Figure 4. 11. Randles-Sevčik plot showing a linear relationship between the forward peak current for TMA^+ ion transfer across the unmodified water/DCE interface and square root of the scan rate.

The transfer of the TMA^+ ion was repeated but now in the presence of SWCNT films prepared from bulk nanotube dispersion concentrations of 1 mg L^{-1} and 6 mg L^{-1} (Figure 4.12). It can be seen that when the SWCNT concentration used in film formation was 1 mg L^{-1}, the CV response (Figure 4.12a) was very similar to that observed in the absence of an interfacial SWCNT film. There was only a small increase in ΔE_p and a slight reduction in the peak current magnitude. However, when the nanotube dispersion concentration was increased to 6 mg L^{-1}, the response (Figure 4.12b) was significantly altered, as compared to the one recorded at the bare interface. Both forward and reverse transfer peaks were broadened and shifted away

from each other and their magnitudes decreased. This behavior indicates that increasing the SWCNT dispersion concentration lead to a higher surface coverage, resulting in a greater part of the interface available for ion transfer being blocked by the SWCNTs.

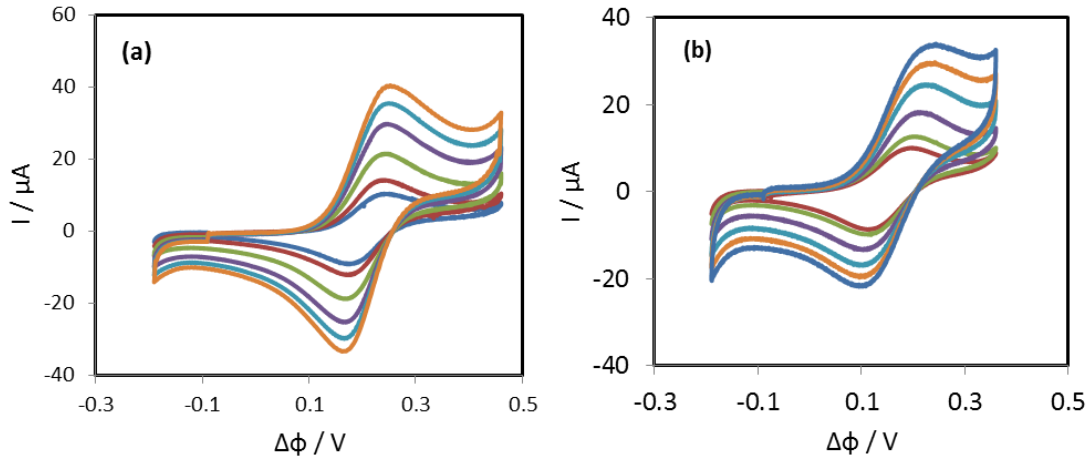

Figure 4. 12. Cyclic voltammograms of TMA^+ transfer across water/DCE interface modified with SWCNT films prepared using SWCNT dispersion concentration of (a) 1 mg L^{-1} (b) 6 mg L^{-1}. Scan rates: 0.005, 0.01, 0.025, 0.05, 0.075, and 0.1 V s^{-1}.

The plot of I_p versus $v^{1/2}$ (Figure 4.13) is linear, indicating that the TMA^+ ion transfer process across the interfacial nanotubes is still controlled by diffusion.

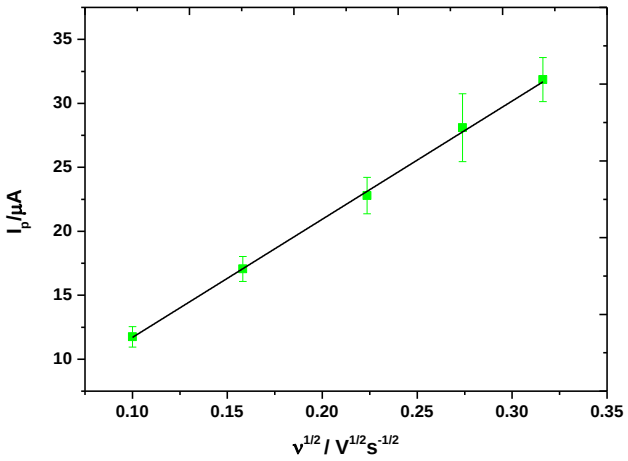

Figure 4. 13. Randles-Sevčik plot showing a linear trend between the forward peak current for TMA^+ ion transfer across SWCNT modified water/DCE interface and square root of the scan rate. The C_{SWCNT} used in adsorbed layer formation was 6 mg L^{-1}.

The direct comparison of the TMA^+ ion transfer without and with SWCNT film present is shown in Figure 4.14. The scan rate used in each case was 50 mV s^{-1}.

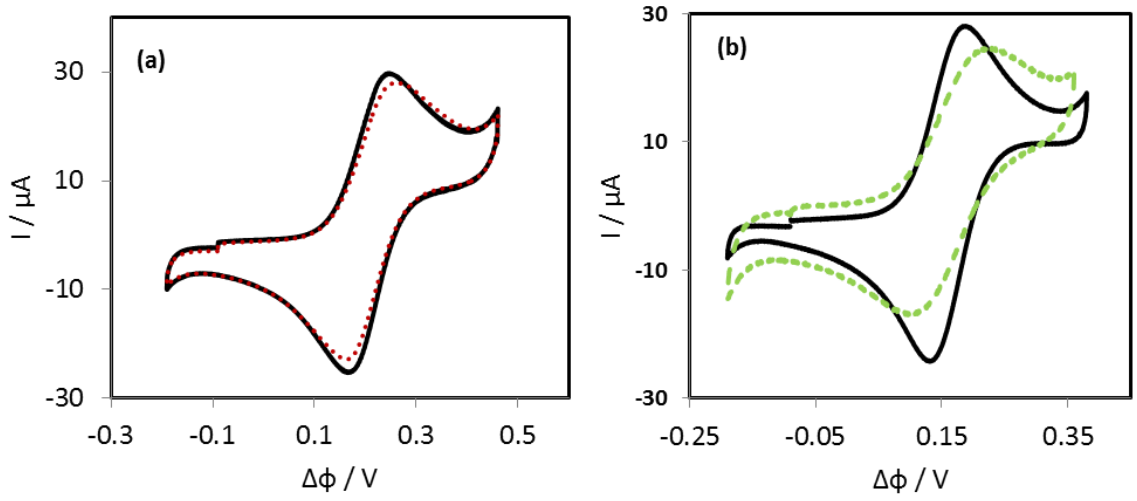

Figure 4. 14. Cyclic voltammograms recorded for the transfer of TMA^+ ion across water/DCE interface in (a) the absence (solid lines) and presence of SWCNTs films (dash lines) formed using C_{SWCNT} of (a) 1 mg L^{-1} (b) 6 mg L^{-1}. Scan rate was 0.05 V s^{-1}.

Similar behaviour was also observed for the transfer of PF_6^- ion across the liquid/liquid interface. At the unmodified water/DCE interface, a quasi-reversible

response (Figure 4.15) was seen for this ion; ΔE_p increased from 60 mV to 83 mV when the scan rate was changed from 10 mV s^{-1} to 150 mV s^{-1}. This change in ΔE_p as a function of the scan rate can be attributed to the remaining uncompensated *iR* drop, which is often difficult to eliminate completely in the case of liquid/liquid systems. The plot of I_p against $v^{1/2}$ was found to be linear and allowed the calculation of D_w for the transferring ion. The value of D_w obtained (1.4×10^{-5} cm^2 s^{-1}) compares well with a literature value of 1.5×10^{-5} cm^2 s^{-1}.[204]

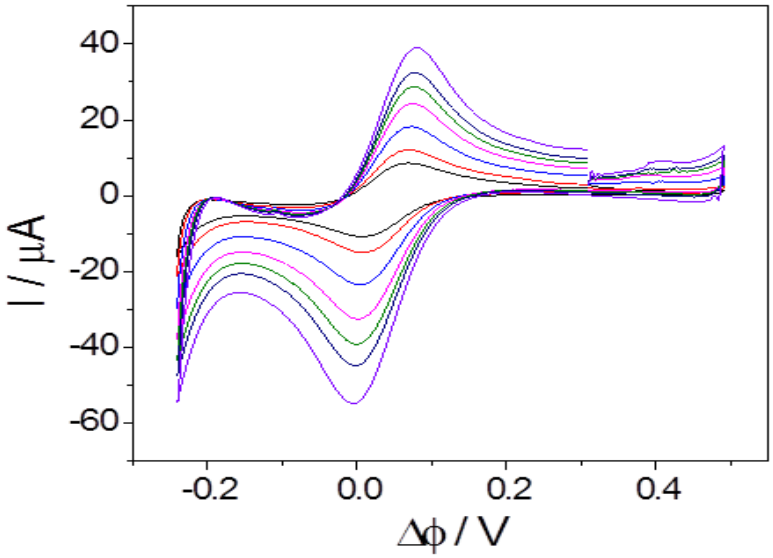

Figure 4. 15. Cyclic voltammogram obtained for PF_6^- ion transfer across unmodified water/DCE interface. Scan rates: 0.005, 0.01, 0.025, 0.05, 0.075, 0.1 and 0.15 V s^{-1}.

Figure 4.16 (a and b) shows the CV responses acquired at increasing scan rate for the transfer of the same ion but now in the presence of SWCNT films prepared using nanotube dispersion concentrations of 1 and 6 mg L^{-1}. Also displayed in Figure 4.16 (c and d) is a direct comparison of the CV traces obtained at a scan rate of 50 mV s^{-1} for the PF_6^- transfer across unmodified and SWCNT-modified interfaces. As can be clearly seen, the effect of the interfacial films on the

transferring ion is quite similar to the effect the film had on the TMA^+ ion transfer; at low nanotube concentration (1 mg L^{-1}) very little differences can be found between the CVs recorded in the absence and in the presence of the interfacial film, while at higher nanotube concentration (6 mg L^{-1}) the response was significantly distorted. Substantial increase in ΔE_p and a small decrease in I_p were observed at the higher nanotube concentration. The I_p, however remained linearly related to the $v^{1/2}$, indicating that that the transfer process is still diffusion controlled. This behaviour again suggests that the interfacial SWCNT film has a blocking effect on the PF_6^- ion transfer process.

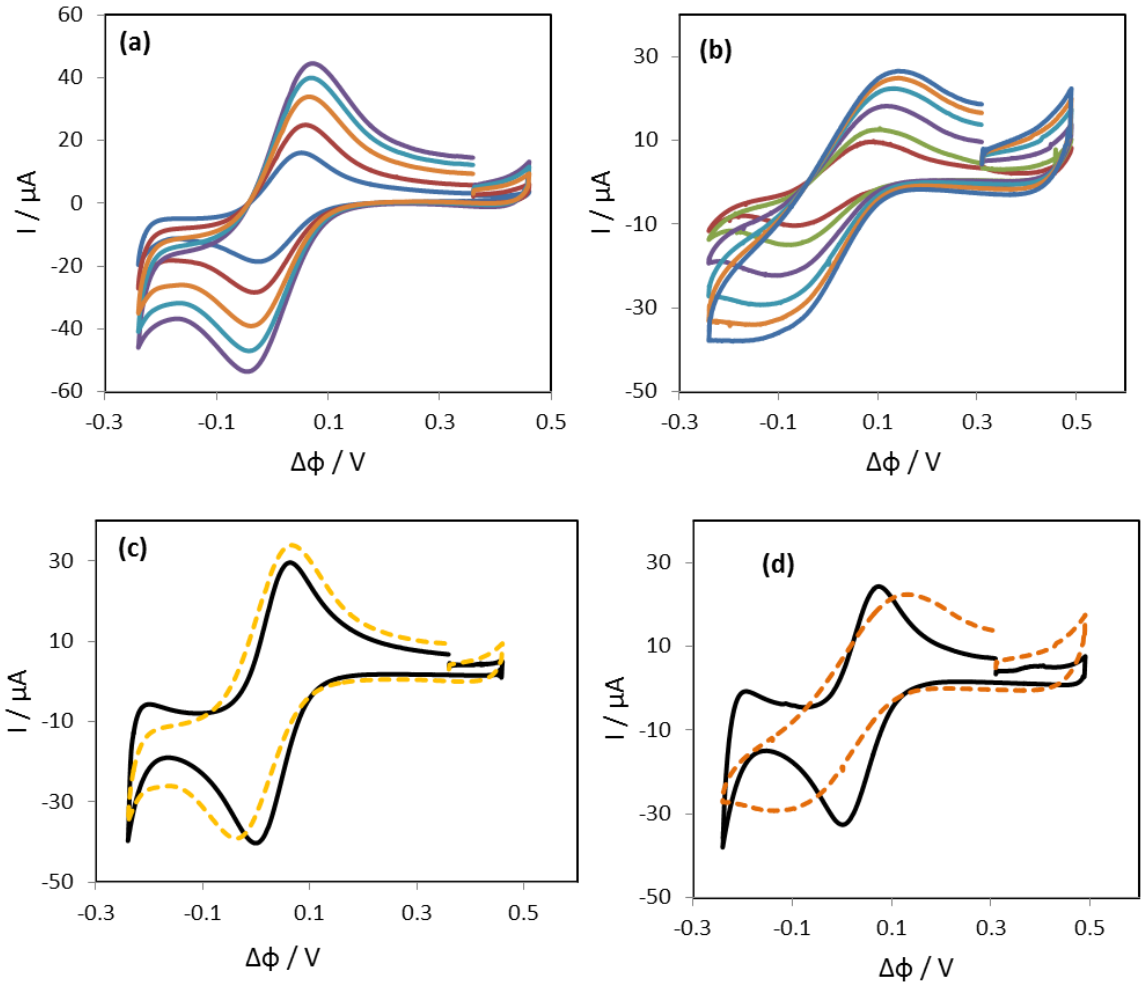

Figure 4. 16. (a-b) Cyclic voltammograms of PF_6^- transfer across water/DCE interface modified with SWCNT films prepared using SWCNT dispersion concentration of (a) 1 mg L^{-1} (b) 6 mg L^{-1}, scan rates used were 0.005, 0.01, 0.025, 0.05, 0.075, and 0.1 V s^{-1}. (c-d) Direct comparison of CVs for the transfer of PF_6^- ion in the absence (solid lines) and in the presence of SWCNT films (dash lines) formed using C_{SWCNT} of (a) 1 mg L^{-1} and (b) 6 mg L^{-1}. Scan rate was 50 mV s^{-1} in each case.

The direct comparison between the two probe ions in terms of the effect of SWCNT interfacial film on I_p and ΔE_p was performed, as shown in Figure 4.17.

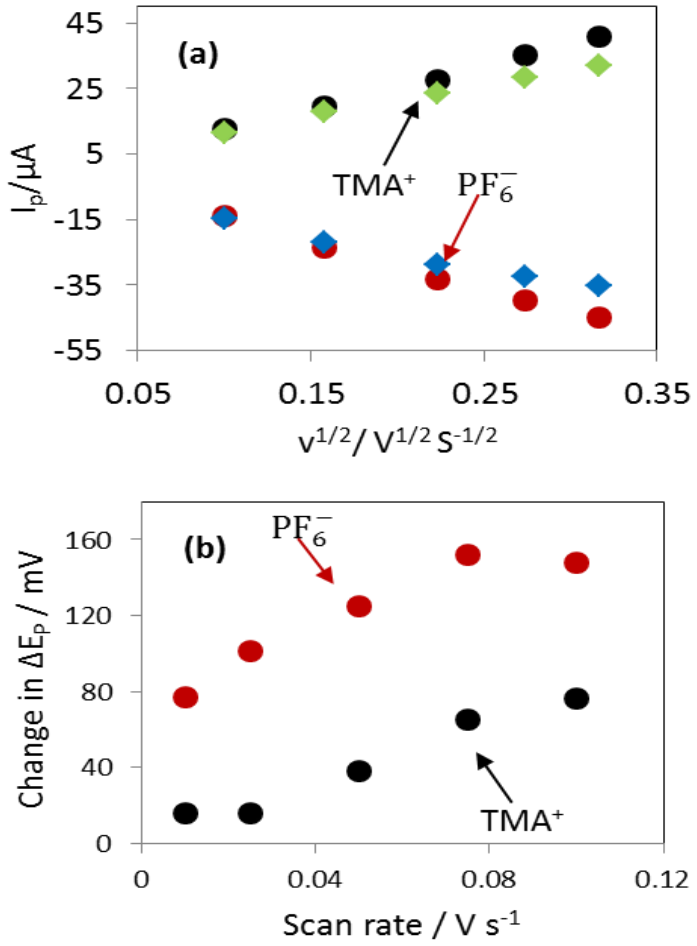

Figure 4. 17. (a) Plot of forward transfer peak current for TMA^+ and PF_6^- ions as a function of $V^{1/2}$ in the absence (circles) and in the presence (squares) of SWCNTs film prepared using C_{SWCNTs} of 6 mg L^{-1}. (b) Change in ΔE_p (ΔE_p in the presence of SWCNTs – ΔE_p in the absence of SWCNTs) as a function of scan rate for each probe ion. C_{SWCNTs} used for the assembly was 6 mg L^{-1}.

For both probe ions (TMA^+ and PF_6^-), the decrease in I_p due to the presence of SWCNT film appears to be identical, though errors introduced in scaling the peak height are likely to be higher in the case of PF_6^- than TMA^+ due to the transfer potential of the anion being shifted more to the negative value making it to merge with the potential of the background electrolyte ion, Cl^-, transfer thereby contributing substantially to the measured current. On the contrary, the increase in ΔE_p due to the presence of the interfacial film was much higher in the PF_6^- case than TMA^+,

suggesting that the transfer of the anion was more strongly inhibited by the interfacial SWCNTs, as compared to TMA^+ ion.

In order to rationalise the observed ion selectivity by the interfacial SWCNT film, the possible adsorption of either the probe ions or the organic background electrolyte ions on the adsorbed SWCNTs was investigated by performing chronoamperometry and XPS measurements. Firstly, potential step experiments were carried out for each probe ion in the presence of SWCNT interfacial film. The interfacial potential was stepped from a potential where no ion transfer occurs (–0.1 V and +0.25 V for TMA^+ and PF_6^-, respectively) to a potential where ion transfer from water to organic phase takes place (+0.25 Vand –0.18 V for TMA^+ and PF_6^- respectively). The interfacial potential was held at the ion transfer potential for 10 mins, after which the SWCNT film was carefully transferred onto a Si/SiO_2 wafer. The transferred layers were then washed in ethanol, isopropanol and acetone and dried before subsequent analysis by XPS. A control sample was treated in a similar way, with the exception that neither of the probe ions nor the supporting electrolyte ions were present and no interfacial potential was applied. Figure 4.18a shows the XPS survey spectra of the aforementioned SWCNT films. The spectra showed the presence of B, N, Cl and P in films obtained with either TMA^+ or PF_6^- present, but not in the control sample. The appearance of signals attributable to B, Cl and P in the TMA^+ and PF_6^- samples is indicative of adsorption of the aromatic cation, $BTPPA^+$ and anion, $TPBCl^-$ of the organic supporting electrolyte on the SWCNT surface, since substantial amounts of these elements could only be reasonably attributed to the supporting electrolyte ions. The absence of a significant signal for fluorine in any sample, and particularly in the sample obtained with PF_6^- present, suggests that the PF_6^- was either weakly adsorbed or not adsorbed at all. The percentage atomic

concentrations of B, N, Cl and P determined from the survey spectra of TMA^+ and PF_6^- samples were normalized to that of C and the results are summarized in Figure 4.17b. The P/N ratio of *ca.* 2:1 is consistent with the stoichiometric composition of $BTPPA^+$. The absence of additional N in the TMA^+ sample suggests that the TMA^+ ion only weakly adsorbs, or not at all, on the SWCNT surface. Similarly, the B/Cl ratio was found to be close to the 1:4 expected for the $TPBCl^-$ anion. The slight excess of B was attributed to overlap of the B1s and P2s peaks, which made it difficult to accurately subtract the contribution of the P2s signal. Nevertheless, the XPS data clearly demonstrate the preferential adsorption of $BTPPA^+$ and $TPBCl^-$ on the SWCNTs surface over the TMA^+ and PF_6^- ions, which is plausible considering that both $BTPPA^+$ and $TPBCl^-$ are charged and could also interact with the SWCNTs via π-π stacking.[240, 241] Furthermore, the XPS data implied a potential dependent adsorption of the supporting electrolyte ions on the interfacial SWCNTs as illustrated by the relative intensities of the components obtained for the samples containing TMA^+ and PF_6^-. It can be seen that at the TMA^+ transfer potential (+0.25 V), the N and P peaks, attributable to $BTPPA^+$, are lower in intensity compared to those measured at the PF_6^- transfer potential (−0.18 V), whilst the intensities of the B and Cl peaks from the $TPBCl^-$ are lower for the PF_6^- transfer potential than TMA^+. Overall, the XPS result suggests that asymmetric adsorption of the supporting electrolyte ions occurs on the interfacial SWCNTs, introducing a net negative and positive surface charge on the SWCNTs at the TMA^+ and PF_6^- transfer potentials, respectively, thereby resulting in the retardation of the ion transfer across the interface through electrostatic attraction between the transferring ion and the adsorbed supporting electrolyte counter ion. The difference in the extent of charge transfer suppression between the two probe ions is associated with the relative

positions of the transfer potentials of the probe ions with respect to the potential of zero charge (PZC). The fact that the kinetics of PF_6^- ion ((ionic radius, 0.259 nm[242]) transfer is affected more than that of the TMA^+ ion (ionic radius, 0.279 nm[243]) implies that the SWCNT film is more charged at the PF_6^- transfer potential, causing more electrolyte ions to adsorb on its surface and consequently increasing the electrostatic attraction between the PF_6^- ion and the adsorbed $BTPPA^+$ cation. For the TMA^+ ion transfer to be less hindered, its transfer potential must be close to the PZC of the system (*i.e.*, when the SWCNT film is less charged), which results in less attraction between the TMA^+ and the adsorbed $TPBCl^-$ anion.

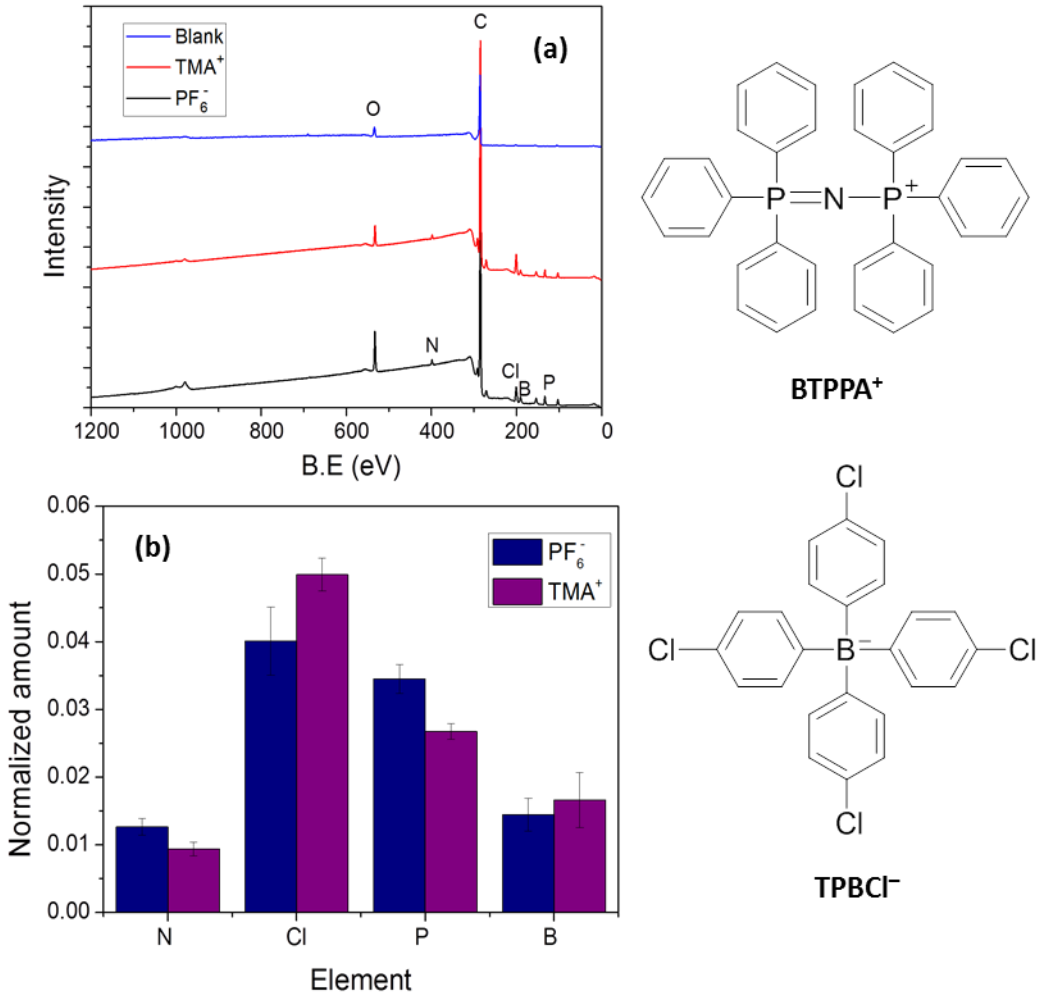

Figure 4. 18. (a) XPS survey spectra obtained for SWCNTs layer extracted from water/DCE interface after the transfer of TMA^+ and PF_6^- probe ions from water to DCE phase. (b) Atomic concentrations of B, N, Cl and P (normalized to carbon) evaluated from XPS survey spectra.

4.5.3 Kinetics of Ion Transfer across the SWCNT Interfacial Films

The apparent rate constant (k^o_{app}) for the TMA^+ and PF_6^- ion transfer in the presence of SWCNT films formed at different nanotube concentrations was determined using the Nicholson method, in accordance with Equation 4.4.[244]

$$\psi = \frac{(D_w/D_o)^{\alpha/2} k^o_{app}}{(\pi D_w n F v/RT)^{1/2}} \qquad (4.4)$$

Where, for simplicity, the aqueous (D_w) and organic (D_o) diffusion coefficients of the transferring ions were assumed to be equal and the transfer coefficient (α) taken to be 0.5; ψ is a dimensionless kinetic parameter and is related to ΔE_p. The relationship between the former and the latter parameters was originally obtained by Nicolson for ΔE_p values ranging from 61 to 212. Using numerical simulation, Mahe *et al*[245] presented a working curve ($n\Delta E_p$ vs log ψ) that extended the limit to higher ΔE_p values. The remaining terms in Equation 4.4 have their usual meanings.

The ΔE_p values measured at scan rates higher than 25 mV s^{-1} were used in calculating the values of ψ. Figure 4.19 shows the k^o_{app} values determined for both ions as a function of SWCNT concentration used in film formation. It is evident that in the case of TMA^+ ion transfer, increasing the SWCNT concentration resulted in a decrease in k^o_{app} as expected for an interfacial area becoming increasingly covered by the SWCNTs. This behavior can be analysed using Amatore's theory of voltammetry[246] at a partially blocked electrode if we assume that the SWCNTs have transformed the single continuous interfacial area into large number of smaller randomly distributed micro/nano pores, the size and/or density of which decreases with increased interfacial coverage. According to this theory,[246] under conditions of total overlap of the diffusion layers, k^o_{app} is lowered by a factor of $1 - \theta$:

$$k^o_{app} = k_o (1 - \theta) \tag{4.5}$$

Where, θ is defined as the fractional area covered by the blocking nanotube film. The fact that the voltammetric profile of TMA^+ transfer exhibited a peak shaped response rather than a sigmoidal one indicates that an overlapping linear diffusion field was achieved. The interfacial coverage was estimated from the SEM data using Image J

software to be approximately 77.5%, 88.0% and 91.7% when the SWCNT concentration used in film preparation was 6, 12 and 18 mg L^{-1} respectively. Therefore applying the $(1 - \theta)$ correction factor gave an average k_o value of 100 ± 7 $\times 10^{-4}$ cm s^{-1}, which falls in the range of k_o values reported for ion transfer.

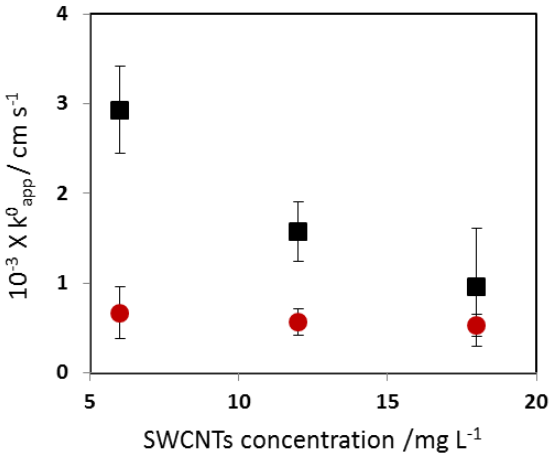

Figure 4. 19. **Plot of the apparent rate constant versus SWCNTs concentration used in film preparation. Black squares and red circles denote kinetic data for TMA^+ and PF_6^- respectively.**

Aside from the slower kinetics displayed by the PF_6^- ion compared to TMA^+ transfer in the presence of interfacial SWCNT films at all concentrations (Figure 4.19), it is also clear from Figure 4.19 that the negatively charged probe ion also show a less clear dependence of k^o_{app} on SWCNT concentration. The ion transfer and the XPS data indicate that there is a potential-dependent change in surface composition of the nanotubes, which in turn suggests that the nanotubes adsorb on the interface from the organic phase, that is, they constitute part of organic double layer. This effect is then associated with the high surface charge density exhibited by the interfacial SWCNT at the PF_6^- transfer potential, which leads to the attainment of

maximum blockage at the SWCNT concentration of 6 mg L^{-1}, as against the TMA^+ ion.

Facilitated K^+ Ion Transfer

In addition to simple ion transfer, the facilitated transfer of K^+ ion by DB18C6 (ionophore) across the SWCNT-modified liquid/liquid interface was also studied. Following the same procedure employed before, the transfer of this ion in the absence of an interfacial SWCNT film was initially performed and the CV obtained is shown in Figure 4.20a.

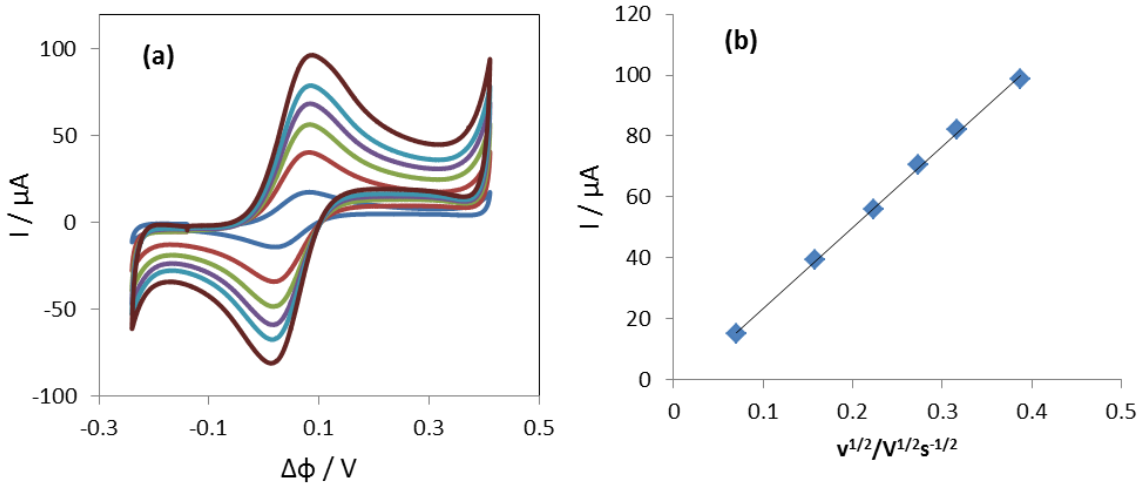

Figure 4. 20. (a) Cyclic voltammogram recorded for the K^+ transfer facilitated by DB18C6 across unmodified water/DCE interface. Scan rate used: 0.005, 0.01, 0.025, 0.05, 0.075, and 0.1 V s^{-1} (b) Plot of forward peak current as a function of the square root of the scan rate.

The current is limited by the linear diffusion of the ionophore since its concentration in the organic phase is far less (0.4 mM) than that of the K^+ ion dissolved in the aqueous phase (10 mM). Similar to TMA^+ the facilitated K^+ ion transfer also shows a reversible behaviour; ΔE_p measured at 50 mV s^{-1} was *ca.* 60

mV and did not vary significantly with scan rate. A linear dependence of the I_p on the square root of the scan rate (Figure 4. 20b) was also obtained. The diffusion coefficient of the DB18C6 in the DCE phase was calculated from the negative gradient of the plot shown in Figure 4.20b as 5.2 $\times 10^6$ cm^2 s^{-1}, which agrees with a literature value of 4.8 $\times 10^6$ cm^2 s^{-1}.[139]

When SWCNTs (6 mg L^{-1}) were adsorbed at the interface, the CV response at increasing scan rates (Figure 4.21) exhibit clearly defined peak currents only when slow scan rates were applied (10 and 25 mV s^{-1}). The measured peak separation (254 mV) at the 25 mV s^{-1} scan rate is much higher than those obtained at the same scan rate in the case of TMA^+ (76 mV) and PF_6^- (169 mV) ions. When higher scan rates (> 25 mV s^{-1}) were employed, the peak currents, especially the forward transfer ones (*i.e.* those corresponding to the K^+ ion transfer from aqueous to organic phase), become very large and difficult to measure. This behaviour indicates that the kinetics of the facilitated K^+ transfer is more strongly inhibited by the SWCNT film than those of simple ion transfer of TMA^+ and PF_6^-. Additionally, the nonlinear trend of the plot of I_p against $v^{1/2}$ (Figure 4.21b) further support that the ion transfer kinetics is more complicated when SWCNT film is present at the liquid/liquid interface. The increased sluggishness of this ion transfer process may be attributed to the possible interaction of DB18C6 and the SWCNT surface, since the ionophore (Figure 4.21) also possesses π-electrons and is also hydrophobic. This π-stacking interaction would slow transfer process further.

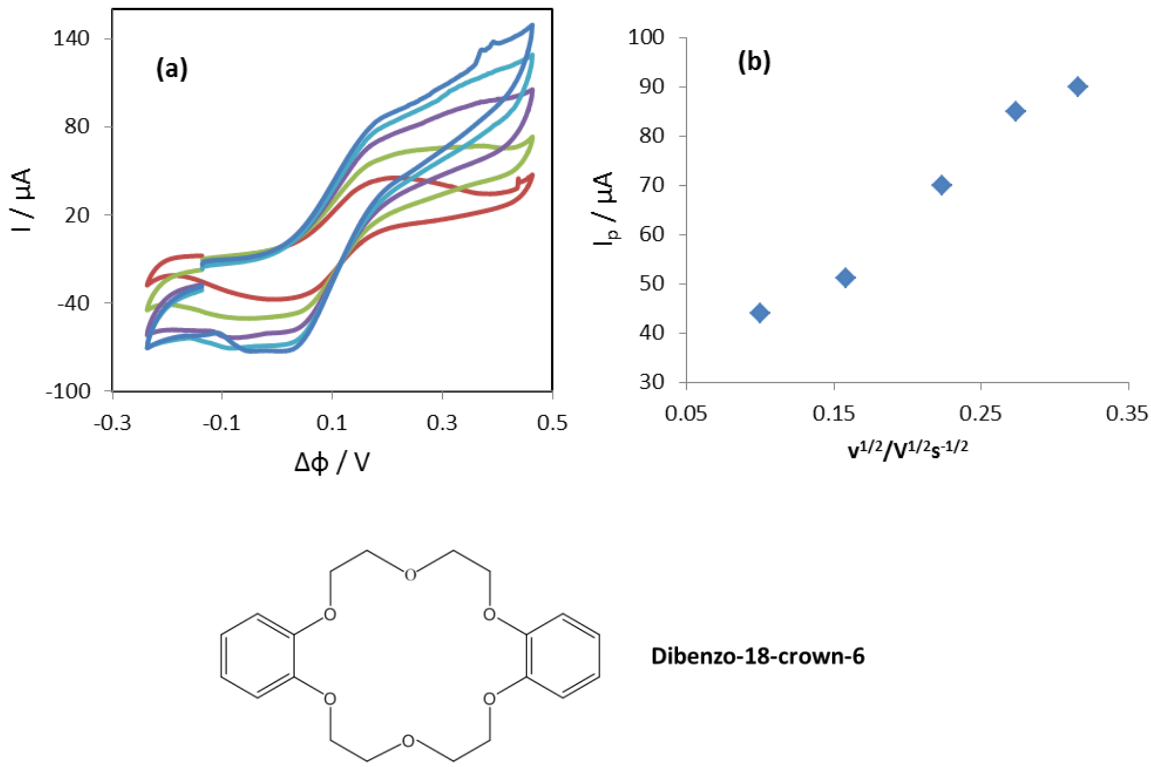

Figure 4. 21. (a) Cyclic voltammogram for the K^+ transfer facilitated by DB18C6 across SWCNT-modified water/DCE interface. C_{SWCNT} used in film formation was 6 mg L^{-1}. Scan rates: 10, 25, 50, 75 and 100 mV s^{-1} (b) Plot of the forward peak current as a function of the square root of the scan rate.

4.6 Conclusion

The adsorption of SWCNTs at the water/DCE interface and the use of liquid/liquid electrochemistry to characterise the electrical properties of the adsorbed nanotubes have been described. SWCNTs were shown to adsorb strongly at the interface, forming a thin interfacial film/layer, regardless of the presence or absence of electrolyte in either or both of the phases. The stabilisation energy (ΔE) resulting from the localisation of an individual SWCNT at the four water/DCE interfaces containing different combinations of electrolytes was estimated to be orders of magnitude higher than the thermal energy, thus rationalising the strong adsorption

behaviour of the SWCNTs at these interfaces. *In-situ* optical microscopy characterisation revealed that the SWCNT interfacial layer formed was composed of multiple emulsion droplets, which were stable against coalescence even when the liquid/liquid interface was polarized. The formed SWCNT interfacial layers were found to suppress the transfer of ions across the liquid/liquid interface and the blocking effect was shown to be charge selective; the transfer of the positively charged TMA^+ ion was less inhibited than that of the corresponding negatively charged PF_6^- ion. The blocking effect of the SWCNTs on both ions was attributed to the potential dependent adsorption of the organic supporting electrolyte ions on the interfacial SWCNTs, as indicated by XPS measurements, which caused electrostatic interaction between the transferring ion and the SWCNT surface, thereby inhibiting the ion transfer. On the other hand, the selectivity between the two ions may be derived from the change in the PZC of the liquid/liquid system due to the presence of charged SWCNT, causing the relative positions of the transfer potentials of the probe ions to change with respect to the PZC. In the case of the facilitated K^+ ion transfer, the suppression of the ion transfer across the SWCNT interfacial layer was found to be even greater than those of the simple ion transfer. This can be due to the presence of additional π-π interactions between the ligand and the surface of the interfacial SWCNTs.

Chapter 5

Controlled Preparation of Carbon nanotubes/Conducting Polymer Composites at Polarisable Water/Organic Interface

5. Introduction

Intrinsically conducting polymers (CPs) including polypyrrole (Py), polyaniline (PANI) and polythiophene (PTh) have been extensively studied for more than thirty years due to their relatively high electron conductivity coupled with the properties of conventional organic polymers (*e.g.,* ease of synthesis, mechanical properties, light weight and processibility).[247-249] These combined properties are the basis of many important applications of CPs such as batteries and supercapacitors, artificial muscles, sensors, anticorrosive coatings and smart windows.[249-251] However, it is well known that all CPs are mechanically weak and, also, must be oxidised and doped with a counter ion to make them sufficiently conductive.[252, 253] One approach that has been used to compensate for some of the shortcomings of CPs is to combine them with carbon nanotubes (CNTs) to form nanocomposites,[254, 255] since CNTs exhibit high surface area, excellent electron conductivity, chemical stability and remarkable mechanical properties.[5] This combination has been shown to yield hybrid materials with synergistic effect.[252, 253, 256] For instance, in applications involving supercapacitors, the large pseudocapacitance of the CPs combined with the mechanical strength, high surface area and excellent electrical conductivity of the CNTs have been shown to dramatically enhance the performance of the supercapacitors fabricated from the composite material.[257-260]

One of the most important factors relating to the CNT/CP composites is their preparation method.[253, 261] Previous studies have shown that the nature of interaction between the CNT and the CP is important for obtaining the synergistic effect in the resultant composite.[262-264] CNT/CP composites are commonly prepared either by chemical or electrochemical polymerisation methods. The advantage of electrochemical synthesis, over the chemical method, is that it allows for the deposition of thin films of the CP with a well-controlled morphology and thickness.[248, 265, 266] Several efforts in this direction have been reported, with the majority of the studies being carried out on solid electrodes.[252, 267, 268] Electrochemical synthesis of CNT/CP composite has been carried out by electrodeposition of CPs on preformed CNT-based electrodes (e.g., well-aligned CNT arrays,[268, 269] CNT films made by solvent casting[270] and CNT "buckypaper"[271]). In some studies, however, the CNT/CP composites were prepared by co-electrodeposition from a CNT suspension containing the monomer units.[252, 253] Here, the CNTs are chemically oxidised (e.g., by acid treatment[272]) to introduce oxygen groups (particularly, acidic, such as COOH) onto the surface of the nanotubes.[252, 273] This treatment makes the CNTs readily dispersible in water, and induces the creation of negatively charged surface through ionisation of the acidic groups.[272] Because the nanotubes are ionised (anionic), they can serve as both the supporting electrolyte during the electropolymerisation reaction and, also, as the doping species for the deposited PPy.[252, 267, 273] This latter approach, where the CNTs and CPs are simultaneously deposited, is believed to yield superior synergistic properties over the electrochemical deposition on preformed CNT substrates, as it allows the polymer layer to be uniformly coated on the CNTs surface leading to a homogeneous CNT/CPs nanocomposite structure.[253, 264]

On the other hand, there are only a few studies focusing on the electrochemical synthesis of CP at the ITIES (interface between two immiscible electrolyte solutions). Cunnane and Evans[274] first demonstrated the formation of oligomers of Py derivatives in the organic phase (1-methylpyrrole and 1-phenylpyrrole) brought about by a heterogeneous electron transfer between an organic-based monomer (1-methylpyrrole or 1-phenylpyrrole) and an aqueous-based redox couple (Fe^{2+}/Fe^{3+}) under electrochemical control at the water/DCE interface. This early work was followed by studies involving the electrochemical synthesis[275-277] and characterisation[278] of polythiophene (or its oligomers) at the ITIES by the Cunnane group. Here, the influence of different polymerisation conditions (interfacial potential, monomer concentration and electrochemical method) was studied. Using tetraethylammonium (TEA^+) and terapropylammonium ($TPrA^+$) as potential determining ions, it was shown that the heterogeneous electron transfer between 2,2′:5′2″ terthiophene monomers present in the DCE phase and the Ce^{3+}/Ce^{4+} redox couple dissolved in the aqueous phase depended on the interfacial potential; *in-situ* visible absorption spectra were used to show that different thiophene oligomers were formed at different interfacial potentials.[276] It is important to mention that there is no previous study to the best of our knowledge of the preparation of CNT/CP at the ITIES. However, there are a number of studies that reported the formation of CNTs/CP at the non-polarised liquid/liquid interfaces. For instance, the Zarbin group has described in several papers the interfacial polymerisation of PANI in the presence of CNTs, or graphene at the water/toluene interface, mainly using ammonium persulphate as the chemical oxidising agent.[264, 279-281]

In the previous chapter, it has been demonstrated that SWCNTs – initially dispersed in the organic phase – can self-assemble at the water/organic interface forming an interfacial thin film whose thickness/density can be controlled simply by changing the initial concentration of the SWCNT dispersed in the organic phase. The interfacial film was also shown to be stable, but permeable to ions when the interface was polarised with the help of an external potential control. In the present chapter, we report the interfacial electropolymerisation process for the controlled, potentiodynamic proparation of PPy at the bare water/DCB interface, and in the presence of an interfacial SWCNT film, with the overall aim of preparing SWCNT/PPy composites. The prepared free-standing films were transferred to solid substrates and characterised using atomic force microscopy (AFM), scanning electron microscopy (SEM) and Raman spectroscopy.

5.1 Mechanism of Electropolymerisation of Pyrrole

Although there have been many mechanisms proposed till date for the electropolymerisation of pyrrole, the Diaz's[282] mechanism is the most widely accepted in the literature.[247, 283] The mechanism is based on coupling between radical cations. During the initiation step (scheme 5.1), the Py monomer is oxidised to form a radical cation, which then couples with another monomer radical cation to produce dihydrodimer cation, which after losing two protons produces a dimer:

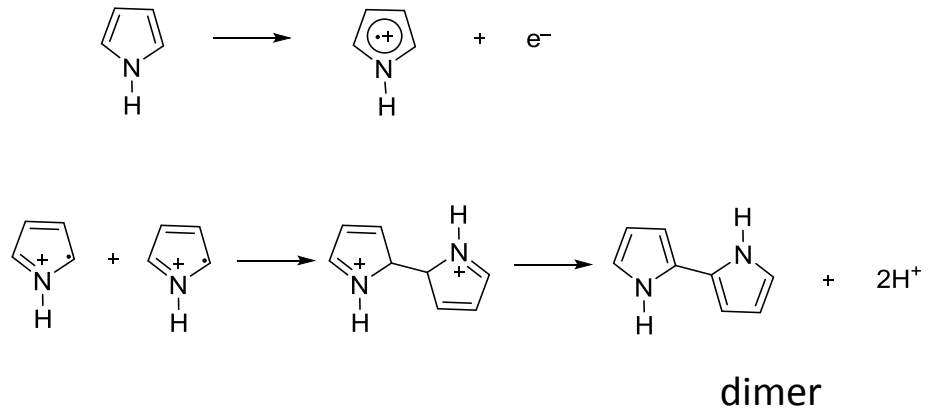

Scheme 5.1

In the propagation step, the dimer is oxidised to a radical cation, which then reacts with a monomer radical cation to form a neutral trimer after losing two protons (scheme 5.1):

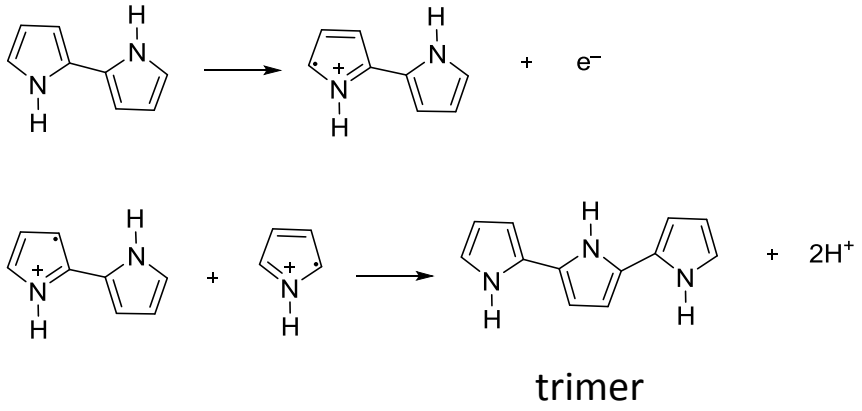

Scheme 5.2

The propagation continues in the established sequence: oxidation, coupling and deprotonation forming oligomers until the final PPy is obtained (scheme 5.3).

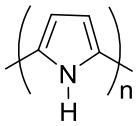

Scheme 5.3

The PPy is typically obtained in the oxidised (cationic) conducting form and doped with counterion from the electrolyte solution (scheme 5.4).

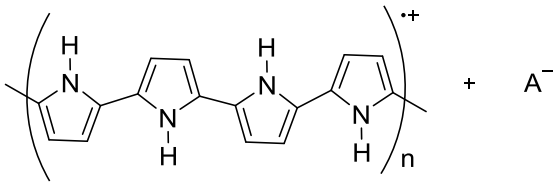

Scheme 5.4

5.2 Electropolymerisation of Pyrrole in DCB at a Metallic Electrode

In the literature, PPy films are often prepared in acetonitrile solution in the presence of small amount of water and electrolytes with different counter ions, most commonly, ClO_4^- and BF_4^-.[284-286] As both the nature of the solvent and the electrolyte are known to influence the PPy film formation and properties,[249] the electropolymerisation of Py in 1,2-dichlorobenzene (DCB) was initially carried out on a polished Pt disc electrode (2.07 mm in diameter) using Pt mesh and SCE as counter and reference electrodes, respectively. The PPy film was prepared by cyclic voltammetry at 0.1 V s^{-1} scan rate, and the polymerisation solution consisted of 0.1 M Py and 0.01 M BTPPATPBFB supporting electrolyte. Figure 5.1 shows the CVs

recorded for the electropolymerisation process. As can be seen, the voltammograms displayed features characteristic of conducting polymer formation. Monomer oxidation starts at about +0.6 V, followed by a significant increase in current at potentials greater than +0.8 V owing to PPy deposition on the Pt electrode. On the reverse scan, there is a small cathodic peak, which is associated with the reduction of the PPy film from cationic to neutral.[287] Also consistent with the literature observations,[286, 287] the subsequent monomer oxidation potentials were lower than the first scan, a feature that indicates Py oxidation on the PPy film is more favourable than on the Pt surface. The prepared film could be cycled reversibly between the oxidised (conducting) and neutral (insulating) form. This result suggests that PPy can be grown in DCB with the bulky BTPPATFPB electrolyte.

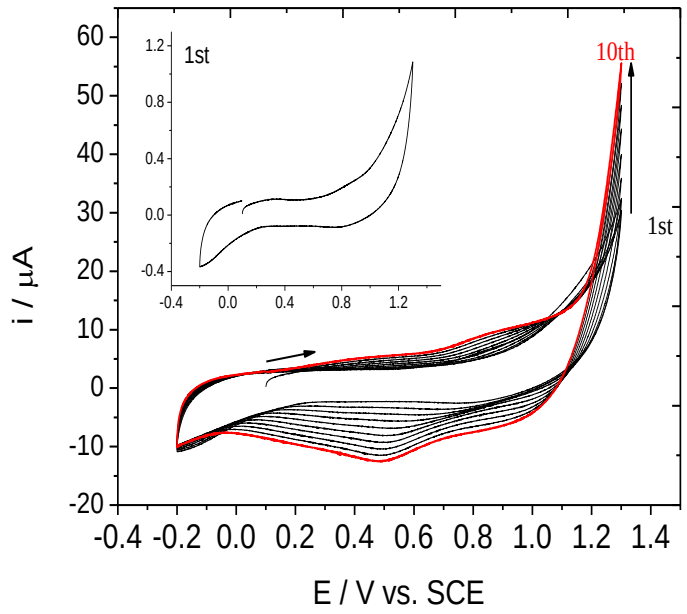

Figure 5. 1. Cyclic voltammograms of polypyrrole electropolymerisation at Pt electrode in 10 mM BTPPATFPB organic (DCB) solution. Scan rate: 0.1 Vs^{-1}.

5.3 Voltammetry at the water/DCB interface

The compositions of the cells used for all electrochemical studies at the ITIES are schematically represented in Figure 5.2. DCB was chosen as the organic phase because it has a wider potential window in comparison to DCE (which was used in the ion transfer studies presented in chapter 4), and has been employed previously to suspend SWCNTs.[148] Similarly, the aqueous redox couple, $IrCl_6^{2-/3-}$ was selected as the oxidising agent because its standard reduction potential (E^0 = 0.866 V *vs.* SHE) is high enough to cause the oxidation of the Py monomer (oxidation potential ≥ 0.8 V *vs* SHE,[287, 288] see also Figure 5.1).

Figure 5.3 shows the CV response obtained with only the supporting electrolytes, $LiCl_{(aq)}$ and $BTPPATFPB_{(DCB)}$, in the absence (black curve) and in the presence of 0.1 M Py monomer in the organic phase (red curve). A large potential window, limited by the transfer of Li^+ and Cl^- ions on the positive and negative ends, respectively,[230] can be observed (black curve) when the Py was absent. However, in the presence of Py, the potential window becomes smaller by about 10 mV; this decrease in the potential window is attributed to the facilitated ion transfer of Li^+ by the Py monomer present in the DCB phase. A similar result in which the transfer of aqueous Ag^+ was facilitated by N-phenylpyrrole present in DCE phase has been reported previously.[289]

Cell 1

Ag(s) | AgCl(s) | 0.1 M LiCl (aq) || 10 mM BTPPATPFB (DCB) | 0.1 M LiCl, 1mM BTPPACl (aq) | Ag(s) | AgCl(s)

Cell 2

Ag(s) | AgCl(s) | 0.1 M LiCl (aq) || 10 mM BTPPATPFB, 0.1 M pyrrole (DCB) | 0.1 M LiCl, 1mM BTPPACl (aq) | Ag(s) AgCl(s)

Cell 3

Ag(s) | AgCl(s) | 0.1 M LiCl, 0.125 mM $IrCl_6^{3-}$ (aq) || 10 mM BTPPATPFB (DCB) | 0.1 M LiCl, 1mM BTPPACl (aq) | Ag(s) | AgCl(s)

Cell 4

Ag(s) | AgCl(s) | 0.1 M LiCl, 10^{-2} M $IrCl_6^{2-}$, 1 mM $IrCl_6^{3-}$ (aq) || 10 mM BTPPATPFB, 0.1 M pyrrole (DCB) | 0.1 M LiCl, 1mM BTPPACl (aq) | Ag(s) | AgCl(s)

Figure 5. 2. Schematics of electrochemical cells used for the electropolymerisation process.

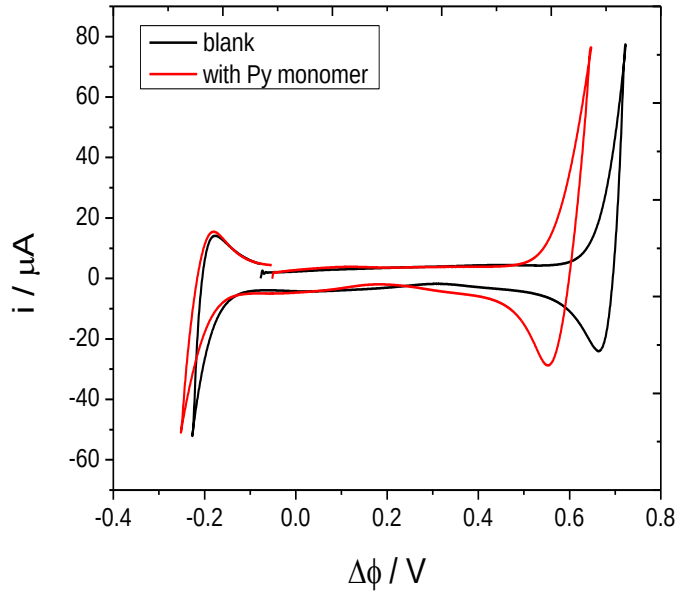

Figure 5. 3. Cyclic voltammograms of the supporting electrolytes obtained in the absence (black curve, cell 1) and in the presence of 0.1 M Py in DCB (red curve, cell 2). Scan rate: 0.1 V s^{-1}.

The CV response recorded when $IrCl_6^{2-}$ or $IrCl_6^{2-/3-}$ was added to the aqueous phase without the Py monomer in the organic phase (cell 3) is shown in

Figure 5.4. Negative and positive current peaks can be observed at $\Delta\phi$ = –0.088 V and $\Delta\phi$ = –0.129 V, respectively. These peaks were attributed to the transfer of $IrCl_6^{2-}$ ion from water to the organic phase and vice-versa. The peak-to-peak separation of 39 mV is consistent with the quasi-reversible transfer of a divalent ion.

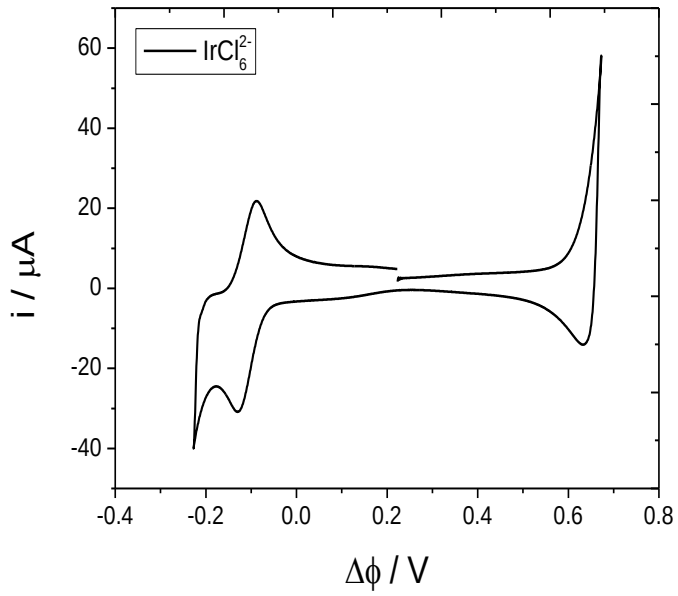

Figure 5. 4. Cyclic voltammogram for $IrCl_6^{2-}$ transfer across water/DCB interface in the absence of Py in DCB phase. Scan rate: 0.1 V s^{-1}.

5.4 Electropolymerization of Py at Bare ITIES

Figure 5.5 shows the CV response recorded in the presence of both the Py monomer in the organic phase and the $IrCl_6^{2-/3-}$ in the aqueous phase. The reversible current peak due to the transfer of $IrCl_6^{2-}$ is almost absent, indicating that this species has been consumed, whilst a new irreversible current peak appeared at $\Delta\phi$ = +0.46 V. The new current peak can be associated with the oxidation of Py to PPy on the organic side of the ITIES and the associated reduction of $IrCl_6^{2-}$ to $IrCl_6^{3-}$ on the aqueous side of the interface, as depicted by the following reaction:

$n\mathrm{IrCl_6^{2-}}$ (aq) + nPy (DCB) → $n\mathrm{IrCl_6^{3-}}$ (aq) + $(\mathrm{Py})_n$ (s) + $n\mathrm{H^+}$ (aq) (5.1)

where *n* represents an oligomeric pyrrole species. The increase in negative peak current on reverse scan can be attributed to the transfer of the organic electrolyte anion, $\mathrm{TPBCl^-}$ from the interfacial polymer to the organic phase along with proton transfer. In order to study the influence of potential cycling on the PPy film morphology, cyclic voltammograms with 25, 50, and 75 cycles were applied. Additionally, another PPy film was prepared by potential steps method.

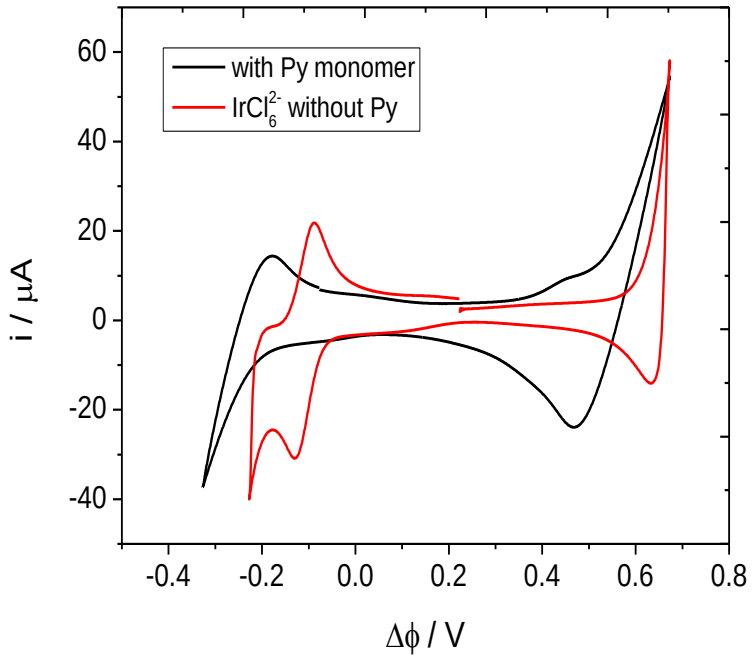

Figure 5. 5. Cyclic voltammogram recorded in the presence of both pyrrole and $\mathrm{IrCl_6^{2-/3-}}$ redox couple (black curve). For comparison, the cyclic voltammogram recorded in the presence of only $\mathrm{IrCl_6^{2-/3-}}$ is shown (red curve). Scan rate: 0.1 V $\mathrm{s^{-1}}$.

In Figure 5.6(a-c), the last CV recorded for each polymerisation reaction is compared with that measured using only the supporting electrolytes (cell 1). The current response in the presence of the PPy film is seen to be much higher,

particularly at the positive end of the potential window in comparison to the blank response, suggesting an increase in electro-activity of the liquid/liquid interface. It is also evident that the polymerisation CVs obtained for the 25 and 75 cycles protocols exhibit the "nucleation loop" or "trace crossing" (*i.e.* current on the reverse scan being higher than that on the forward scan) feature commonly observed for electrochemical phase formation, specifically, this feature has recently been observed at the liquid/liquid interface for the growth of polyterthiophene.[278] In the case of the liquid/liquid electropolymerisation, it has been suggested that the "nucleation loop" could result from the presence of chemically produced polymer/oligomer at the interface that can act as nucleation site or due to an increase in interfacial area.[278] Although the nucleation loops were observed for the electropolymerisation employing 25 and 75 cycles and in every scan, the absence of this effect when 50 cycles were used did not hinder the growth of the PPy film (see SEM characterisation, Figure 5.8b).

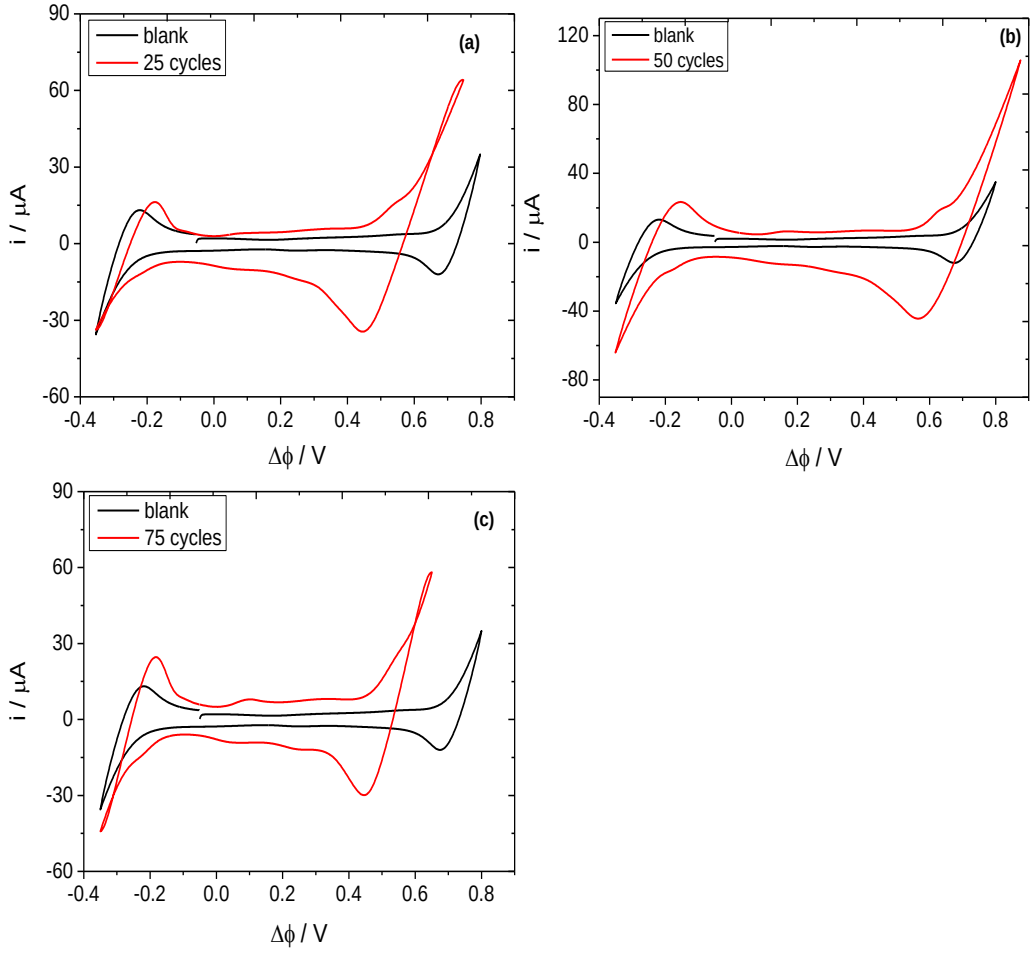

Figure 5. 6. Cyclic voltammogram response recorded at water/DCB interface in the presence of only the supporting electrolytes (black curve) and for the electropolymerisation of pyrrole (red curve) applying (a) 25 (b) 50 and (c) 75 cycles. Scan rate: 0.1 V s^{-1}.

5.4.1 SEM and Raman Characterisation of PPy Prepared at the Water/DCB Interface

The PPy films formed at the ITIES were transferred to previously cleaned Si/SiO_2 substrates. The transferred films were seen by the naked eye to exhibit continuous surface coverage on the Si/SiO_2 substrates. Firstly, Raman spectrocospy was employed to characterise the deposited PPy films. The main features of the PPy Raman spectra shown in Figure 5.7 (marked by asterisks) were assigned according to the literature[290] as follows: the ring deformation (933 cm^{-1}), the C–H in plane bending (984 cm^{-1}), the C–C backbone stretching (1318 cm^{-1}), the C=C backbone

stretching (1562 cm^{-1}) vibration modes for the neutral form; and the C–H in-plane bending (1048 cm^{-1}), N–H in-plane bending (1254 cm^{-1}), C–C backbone stretching (1333–1415 cm^{-1}), C=C backbone stretching (1587–1589 cm^{-1}) for the cationic form. The presence of both the neutral (which is in resonance with the 532 nm excitation laser) and cationic forms indicates that the prepared PPy films were partially doped. The presence of partially doped PPy suggests that the organic anion, $TFPB^-$, is incorporated into the polymeric film. $TFPB^-$ also possesses Raman features in the same region as the PPy film, with its main peaks[291] overlapping with those of PPy, specifically, the peaks around 1000 cm^{-1} and 1350 cm^{-1}. Additionally, the weak signal around 650 cm^{-1} can be attributed to the organic anion.[291]

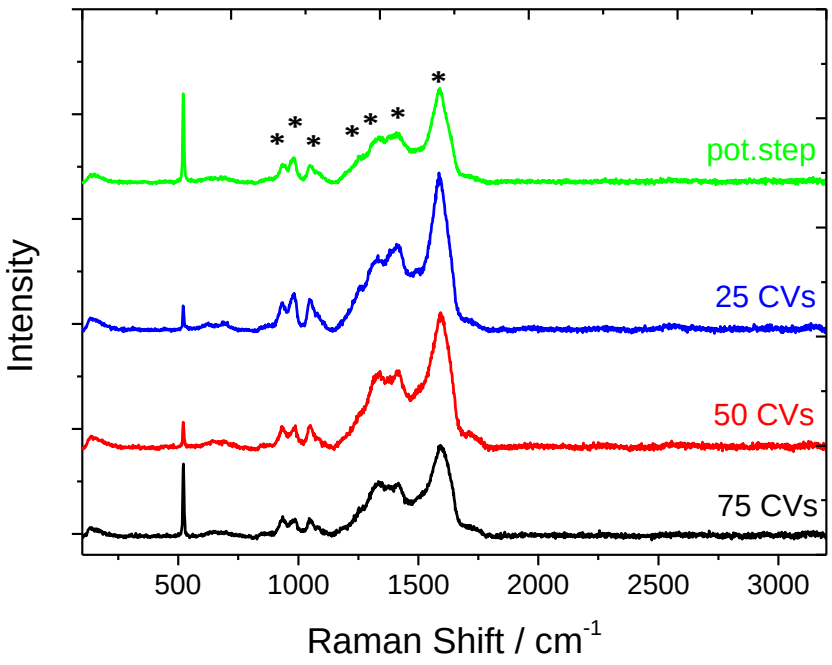

Figure 5. 7. Raman spectra of the PPy films prepared at water/DCB interface by four different dynamic electropolymerisation protocols: CVs at 0.1 V s^{-1} scan rate with 25, 50, and 75 cycles using the potential range –0.35 V to 0.87 V and by using multiple potential steps: 0.6 V, 0.09 V (open circuit potential, OPC), 0.7 V, 0.09 V and 0.8 V for 120 s, 30 s, 120 s, 30 s and 120 s, respectively. The Raman spectra were obtained at 532 nm excitation wavelength and the Raman signals associated with the PPy are marked with asterisks.

Next, the morphological features of the deposited PPy films were analysed by SEM (Figure 5.8). As can be seen from the SEM images, the extent of surface coverage increases with the number of potential cycles used for the electropolymerisation of the PPy, which is as expected. Moreover, there is a clear difference in the morphologies of the PPy films deposited using 25 (Figure 5.8a), 50 (Figure 5.8b), and 75 (Figure 5.8c) CV cycles. The initial deposits are globular, and consist of more discrete particles, whereas with cycling the structure becomes more coherent, *i.e.* the PPy film in Figure 5.8c is built up from layers/flakes. In comparison, when potential steps were used to prepare the PPy film, a more globular structure was achieved (Figure 5.8d).

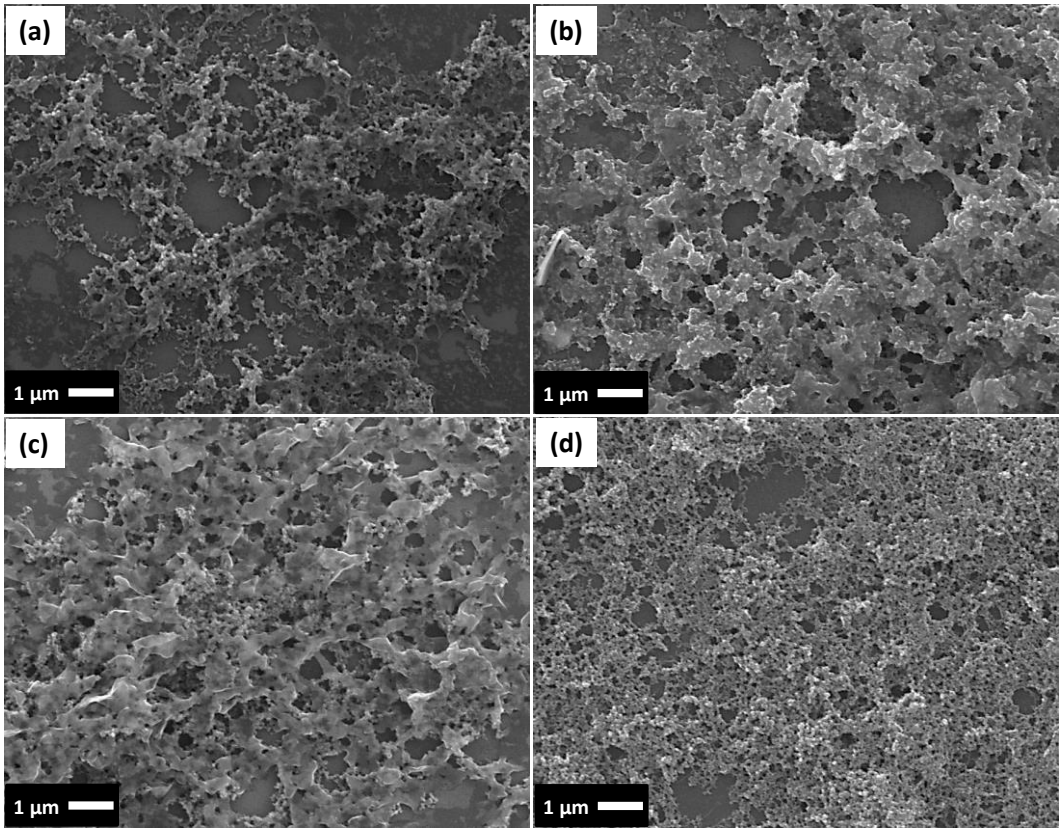

Figure 5. 8. SEM images showing the morphologies of the deposited PPy films prepared at water/DCB interface by CVs at 0.1 V s^{-1} scan rate with (a) 25 cycles (b) 50 cycles (c) 75 cycles, and by (d) multiple potential steps method. Charge passed was estimated to be 0.37 C, 0.84 C, 1.37 C and 0.3 C for PPy film shown in a-d, respectively.

5.5 Preparation of SWCNT/PPy Composite at Water/DCB Interface

Arc discharge SWCNTs were employed for the work presented in this chapter. The nanotubes were dispersed in DCB at a concentration of ~ 6 mg L^{-1} and then assembled at the water/DCB interface by sonication, as previously described in chapter 4. The density of SWCNT was estimated as 8.67 µg cm^{-2} assuming that all the previously dispersed SWCNT were assembled at the interface.[100] After the assembly was completed (sonicated cells were typically allowed to stand for 12 h), the Py monomer and the $IrCl_6^{2-}$/ $IrCl_6^{3-}$ redox couple were introduced into the organic and the aqueous phase, respectively (Scheme 1). Cyclic voltammetry with 50 cycles at 0.1 V s^{-1} scan rate was employed for the electropolymerisation of the Py in

the presence of the adsorbed SWCNTs, as this preparation protocol was found to form PPy with optimised film structure; changes in morphology on going to 75 cycles had no much difference. During the reduction of the $IrCl_6^{2-}$ to $IrCl_6^{3-}$ on the aqueous side of the interface, the oxidation of the Py occurred through the assembled SWCNT layer on the organic side of the ITIES, by analogy with similar redox reactions at the SWCNT-modified ITIES, *e.g.* Pd electrodeposition.[99] As before, the last CV recorded during the polymerisation reaction is compared with that measured in the absence of the Py monomer (Figure 5.9) to enable the increase in current to be observed.

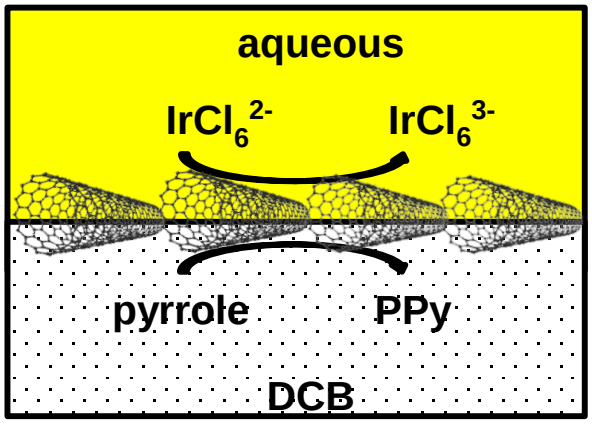

Scheme 5.5. Illustration of the preparation process of SWCNT/PPy composite at the water/DCB interface.

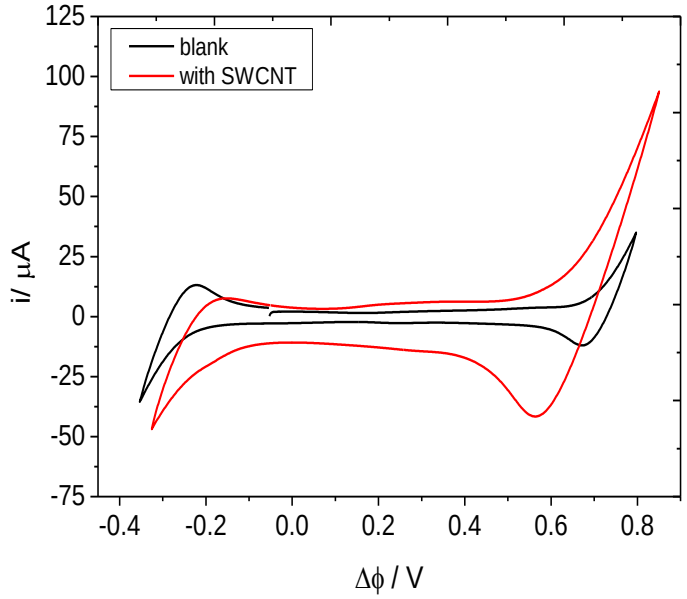

Figure 5. 9. Cyclic voltammetric response obtained at the water/DCB interface for the electropolymerisation of pyrrole in the presence of adsorbed SWCNTs (redline) compared to a blank response (black line). Scan rate used was 0.1 Vs^{-1}

5.5.1 SEM and AFM Analysis of the SWCNT/PPy Composite

Figure 5.10 shows the SEM and AFM images of the SWCNT/PPy composite deposited on Si/SiO_2 substrate. Also shown in the Figure is the SEM image of SWCNT assembled at the water/DCB interface in the absence of both the Py monomer and aqueous redox couple. The SEM image of the pristine SWCNT indicated that (Figure 5.10c) the interfacially assembled nanotubes were bundled either due to the effect of transfer to a solid substrate or because of the presence of BTPPATFB electrolyte in the organic phase, since the organic electrolyte can cause aggregation of the SWCNT even before their interfacial assembly, as shown in chapter 3. In the SEM image of the composite, the PPy forms a continuous film over the assembled SWCNTs, forming a well-structured coating on the Si/SiO_2 substrate. The nanotubes embedded in the polymer matrix appeared thinner or more individualized than pristine interfacial nanotubes, suggesting that the drying process also contributes significantly to the bundling event. The AFM image (Figure 5.10d)

of the composite was used to estimate the thickness of the SWCNT/PPy, which was found to be 31.8 ± 0.3 nm. A closer look at the AFM image revealed that the composite is composed of regions of agglomerated PPy particles in addition to polymer embedded SWCNTs.

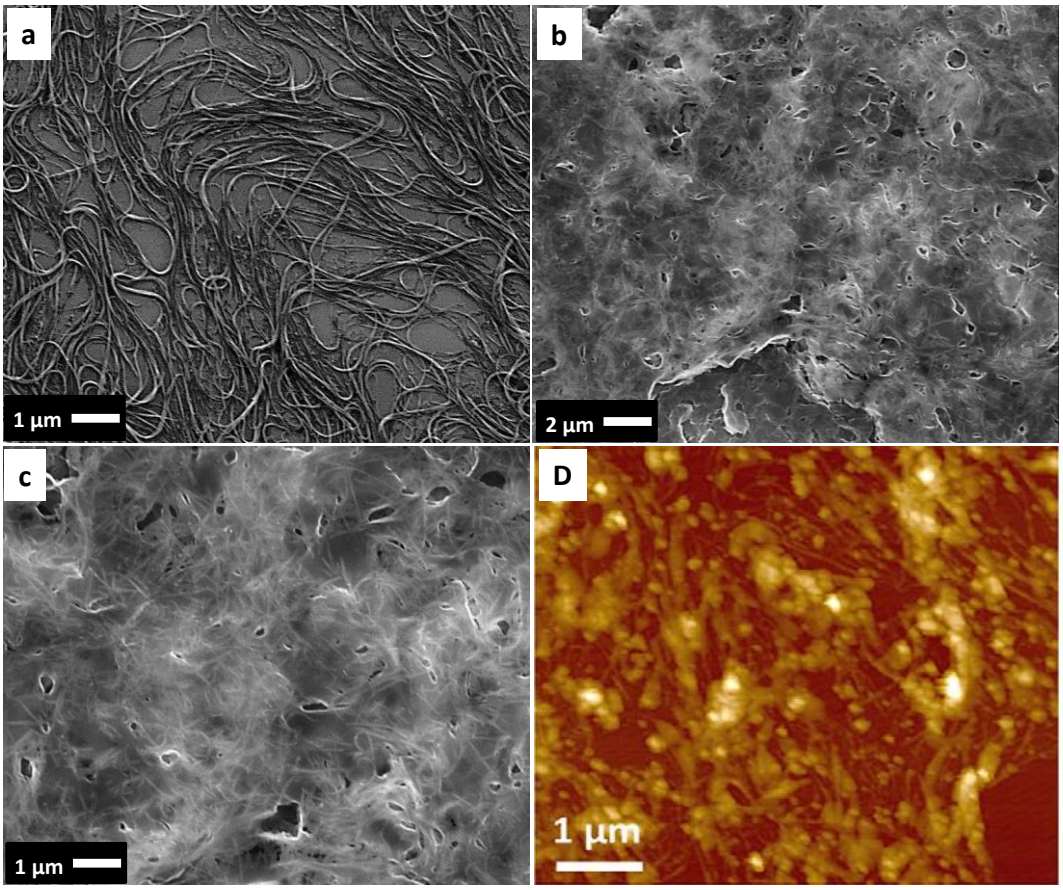

Figure 5. 10. SEM images of (a) pristine interfacial SWCNTs, (b) SWCNT/PPy composite and (c) magnified view of SWCNT/PPy composite. (d) AFM image of the composite material.

5.5.2 Raman Analysis of the SWCNT/PPy Composite

Raman characterization was also performed on the SWCNT/PPy composite, as this technique is widely used to confirm the successful preparation of CNT/CP or CP/graphene[292, 293] composites as well as to probe any possible interaction between

the two. Figure 5.11 shows the Raman spectra of the SWCNT/PPy composite collected using the 532 nm laser excitation wavelength. The main Raman features of SWCNTs, the G-, D- and RBM bands, as discussed in chapter 3, dominate the Raman signals seen in the spectrum of the SWCNT/PPy composite material. As the PPy Raman features are quite weak in comparison[294] and coincide with the D- and G- bands of the SWCNT, it is difficult to observe clearly the Raman bands of PPy, as observed previously for the neat polymer. Nevertheless, the following vibration modes for the neutral form of PPy, marked by asterisks, can still be seen in the composite spectrum (left inset): the ring deformation (942 – 1005 cm^{-1}), the C–H in-plane bending (1080 – 1121 cm^{-1}), as well as the C–C backbone stretching (1243 – 1275 cm^{-1}), thus confirming the presence of both materials. Moreover, the small up-shift of the SWCNT G^- mode from 1569 cm^{-1} in the pristine SWCNT (black curve) to 1572 cm^{-1} in the SWCNT/PPy composite (red curve) indicating that there is a charge transfer interaction between the two components in the composite material. Similar observations has been reported previously in the literature.[295] The properties of the resulting carbon nanotubes/conducting polymer composites would be dependent on the semiconducting or metallic nature of the SWCNT and on the properties of the conducting polymer used.[295, 296] Therefore, by selecting an appropriate type of SWCNT and conducting polymer, it is possible to tune the properties of composites. The *in-situ* electrochemical methods for functionalising carbon nanomaterials with CPs offer alternative possibilities to control the structural properties of the deposited polymer and, thus, the composite material.

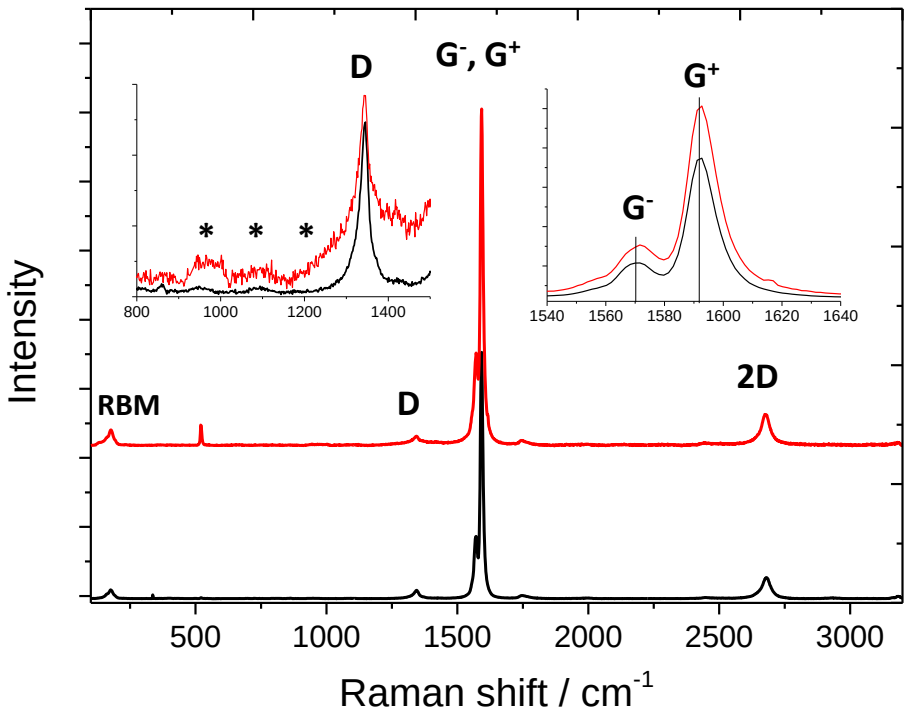

Figure 5. 11. Raman spectra of SWCNT/PPy film (red line) prepared at water/DCB interface by 50 CV cycles at 0.1 V s^{-1} scan rate. The Raman signals associated with the PPy are marked with asterisks. For comparison the Raman spectra of pristine SWCNT is also shown (black).

5.6 Conclusions

In this chapter, we described the successful electropolymerisation of pyrrole at the water/DCB interface, in the absence and in the presence of interfacial SWCNTs, adsorbed from the DCB phase is described. The different potentiodynamic methods applied in film preparation affected the morphology of the resulting PPy film, with an increase in the number of CV cycles for the polymer growth yielding better surface coverage after transfer to the solid substrate. Carbon nanotube-based PPy nanocomposites were obtained using the optimized polymerisation conditions. Evidence of the formation of the SWCNT/PPy layer was derived from its transfer to solid substrates and subsequent microscopic and spectroscopic analysis. The resultant composite structure showed that the SWCNTs were embedded in the PPy

matrix, *i.e.*, the Py monomer was polymerized around the SWCNTs. The Raman data, based on changes in the intensity and position of the nanotube's D- and G-bands, indicated a partial doping of the SWCNTs, caused by the formation of the composite material. The applied dynamic preparation of SWCNT/PPy at the ITIES allows for PPy to grow uniformly on the surface of SWCNTs, and is suitable for the preparation of free-standing, conductive and continuous SWCNT/PPy films, which are immediately transferable, compared to the traditional electropolymerisation procedures using carbon nanotube networks grown or assembled at solid substrates (*e.g.*, vertically aligned CNT "forest"). The proposed electropolymerisation method therefore represents a new approach for the preparation of carbon-nanomaterial/CP composites, which could be extended to the production of metal NP/CP composites, using metal precursors in the aqueous phase. Fabrication of novel and modified, functional electrodes is also possible by transferring these composite layers to a solid substrate.

Chapter 6

Aggregation Kinetics of MoS_2 Dispersed in 1,2-dichlorobenzene

6. Introduction

Liquid-phase exfoliation of layered transition metal dichalcogenides (TMDs), such as MoS_2, is widely considered as a viable route to produce atomically thin flakes of these layered materials in large quantities.[56, 68, 78] Although there are many forms of this approach, as discussed in chapter one (section 1.2.1), solvent exfoliation has received considerable attention due to its simplicity, absence of a third phase component (*e.g.*, a surfactant) and preservation of the pristine nature of the MoS_2 nanosheets.[77, 89, 297] Similar to CNTs, a range of non-aqueous solvents, including *N*-methyl-2-pyrrolidinone (NMP), *N*-cyclohexyl-2-pyrrolidinone (CHP) and 1,2-dichlorobenzene (DCB) have been demonstrated to be effective in exfoliating and dispersing MoS_2.[77, 79, 89] It was suggested, in these previous studies, that good solvents are those with a surface energy which matches that of the MoS_2 nanosheets (~70 mJ m^{-2}).[79, 89] However, as in the case of dispersions of CNTs[190] and graphene,[194] liquid phase dispersions of MoS_2 are not thermodynamically stable,[89] though dispersions prepared in NMP and DCB were found to be stable for more than one month.[79] Therefore, understanding their kinetic stability is important for both fundamental investigation and practical applications.

To date, little is known about the effects of other dispersion components, such as the presence of electrolyte, which may have substantial influence on dispersion stability as well as the properties of the dispersed MoS_2 nanomaterials.

The recent work by Li et al[298] is the only study reporting the aggregation behaviour of MoS_2 in some details. In this work,[298] salt-induced aggregation and sedimentation of the MoS_2 dispersed in aqueous surfactant solution was monitored by optical absorption. It was suggested that the aggregation of the MoS_2 initially resulted in the increase in both the thickness and length of the MoS_2 flakes before subsequent sedimentation of the particles out of the solution.[298] In other related studies, the stability of aqueous MoS_2 dispersions, which were prepared by different methods including, chemical modification,[299] surfactant-stabilisation[81, 90] and by simply increasing the temperature of the solution during exfoliation,[300] were studied through the measurement of the zeta potential of the dispersed particles. What is common in all these previous works was that they all suggested that the aqueous dispersions of MoS_2 were stabilised by electrostatic repulsion between the charged MoS_2 particles. On the contrary, no literature report has been found with regards to the contribution of electrostatic repulsion to the stability of MoS_2 particles in non-aqueous solvents.

However, as described in chapter 3 and demonstrated by several recent studies,[162, 190-192, 194] electrostatic repulsion can play an important role in stabilising non-aqueous dispersion of 1D and 2D nanomaterials. Often, the aggregation of these types of colloidal suspensions is described using the DLVO theory.[192, 194, 301] According to this theory, colloidal particles in a suspension interact with each other through electrical double layer (EDL) repulsion forces, which prevent the particles from aggregating, and van der Waals attractive forces, which tend to bring the dispersed particles together. On the basis of this, colloidal dispersions are expected to remain stable, at least for some time, if the EDL forces dominate. Thus, one of the commonest methods used to understand the stability of these types of dispersions is by measuring their resistance to coagulation in the presence of added electrolyte. By

increasing the amount of electrolyte in the dispersion, the EDL barrier is reduced progressively until particles aggregation is solely controlled by diffusion. At this point, the EDL barrier is eliminated and the concentration of electrolyte that causes this is known as the critical coagulation concentration (CCC).

In this chapter, the aggregation kinetics of MoS_2 dispersed in 1,2-dichlorobenzene (DCB) was studied in the presence of different concentrations of organic electrolyte, bis(triphenylphosphoranylidene) ammonium tetrakis (4-chlorophenyl) borate (BTPPATPBCl). The measured aggregation data was used to derive stability curves, from which the CCC was determined, demonstrating that electrostatic forces are important for the stabilisation of the MoS_2 nanosheets dispersed in DCB.

6.1 MoS_2 Exfoliation in 1,2-dichlorobenzene

MoS_2 dispersion was produced by solvent phase exfoliation of the bulk MoS_2 powder using bath ultra-sonication in DCB. The resulting dispersion was further processed by centrifugation to remove non-exfoliated or very thick MoS_2 particles. The detailed experimental procedure can be found in section 2.2.1 (experimental chapter). The choice of DCB (ε_r= 10.36)[6] as the exfoliation solvent was based on its common use in liquid/liquid electrochemistry studies and, also, because it has been demonstrated to effectively exfoliate and stabilise MoS_2 dispersion for at least one month.[79, 101] In Figure 6.1 the photograph of the processed MoS_2 is shown. The greenish-yellow dispersion was stable for several months in the absence of any added electrolyte.

Figure 6. 1. Photographs of MoS_2 illustrating the different dispersion processing stages.

6.2 MoS_2 Dispersion Characterisation

6.2.1 UV-Vis Absorbance and Extinction Coefficient Measurements

Figure 6.2 shows the UV-Vis absorption spectra of MoS_2 dispersions in DCB at different concentrations. The spectra exhibit characteristic absorption peaks at 670 nm (1.85 eV) and 610 nm (2.03 eV), designated as A and B, respectively.[73, 77] These peaks arise from the interband excitonic transitions at the *K* point of the Brillouin zone of MoS_2 and their presence suggests that the as-prepared dispersion is composed of pristine 2H-MoS_2 layered material.[73, 302]

In order to allow UV-Vis absorption spectroscopy to be used to determine the concentration of the MoS_2 dispersions, the extinction coefficient (α) was estimated, as previously described in chapter 3, for the case of SWCNTs. Here, the absorbance values of the different concentrations of MoS_2 dispersion were recorded at 670 nm for the calibration. Figure 6.3 shows the calibration graph obtained. The extinction coefficient (α) was estimated from the slope of the calibration graph and

by applying the Beer-Lambert law ($A = \alpha Cl$). The value of α calculated (1060 ± 42 mL mg^{-1} m^{-1}) is very similar to that reported in the literature (1020 ± 42 mL mg^{-1} m^{-1}) for MoS_2 dispersion in NMP at the same wavelength.[77]

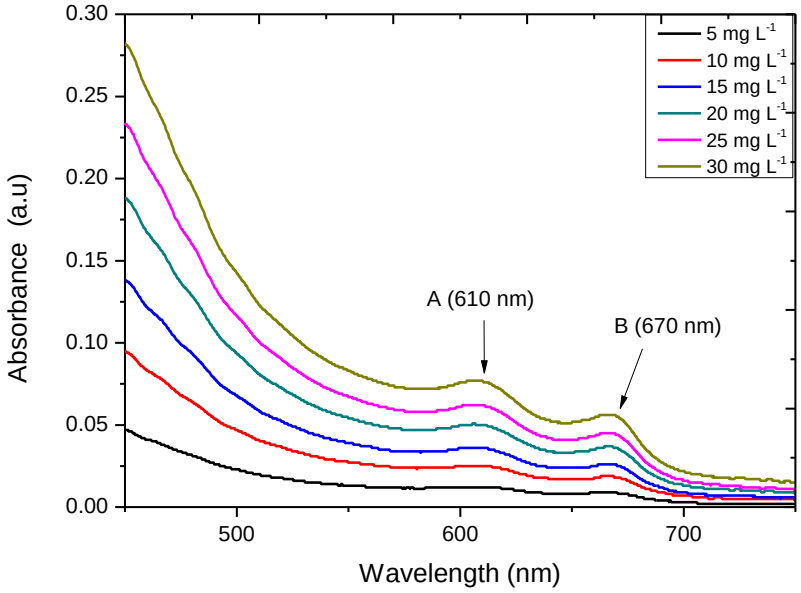

Figure 6. 2. UV-Vis absorption spectra of MoS_2 dispersion in DCB at several dilutions.

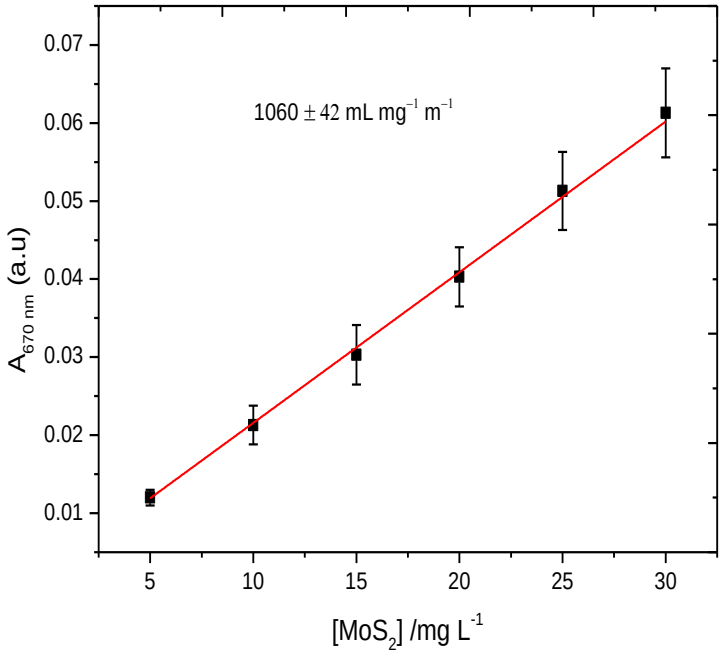

Figure 6. 3. Plot of absorbance at 670 nm as a function of MoS_2 dispersion concentration.

6.2.2 AFM and SEM Characterisation

The as-prepared MoS_2 dispersion was analysed using SEM and AFM in order to determine both the thickness and the lateral dimensions of the exfoliated nanosheets. The same sample was used for both SEM and AFM measurements and was prepared by spin coating few drops of the MoS_2 dispersion (~9.3 mg L^{-1}) onto a previously cleaned Si/SiO_2 wafer. Figure 6.4 (a-b) shows representative SEM and AFM images of the exfoliated MoS_2. Both images show a number of objects with a range of size distribution. The lateral dimensions of the observed objects was estimated from both the SEM and AFM images by manually measuring the length of the particles along their major axis, whilst the thickness was estimated from only the AFM image, through height analysis. Figure 6.4 (c-d) presents the histograms of length and thickness distributions of the imaged MoS_2 dispersion. It can be seen, from the length histograms that the observed objects exhibit a wide variety of sizes, which range from ~ 50 nm to about 3µm. But the majority of the particle had lengths

in the range 50 nm to approximately 400 nm, which is expected considering the high centrifugation speed (12000 rpm) used to prepare the dispersion.

The thickness of the imaged objects is also seen to vary from about 1.5 to 30 nm, with the average thickness estimated to be 14.4 nm (~20 layers). It is reported that the height of a monolayer MoS_2 deposited on a SiO_2 wafer is approximately 0.8–1.2 nm.[77, 303] Although this value differs from the theoretical thickness of 0.615 nm for a single layer of MoS_2,[304] the difference is commonly attributed to adsorbed impurities[76, 303] that might be present on the SiO_2 substrate and/or the result of interaction between the MoS_2 monolayer and the SiO_2 substrate.[76] In the study presented here, the population of the observed objects with a thickness less than 5 nm, which potentially corresponds to MoS_2 nanosheets with $\leq$ 5 layers was quite small (only about 7%). No evidence of monolayer formation was observed.

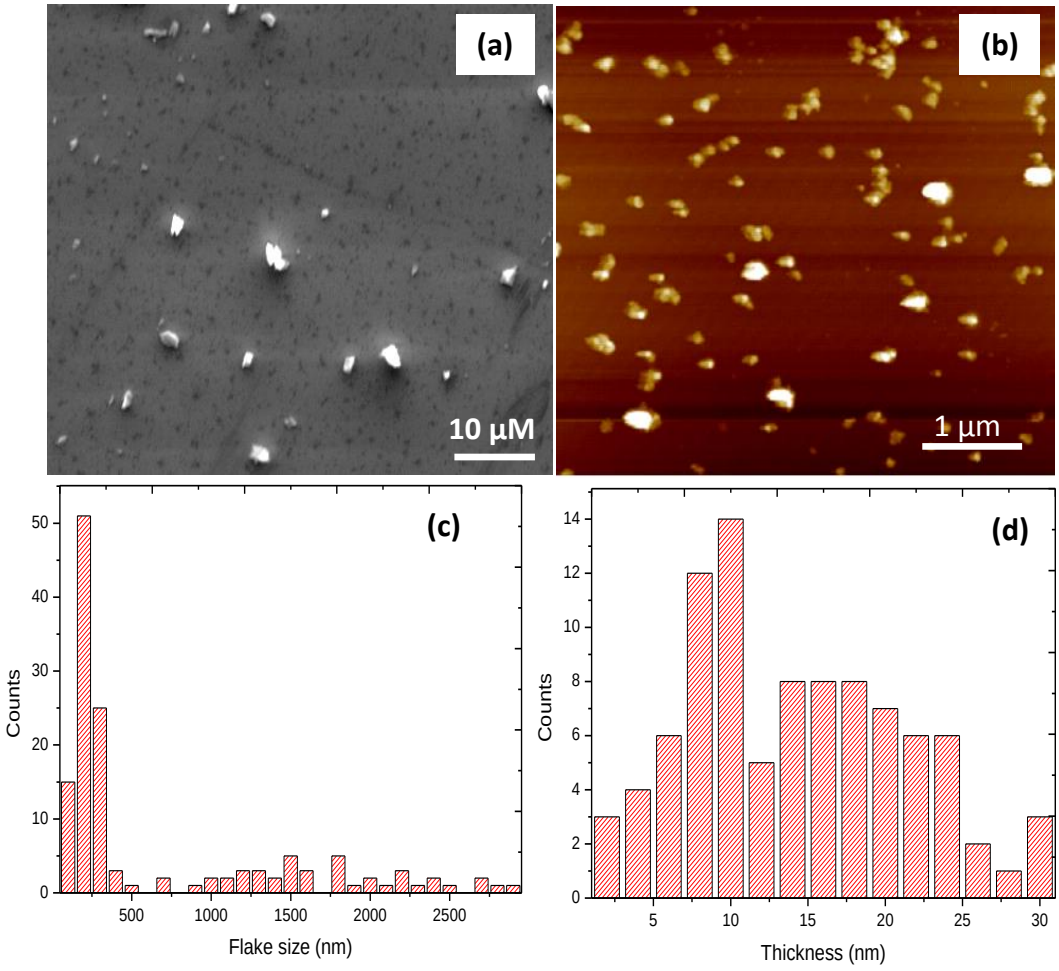

Figure 6. 4. (a) SEM and (b) AFM images of solvent-phase exfoliated MoS_2 in DCB deposited on a Si/SiO_2 wafer. (c–d) Histograms of the counted objects length and height (thickness) respectively.

6.2.3 Ultra-sonication Induced Sonopolymer Formation

The statistics presented in Figure 6.4 assumed that all the objects observed in the SEM and AFM images were MoS_2. However, it has been reported previously that ultra-sonication causes DCB to decompose and polymerise.[47, 305] In sonochemistry, it is well known that ultra-sonication in liquids produces cavitation bubbles, which collapse rapidly generating a local hot spot where the local temperature can be higher than 5000 K.[306-308] The effect of this is that organic solvents including benzene and haloaromatics can be decomposed into smaller units at the hot spot during the primary reaction stage.[309] Because the temperature of the liquid surrounding the hot

spot decreases rapidly after the collapse of the cavitation bubble (quenching step),[308, 309] the smaller decomposition products develop into a more stable primary products, such as oligomeric species, molecular radicals and polymers (also called sonopolymer).[309, 310] The radicals can further react with solvent molecules or another radical to form a secondary product.[309] In the case of DCB, ultrasonic treatment has been observed to produce a change in colour of the DCB from colourless to yellow and to dark brown during extended sonication.[305] This change was ascribed to the decomposition of the DCB, with the reaction products suggested to be mainly bulky sonopolymer (cross-liked polystyrene), which precipitated when the solution was left to stand overnight.[47, 305] In addition, small oligomeric and aliphatic species were also reported to have been formed.[47] Kim *et al.*[47] observed that the low molecular weight oligomers remained in solution even when the sonicated DCB was subjected to an ultracentrifugation at 325000g for 2 h. While the presence of these impurities may be undesirable in some applications, the formation of the sonopolymer has been suggested to aid in the dispersion of SWCNT,[47, 305] exfoliation of graphene[311] and MoS_2.[79] In the case of MoS_2, the sonopolymer is believed to interact only weakly with the exfoliated material and, therefore, does not disrupt the 2H phase of the MoS_2.[79] In order to investigate whether impurities arising from the decomposition of the DCB used in the present exfoliation work contributes significantly or not to the statistics presented in Figure 6.4, pure DCB (colourless) was sonicated under the same conditions as the original dispersion. This treatment resulted in the change of colour of the DCB from colourless liquid to light brown solution (Figure 6.5a). When a few drops of the solution were drop cast onto a Si/SiO_2 wafer and analysed by AFM, large quantity of particles were seen (Figure 6.5b). Statistical analysis (Figure 6.5 c-d) of the observed particles revealed that the decomposition products had

length and thickness in the same range as those found for the exfoliated MoS_2 dispersion. This result suggests that, in addition to MoS_2 particles, significant amount of impurities from the solvent decomposition is also present, which might contribute to dispersion stability, but which also complicates the size analysis of the materials.

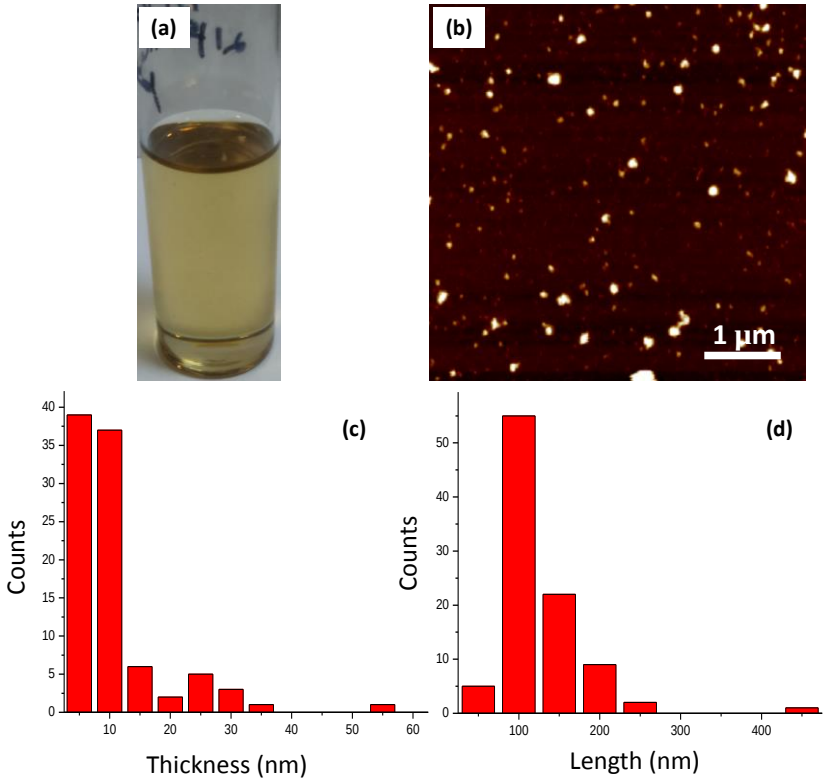

Figure 6. 5. (a) Pure-DCB ultra-sonicated for 12 hrs in a bath sonicator (b) AFM image of the sonicated DCB deposited on a $SiSiO_2$ wafer. (c–d) Histograms of the counted objects thickness and length, respectively.

There are two ways the decomposition of DCB could contribute to the statistics of the MoS_2 size distribution. First, the sonopolymer may coat the MoS_2 nanosheets, leading to an increase in their size. Second, the sonopolymer particles may be present as separate entities, where they will be counted as MoS_2 particles. However, using high angle annular dark field (HAADF) imaging and energy dispersive X-ray (EDX) map of carbon and molybdenum atoms, Yu *et al.*[79] observed that the sonopolymer phase was not associated with the MoS_2 nanosheets. Therefore,

the solvent decomposition products may not have a strong influence on the surface of the MoS_2 nanosheets. The latter point is supported by the effect of electrolyte on the dispersion of MoS_2 in DCB. When 10 mM BTPPATPBCl electrolyte was added to the as-prepared MoS_2 dispersion, the MoS_2 nanosheets were seen to aggregate and sediment out of the suspension after 48 h of standing (Figure 6.6, left). When the UV-Vis absorption spectrum (Figure 6.6, right) of the supernatant was recorded, the characteristic A and B optical absorption peaks were found to have disappeared, suggesting that most of the MoS_2 nanosheets have been coagulated by the electrolyte. It can be observed from the same Figure, that the absorption spectrum of the supernatant is very similar to that obtained for the pure sonicated DCB. Additionally, the colour of the two solutions is almost the same, which suggest that the supernatant is predominantly composed of the DCB decomposition products and that the electrolyte could selectively remove the MoS_2 particles by charge screening.

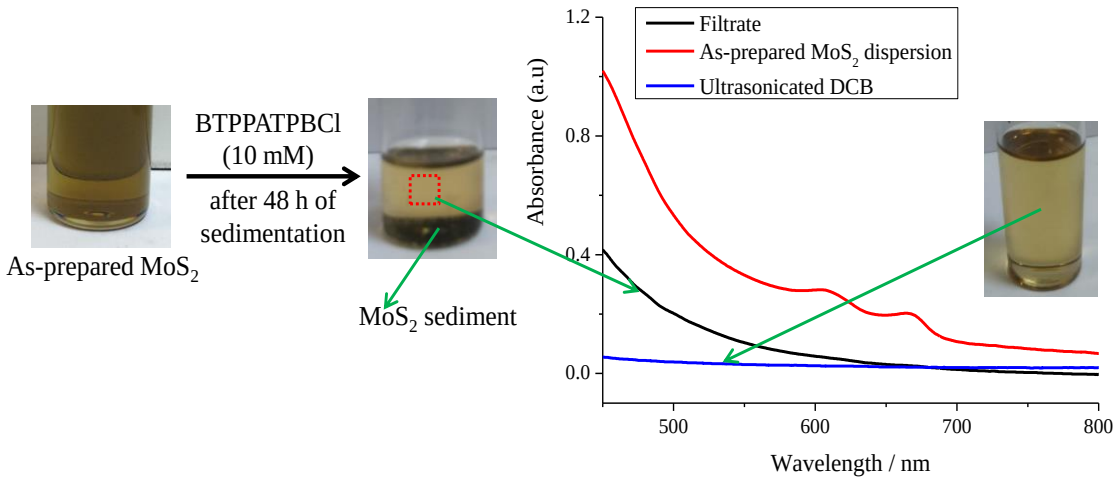

Figure 6. 6. Effect of electrolyte on MoS_2 dispersion in DCB.

6.2.4 Raman Spectroscopy

In order to verify that the particles observed in the AFM and SEM images (Figure 6.4) were composed of MoS_2 nanosheets, Raman spectra were collected at different locations on the sample that was used for the SEM and AFM measurements. Figure 6.7 shows the Raman spectrum of the solvent exfoliated MoS_2 flakes. Also shown in Figure 6.7 is the Raman spectrum of the bulk MoS_2 powder for comparison. The excitation wavelength used to record the spectra was 532 nm. The spectra of both samples showed the presence of two prominent peaks, the E^1_{2g} and the A^1_g. These peaks are characteristic Raman features of 2H-MoS_2 and are commonly used to characterise exfoliated MoS_2.[76] The E^1_{2g} (in-plane) mode is related to the vibrations of the two S atoms in opposite directions with respect to the Mo atom, while the A^1_g mode originates from the out-of-plane vibration of only the S atoms in the opposite directions (see Figure 6.7).[303] The wavenumbers of these peaks and their difference ($\Delta\omega$) with respect to bulk can be used to gain information on the MoS_2 layer thickness (number of layers).[76, 303] The $\Delta\omega$ has been found to increase from around 19 cm^{-1} for a monolayer to about 26 cm^{-1} for bulk MoS_2 crystal.[76, 303]

For the bulk MoS_2 sample, the position of the E^1_{2g} and the A^1_g peaks was found to be 374.2 cm^{-1} and 400.9 cm^{-1}, respectively, which agrees with the values reported in the literature for bulk MoS_2 powder.[312] After exfoliation, both the E^1_{2g} and the A^1_g were seen to redshift to 383.1 cm^{-1} and 407.5 cm^{-1}, respectively. The redshift of both peaks has been observed previously for liquid phase exfoliated MoS_2 flakes and the effect was attributed to sonication.[312] Compared to the bulk MoS_2 powder ($\Delta\omega$ = 26.7 cm^{-1}), a significant decrease in peak-to-peak distance ($\Delta\omega$ = 24.4 cm^{-1}) was observed after exfoliation, which is consistent with a few (3-4) layer MoS_2.[112, 303] The Raman result therefore confirmed the presence of MoS_2 nanosheets

in the sample, as well as the successful exfoliation of the bulk material down to few layers.

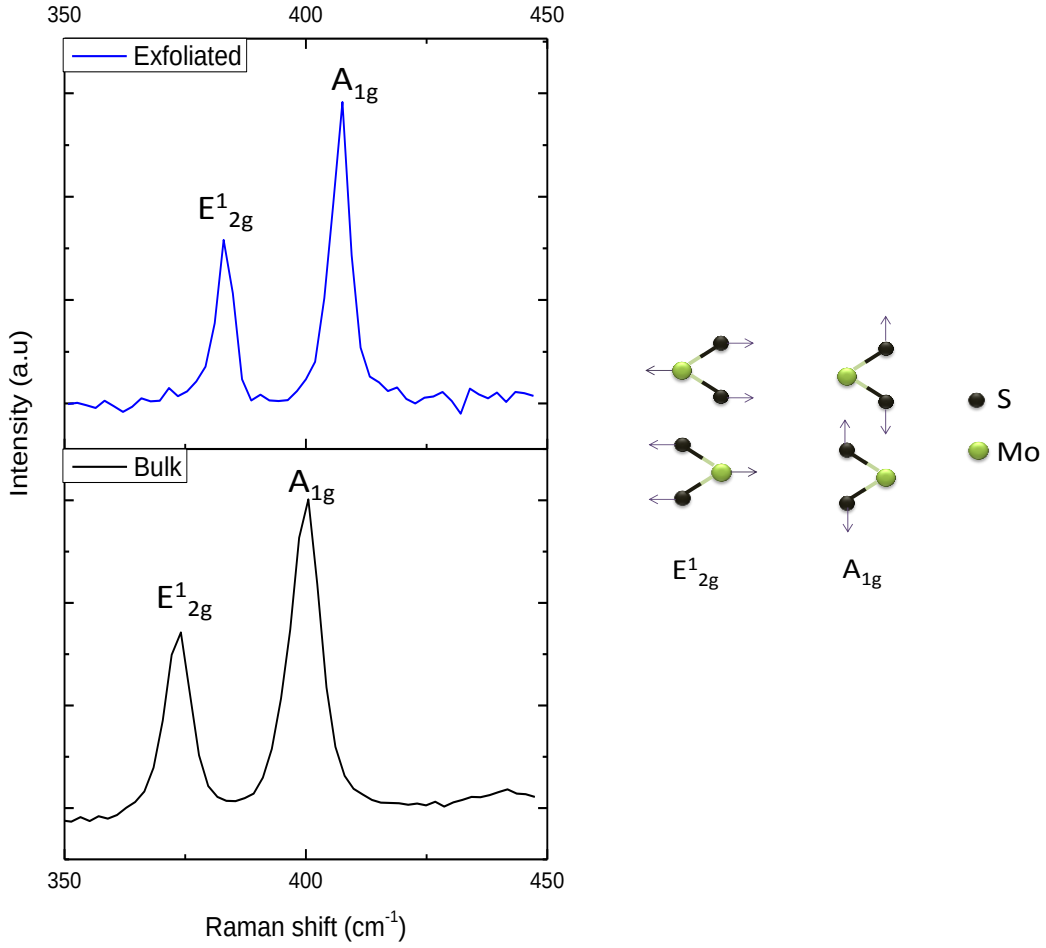

Figure 6. 7. Raman spectra of bulk and solvent exfoliated MoS_2. The two main vibrational modes are schematically shown on the right of the Raman spectra.

6.2.5 Zeta Potential of the MoS_2 dispersion

Zeta potential (ζ) is commonly used to assess the electrical double layer (EDL) properties of colloidal particles in a suspension. The extent of the EDL repulsion can be understood from the magnitude of ζ. Typically, dispersed colloidal particles are considered stable if their ζ value is around or above ±30 mV,[176 174] because of the repulsive electrostatic effect discussed previously.

The zeta potential value of the as-prepared MoS_2 dispersion measured at room temperature (25 °C) was found to be 79.6 ± 1.61 mV. Previously in the literature, values of ζ have been determined only for aqueous MoS_2 dispersions, which ranged from –30 mV for pristine MoS_2 dispersed in water under controlled temperature[300] to –50 mV for chemically exfoliated MoS_2 through lithium intercalation.[299] The charging mechanisms for these systems were believed to be different. For pristine MoS_2, the origin of the charge was attributed to charge polarity in which the S atoms are considered to impart negative surface charge to the MoS_2 sheets with the Mo counter charges remaining inside,[300] while in the case of the chemically exfoliated MoS_2, surface charging is believed to results from the effect of the Li intercalation reaction.[85]

In general, in the absence of an added electrolyte, particle surface charging can occur due to dissociation of surface ionic groups, preferential dissolution or electron transfer between the particle and the dispersing medium. The actual mechanism responsible for charging in MoS_2 non-aqueous dispersion is currently unknown, but could result from either dissociation of surface groups, which could arise from impurities or through electron transfer, as previously observed for both graphene and carbon nanotubes.

6.3 Aggregation Studies

6.3.1 Dissociation of BTPPATPBCl in DCB

Before measuring the effect of electrolyte on dispersion stability, it is important to know the extent to which the electrolyte dissociates in the solvent of interest. Therefore, conductivity measurements were used to assess the dissociation of the BTPPATPBCl electrolyte in DCB into its component ions, $BTPPA^+$ and

TPBCl⁻. The measured conductivity data were fitted to Kohlrausch's law (given by equation 6.1), as shown in Figure 6.8.

$$\Lambda_m = \Lambda_m^0 - K\sqrt{[\text{BTPPATPBCl}]} \qquad 6.1$$

where Λ_m and Λ_m^0 are the molar and the limiting molar conductivities, respectively, while *K* is an empirical constant. Over the concentration range of 0.6 mM to 2.4 mM shown in Figure 6.8, the molar conductivity of the BTPPATPBCl in DCB can be seen to decrease with increase in the square root of electrolyte concentration, which is consistent with the behaviour of a strong electrolyte, which the salt can be assumed to be over this low concentration range. The limiting molar conductivity of the electrolyte was estimated and is shown in the same Figure. As the electrolyte concentrations used for the aggregation studies were lower (1 mM to 2 µM), it is expected that the majority of the electrolyte is dissociated at these concentrations.

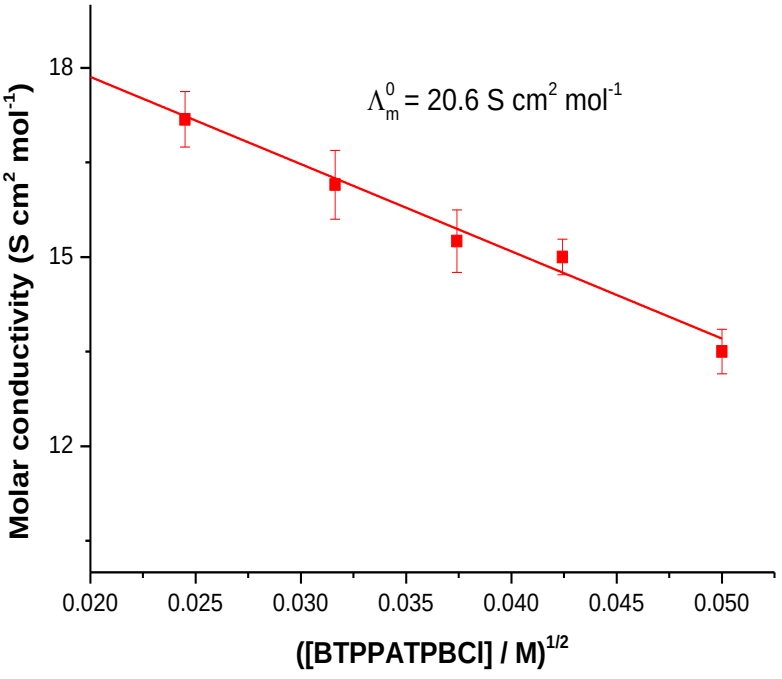

Figure 6. 8. Molar conductivity of BTPPATPBCl in DCB as a function of the square root of the electrolyte concentration. The limiting molar conductivity of the electrolyte derived from fitting the data to the Kohlraush's law for strong electrolyte is also shown in the graph.

6.3.2 Aggregation of Dispersed MoS_2 in Electrolyte Solution

The aggregation kinetics of exfoliated MoS_2 stably dispersed in DCB was studied in the presence of different concentrations (2–1000 μM) of the organic electrolyte (BTPPATPBCl) using the sedimentation procedure described in the literature.[192] Briefly, the procedure involves measuring the optical absorption of the MoS_2 supernatant obtained after centrifuging the dispersion containing a fixed amount of the electrolyte for a given period of time. The detailed experimental procedure can be found in chapter 2. In the absence of any added electrolyte, no sedimentation of the MoS_2 particles occurred (Figure 6.9) during the 20 min centrifugation time used for the aggregation studies in the presence of electrolyte. Therefore, any sedimentation of the dispersed MoS_2 can be attributed to the effect of added electrolyte.

Figure 6.10 shows the aggregation profiles of the MoS_2 particles dispersed in DCB at several electrolyte concentrations. It is clear that the presence of electrolyte causes the dispersed MoS_2 particle to sediment with time. Previous studies have shown that the concentration of the sedimenting phase in a dispersion decreases exponentially with time.[89, 194, 313] The aggregation data shown in Figure 6.9 could be fitted to the following single exponential decay equation:[194]

$$[\mathrm{MoS_2}] = [\mathrm{MoS_2}]_{unst}\, e^{-kt} + [\mathrm{MoS_2}]_{\infty} \qquad (2)$$

where $[\mathrm{MoS_2}]_{unst}$ relates to the concentration of the unstable fraction (destabilised by the electrolyte) and $[\mathrm{MoS_2}]_{\infty}$ describes the concentration of kinetically stable fractions of the dispersed MoS_2 over the time period longer than that studied here; *t* is the aggregation time and *k* is the aggregation rate constant. The single exponential decay fits are shown as solid lines in Figure 6.10, while Figure 6.11 shows the

aggregation rate constant of MoS_2 particles in DCB, determined from the fits of the aggregation data plotted as a function of electrolyte concentration. It is seen that although the absolute amount of MoS_2 always decreased exponentially with time, the magnitude of the aggregation rate was, however, dependant on electrolyte concentration. According to the DLVO theory, there are two distinct particle aggregation regimes: reaction-limited colloid aggregation regime (RLCA) and diffusion-limited colloid aggregation regime (DLCA). In the RLCA regime, an increase in the electrolyte concentration compresses the EDL around each particle, which leads to a reduction in the energy barrier against particle. This aggregation regime is, therefore, sensitive to electrolyte concentration. On the other hand, in the DLCA regime, the electrolyte concentration is sufficiently high to effectively eliminate the electrostatic energy barrier and aggregation is controlled solely by particle diffusion. Experimentally, the DLCA regime is considered to be attained when further increases in electrolyte concentration do not result in increased aggregation rate. It is clear from Figures 6.10 and 6.11 that, at lower BTPPATPBCl concentrations ($\leq$ 20 μM), any increase in BTPPATPBCl concentration results in a corresponding increase in MoS_2 aggregation rates. However, at higher BTPPATPBCl concentrations, only a slight change in the aggregation rates can be observed with an increase in BTPPATPBCl concentration. The observed behaviour is consistent with the DLVO-type interactions, with the two regimes predicted from the theory clearly visible in Figure 6.11.

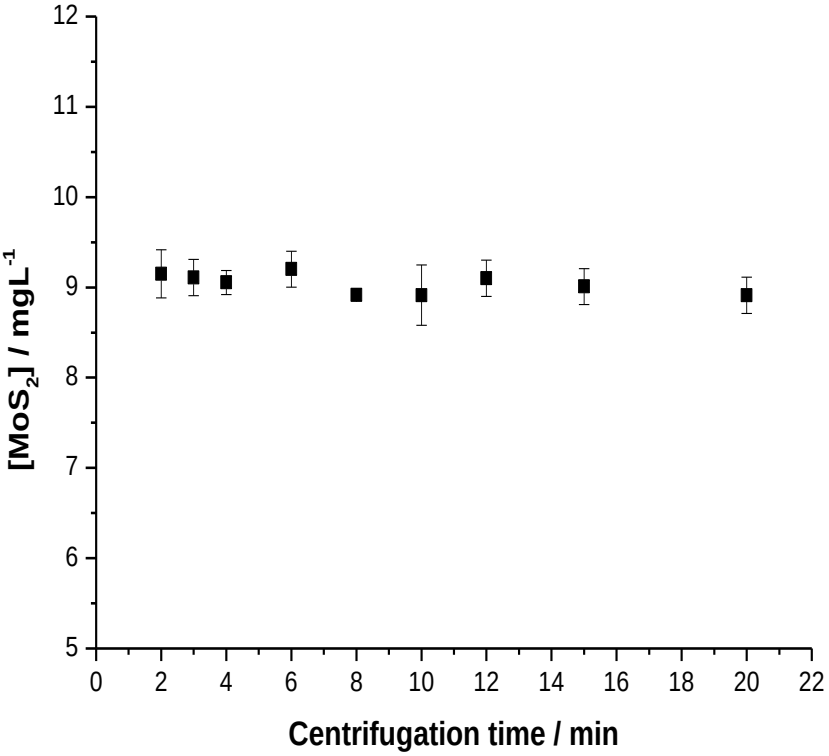

Figure 6. 9. Concentration of MoS_2 as a function of sedimentation time showing that no sedimentation of the MoS_2 particles occurred during centrifugation of the control samples at 8000 rpm. Initial dispersion concentration was 9.3 mg L^{-1}.

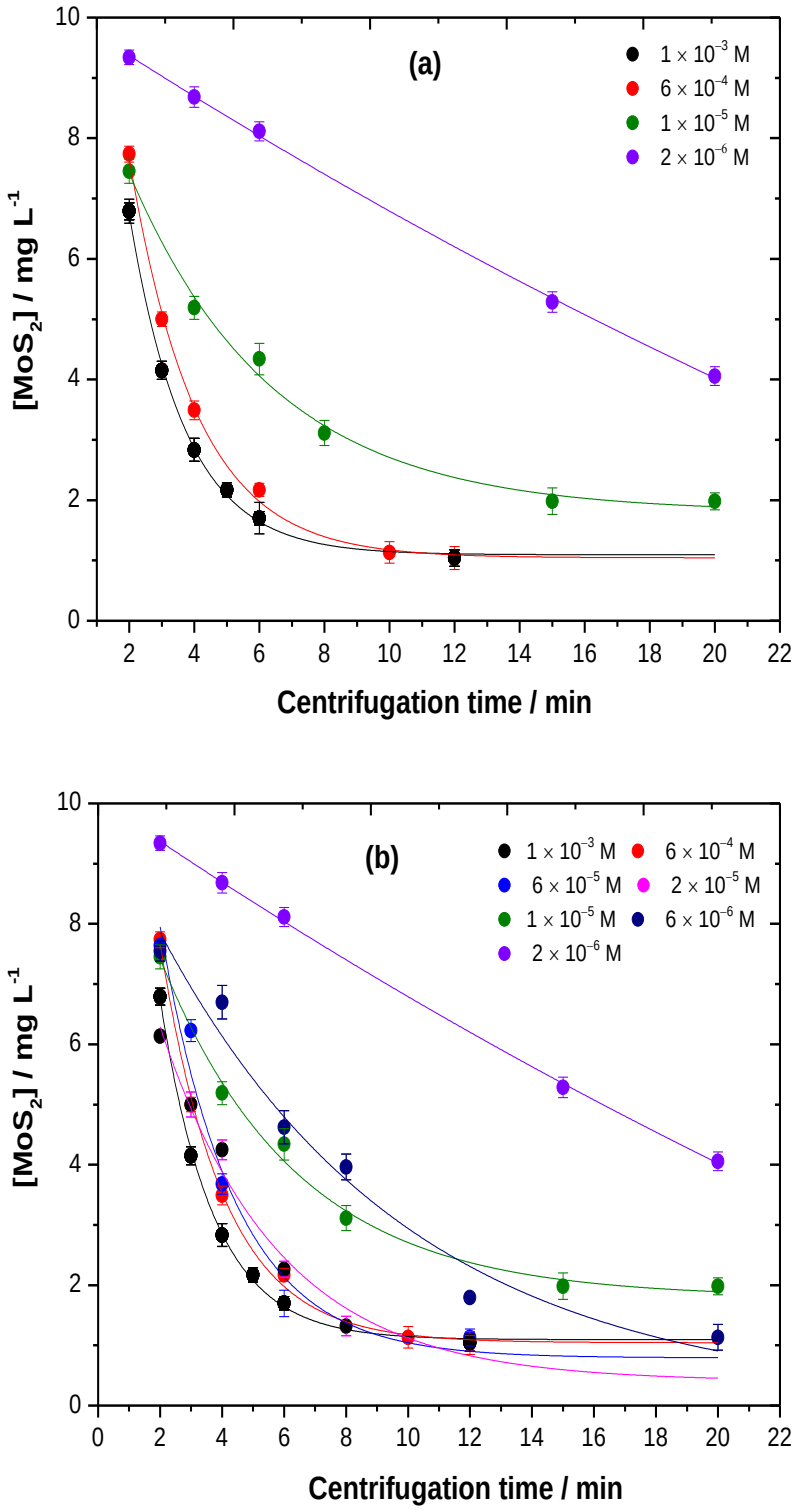

Figure 6. 10. Aggregation profiles of MoS_2 in the presence of different concentrations of BTPPATPBCl in DCB. Each aggregation profile was acquired at an MoS_2 starting concentration of 9.3 mg L^{-1}. The (a) part of the Figure shows the aggregation data for only four BTPPATPCl concentrations for visual clarity, while (b) shows the complete set of data. The single exponential fits are shown as solid lines.

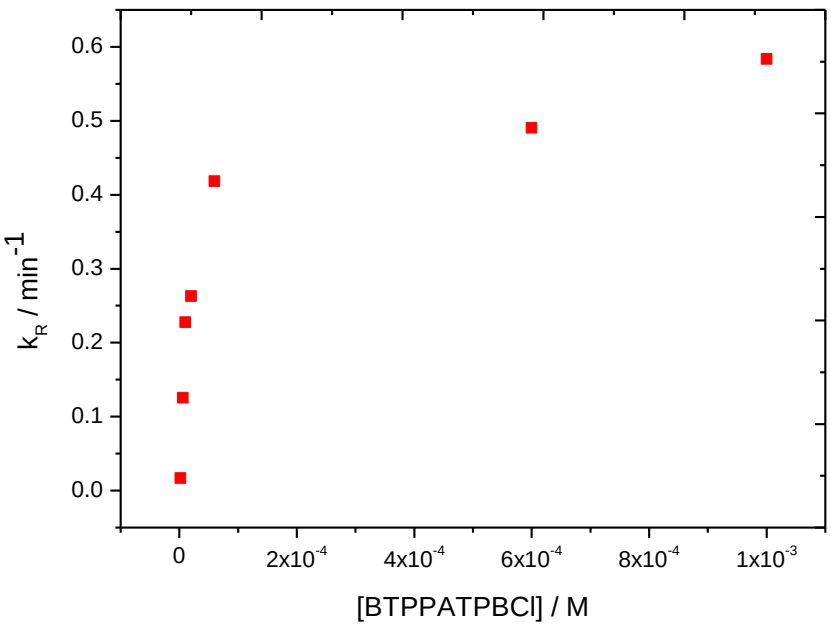

Figure 6. 11. Aggregation rate constant of MoS_2 dispersed in DCB as a function of BTPPATPBCl concentration.

In order to determine the CCC, which is the minimum electrolyte concentration needed for particle aggregation to be solely controlled by diffusion, the inverse stability ratio (1/W) was first estimated, as given by Equation 3:[192, 314]

$$\frac{1}{W} = \frac{k_R}{k_D} \tag{3}$$

where, k_R and k_D correspond to the aggregation rate constants measured in the RLCA regime and DLCA regime, respectively. The k_R values obtained are shown in Figure 6.11. The highest k_R value, which occurs in the plateau region of the plot (i.e., diffusion-controlled aggregation region), was taken as the value of k_D. Figure 6.12 shows the plot of 1/W as a function of BTPPATPBCl electrolyte concentration. The experimental data was fitted with the following empirical equation;[192, 314]

$$\frac{1}{\mathrm{W}} = \frac{1}{1 + (\mathrm{CCC}/[\mathrm{BTPPATPBCl}])^{\beta}} \tag{4}$$

where β is the slope d log(1/W)/d log[BTPPATPBCl] in the RLCA regime. The CCC obtained from the fitting of the experimental data shown in Figure 6.12, is 21.8 μM. The CCC obtained is significantly lower than 4.4 mM reported for surfactant stabilised MoS_2 dispersion in water aggregated with single charge Na^+. The results of the aggregation studies presented indicate that electrostatic repulsion plays an important role in the stabilisation of the MoS_2 particles dispersed in DCB, which is consistent with the lower relative permittivity of the organic solvent.

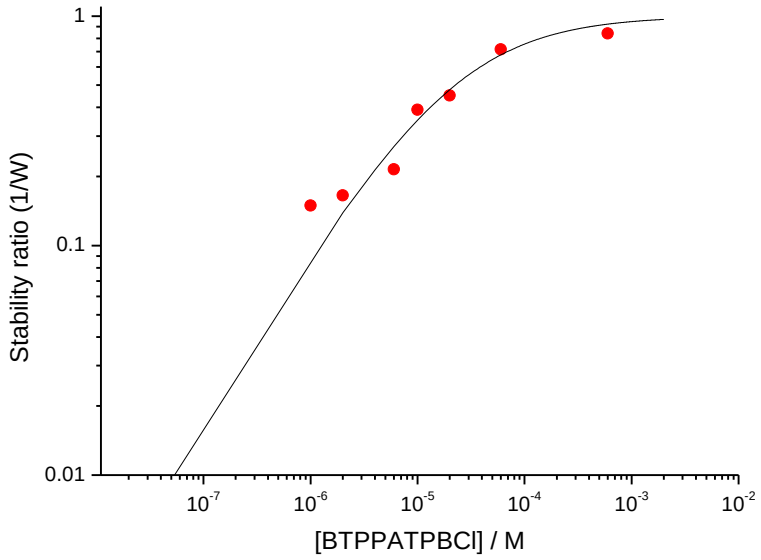

Figure 6. 12. Inverse stability ratio of MoS_2 aggregation as a function of electrolyte concentration. The solid line shows the best fit of the empirical model (Equation 4).

6.4 Conclusions

In this chapter, the electrolyte-induced aggregation kinetics of layered MoS_2 in DCB was studied by optical absorption. Increasing electrolyte concentration in the dispersion was found to cause a corresponding increase in the aggregation rate constant of the MoS_2 due to increased screening of the EDL repulsion barrier around each particle until the CCC was reached, when further increases in electrolyte

concentration did not result in any significant increase in aggregation rate constant. The observed behaviour demonstrates that electrostatic repulsion contributes substantially to the stability of the MoS_2 dispersed in DCB. However, further work is needed to understand the role of the sonopolymer, which is formed during sonication as well as the origin of surface charge formed for the exfoliation of MoS_2 nanoflakes in non-aqueous solvents. The electrolyte is shown to selectively remove the MoS_2 from the MoS_2-sonopolymer mixture, suggesting an interesting role for electrolyte as a tool to separate 2D materials from low polarity organic solvents.

Chapter 7

General Conclusions and Remarks for Further work

This thesis investigated the effect of organic electrolyte on the stability of non-aqueous dispersions of single-wall carbon nanotubes (SWCNTs) and molybdenum disulphide (MoS_2), adsorption of SWCNTs at the liquid/liquid interface and preparation of SWCNT/conducting polymer composites at the interface between two immiscible electrolyte solutions.

The stability of both SWCNT and MoS_2 dispersions prepared in DCE and DCB, respectively, were studied by destabilising the dispersions with varying concentrations of organic electrolyte and monitoring the change in concentration of the dispersed amount over time. In the case of SWCNTs, the "onset of aggregation" as defined by Forney et al.[191] was used to compare the stability of dispersions of two commercially obtained SWCNTs synthesised using different production technique and differing in levels impurities, size and oxygen content. For both nanotube dispersions, the concentration of the material remaining dispersed after 48 h of aggregation was found to decrease sigmoidally with increasing electrolyte concentration, which is in line with an electrostatic stabilisation mechanism, where the added electrolyte causes the compression of the electrical double layer around a charge stabilised particle. Although the concentration of oxygen on the SWCNT is expected to increase its surface charge and hence dispersion stability, the small difference in oxygen impurity levels on the two pristine SWCNTs studied here was found to be insignificant, suggesting that other factors such as the size of nanotubes, their type as well as impurity levels may play a dominant role in dispersion stability of non-functionalised SWCNTs in non-aqueous solvents. The present findings may

further suggest that the charge transfer between the SWCNT and the solvent suggested previously[195] may be the dominant charge stabilisation mechanism in these non-aqueous dispersions. Further studies should be carried with nanotubes of the same quality but differing only oxygen content, so as to establish the contribution of oxygen to SWCNTs dispersion stability.

In the case of MoS_2 dispersion, the critical coagulation concentration, CCC, was studied by measuring the aggregation rate of the MoS_2 in DCB at various electrolyte concentrations. It was found that the aggregation rate constant increased with increasing electrolyte concentration due to the increased screening of the electrical double layer around the MoS_2 nanosheets until the CCC was reached. As with the SWCNT, the behaviour displayed by the MoS_2 dispersion was similarly consistent with the nanosheets being electrostatically stabilised. However, additional complications arise due to solvent decomposition as a result of ultra-sonication. The contribution of the products of this decomposition is currently unknown, suggesting that further investigation is needed. In addition, more work needs to be carried out to establish the charging mechanism of MoS_2 in non-aqueous dispersions. Nonetheless, it was found that the organic electrolyte can selectively remove the MoS_2 from the MoS_2-sonopolymer mixture, suggesting an interesting role for electrolyte as a tool to separate 2D materials from low polarity organic solvents. In general, the results of the dispersion stability studies demonstrated the importance of electrostatic repulsion to the dispersibility of both the SWCNT and MoS_2 in non-aqueous solvents.

The SWCNTs, initially dispersed in the organic phase, were shown to adsorb strongly at the water/DCE interface regardless of whether electrolyte is present or not. The interfacial SWCNT layer formed was found to be composed of multiple emulsion droplets effectively stabilised by the nanotubes. Ion transfer voltammetry

was used to characterise the electrical properties of the interfacial SWCNTs. The transfer of the negatively charged PF_6^- ion across the interfacial SWCNT layer of differing density/thickness was found to be suppressed more than the corresponding transfer of positively charged TMA^+ ion across the same interface. The diminution of the ion transfer across the SWCNT layers was analysed using the theory of voltammetry at partially blocked electrode. The selectivity of the SWCNT interfacial layer between PF_6^- and TMA^+ was attributed to the potential dependent change in chemical composition of the interfacial SWCNTs *via* the adsorption of organic electrolyte from the organic side of the liquid/liquid interface, as confirmed by XPS measurements. This causes the electrostatic interaction between the SWCNTs adsorbed at the liquid/liquid interface and the transferring ions, thus, retarding their transfer across the interface. Due to additional possible π-π interaction between the nanotube and dibenzo-18-crown-6 ligand, the facilitated transfer of K^+ ion across the interface was found to be even more suppressed by the interfacial SWCNTs. The findings may be particularly important in ion detection, removal and modification of SWCNTs.

The successful preparation of SWCNT/conducting polymer nanocomposites *via* electropolymerisation at the interface between two immiscible electrolyte solutions has been demonstrated for the first time. Evidence of the formation of the SWCNT/poplypyrrole film was obtained after the nanocomposite layer has been transferred to a solid substrate and subsequent characterisation by SEM, AFM and Raman spectroscopy. It was found that the pyrrole monomer was grown around the SWCNTs forming a nanocomposite in which the nanotubes were embedded in the polyporrole matrix. The Raman characterisation suggests that the SWCNT are doped by the polypyrrole, as a result of the composite formation. This is expected to

enhance the conductivity of the composite material. The electropolymerisation of pyrrole at the "bare" water/DCB interface was initially studied employing different potentiodynamic methods. The morphology of the polypyrrole film formed at the interface was affected by the polymerisation conditions used. For example, an increase in the number of CV cycles applied for the polymer growth yielded a polymer film with better surface coverage. Further work in this direction is needed to understand fully the mechanism of the electropolymerisation process at the liquid/liquid interface, but the work presented offers promising avenues for future exploration. One aspect of future interest is to investigate their technological applications in supercapacitors, batteries, solar cells, sensors and other related devices.

References

1. Thostenson, E.T., Ren, Z., and Chou, T.-W., *Advances in the Science and Technology of Carbon Nanotubes and Their Composites: A Review.* Compos. Sci. Technol., 2001. **61**(13): 1899-1912.
2. De Volder, M.F.L., Tawfick, S.H., Baughman, R.H., and Hart, A.J., *Carbon Nanotubes: Present and Future Commercial Applications.* Science, 2013. **339**(6119): 535-539.
3. Zhifeng Ren, Y.L., Yang Wang, *Aligned Carbon Nanotubes, Physics, Concepts, Fabrication and Devices*. Nanosci. and Technol.. 2013, New York: Springer Berlin Heidelberg.
4. Jariwala, D., Sangwan, V.K., Lauhon, L.J., Marks, T.J., and Hersam, M.C., *Carbon Nanomaterials for Electronics, Optoelectronics, Photovoltaics, and Sensing.* Chem. Soc. Rev., 2013. **42**(7): 2824-2860.
5. Baughman, R.H., Zakhidov, A.A., and De Heer, W.A., *Carbon Nanotubes--the Route toward Applications.* Science, 2002. **297**(5582): 787-792.
6. Abboud, J.-L.M. and Notari, R., *Critical Compilation of Scales of Solvent Parameters. Part I. Pure, Non-Hydrogen Bond Donor Solvents.* Pure Appl. Chem., 1999. **71**(4): 645-718.
7. Martel, R., Schmidt, T., Shea, H.R., Hertel, T., and Avouris, P., *Single- and Multi-Wall Carbon Nanotube Field-Effect Transistors.* Appl. Phys. Lett., 1998. **73**(17): 2447-2449.
8. Nish, A., Hwang, J.-Y., Doig, J., and Nicholas, R.J., *Highly Selective Dispersion of Single-Walled Carbon Nanotubes Using Aromatic Polymers.* Nat. Nano, 2007. **2**(10): 640-646.
9. Bian, X., Scanlon, M.D., Wang, S., Liao, L., Tang, Y., Liu, B., and Girault, H.H., *Floating Conductive Catalytic Nano-Rafts at Soft Interfaces for Hydrogen Evolution.* Chemical Science, 2013. **4**(9): 3432-3441.
10. Wang, C., Waje, M., Wang, X., Tang, J.M., Haddon, R.C., and Yan, *Proton Exchange Membrane Fuel Cells with Carbon Nanotube Based Electrodes.* Nano Lett., 2004. **4**(2): 345-348.
11. Sgobba, V. and Guldi, D.M., *Carbon Nanotubes-Electronic/Electrochemical Properties and Application for Nanoelectronics and Photonics.* Chem. Soc. Rev., 2009. **38**(1): 165-184.
12. Pop, E., Mann, D., Wang, Q., Goodson, K., and Dai, H., *Thermal Conductance of an Individual Single-Wall Carbon Nanotube above Room Temperature.* Nano Lett., 2006. **6**(1): 96-100.
13. Endo, M., Strano, M.S., and Ajayan, P.M., *Potential Applications of Carbon Nanotubes*, in *Carbon Nanotubes: Advanced Topics in the Synthesis, Structure, Properties and Applications*, A. Jorio, G. Dresselhaus, and M.S. Dresselhaus, Editors. 2008, Springer Berlin Heidelberg: Berlin, Heidelberg. p. 13-62.
14. Collins, P.G., Arnold, M.S., and Avouris, P., *Engineering Carbon Nanotubes and Nanotube Circuits Using Electrical Breakdown.* Science, 2001. **292**(5517): 706-709.
15. Javey, A., Guo, J., Wang, Q., Lundstrom, M., and Dai, H., *Ballistic Carbon Nanotube Field-Effect Transistors.* Nature, 2003. **424**(6949): 654-657.
16. Dillon, A.C., *Carbon Nanotubes for Photoconversion and Electrical Energy Storage.* Chem. Rev., 2010. **110**(11): 6856-6872.

17. Dresselhaus, M.S., Dresselhaus, G., Saito, R., and Jorio, A., *Raman Spectroscopy of Carbon Nanotubes.* Phys. Rep., 2005. **409**(2): 47-99.
18. Charlier, J.-C., Blase, X., and Roche, S., *Electronic and Transport Properties of Nanotubes.* Rev. Mod. Phys., 2007. **79**(2): 677-732.
19. Nessim, G.D., *Properties, Synthesis, and Growth Mechanisms of Carbon Nanotubes with Special Focus on Thermal Chemical Vapor Deposition.* Nanoscale, 2010. **2**(8): 1306-1323.
20. Terrones, M., *Carbon Nanotubes: Synthesis and Properties, Electronic Devices and Other Emerging Applications.* Int. Mater. Rev., 2004. **49**(6): 325-377.
21. Dumitrescu, I., Unwin, P.R., and Macpherson, J.V., *Electrochemistry at Carbon Nanotubes: Perspective and Issues.* Chem. Commun., 2009(45): 6886-6901.
22. Joselevich, E., Dai, H., Liu, J., Hata, K., and H. Windle, A., *Carbon Nanotube Synthesis and Organization*, in *Carbon Nanotubes: Advanced Topics in the Synthesis, Structure, Properties and Applications*, A. Jorio, G. Dresselhaus, and M.S. Dresselhaus, Editors. 2008, Springer Berlin Heidelberg: Berlin, Heidelberg. p. 101-165.
23. Bethune, D.S., Klang, C.H., De Vries, M.S., Gorman, G., Savoy, R., Vazquez, J., and Beyers, R., *Cobalt-Catalysed Growth of Carbon Nanotubes with Single-Atomic-Layer Walls.* Nature, 1993. **363**(6430): 605-607.
24. Iijima, S. and Ichihashi, T., *Single-Shell Carbon Nanotubes of 1-nm Diameter.* Nature, 1993. **363**(6430): 603-605.
25. Choudhary, V. and Gupta, A., *Polymer/Carbon Nanotube Nanocomposites*. Carbon Nanotubes - Polymer Nanocomposites. 2011.
26. Journet, C., Maser, W.K., Bernier, P., Loiseau, A., De La Chapelle, M.L., Lefrant, S., Deniard, P., Lee, R., and Fischer, J.E., *Large-Scale Production of Single-Walled Carbon Nanotubes by the Electric-Arc Technique.* Nature, 1997. **388**(6644): 756-758.
27. Bandaru, P.R., *Electrical Properties and Applications of Carbon Nanotube Structures.* J. Nanosci. Nanotechnol., 2007. **7**(4-1): 1239-1267.
28. Dai, H., *Nanotube Growth and Characterization*, in *Carbon Nanotubes: Synthesis, Structure, Properties, and Applications*, M.S. Dresselhaus, G. Dresselhaus, and P. Avouris, Editors. 2001, Springer Berlin Heidelberg: Berlin, Heidelberg. p. 29-53.
29. Guo, T., Nikolaev, P., Thess, A., Colbert, D.T., and Smalley, R.E., *Catalytic Growth of Single-Walled Manotubes by Laser Vaporization.* Chem. Phys. Lett., 1995. **243**(1): 49-54.
30. Thess, A., Lee, R., Nikolaev, P., Dai, H., Petit, P., Robert, J., Xu, C., Lee, Y.H., Kim, S.G., Rinzler, A.G., Colbert, D.T., Scuseria, G.E., Tománek, D., Fischer, J.E., and Smalley, R.E., *Crystalline Ropes of Metallic Carbon Nanotubes.* Science, 1996. **273**(5274): 483-487.
31. Islam, M.F., Rojas, E., Bergey, D.M., Johnson, A.T., and Yodh, A.G., *High Weight Fraction Surfactant Solubilization of Single-Wall Carbon Nanotubes in Water.* Nano Lett., 2003. **3**(2): 269-273.
32. Vaisman, L., Wagner, H.D., and Marom, G., *The Role of Surfactants in Dispersion of Carbon Nanotubes.* Adv. Colloid Interface Sci., 2006. **128–130**: 37-46.
33. O'connell, M.J., Boul, P., Ericson, L.M., Huffman, C., Wang, Y., Haroz, E., Kuper, C., Tour, J., Ausman, K.D., and Smalley, R.E., *Reversible Water-*

Solubilization of Single-Walled Carbon Nanotubes by Polymer Wrapping. Chem. Phys. Lett., 2001. **342**(3–4): 265-271.
34. Zheng, M., Jagota, A., Semke, E.D., Diner, B.A., Mclean, R.S., Lustig, S.R., Richardson, R.E., and Tassi, N.G., *DNA-Assisted Dispersion and Separation of Carbon Nanotubes.* Nat Mater, 2003. **2**(5): 338-342.
35. Coleman, J.N., *Liquid-Phase Exfoliation of Nanotubes and Graphene.* Adv. Funct. Mater., 2009. **19**(23): 3680-3695.
36. Zhao, B., Hu, H., Yu, A., Perea, D., and Haddon, R.C., *Synthesis and Characterization of Water Soluble Single-Walled Carbon Nanotube Graft Copolymers.* J. Am. Chem. Soc., 2005. **127**(22): 8197-8203.
37. Chen, J., Hamon, M.A., Hu, H., Chen, Y., Rao, A.M., Eklund, P.C., and Haddon, R.C., *Solution Properties of Single-Walled Carbon Nanotubes.* Science, 1998. **282**(5386): 95-98.
38. Kim, S.W., Kim, T., Kim, Y.S., Choi, H.S., Lim, H.J., Yang, S.J., and Park, C.R., *Surface Modifications for the Effective Dispersion of Carbon Nanotubes in Solvents and Polymers.* Carbon, 2012. **50**(1): 3-33.
39. Garg, A. and Sinnott, S.B., *Effect of Chemical Functionalization on the Mechanical Properties of Carbon Nanotubes.* Chem. Phys. Lett., 1998. **295**(4): 273-278.
40. Cheng, Q., Debnath, S., O'neill, L., Hedderman, T.G., Gregan, E., and Byrne, H.J., *Systematic Study of the Dispersion of Swnts in Organic Solvents.* J. Phys. Chem. C, 2010. **114**(11): 4857-4863.
41. Bahr, J.L., Mickelson, E.T., Bronikowski, M.J., Smalley, R.E., and Tour, J.M., *Dissolution of Small Diameter Single-Wall Carbon Nanotubes in Organic Solvents?* Chem. Commun., 2001(2): 193-194.
42. Bergin, S.D., Sun, Z., Rickard, D., Streich, P.V., Hamilton, J.P., and Coleman, J.N., *Multicomponent Solubility Parameters for Single-Walled Carbon Nanotube−Solvent Mixtures.* ACS Nano, 2009. **3**(8): 2340-2350.
43. Ausman, K.D., Piner, R., Lourie, O., Ruoff, R.S., and Korobov, M., *Organic Solvent Dispersions of Single-Walled Carbon Nanotubes: Toward Solutions of Pristine Nanotubes.* J. Phys. Chem. B, 2000. **104**(38): 8911-8915.
44. Kim, K.K., Bae, D.J., Yang, C.-M., An, K.H., Lee, J.Y., and Lee, Y.H., *Nanodispersion of Single-Walled Carbon Nanotubes Using Dichloroethane.* J. Nanosci. Nanotechnol., 2005. **5**(7): 1055-1059.
45. Li, X., Zhang, L., Wang, X., Shimoyama, I., Sun, X., Seo, W.-S., and Dai, H., *Langmuir−Blodgett Assembly of Densely Aligned Single-Walled Carbon Nanotubes from Bulk Materials.* J. Am. Chem. Soc., 2007. **129**(16): 4890-4891.
46. Kim, S., Yim, J., Wang, X., Bradley, D.D.C., Lee, S., and Demello, J.C., *Spin- and Spray-Deposited Single-Walled Carbon-Nanotube Electrodes for Organic Solar Cells.* Adv. Funct. Mater., 2010. **20**(14): 2310-2316.
47. Kim, D.S., Nepal, D., and Geckeler, K.E., *Individualization of Single-Walled Carbon Nanotubes: Is the Solvent Important?* Small, 2005. **1**(11): 1117-1124.
48. Cheng, Q., Debnath, S., Gregan, E., and Byrne, H.J., *Effect of Solvent Solubility Parameters on the Dispersion of Single-Walled Carbon Nanotubes.* J. Phys. Chem. C, 2008. **112**(51): 20154-20158.
49. Detriche, S., Zorzini, G., Colomer, J.F., Fonseca, A., and Nagy, J.B., *Application of the Hansen Solubility Parameters Theory to Carbon Nanotubes.* J. Nanosci. Nanotechnol., 2008. **8**(11): 6082-6092.

50. Ham, H.T., Choi, Y.S., and Chung, I.J., *An Explanation of Dispersion States of Single-Walled Carbon Nanotubes in Solvents and Aqueous Surfactant Solutions Using Solubility Parameters.* J. Colloid Interface Sci., 2005. **286**(1): 216-223.
51. Burke, J., *Solubility Parameters: Theory and Application*, in *Book and paper group annual*. 1984, Book and paper group.
52. Hansen, C.M., *Hansen Solubility Parameters: A User's Handbook, Second* Second Edition ed. 2007, Boca Raton: CRC Press.
53. Bergin, S.D., Nicolosi, V., Streich, P.V., Giordani, S., Sun, Z., Windle, A.H., Ryan, P., Niraj, N.P.P., Wang, Z.-T.T., Carpenter, L., Blau, W.J., Boland, J.J., Hamilton, J.P., and Coleman, J.N., *Towards Solutions of Single-Walled Carbon Nanotubes in Common Solvents.* Adv. Mater., 2008. **20**(10): 1876-1881.
54. Novoselov, K.S., Geim, A.K., Morozov, S.V., Jiang, D., Zhang, Y., Dubonos, S.V., Grigorieva, I.V., and Firsov, A.A., *Electric Field Effect in Atomically Thin Carbon Films.* Science, 2004. **306**(5696): 666-669.
55. Castro Neto, A.H., Guinea, F., Peres, N.M.R., Novoselov, K.S., and Geim, A.K., *The Electronic Properties of Graphene.* Rev. Mod. Phys., 2009. **81**(1): 109-162.
56. Wang, Q.H., Kalantar-Zadeh, K., Kis, A., Coleman, J.N., and Strano, M.S., *Electronics and Optoelectronics of Two-Dimensional Transition Metal Dichalcogenides.* Nat Nano, 2012. **7**(11): 699-712.
57. Butler, S.Z., Hollen, S.M., Cao, L., Cui, Y., Gupta, J.A., Gutiérrez, H.R., Heinz, T.F., Hong, S.S., Huang, J., Ismach, A.F., Johnston-Halperin, E., Kuno, M., Plashnitsa, V.V., Robinson, R.D., Ruoff, R.S., Salahuddin, S., Shan, J., Shi, L., Spencer, M.G., Terrones, M., Windl, W., and Goldberger, J.E., *Progress, Challenges, and Opportunities in Two-Dimensional Materials Beyond Graphene.* ACS Nano, 2013. **7**(4): 2898-2926.
58. Xu, M., Liang, T., Shi, M., and Chen, H., *Graphene-Like Two-Dimensional Materials.* Chem. Rev., 2013. **113**(5): 3766-3798.
59. Stephenson, T., Li, Z., Olsen, B., and Mitlin, D., *Lithium Ion Battery Applications of Molybdenum Disulfide (MoS_2) Nanocomposites.* Energy Environ. Sci., 2014. **7**(1): 209-231.
60. Chianelli, R.R., Siadati, M.H., De La Rosa, M.P., Berhault, G., Wilcoxon, J.P., Bearden, R., and Abrams, B.L., *Catalytic Properties of Single Layers of Transition Metal Sulfide Catalytic Materials.* Cat. Rev., 2006. **48**(1): 1-41.
61. Lv, R., Robinson, J.A., Schaak, R.E., Sun, D., Sun, Y., Mallouk, T.E., and Terrones, M., *Transition Metal Dichalcogenides and Beyond: Synthesis, Properties, and Applications of Single- and Few-Layer Nanosheets.* Acc. Chem. Res., 2015. **48**(1): 56-64.
62. Pan, H., *Progress on the Theoretical Study of Two-Dimensional MoS_2 Monolayer and Nanoribbon*, in *MoS_2: Materials, Physics, and Devices*, Z.M. Wang, Editor. 2014, Springer International Publishing: p. 1-35.
63. Song, I., Park, C., and Choi, H.C., *Synthesis and Properties of Molybdenum Disulphide: From Bulk to Atomic Layers.* RSC Advances, 2015. **5**(10): 7495-7514.
64. Schmidt, H., Giustiniano, F., and Eda, G., *Electronic Transport Properties of Transition Metal Dichalcogenide Field-Effect Devices: Surface and Interface Effects.* Chem. Soc. Rev., 2015. **44**(21): 7715-7736.

65. Splendiani, A., Sun, L., Zhang, Y., Li, T., Kim, J., Chim, C.-Y., Galli, G., and Wang, F., *Emerging Photoluminescence in Monolayer MoS_2.* Nano Lett., 2010. **10**(4): 1271-1275.
66. Radisavljevicb, Radenovica, Brivioj, Giacomettiv, and Kisa, *Single-Layer MoS_2 Transistors.* Nat Nano, 2011. **6**(3): 147-150.
67. Chia, X., Eng, A.Y.S., Ambrosi, A., Tan, S.M., and Pumera, M., *Electrochemistry of Nanostructured Layered Transition-Metal Dichalcogenides.* Chem. Rev., 2015. **115**(21): 11941-11966.
68. Chhowalla, M., Shin, H.S., Eda, G., Li, L.-J., Loh, K.P., and Zhang, H., *The Chemistry of Two-Dimensional Layered Transition Metal Dichalcogenide Nanosheets.* Nat Chem, 2013. **5**(4): 263-275.
69. Voiry, D., Salehi, M., Silva, R., Fujita, T., Chen, M., Asefa, T., Shenoy, V.B., Eda, G., and Chhowalla, M., *Conducting MoS_2 Nanosheets as Catalysts for Hydrogen Evolution Reaction.* Nano Lett., 2013. **13**(12): 6222-6227.
70. Lukowski, M.A., Daniel, A.S., Meng, F., Forticaux, A., Li, L., and Jin, S., *Enhanced Hydrogen Evolution Catalysis from Chemically Exfoliated Metallic MoS_2 Nanosheets.* J. Am. Chem. Soc., 2013. **135**(28): 10274-10277.
71. Zhang, G., Liu, H., Qu, J., and Li, J., *Two-Dimensional Layered MoS_2: Rational Design, Properties and Electrochemical Applications.* Energy Environ. Sci., 2016. **9**(4): 1190-1209.
72. Py, M.A. and Haering, R.R., *Structural Destabilization Induced by Lithium Intercalation in MoS_2 and Related Compounds.* Can. J. Phys., 1983. **61**(1): 76-84.
73. Eda, G., Yamaguchi, H., Voiry, D., Fujita, T., Chen, M., and Chhowalla, M., *Photoluminescence from Chemically Exfoliated MoS_2.* Nano Lett., 2011. **11**(12): 5111-5116.
74. Jiménez Sandoval, S., Yang, D., Frindt, R.F., and Irwin, J.C., *Raman Study and Lattice Dynamics of Single Molecular Layers of MoS_2.* Phys. Rev. B, 1991. **44**(8): 3955-3962.
75. Novoselov, K.S., Jiang, D., Schedin, F., Booth, T.J., Khotkevich, V.V., Morozov, S.V., and Geim, A.K., *Two-Dimensional Atomic Crystals.* Proc. Natl. Acad. Sci. U.S.A., 2005. **102**(30): 10451-10453.
76. Lee, C., Yan, H., Brus, L.E., Heinz, T.F., Hone, J., and Ryu, S., *Anomalous Lattice Vibrations of Single- and Few-Layer MoS_2.* ACS Nano, 2010. **4**(5): 2695-2700.
77. Coleman, J.N., Lotya, M., O'neill, A., Bergin, S.D., King, P.J., Khan, U., Young, K., Gaucher, A., De, S., Smith, R.J., Shvets, I.V., Arora, S.K., Stanton, G., Kim, H.-Y., Lee, K., Kim, G.T., Duesberg, G.S., Hallam, T., Boland, J.J., Wang, J.J., Donegan, J.F., Grunlan, J.C., Moriarty, G., Shmeliov, A., Nicholls, R.J., Perkins, J.M., Grieveson, E.M., Theuwissen, K., Mccomb, D.W., Nellist, P.D., and Nicolosi, V., *Two-Dimensional Nanosheets Produced by Liquid Exfoliation of Layered Materials.* Science, 2011. **331**(6017): 568-571.
78. Nicolosi, V., Chhowalla, M., Kanatzidis, M.G., Strano, M.S., and Coleman, J.N., *Liquid Exfoliation of Layered Materials.* Science, 2013. **340**(6139).
79. Yu, X., Prévot, M.S., and Sivula, K., *Multiflake Thin Film Electronic Devices of Solution Processed 2D MoS_2 Enabled by Sonopolymer Assisted Exfoliation and Surface Modification.* Chem. Mater., 2014. **26**(20): 5892-5899.

80. Yu, X., Prévot, M.S., Guijarro, N., and Sivula, K., *Self-Assembled 2D WSe_2 Thin Films for Photoelectrochemical Hydrogen Production.* Nat. Commun., 2015. **6**: 7596.
81. Smith, R.J., King, P.J., Lotya, M., Wirtz, C., Khan, U., De, S., O'neill, A., Duesberg, G.S., Grunlan, J.C., Moriarty, G., Chen, J., Wang, J., Minett, A.I., Nicolosi, V., and Coleman, J.N., *Large-Scale Exfoliation of Inorganic Layered Compounds in Aqueous Surfactant Solutions.* Adv. Mater., 2011. **23**(34): 3944-3948.
82. May, P., Khan, U., Hughes, J.M., and Coleman, J.N., *Role of Solubility Parameters in Understanding the Steric Stabilization of Exfoliated Two-Dimensional Nanosheets by Adsorbed Polymers.* J. Phys. Chem. C, 2012. **116**(20): 11393-11400.
83. Joensen, P., Frindt, R.F., and Morrison, S.R., *Single-Layer MoS_2.* Mater. Res. Bull., 1986. **21**(4): 457-461.
84. Ramakrishna Matte, H.S.S., Gomathi, A., Manna, A.K., Late, D.J., Datta, R., Pati, S.K., and Rao, C.N.R., *MoS_2 and WS_2 Analogues of Graphene.* Angew. Chem., 2010. **122**(24): 4153-4156.
85. Divigalpitiya, W.M.R., Frindt, R.F., and Morrison, S.R., *Inclusion Systems of Organic Molecules in Restacked Single-Layer Molybdenum Disulfide.* Science, 1989. **246**(4928): 369-371.
86. Ramakrishna Matte, H.S.S., Gomathi, A., Manna, A.K., Late, D.J., Datta, R., Pati, S.K., and Rao, C.N.R., *MoS_2 and WS_2 Analogues of Graphene.* Angew. Chem. Int. Ed., 2010. **49**(24): 4059-4062.
87. Zeng, Z., Yin, Z., Huang, X., Li, H., He, Q., Lu, G., Boey, F., and Zhang, H., *Single-Layer Semiconducting Nanosheets: High-Yield Preparation and Device Fabrication.* Angew. Chem. Int. Ed., 2011. **50**(47): 11093-11097.
88. Fan, X., Xu, P., Zhou, D., Sun, Y., Li, Y.C., Nguyen, M.a.T., Terrones, M., and Mallouk, T.E., *Fast and Efficient Preparation of Exfoliated 2H MoS_2 Nanosheets by Sonication-Assisted Lithium Intercalation and Infrared Laser-Induced 1T to 2H Phase Reversion.* Nano Lett., 2015. **15**(9): 5956-5960.
89. Cunningham, G., Lotya, M., Cucinotta, C.S., Sanvito, S., Bergin, S.D., Menzel, R., Shaffer, M.S.P., and Coleman, J.N., *Solvent Exfoliation of Transition Metal Dichalcogenides: Dispersibility of Exfoliated Nanosheets Varies Only Weakly between Compounds.* ACS Nano, 2012. **6**(4): 3468-3480.
90. Gupta, A., Arunachalam, V., and Vasudevan, S., *Water Dispersible, Positively and Negatively Charged MoS_2 Nanosheets: Surface Chemistry and the Role of Surfactant Binding.* J. Phys. Chem. Lett., 2015. **6**(4): 739-744.
91. Ramsden, W., *Separation of Solids in the Surface-Layers of Solutions and 'Suspensions' (Observations on Surface-Membranes, Bubbles, Emulsions, and Mechanical Coagulation). -- Preliminary Account.* Proc. R. Soc. London, 1903. **72**(477-486): 156-164.
92. Pickering, S.U., *Cxcvi.-Emulsions.* J. Chem. Soc., Faraday Trans., 1907. **91**(0): 2001-2021.
93. Binks, B.P., *Particles as Surfactants—Similarities and Differences.* Curr. Opin. Colloid Interface Sci., 2002. **7**(1–2): 21-41.
94. Chevalier, Y. and Bolzinger, M.-A., *Emulsions Stabilized with Solid Nanoparticles: Pickering Emulsions.* Colloids Surf. A, 2013. **439**: 23-34.
95. Booth, S.G. and Dryfe, R.a.W., *Assembly of Nanoscale Objects at the Liquid/Liquid Interface.* J. Phys. Chem. C, 2015. **119**(41): 23295-23309.

96. Binder, W.H., *Supramolecular Assembly of Nanoparticles at Liquid–Liquid Interfaces.* Angew. Chem. Int. Ed., 2005. **44**(33): 5172-5175.
97. Reincke, F., Hickey, S.G., Kegel, W.K., and Vanmaekelbergh, D., *Spontaneous Assembly of a Monolayer of Charged Gold Nanocrystals at the Water/Oil Interface.* Angew. Chem. Int. Ed., 2004. **43**(4): 458-462.
98. Xu, J., Chen, L., Choi, H., Konish, H., and Li, X., *Assembly of Metals and Nanoparticles into Novel Nanocomposite Superstructures.* Sci. Rep., 2013. **3**: 1730.
99. Toth, P.S., Rodgers, A.N.J., Rabiu, A.K., and Dryfe, R.a.W., *Electrochemical Activity and Metal Deposition Using Few-Layer Graphene and Carbon Nanotubes Assembled at the Liquid–Liquid Interface.* Electrochem. Commun., 2015. **50**: 6-10.
100. Rodgers, A.N.J. and Dryfe, R.a.W., *Oxygen Reduction at the Liquid–Liquid Interface: Bipolar Electrochemistry through Adsorbed Graphene Layers.* ChemElectroChem, 2016. **3**(3): 472-479.
101. Toth, P.S., Velický, M., Bissett, M.A., Slater, T.J.A., Savjani, N., Rabiu, A.K., Rakowski, A.M., Brent, J.R., Haigh, S.J., O'brien, P., and Dryfe, R.A.W., *Asymmetric MoS_2/Graphene/Metal Sandwiches: Preparation, Characterization, and Application.* Adv. Mater., 2016. **28**(37): 8256-8264.
102. Matsui, J., Yamamoto, K., Inokuma, N., Orikasa, H., Kyotani, T., and Miyashita, T., *Fabrication of Densely Packed Multi-Walled Carbon Nanotube Ultrathin Films Using a Liquid-Liquid Interface.* J. Mater. Chem., 2007. **17**(36): 3806-3811.
103. Matsui, J., Yamamoto, K., Inokuma, N., Orikasa, H., Kyotani, T., and Miyashita, T., *Multi-Walled Carbon Nanotube Ultrathin Film Using a Liquid-Liquid Interface: Effect of Alcohol Type to the Film Property.* Mol. Cryst. Liq. Cryst., 2008. **491**(1): 9-13.
104. Wang, H. and Hobbie, E.K., *Amphiphobic Carbon Nanotubes as Macroemulsion Surfactants.* Langmuir, 2003. **19**(8): 3091-3093.
105. Wang, R.K., Reeves, R.D., and Ziegler, K.J., *Interfacial Trapping of Single-Walled Carbon Nanotube Bundles.* J. Am. Chem. Soc., 2007. **129**(49): 15124-15125.
106. Wang, W., Laird, E.D., Gogotsi, Y., and Li, C.Y., *Bending Single-Walled Carbon Nanotubes into Nanorings Using a Pickering Emulsion-Based Process.* Carbon, 2012. **50**(5): 1769-1775.
107. Dinsmore, A.D., Hsu, M.F., Nikolaides, M.G., Marquez, M., Bausch, A.R., and Weitz, D.A., *Colloidosomes: Selectively Permeable Capsules Composed of Colloidal Particles.* Science, 2002. **298**(5595): 1006-1009.
108. Pieranski, P., *Two-Dimensional Interfacial Colloidal Crystals.* Phys. Rev. Lett., 1980. **45**(7): 569-572.
109. Boker, A., He, J., Emrick, T., and Russell, T.P., *Self-Assembly of Nanoparticles at Interfaces.* Soft Matter, 2007. **3**(10): 1231-1248.
110. Hu, L., Chen, M., Fang, X., and Wu, L., *Oil-Water Interfacial Self-Assembly: A Novel Strategy for Nanofilm and Nanodevice Fabrication.* Chem. Soc. Rev., 2012. **41**(3): 1350-1362.
111. Binks, B.P. and Horozov, T., *Colloidal Particles at Liquid Interfaces: An Introduction*, in *Colloidal Particles at Liquid Interfaces*, B.P. Binks and T. Horozov, Editors. 2006, Cambridge University Press: Cambridge. p. 1-74.

112. Binks, B.P. and Lumsdon, S.O., *Influence of Particle Wettability on the Type and Stability of Surfactant-Free Emulsions.* Langmuir, 2000. **16**(23): 8622-8631.
113. Wang, R.K., Park, H.-O., Chen, W.-C., Silvera-Batista, C., Reeves, R.D., Butler, J.E., and Ziegler, K.J., *Improving the Effectiveness of Interfacial Trapping in Removing Single-Walled Carbon Nanotube Bundles.* J. Am. Chem. Soc., 2008. **130**(44): 14721-14728.
114. Lewandowski, E.P., Cavallaro, M., Botto, L., Bernate, J.C., Garbin, V., and Stebe, K.J., *Orientation and Self-Assembly of Cylindrical Particles by Anisotropic Capillary Interactions.* Langmuir, 2010. **26**(19): 15142-15154.
115. Botto, L., Lewandowski, E.P., Cavallaro, M., and Stebe, K.J., *Capillary Interactions between Anisotropic Particles.* Soft Matter, 2012. **8**(39): 9957-9971.
116. Yi, H., Song, H., and Chen, X., *Carbon Nanotube Capsules Self-Assembled by W/O Emulsion Technique.* Langmuir, 2007. **23**(6): 3199-3204.
117. Dryfe, R.a.W., *The Electrified Liquid-Liquid Interface*, in *Adv. Chem. Phys.* 2009, John Wiley & Sons, Inc. p. 153-215.
118. Wandlowski, T., Mareček, V., and Samec, Z., *Galvani Potential Scales for Water—Nitrobenzene and Water-1,2-Dichloroethane Interfaces.* Electrochim. Acta, 1990. **35**(7): 1173-1175.
119. Vanysek, P., *Electrochemical Processes at Liquid Interfaces.* Anal. Chem., 1990. **62**(15): 827A-835A.
120. Vanýsek, P., *Analytical Applications of Electrified Interfaces between Two Immiscible Solutions.* Trends Anal. Chem., 1993. **12**(9): 363-373.
121. Ballantyne, A.D., Brisdon, A.K., and Dryfe, R.a.W., *Immiscible Electrolyte Systems Based on Asymmetric Hydrophobic Room Temperature Ionic Liquids.* Chem. Commun., 2008(40): 4980-4982.
122. Samec, Z., Langmaier, J., and Kakiuchi, T., *Charge-Transfer Processes at the Interface between Hydrophobic Ionic Liquid and Water*, in *Pure Appl. Chem.* 2009. p. 1473.
123. Samec, Z., *Dynamic Electrochemistry at the Interface between Two Immiscible Electrolytes.* Electrochim. Acta, 2012. **84**: 21-28.
124. Vanýsek, P., *Charge Transfer Processes on Liquid/Liquid Interfaces: The First Century.* Electrochim. Acta, 1995. **40**(18): 2841-2847.
125. Vanýsek, P. and Basáez Ramírez, L., *Interface between Two Immiscible Liquid Electrolytes: A Review.* J. Chil. Chem. Soc., 2008. **53**: 1455-1463.
126. Vanýsek, P. and Buck, R.P., *Properties of the Interface of Two Immiscible Electrolytes Mediated by Molecules of Biological Importance: A Literature Review.* J. Electrochem. Soc., 1984. **131**(8): 1792-1796.
127. Vanysek, P., *Electrochemistry on Liquid/Liquid Interfaces*. 1985, Berlin: Springer-Verlag.
128. Gavach, C., Seta, P., and Henry, F., *A Study of the Ionic Transfer across an Aqueous Solution Liquid Membrane Interface by Chronopotentiometric and Impedance Measurements.* Bioelectrochem. Bioenerg., 1974. **1**(3): 329-342.
129. Gavach, C. and Henry, F., *Chronopotentiometric Investigation of the Diffusion Overvoltage at the Interface between Two Non-Miscible Solutions.* Journal of Electroanalytical Chemistry and Interfacial Electrochemistry, 1974. **54**(2): 361-370.
130. Samec, Z., Mareček, V., Koryta, J., and Khalil, M.W., *Investigation of Ion Transfer across the Interface between Two Immiscible Electrolyte Solutions*

by Cyclic Voltammetry. J. Electroanal. Chem. and Interfacial Electrochem., 1977. **83**(2): 393-397.
131. Koryta, J., *Electrochemical Polarization Phenomena at the Interface of Two Immiscible Electrolyte Solutions.* Electrochim. Acta, 1979. **24**(3): 293-300.
132. Koryta, J., Vanýsek, P., and Březina, M., *Electrolysis with an Electrolyte Dropping Electrode.* J. Electroanal. Chem. Interfacial Electrochem., 1976. **67**(2): 263-266.
133. Samec, Z., Mareček, V., and Weber, J., *Charge Transfer between Two Immiscible Electrolyte Solutions.* J. Electroanal. Chem. Interfacial Electrochem., 1979. **100**(1): 841-852.
134. Kakiuchi, T., Kondo, T., Kotani, M., and Senda, M., *Ion Permeability of Dilauroylphosphatidylethanolamine Monolayer at the Polarized Nitrobenzene/Water Interface.* Langmuir, 1992. **8**(1): 169-175.
135. Schiffrin, D.J., Cheng, Y., Silva, F.A., Vigato, S., Tamburini, S., Gilroy, D., Bustero, I., and Mugica, J.C., *Electroassisted Separation of Metals by Solvent Extraction and Supported-Liquid Membranes*, in *Hydrometallurgy '94: Papers Presented at the International Symposium 'Hydrometallurgy '94' Organized by the Institution of Mining and Metallurgy and the Society of Chemical Industry, and Held in Cambridge, England, from 11 to 15 July, 1994*. 1994, Springer Netherlands: Dordrecht. p. 655-673.
136. Su, B., Girault, H.H., and Samec, Z., *Electrocatalysis at Liquid–Liquid Interfaces*, in *Catalysis in Electrochemistry*. 2011, John Wiley & Sons, Inc. p. 427-451.
137. Mendez, M.A., Partovi-Nia, R., Hatay, I., Su, B., Ge, P., Olaya, A., Younan, N., Hojeij, M., and Girault, H.H., *Molecular Electrocatalysis at Soft Interfaces.* PCCP, 2010. **12**(46): 15163-15171.
138. Tan, S.N., Dryfe, R.A., and Girault, H.H., *Electrochemical Study of Phase-Transfer Catalysis Reactions: The Williamson Ether Synthesis.* Helv. Chim. Acta, 1994. **77**(1): 231-242.
139. Osborne, M.D. and Girault, H.H., *Amperometric Detection of the Ammonium Ion by Facilitated Ion Transfer across the Interface between Two Immiscible Electrolyte Solutions.* Electroanalysis, 1995. **7**(5): 425-434.
140. Amemiya, S., Kim, J., Izadyar, A., Kabagambe, B., Shen, M., and Ishimatsu, R., *Electrochemical Sensing and Imaging Based on Ion Transfer at Liquid/Liquid Interfaces.* Electrochim. Acta, 2013. **110**: 836-845.
141. Hubert, G., Alexei, A.K., Charles, W.M., and Michael, U., *Functionalized Liquid–Liquid Interfaces.* J. Phys. Condens. Matter, 2007. **19**(37): 370301.
142. Flatte, M.E., Kornyshev, A.A., and Urbakh, M., *Nanoparticles at Electrified Liquid-Liquid Interfaces: New Options for Electro-Optics.* Faraday Discuss., 2009. **143**(0): 109-115.
143. Gschwend, G.C., Smirnov, E., Peljo, P., and Girault, H., *Electrovariable Gold Nanoparticle Films at Liquid-Liquid Interfaces: From Redox Electrocatalysis to Marangoni-Shutters.* Faraday Discuss., 2016.
144. Peljo, P. and Girault, H.H., *Liquid/Liquid Interfaces, Electrochemistry At*, in *Encyclopedia of Analytical Chemistry*. 2006, John Wiley & Sons, Ltd.
145. Reymond, F., FermíN, D., Lee, H.J., and Girault, H.H., *Electrochemistry at Liquid/Liquid Interfaces: Methodology and Potential Applications.* Electrochim. Acta, 2000. **45**(15–16): 2647-2662.

146. Kakiuchi, T., *Partition Equilibruim of Ionic Components in Two Immiscible Electrolyte Solutions*, in *Liquid-Liquid Interfaces: Theory and Methods*, G.A. Volkov and W.D. Deamer, Editors. 1996, CRC press: London. p. 1-18.
147. Olaya, A.J., Ge, P., and Girault, H.H., *Ion Transfer across the Water|Trifluorotoluene Interface.* Electrochem. Commun., 2012. **19**: 101-104.
148. Peljo, P., Rauhala, T., Murtomäki, L., Kallio, T., and Kontturi, K., *Oxygen Reduction at a Water-1,2-Dichlorobenzene Interface Catalyzed by Cobalt Tetraphenyl Porphyrine – a Fuel Cell Approach.* Int. J. Hydrogen Energy, 2011. **36**(16): 10033-10043.
149. Parker, A.J., *Solvation of Ions—Enthalpies, Entropies and Free Energies of Transfer.* Electrochim. Acta, 1976. **21**(9): 671-679.
150. Shao, Y., *17.3 - Electrochemistry at Liquid/Liquid Interfaces A2 - Zoski, Cynthia G*, in *Handbook of Electrochemistry*. 2007, Elsevier: Amsterdam. p. 785-809.
151. Senda, M., Kakiuchi, T., and Osaka, T., *Electrochemistry at the Interface between Two Immiscible Electrolyte Solutions.* Electrochim. Acta, 1991. **36**(2): 253-262.
152. *On the Facilitation Effect of Neutral Macrocyclic Ligands on the Ion Transfer across the Interface between Aqueous and Organic Solutions. I. Theoretical Equation of Ion-Transfer-Polarographic Current-Potential Curves and Its Experimental Verification.* Bull. Chem. Soc. Jpn., 1991. **64**(5): 1497-1508.
153. Shao, Y., Osborne, M.D., and Girault, H.H., *Assisted Ion Transfer at Micro-Ities Supported at the Tip of Micropipettes.* J. Electroanal. Chem. Interfacial Electrochem., 1991. **318**(1): 101-109.
154. Eugster, N., Fermín, D.J., and Girault, H.H., *Photoinduced Electron Transfer at Liquid/Liquid Interfaces. Part Vi. On the Thermodynamic Driving Force Dependence of the Phenomenological Electron-Transfer Rate Constant.* J. Phys. Chem. B, 2002. **106**(13): 3428-3433.
155. Atkin, P. and De Paula, J., *Physical Chemistry*. 2006, Great Britain: Oxford University Press.
156. Burgot, J.-L., *Ionic Equilibria in Analytical Chemistry*. 2012, New York: Springer.
157. Girault, H.H., *Analytical and Physical Electrochemistry*. First ed. 2004, Italy: EPFL Press.
158. Monk, M.S.P., *Fundamentals of Electroanalytical Chemistry*. 2001, England: Joh Wiley & Sons Ltd.
159. Alderich, S. 22/03/2014]; Available from: http://www.sigmaaldrich.com/catalog/product/aldrich/750514?lang=en&region=GB.
160. Swan, T. *Product Data Sheet*. Available from: http://www.thomas-swan.co.uk.
161. Lee, H.J., Beattie, P.D., Seddon, B.J., Osborne, M.D., and Girault, H.H., *Amperometric Ion Sensors Based on Laser-Patterned Composite Polymer Membranes.* J. Electroanal. Chem., 1997. **440**(1–2): 73-82.
162. Giordano, A.N., Chaturvedi, H., and Poler, J.C., *Critical Coagulation Concentrations for Carbon Nanotubes in Nonaqueous Solvent.* J. Phys.l Chem. C, 2007. **111**(31): 11583-11589.

163. Cornel, J., Lindenberg, C., Schöll, J., and Mazzotti, M., *Raman Spectroscopy*, in *Industrial Crystallization Process Monitoring and Control*. 2012, Wiley-VCH Verlag GmbH & Co. KGaA. p. 93-103.
164. Inkson, B.J., *2 - Scanning Electron Microscopy (SEM) and Transmission Electron Microscopy (TEM) for Materials Characterization*, in *Materials Characterization Using Nondestructive Evaluation (NDE) Methods*. 2016, Woodhead Publishing. p. 17-43.
165. Goldstein, J.I., Newbury, D.E., Echlin, P., Joy, D.C., Lyman, C.E., Lifshin, E., Sawyer, L., and Michael, J.R., *Introduction*, in *Scanning Electron Microscopy and X-Ray Microanalysis: Third Edition*. 2003, Springer US: Boston, MA. p. 1-20.
166. Stokes, D.J., *Principles of Sem*, in *Principles and Practice of Variable Pressure/Environmental Scanning Electron Microscopy (VP-ESEM)*. 2008, John Wiley & Sons, Ltd. p. 17-62.
167. Schneider, C., Rasband, W., and Eliceiri, K., *Nih Image to Imagej: 25 Years of Image Analysis.* Nature Methods, 2012. **9**(7): 671-5.
168. Binnig, G., Quate, C.F., and Gerber, C., *Atomic Force Microscope.* Phys. Rev. Lett., 1986. **56**(9): 930-933.
169. Khan, M.K., Wang, Q.Y., and Fitzpatrick, M.E., *1 - Atomic Force Microscopy (AFM) for Materials Characterization*, in *Materials Characterization Using Nondestructive Evaluation (NDE) Methods*. 2016, Woodhead Publishing. p. 1-16.
170. West, P. Eaton, P., *Atomic Force Microscopy*. 2010, Oxford Oxford University Press
171. Jalili, N. and Laxminarayana, K., *A Review of Atomic Force Microscopy Imaging Systems: Application to Molecular Metrology and Biological Sciences.* Mechatronics, 2004. **14**(8): 907-945.
172. Fujimoto, S., *Advanced Analysis of Surface Films Formed on Passive Metals and Alloys Using X-Ray Photoelectron Spectroscopy*, in *Progress in Advanced Structural and Functional Materials Design*, T. Kakeshita, Editor. 2013, Springer Japan: Tokyo. p. 69-81.
173. Neal, F., *CASAXPS Manual 2.3.15 Rev 1.2*. 2009: CASA software Ltd.
174. Bhattacharjee, S., *DLS and Zeta Potential – What They Are and What They Are Not?* J. Controlled Release, 2016. **235**: 337-351.
175. Malvern. *Zeta Potential - an Introduction in 30 Minutes (Technical Note)*. 2016 [cited 2017 10th February]; Available from: http://www.malvern.com/en/support/resource-center/technical-notes/TN101104ZetaPotentialIntroduction.aspx.
176. Antonio Alves Júnior, J. and Baptista Baldo, J., *The Behavior of Zeta Potential of Silica Suspensions.* New Journal of Glass and Ceramics, 2014. **4**: 29-37.
177. Lowry, G.V., Hill, R.J., Harper, S., Rawle, A.F., Hendren, C.O., Klaessig, F., Nobbmann, U., Sayre, P., and Rumble, J., *Guidance to Improve the Scientific Value of Zeta-Potential Measurements in Nanoehs.* Environmental Science: Nano, 2016. **3**(5): 953-965.
178. Malvern. *Zeta Potential Measurements of Non-Aqueous Particulate Suspension (Application Note)*. 2016 [cited 2017 10th February]; Available from: http://www.malvern.com/en/support/resource-center/application-notes/AN101104ZetaPotentialMeasurements.aspx.

179. Gründer, Y., Fabian, M.D., Booth, S.G., Plana, D., Fermín, D.J., Hill, P.I., and Dryfe, R.A.W., *Solids at the Liquid–Liquid Interface: Electrocatalysis with Pre-Formed Nanoparticles.* Electrochim. Acta, 2013. **110**: 809-815.
180. Rodgers, A.N.J., *Dispersion, Assembly and Electrochemical Properties of Graphene at the Liquid/Liquid Interface*, PhD Thesis, University of Manchester, 2015.
181. Hundhammer, B., Müller, C., Solomon, T., Alemu, H., and Hassen, H., *Ion Transfer across the Water-o-Dichlorobenzene Interface.* J. Electroanal. Chem. and Interfacial Electrochem., 1991. **319**(1): 125-135.
182. Furtado, C.A., Kim, U.J., Gutierrez, H.R., Pan, L., Dickey, E.C., and Eklund, P.C., *Debundling and Dissolution of Single-Walled Carbon Nanotubes in Amide Solvents.* J. Am. Chem. Soc., 2004. **126**(19): 6095-6105.
183. Giordani, S., Bergin, S.D., Nicolosi, V., Lebedkin, S., Kappes, M.M., Blau, W.J., and Coleman, J.N., *Debundling of Single-Walled Nanotubes by Dilution: Observation of Large Populations of Individual Nanotubes in Amide Solvent Dispersions.* J. Phys.l Chem. B, 2006. **110**(32): 15708-15718.
184. Bergin, S.D., Sun, Z., Streich, P., Hamilton, J., and Coleman, J.N., *New Solvents for Nanotubes: Approaching the Dispersibility of Surfactants.* J. Phys. Chem. C, 2010. **114**(1): 231-237.
185. Sano, M., Okamura, J., and Shinkai, S., *Colloidal Nature of Single-Walled Carbon Nanotubes in Electrolyte Solution: The Schulze−Hardy Rule.* Langmuir, 2001. **17**(22): 7172-7173.
186. Saleh, N.B., Pfefferle, L.D., and Elimelech, M., *Aggregation Kinetics of Multiwalled Carbon Nanotubes in Aquatic Systems: Measurements and Environmental Implications.* Environ. Sci. Technol., 2008. **42**(21): 7963-7969.
187. Smith, B., Wepasnick, K., Schrote, K.E., Cho, H.-H., Ball, W.P., and Fairbrother, D.H., *Influence of Surface Oxides on the Colloidal Stability of Multi-Walled Carbon Nanotubes: A Structure−Property Relationship.* Langmuir, 2009. **25**(17): 9767-9776.
188. Mac Kernan, D. and Blau, W.J., *Exploring the Mechanisms of Carbon-Nanotube Dispersion Aggregation in a Highly Polar Solvent.* EPL, 2008. **83**(6).
189. Azar, N.S. and Pourfath, M., *Aggregation Kinetics and Stability Mechanisms of Pristine and Oxidized Nanocarbons in Polar Solvents.* J. Phys. Chem. C, 2016. **120**(30): 16804-16814.
190. Ameen, A.A., Giordano, A.N., Alston, J.R., Forney, M.W., Herring, N.P., Kobayashi, S., Ridlen, S.G., Subaran, S.S., Younts, T.J., and Poler, J.C., *Aggregation Kinetics of Single-Walled Carbon Nanotubes Investigated Using Mechanically Wrapped Multinuclear Complexes: Probing the Tube-Tube Repulsive Barrier*. PCCP, 2014. **16**(12): 5855-5865.
191. Forney, M.W. and Poler, J.C., *Significantly Enhanced Single-Walled Carbon Nanotube Dispersion Stability in Mixed Solvent Systems.* J. Phys. Chem. C, 2011. **115**(21): 10531-10536.
192. Forney, M.W., Anderson, J.S., Ameen, A.L., and Poler, J.C., *Aggregation Kinetics of Single-Walled Carbon Nanotubes in Nonaqueous Solvents: Critical Coagulation Concentrations and Transient Dispersion Stability.* J. Phys. Chem. C, 2011. **115**(47): 23267-23272.
193. Trefalt, G., Szilagyi, I., and Borkovec, M., *Poisson–Boltzmann Description of Interaction Forces and Aggregation Rates Involving Charged Colloidal*

Particles in Asymmetric Electrolytes. J. Colloid Interface Sci., 2013. **406**: 111-120.
194. Rodgers, A.N.J., Velický, M., and Dryfe, R.A.W., *Electrostatic Stabilization of Graphene in Organic Dispersions.* Langmuir, 2015. **31**(48): 13068-13076.
195. Francisco, T., *Calculations on Solvents and Co-Solvents of Single-Wall Carbon Nanotubes: Cyclo Pyranoses.* Nanotechnology, 2005. **16**(5): S181.
196. Song, Y.I., Kim, G.Y., Choi, H.K., Jeong, H.J., Kim, K.K., Yang, C.M., Lim, S.C., An, K.H., Jung, K.T., and Lee, Y.H., *Fabrication of Carbon Nanotube Field Emitters Using a Dip-Coating Method.* Chem. Vap. Deposition, 2006. **12**(6): 375-379.
197. Weisman, R.B., *Chapter 5 Optical Spectroscopy of Single-Walled Carbon Nanotubes*, in *Contemporary Concepts of Condensed Matter Science*, S. Saito and A. Zettl, Editors. 2008, Elsevier. p. 109-133.
198. Hodge, S.A., Bayazit, M.K., Coleman, K.S., and Shaffer, M.S.P., *Unweaving the Rainbow: A Review of the Relationship between Single-Walled Carbon Nanotube Molecular Structures and Their Chemical Reactivity.* Chem. Soc. Rev., 2012. **41**(12): 4409-4429.
199. O'connell, M.J., Bachilo, S.M., Huffman, C.B., Moore, V.C., Strano, M.S., Haroz, E.H., Rialon, K.L., Boul, P.J., Noon, W.H., Kittrell, C., Ma, J., Hauge, R.H., Weisman, R.B., and Smalley, R.E., *Band Gap Fluorescence from Individual Single-Walled Carbon Nanotubes.* Science, 2002. **297**(5581): 593-596.
200. Koh, B., Park, J.B., Hou, X., and Cheng, W., *Comparative Dispersion Studies of Single-Walled Carbon Nanotubes in Aqueous Solution.* J. Phys. Chem. B, 2011. **115**(11): 2627-2633.
201. Rosner, B., Guldi, D.M., Chen, J., Minett, A.I., and Fink, R.H., *Dispersion and Characterization of Arc Discharge Single-Walled Carbon Nanotubes - Towards Conducting Transparent Films.* Nanoscale, 2014. **6**(7): 3695-3703.
202. Nanointegris. *Technical Specification of HiPco SWCNTs*. 20/11/16; Available from: http://www.nanointegris.com/en/hipco.
203. Hou, P.-X., Liu, C., and Cheng, H.-M., *Purification of Carbon Nanotubes.* Carbon, 2008. **46**(15): 2003-2025.
204. Haynes, W.M., ed. *Crc Handbook of Chemistry and Physics*. 95 ed. 2014.
205. Jorio, A., Pimenta, M.A., Filho, A.G.S., Saito, R., Dresselhaus, G., and Dresselhaus, M.S., *Characterizing Carbon Nanotube Samples with Resonance Raman Scattering.* New J. Phys., 2003. **5**(1): 139.
206. Dresselhaus, M.S., Dresselhaus, G., and Jorio, A., *Raman Spectroscopy of Carbon Nanotubes in 1997 and 2007.* J. Phys. Chem. C, 2007. **111**(48): 17887-17893.
207. Kataura, H., Kumazawa, Y., Maniwa, Y., Umezu, I., Suzuki, S., Ohtsuka, Y., and Achiba, Y., *Optical Properties of Single-Wall Carbon Nanotubes.* Synth. Met., 1999. **103**(1): 2555-2558.
208. Kalbac, M., Kavan, L., and Dunsch, L., *Effect of Bundling on the Tangential Displacement Mode in the Raman Spectra of Semiconducting Single-Walled Carbon Nanotubes During Electrochemical Charging.* J. Phys. Chem. C, 2009. **113**(4): 1340-1345.
209. Dresselhaus, M.S., Jorio, A., Hofmann, M., Dresselhaus, G., and Saito, R., *Perspectives on Carbon Nanotubes and Graphene Raman Spectroscopy.* Nano Lett., 2010. **10**(3): 751-758.

210. Rao, A.M., Richter, E., Bandow, S., Chase, B., Eklund, P.C., Williams, K.A., Fang, S., Subbaswamy, K.R., Menon, M., Thess, A., Smalley, R.E., Dresselhaus, G., and Dresselhaus, M.S., *Diameter-Selective Raman Scattering from Vibrational Modes in Carbon Nanotubes.* Science, 1997. **275**(5297): 187-191.
211. Maruyama. [cited 2016 1/11/2016]; Available from: http://www.photon.t.u-tokyo.ac.jp/~maruyama/kataura/kataura.html.
212. Krupke, R., Hennrich, F., Löhneysen, H.V., and Kappes, M.M., *Separation of Metallic from Semiconducting Single-Walled Carbon Nanotubes.* Science, 2003. **301**(5631): 344-347.
213. Kalbac, M., Hsieh, Y.-P., Farhat, H., Kavan, L., Hofmann, M., Kong, J., and Dresselhaus, M.S., *Defects in Individual Semiconducting Single Wall Carbon Nanotubes: Raman Spectroscopic and in Situ Raman Spectroelectrochemical Study.* Nano Lett., 2010. **10**(11): 4619-4626.
214. Frolov, A.I., Arif, R.N., Kolar, M., Romanova, A.O., Fedorov, M.V., and Rozhin, A.G., *Molecular Mechanisms of Salt Effects on Carbon Nanotube Dispersions in an Organic Solvent (N-Methyl-2-Pyrrolidone).* Chemical Science, 2012. **3**(2): 541-548.
215. Fedorov, M.V., Arif, R.N., Frolov, A.I., Kolar, M., Romanova, A.O., and Rozhin, A.G., *Salting out in Organic Solvents: A New Route to Carbon Nanotube Bundle Engineering.* PCCP, 2011. **13**(27): 12399-12402.
216. Chen, W., Liu, X., Liu, Y., Bang, Y., and Kim, H.-I., *Preparation of O/W Pickering Emulsion with Oxygen Plasma Treated Carbon Nanotubes as Surfactants.* J. Ind. Eng. Chem., 2011. **17**(3): 455-460.
217. D'arcy, J.M., Tran, H.D., Stieg, A.Z., Gimzewski, J.K., and Kaner, R.B., *Aligned Carbon Nanotube, Graphene and Graphite Oxide Thin Films Via Substrate-Directed Rapid Interfacial Deposition.* Nanoscale, 2012. **4**(10): 3075-3082.
218. Matsui, J., Yamamoto, K., and Miyashita, T., *Assembly of Untreated Single-Walled Carbon Nanotubes at a Liquid–Liquid Interface.* Carbon, 2009. **47**(6): 1444-1450.
219. Rinzler, A.G., Liu, J., Dai, H., Nikolaev, P., Huffman, C.B., Rodríguez-Macías, F.J., Boul, P.J., Lu, A.H., Heymann, D., Colbert, D.T., Lee, R.S., Fischer, J.E., Rao, A.M., Eklund, P.C., and Smalley, R.E., *Large-Scale Purification of Single-Wall Carbon Nanotubes: Process, Product, and Characterization.* Appl. Phys. A, 1998. **67**(1): 29-37.
220. Feng, T., Hoagland, D.A., and Russell, T.P., *Assembly of Acid-Functionalized Single-Walled Carbon Nanotubes at Oil/Water Interfaces.* Langmuir, 2014. **30**(4): 1072-1079.
221. Briggs, N.M., Weston, J.S., Li, B., Venkataramani, D., Aichele, C.P., Harwell, J.H., and Crossley, S.P., *Multiwalled Carbon Nanotubes at the Interface of Pickering Emulsions.* Langmuir, 2015. **31**(48): 13077-13084.
222. Avendano, C., Brun, N., Fontaine, O., In, M., Mehdi, A., Stocco, A., and Vioux, A., *Multiwalled Carbon Nanotube/Cellulose Composite: From Aqueous Dispersions to Pickering Emulsions.* Langmuir, 2016. **32**(16): 3907-3916.
223. Hobbie, E.K., Bauer, B.J., Stephens, J., Becker, M.L., Mcguiggan, P., Hudson, S.D., and Wang, H., *Colloidal Particles Coated and Stabilized by DNA-Wrapped Carbon Nanotubes.* Langmuir, 2005. **21**(23): 10284-10287.

224. Wu, T., Wang, H., Jing, B., Liu, F., Burns, P.C., and Na, C., *Multi-Body Coalescence in Pickering Emulsions.* Nat Commun, 2015. **6**.
225. Matsui, J., Iko, M., Inokuma, N., Orikasa, H., Mitsuishi, M., Kyotani, T., and Miyashita, T., *Simple Fabrication of Carbon Nanotube Monolayer Film.* Chem. Lett., 2006. **35**(1): 42-43.
226. Zhang, Y., Shen, Y., Kuehner, D., Wu, S., Su, Z., Ye, S., and Niu, L., *Directing Single-Walled Carbon Nanotubes to Self-Assemble at Water/Oil Interfaces and Facilitate Electron Transfer*. Chem. Commun., 2008(36): 4273-4275.
227. Asuri, P., Karajanagi, S.S., Dordick, J.S., and Kane, R.S., *Directed Assembly of Carbon Nanotubes at Liquid−Liquid Interfaces: Nanoscale Conveyors for Interfacial Biocatalysis.* J. Am. Chem. Soc., 2006. **128**(4): 1046-1047.
228. Rodgers, A.N.J., Booth, S.G., and Dryfe, R.A.W., *Particle Deposition and Catalysis at the Interface between Two Immiscible Electrolyte Solutions (Ities): A Mini-Review.* Electrochem. Commun., 2014. **47**: 17-20.
229. David, V.G.A.A.D.W., ed. *Liquid-Liquid Interfaces, Theory and Methods* 1996, CRC Press: Boca Raton.
230. Toth, P.S., Rodgers, A.N.J., Rabiu, A.K., Ibanez, D., Yang, J.X., Colina, A., and Dryfe, R.A.W., *Interfacial Doping of Carbon Nanotubes at the Polarisable Organic/Water Interface: A Liquid/Liquid Pseudo-Capacitor.* J. Mater. Chem. A, 2016. **4**(19): 7365-7371.
231. Toth, P.S., Haigh, S.J., Rabiu, A.K., Rodgers, A.N.J., Rakowski, A.M., and Dryfe, R.A.W., *Preparation of Low-Dimensional Carbon Material-Based Metal Nanocomposites Using a Polarizable Organic/Water Interface.* J. Mater. Res., 2015. **30**(18): 2679-2687.
232. Svitova, T., Theodoly, O., Christiano, S., Hill, R.M., and Radke, C.J., *Wetting Behavior of Silicone Oils on Solid Substrates Immersed in Aqueous Electrolyte Solutions.* Langmuir, 2002. **18**(18): 6821-6829.
233. Borisenko, K.B., Evangelou, E.A., Zhao, Q., and Abel, E.W., *Contact Angles of Diiodomethane on Silicon-Doped Diamond-Like Carbon Coatings in Electrolyte Solutions.* J. Colloid Interface Sci., 2008. **326**(2): 329-332.
234. Binks, P.B., Tommy, H.S., ed. *Colloidal Particles at Liquid-Liquid Interface*. 2006, Cambridge University press: Cambridge, Uk.
235. Binks, B.P. and Clint, J.H., *Solid Wettability from Surface Energy Components: Relevance to Pickering Emulsions.* Langmuir, 2002. **18**(4): 1270-1273.
236. Shen, M. and Resasco, D.E., *Emulsions Stabilized by Carbon Nanotube−Silica Nanohybrids.* Langmuir, 2009. **25**(18): 10843-10851.
237. Daikhin, L.I., Kornyshev, A.A., and Urbakh, M., *Effect of Capillary Waves on the Double Layer Capacitance of the Interface between Two Immiscible Electrolytes.* Electrochim. Acta, 1999. **45**(4–5): 685-690.
238. Daikhin, L.I., Kornyshev, A.A., and Urbakh, M., *Capillary Waves at Soft Electrified Interfaces.* J. Electroanal. Chem., 2000. **483**(1–2): 68-80.
239. Aminur Rahman, M. and Doe, H., *Ion Transfer of Tetraalkylammonium Cations at an Interface between Frozen Aqueous Solution and 1,2-Dichloroethane.* J. Electroanal. Chem., 1997. **424**(1–2): 159-164.
240. Tournus, F., Latil, S., Heggie, M.I., and Charlier, J.C., *π-Stacking Interaction between Carbon Nanotubes and Organic Molecules.* Phys. Rev. B, 2005. **72**(7): 075431.

241. Britz, D.A. and Khlobystov, A.N., *Noncovalent Interactions of Molecules with Single Walled Carbon Nanotubes.* Chem. Soc. Rev., 2006. **35**(7): 637-659.
242. Kakiuchi, T., Noguchi, J., and Senda, M., *Kinetics of the Transfer of Monovalent Anions across the Nitrobenzene-Water Interface.* J. Electroanal. Chem., 1992. **327**(1): 63-71.
243. Osakai, T. and Ebina, K., *Non-Bornian Theory of the Gibbs Energy of Ion Transfer between Two Immiscible Liquids.* J. Phys. Chem. B, 1998. **102**(29): 5691-5698.
244. Nicholson, R.S., *Theory and Application of Cyclic Voltammetry for Measurement of Electrode Reaction Kinetics.* Anal. Chem., 1965. **37**(11): 1351-1355.
245. Mahé, E., Devilliers, D., and Comninellis, C., *Electrochemical Reactivity at Graphitic Micro-Domains on Polycrystalline Boron Doped Diamond Thin-Films Electrodes.* Electrochim. Acta, 2005. **50**(11): 2263-2277.
246. Amatore, C., Savéant, J.M., and Tessier, D., *Charge Transfer at Partially Blocked Surfaces.* J. Electroanal. Chem. Interfacial Electrochem., 1983. **147**(1): 39-51.
247. Sadki, S., Schottland, P., Brodie, N., and Sabouraud, G., *The Mechanisms of Pyrrole Electropolymerization.* Chem. Soc. Rev., 2000. **29**(5): 283-293.
248. Balint, R., Cassidy, N.J., and Cartmell, S.H., *Conductive Polymers: Towards a Smart Biomaterial for Tissue Engineering.* Acta Biomaterialia, 2014. **10**(6): 2341-2353.
249. Tat'yana, V.V. and Oleg, N.E., *Polypyrrole: A Conducting Polymer; Its Synthesis, Properties and Applications.* Russ. Chem. Rev., 1997. **66**(5): 443.
250. Gracia, R. and Mecerreyes, D., *Polymers with Redox Properties: Materials for Batteries, Biosensors and More.* Polym. Chem., 2013. **4**(7): 2206-2214.
251. Adhikari, B. and Majumdar, S., *Polymers in Sensor Applications.* Prog. Polym. Sci., 2004. **29**(7): 699-766.
252. Chen, G.Z., Shaffer, M.S.P., Coleby, D., Dixon, G., Zhou, W., Fray, D.J., and Windle, A.H., *Carbon Nanotube and Polypyrrole Composites: Coating and Doping.* Adv. Mater., 2000. **12**(7): 522-526.
253. Peng, C., Zhang, S., Jewell, D., and Chen, G.Z., *Carbon Nanotube and Conducting Polymer Composites for Supercapacitors.* Prog. Nat. Sci., 2008. **18**(7): 777-788.
254. Lin, H., Li, L., Ren, J., Cai, Z., Qiu, L., Yang, Z., and Peng, H., *Conducting Polymer Composite Film Incorporated with Aligned Carbon Nanotubes for Transparent, Flexible and Efficient Supercapacitor.* Sci. Rep., 2013. **3**: 1353.
255. Huang, F., Vanhaecke, E., and Chen, D., *In Situ Polymerization and Characterizations of Polyaniline on Mwcnt Powders and Aligned Mwcnt Films.* Catal. Today, 2010. **150**(1–2): 71-76.
256. Oueiny, C., Berlioz, S., and Perrin, F.-X., *Carbon Nanotube–Polyaniline Composites.* Prog. Polym. Sci., 2014. **39**(4): 707-748.
257. Gupta, V. and Miura, N., *Polyaniline/Single-Wall Carbon Nanotube (Pani/Swcnt) Composites for High Performance Supercapacitors.* Electrochim. Acta, 2006. **52**(4): 1721-1726.
258. Gupta, V. and Miura, N., *Influence of the Microstructure on the Supercapacitive Behavior of Polyaniline/Single-Wall Carbon Nanotube Composites.* J. Power Sources, 2006. **157**(1): 616-620.

259. Jurewicz, K., Delpeux, S., Bertagna, V., Béguin, F., and Frackowiak, E., *Supercapacitors from Nanotubes/Polypyrrole Composites.* Chem. Phys. Lett., 2001. **347**(1–3): 36-40.
260. Xiao, Q. and Zhou, X., *The Study of Multiwalled Carbon Nanotube Deposited with Conducting Polymer for Supercapacitor.* Electrochim. Acta, 2003. **48**(5): 575-580.
261. Byrne, M.T. and Gun'ko, Y.K., *Recent Advances in Research on Carbon Nanotube–Polymer Composites.* Adv. Mater., 2010. **22**(15): 1672-1688.
262. Cochet, M., Maser, W.K., Benito, A.M., Callejas, M.A., Martinez, M.T., Benoit, J.-M., Schreiber, J., and Chauvet, O., *Synthesis of a New Polyaniline/Nanotube Composite: "In-Situ" Polymerisation and Charge Transfer through Site-Selective Interaction.* Chem. Commun., 2001(16): 1450-1451.
263. Ferrer-Anglada, N., Kaempgen, M., Skákalová, V., Dettlaf-Weglikowska, U., and Roth, S., *Synthesis and Characterization of Carbon Nanotube-Conducting Polymer Thin Films.* Diamond Relat. Mater., 2004. **13**(2): 256-260.
264. Salvatierra, R.V., Oliveira, M.M., and Zarbin, A.J.G., *One-Pot Synthesis and Processing of Transparent, Conducting, and Freestanding Carbon Nanotubes/Polyaniline Composite Films.* Chem. Mater., 2010. **22**(18): 5222-5234.
265. Wallace, G.G., Smyth, M., and Zhao, H., *Conducting Electroactive Polymer-Based Biosensors.* TrAC, Trends Anal. Chem., 1999. **18**(4): 245-251.
266. Herrasti, P., DíAz, L., Ocón, P., Ibáñez, A., and Fatas, E., *Electrochemical and Mechanical Properties of Polypyrrole Coatings on Steel.* Electrochim. Acta, 2004. **49**(22–23): 3693-3699.
267. Wang, J., Dai, J., and Yarlagadda, T., *Carbon Nanotube−Conducting-Polymer Composite Nanowires.* Langmuir, 2005. **21**(1): 9-12.
268. Gao, M., Huang, S., Dai, L., Wallace, G., Gao, R., and Wang, Z., *Aligned Coaxial Nanowires of Carbon Nanotubes Sheathed with Conducting Polymers.* Angew. Chem. Int. Ed., 2000. **39**(20): 3664-3667.
269. Chen, J.H., Huang, Z.P., Wang, D.Z., Yang, S.X., Li, W.Z., Wen, J.G., and Ren, Z.F., *Electrochemical Synthesis of Polypyrrole Films over Each of Well-Aligned Carbon Nanotubes.* Synth. Met., 2001. **125**(3): 289-294.
270. Guo, M., Chen, J., Li, J., Tao, B., and Yao, S., *Fabrication of Polyaniline/Carbon Nanotube Composite Modified Electrode and Its Electrocatalytic Property to the Reduction of Nitrite.* Anal. Chim. Acta, 2005. **532**(1): 71-77.
271. Che, J., Chen, P., and Chan-Park, M.B., *High-Strength Carbon Nanotube Buckypaper Composites as Applied to Free-Standing Electrodes for Supercapacitors.* J. Mater. Chem. A, 2013. **1**(12): 4057-4066.
272. Shaffer, M.S.P., Fan, X., and Windle, A.H., *Dispersion and Packing of Carbon Nanotubes.* Carbon, 1998. **36**(11): 1603-1612.
273. Hughes, M., Chen, G.Z., Shaffer, Milo, S.P., Fray, D.J., and Windle, A.H., *Controlling the Nanostructure of Electrochemically Grown Nanoporous Composites of Carbon Nanotubes and Conducting Polymers.* Compos. Sci. Technol., 2004. **64**(15): 2325-2331.
274. J. Cunnane, V. and Evans, U., *Formation of Oligomers of Methyl- and Phenyl-Pyrrole at an Electrified Liquid/Liquid Interface.* Chem. Commun., 1998(19): 2163-2164.

275. Vignali, M., Edwards, R.a.H., Serantoni, M., and Cunnane, V.J., *Electropolymerized Polythiophene Layer Extracted from the Interface between Two Immiscible Electrolyte Solutions: Current–Time Analysis.* J. Electroanal. Chem., 2006. **591**(1): 59-68.
276. Evans-Kennedy, U., Clohessy, J., and Cunnane, V.J., *Spectroelectrochemical Study of 2,2':5',2'' -Terthiophene Polymerization at a Liquid/Liquid Interface Controlled by Potential-Determining Ions.* Macromolecules, 2004. **37**(10): 3630-3634.
277. Gorgy, K., Fusalba, F., Evans, U., Kontturi, K., and Cunnane, V.J., *Electropolymerization of 2,2':5',2" Terthiophene at an Electrified Liquid–Liquid Interface.* Synth. Met., 2001. **125**(3): 365-373.
278. Vignali, M., Edwards, R., and Cunnane, V.J., *Characterization of Doping and Electropolymerization of Free Standing Films of Polyterthiophene.* J. Electroanal. Chem., 2006. **592**(1): 37-45.
279. Salvatierra, R.V., Cava, C.E., Roman, L.S., and Zarbin, A.J.G., *Ito-Free and Flexible Organic Photovoltaic Device Based on High Transparent and Conductive Polyaniline/Carbon Nanotube Thin Films.* Adv. Funct. Mater., 2013. **23**(12): 1490-1499.
280. Salvatierra, R.V., Moura, L.G., Oliveira, M.M., Pimenta, M.A., and Zarbin, A.J.G., *Resonant Raman Spectroscopy and Spectroelectrochemistry Characterization of Carbon Nanotubes/Polyaniline Thin Film Obtained through Interfacial Polymerization.* J. Raman Spectrosc., 2012. **43**(8): 1094-1100.
281. Salvatierra, R.V., Zitzer, G., Savu, S.A., Alves, A.P., Zarbin, A.J.G., Chassé, T., Casu, M.B., and Rocco, M.L.M., *Carbon Nanotube/Polyaniline Nanocomposites: Electronic Structure, Doping Level and Morphology Investigations.* Synth. Met., 2015. **203**: 16-21.
282. Genies, E.M., Bidan, G., and Diaz, A.F., *Spectroelectrochemical Study of Polypyrrole Films.* J. Electroanal. Chem. Interfacial Electrochem., 1983. **149**(1): 101-113.
283. Cho, S.H., Song, K.T., and Lee, J.Y., *Recent Advances in Polypyrrole*, in *Handbook of Conducting Polymers*, T.A. Skotheim and J.R. Renolds, Editors. 2007, CRC Press: Boca Raton. p. 8-1.
284. Diaz, A.F., Castillo, J.I., Logan, J.A., and Lee, W.-Y., *Electrochemistry of Conducting Polypyrrole Films.* J. Electroanal. Chem. Interfacial Electrochem., 1981. **129**(1): 115-132.
285. Zhou, M. and Heinze, J., *Electropolymerization of Pyrrole and Electrochemical Study of Polypyrrole: 1. Evidence for Structural Diversity of Polypyrrole.* Electrochim. Acta, 1999. **44**(11): 1733-1748.
286. Zotti, G., Cattarin, S., and Comisso, N., *Electrodeposition of Polythiophene, Polypyrrole and Polyaniline by the Cyclic Potential Sweep Method.* J. Electroanal. Chem. Interfacial Electrochem., 1987. **235**(1–2): 259-273.
287. Asavapiriyanont, S., Chandler, G.K., Gunawardena, G.A., and Pletcher, D., *The Electrodeposition of Polypyrrole Films from Aqueous Solutions.* J. Electroanal. Chem. Interfacial Electrochem., 1984. **177**(1): 229-244.
288. Downard, A.J. and Pletcher, D., *The Influence of Water on the Electrodeposition of Polypyrrole in Acetonitrile.* J. Electroanal. Chem. Interfacial Electrochem., 1986. **206**(1): 139-145.

289. Johans, C., Clohessy, J., Fantini, S., Kontturi, K., and Cunnane, V.J., *Electrosynthesis of Polyphenylpyrrole Coated Silver Particles at a Liquid–Liquid Interface.* Electrochem. Commun., 2002. **4**(3): 227-230.
290. Kępas, A., Grzeszczuk, M., Kvarnström, C., Lindfors, T., and Ivaska, A., *Uv-Vis and Raman Spectroelectrochemistry of Electrodeposited Polypyrrole in Hexafluorophosphate.* Pol. J. Chem., 2007. **81**(12): 2207-2214.
291. Booth, S.G., Chang, S.-Y., Uehara, A., La Fontaine, C., Cibin, G., Schroeder, S.L.M., and Dryfe, R.A.W., *In Situ Xafs Study of Palladium Electrodeposition at the Liquid/Liquid Interface.* Electrochim. Acta, 2017. **235**: 251-261.
292. Saswata, B., Nam Hoon, K., Tapas, K., Kin-Tak, L., and Joong Hee, L., *Electrochemical Performance of a Graphene–Polypyrrole Nanocomposite as a Supercapacitor Electrode.* Nanotechnology, 2011. **22**(29): 295202.
293. Bora, C. and Dolui, S.K., *Interfacial Synthesis of Polypyrrole/Graphene Composites and Investigation of Their Optical, Electrical and Electrochemical Properties.* Polym. Int., 2014. **63**(8): 1439-1446.
294. Liu, Y.-C., Hwang, B.-J., Jian, W.-J., and Santhanam, R., *In Situ Cyclic Voltammetry-Surface-Enhanced Raman Spectroscopy: Studies on the Doping–Undoping of Polypyrrole Film.* Thin Solid Films, 2000. **374**(1): 85-91.
295. Kalbáč, M., Kavan, L., and Dunsch, L., *An in Situ Raman Spectroelectrochemical Study of the Controlled Doping of Semiconducting Single Walled Carbon Nanotubes in a Conducting Polymer Matrix.* Synth. Met., 2009. **159**(21–22): 2245-2248.
296. Kalbáč, M., Kavan, L., Zukalová, M., and Dunsch, L., *An in Situ Raman Spectroelectrochemical Study of the Controlled Doping of Single Walled Carbon Nanotubes in a Conducting Polymer Matrix.* Carbon, 2007. **45**(7): 1463-1470.
297. O'neill, A., Khan, U., and Coleman, J.N., *Preparation of High Concentration Dispersions of Exfoliated MoS_2 with Increased Flake Size.* Chem. Mater., 2012. **24**(12): 2414-2421.
298. Li, B.L., Zou, H.L., Lu, L., Yang, Y., Lei, J.L., Luo, H.Q., and Li, N.B., *Size-Dependent Optical Absorption of Layered MoS_2 and DNA Oligonucleotides Induced Dispersion Behavior for Label-Free Detection of Single-Nucleotide Polymorphism.* Adv. Funct. Mater., 2015. **25**(23): 3541-3550.
299. Chou, S.S., De, M., Kim, J., Byun, S., Dykstra, C., Yu, J., Huang, J., and Dravid, V.P., *Ligand Conjugation of Chemically Exfoliated MoS_2.* J. Am. Chem. Soc., 2013. **135**(12): 4584-4587.
300. Kim, J., Kwon, S., Cho, D.-H., Kang, B., Kwon, H., Kim, Y., Park, S.O., Jung, G.Y., Shin, E., Kim, W.-G., Lee, H., Ryu, G.H., Choi, M., Kim, T.H., Oh, J., Park, S., Kwak, S.K., Yoon, S.W., Byun, D., Lee, Z., and Lee, C., *Direct Exfoliation and Dispersion of Two-Dimensional Materials in Pure Water Via Temperature Control.* Nat. Commun., 2015. **6**: 8294.
301. Xu, R., Wu, C., and Xu, H., *Particle Size and Zeta Potential of Carbon Black in Liquid Media.* Carbon, 2007. **45**(14): 2806-2809.
302. Wang, K., Wang, J., Fan, J., Lotya, M., O'neill, A., Fox, D., Feng, Y., Zhang, X., Jiang, B., Zhao, Q., Zhang, H., Coleman, J.N., Zhang, L., and Blau, W.J., *Ultrafast Saturable Absorption of Two-Dimensional MoS_2 Nanosheets.* ACS Nano, 2013. **7**(10): 9260-9267.

303. Li, H., Zhang, Q., Yap, C.C.R., Tay, B.K., Edwin, T.H.T., Olivier, A., and Baillargeat, D., *From Bulk to Monolayer MoS_2: Evolution of Raman Scattering.* Adv. Funct. Mater., 2012. **22**(7): 1385-1390.
304. Frindt, R.F., *Single Crystals of MoS_2 Several Molecular Layers Thick.* J. Appl. Phys., 1966. **37**(4): 1928-1929.
305. Niyogi, S., Hamon, M.A., Perea, D.E., Kang, C.B., Zhao, B., Pal, S.K., Wyant, A.E., Itkis, M.E., and Haddon, R.C., *Ultrasonic Dispersions of Single-Walled Carbon Nanotubes.* J. Phys. Chem. B, 2003. **107**(34): 8799-8804.
306. Flint, E.B. and Suslick, K.S., *The Temperature of Cavitation.* Science, 1991. **253**(5026): 1397-1399.
307. Suslick, K.S., *The Chemical Effect of Ultrasound.* Sci. Am., 1989. **260**(2): 80-86.
308. Suslick, K.S., *Sonochemistry.* Science, 1990. **247**(4949): 1439-1445.
309. Katoh, R., Yokoi, H., Usuba, S., Kakudate, Y., and Fujiwara, S., *Sonochemical Polymerization of Benzene Derivatives: The Site of the Reaction.* Ultrason. Sonochem., 1998. **5**(2): 69-72.
310. Cataldo, F., *Ultrasound-Induced Cracking and Pyrolysis of Some Aromatic and Naphthenic Hydrocarbons.* Ultrason. Sonochem., 2000. **7**(1): 35-43.
311. Hamilton, C.E., Lomeda, J.R., Sun, Z., Tour, J.M., and Barron, A.R., *High-Yield Organic Dispersions of Unfunctionalized Graphene.* Nano Lett., 2009. **9**(10): 3460-3462.
312. Bissett, M.A., Kinloch, I.A., and Dryfe, R.A.W., *Characterization of MoS_2–Graphene Composites for High-Performance Coin Cell Supercapacitors.* ACS Appl. Mater. Interfaces, 2015. **7**(31): 17388-17398.
313. Nicolosi, V., Vrbanic, D., Mrzel, A., Mccauley, J., O'flaherty, S., Mcguinness, C., Compagnini, G., Mihailovic, D., Blau, W.J., and Coleman, J.N., *Solubility of $Mo_6S_4.5I_{4.5}$ Nanowires in Common Solvents: A Sedimentation Study.* J. Phys. Chem. B, 2005. **109**(15): 7124-7133.
314. Smith, B., Wepasnick, K., Schrote, K.E., Bertele, A.R., Ball, W.P., O'melia, C., and Fairbrother, D.H., *Colloidal Properties of Aqueous Suspensions of Acid-Treated, Multi-Walled Carbon Nanotubes.* Environ. Sci. Technol., 2009. **43**(3): 819-825.